LEED CRYSTALLOGRAPHIC STUDIES OF OXYGEN ADSORBED ON THE (0001) SURFACE OF ZIRCONIUM

by

KA-CHUNG HUI

A THESIS SUBMITTED IN PARTIAL FULFILMENT OF

THE REQUIREMENTS FOR THE DEGREE OF

DOCTOR OF PHILOSOPHY

in

THE FACULTY OF GRADUATE STUDIES

Department of Chemistry

We accept this thesis as conforming

to the required standard

THE UNIVERSITY OF BRITISH COLUMBIA

June, 1986

In presenting this thesis in partial fulfilment of the requirements for an advanced degree at the The University of British Columbia, I agree that the Library shall make it freely available for reference and study. I further agree that permission for extensive copying of this thesis for scholarly purposes may be granted by the Head of my Department or by his or her representatives. It is understood that copying or publication of this thesis for financial gain shall not be allowed without my written permission.

Department of Chemistry

The University of British Columbia
2075 Wesbrook Place
Vancouver, Canada
V6T 1W5

Date: June, 1986

Abstract

The work in this thesis includes LEED crystallographic investigations for the (2x2) structure obtained by adsorbing oxygen on the (0001) surface of zirconium at below 250°C, a study of the stability of the intensity of fractional order beams with different coverages of adsorbed species on hcp(0001) metal surfaces, a preliminary structural investigation of the Zr(0001)-(1x1)-O structure, and the setting up of a TV camera system for faster acquisition of diffracted beam intensities.

The LEED crystallographic study for oxygen adsorption on the Zr(0001) surface yields the first structural data for the initial stages of oxidation on any hcp(0001) surface. The zirconium surface was cut from a high purity single crystal, and characterized with LEED and Auger electron spectroscopy. Intensity versus energy (I(E)) curves were measured by the photographic method at normal incidence for seven and two diffracted beams respectively for the (2x2) and (1x1) structures. Theoretical I(E) curves were calculated using the 'combined space' approach to multiple scattering calculations (e.g. composite layer calculations, renormalized forward scattering and layer doubling) for a range of Zr-O interlayer spacings and many different adsorption models. Levels of correspondence between experimental and calculated I(E) curves were assessed with the Pendry R-factor. The analyses suggest that O atoms occupy octahedral holes between successive bulk Zr layers in

the (2x2) structure, and that the substrate Zr layers undergo a fcc type reconstruction which spans the depth of O atoms. The Zr-O interlayer spacing is found to be 1.33 Å; this corresponds to a Zr-O bond length of 2.29 Å, and therefore is in close agreement with the value (2.31 Å) for bulk ZrO. Having only two independent beams for the (1x1) surface precludes any definitive structural conclusions, but the preliminary analysis here indicates that the first three layers resemble (111) layers of ZrO with the Zr-O interlayer spacing equal to 1.37 Å and a consequent bond length of 2.31 Å.

Diffracted beam I(E) curves were calculated at normal incidence with the renormalized forward scattering method for (2x1) and (2x2) structures involving adsorption on (0001) surfaces of titanium and zirconium, and these data were compared with the R-factors of Pendry and of Zanazzi and Jona. This study supports an observation by Yang *et al.* that LEED fractional order beam intensities may be closely constant with changing adsorbate coverage; a new feature found here is that this conclusion holds even for structures where neighboring adsorbed atoms are separated by just the substrate interatomic distance. This observation could be exploited in the Zr(0001)-(2x2)-O analysis by using whichever translational symmetry that gave the easier computational effort. This work provides further support for the neglect-of-beam-set approximation, which was introduced by Van Hove *et al.* for making more tractable the

calculation of LEED intensities from surfaces with large unit meshes.

Also established in this work is an intensity acquisition system, which utilizes a surveilance type TV camera and commercial video LEED analyzer (VLA). Initial examinations were given for two background intensity subtraction schemes. I(E) data collected with the video LEED system in the later stages of this work are compared satisfactorily with the independent measurements obtained by the photographic method.

Table of Contents

List of Tables

List of Figures

CHAPTER 1

STUDIES OF ORDERED AD-LAYERS ON WELL-CHARACTERIZED CRYSTALLOGRAPHIC PLANES

1.1 HISTORICAL DEVELOPMENT

Since the first low energy electron diffraction (LEED) experiment performed by Davisson and Germer[1] in 1927, little progress was made on the studies of well-defined single-crystal surfaces until the 1960's. The main reason for dormancy in this branch of surface science arose from the problem of quantity: one square centimeter of a surface contains only about 10^{15} particles or approximately 10^{-9} mole. In other words, the conventional bulk techniques employed then were not sensitive enough for surface studies. Historically, the deficiency in instrumental sensitivity was countered by working with materials which were extremely porous or consisted of very small particles to ensure a high surface/volume ratio. Although some useful empirical relationships can be derived from these traditional studies, they necessarily give averaged information on 'mixed' crystallographic planes. In order to gain insights to the primary processes that occur on surfaces at the atomic level, the 'clean-surface' approach is favored. Such studies use well oriented crystal faces held in closely controlled environments. As recently as two decades ago this approach was barely feasible because very few studies could answer the most fundamental question of whether a surface was atomically clean, let alone what type of foreign atoms might have been present.

In the last fifteen years or so the 'clean surface' approach has gained strength. This has been especially

because of the developing availability of convenient facilities for readily obtaining ultra-high vacuum(UHV†); also many new and resurrected surface sensitive techniques were developed. In spite of such a short period of growth, surface science has already achieved considerable sophistication. The analysis of simple clean surface structures[2] can now be straightforward. Indeed, considerable knowledge is now available for the relaxation effects at clean surfaces, and a start is being made in studying reconstructed surfaces[3]. Further, since the mid-1970's considerable attention has been directed to systems involving ordered adsorbates. Such studies may involve atoms or small molecules[4] such as CO, or simple hydrocarbons[5] adsorbed on various metal surfaces. Recently there has been a growing interest in studying metal adsorbates on semiconductor surfaces[6]. The latter studies are made possible, in part, by advances in molecular beam epitaxy[7].

Three major stimuli have encouraged this boom in surface science. They are (1) recent developments in materials science, (2) the need for new knowledge in heterogeneous catalysis, spurred especially by society's energy requirements, and (3) exciting developments in small scale electronics device technology. Fundamental processes involving crystal growth, corrosion, surface segregation and embrittlement are the main concerns for material scientists. Chemists, on the other hand, are more interested in the

---

†UHV $\leq 1 \times 10^{-9}$ torr.

energetics and kinetics of surface processes, including the adsorption and desorption mechanisms. With its recent spectacular developments, the electronics industry necessarily devotes much effort to surface research, the objective being to improve quality of thin integrated circuits by utilizing knowledge of metal/semiconductor interfaces in fabrication processes. Their objectives may be different, but the types of research on surfaces carried out by each of the different disciplines have much in common, hence there is inevitably a strong inter-disciplinary component in modern surface science.

1.2 TECHNIQUES RELEVANT TO AD-LAYERS STUDIES

Several criteria are important in the construction of a good adsorbate-sensitive technique. First, it should give reasonably strong signals from even low atomic densities of adsorbate molecules. Second, it must be able either to avoid retrieving information from the bulk of the crystal, or to distinguish signals from the bulk and the surface. Finally, it is often preferred that the probing particles have minimum destructive effect on the adlayers (although of course this is not the case in the thermal, or particle stimulated desorption methods). Aside from techniques dependent on the supply of thermal energy, surface methods can be classified into three categories according to probing sources: electron scattering techniques; ion/atom beam techniques and photon (including synchrotron radiation) beam

techniques. Most of these techniques involve studying the interaction of the probing particles and the surface region of the adsorption system through the measurement of the angular and/or energy distribution of the scattered or emitted particles. Several commonly used techniques and their acronyms are listed in Table 1.1; the experimental details of each individual technique can be found in the references given. However, the principles involved in each category are discussed briefly in the following sections.

1.2.1 ELECTRON SCATTERING TECHNIQUES

Electrons in the energy range to about 1 keV are commonly used as probes in surface science. Seah and Dench[25] have given recent information of electron mean free path for inelastic scattering in solids as a function of the electron energy. For metals, the mean free path versus energy curves exhibit broad minima at between 10^1 and 10^2 eV, with corresponding mean free paths of around 3 to 10 Å. Since high density layers in metals have interlayer spacings of around 2 to 3 Å, low-energy electrons can probe only a very restricted number of atomic layers if the electrons emerge from the surface without losing energy. The mean free path length L for inelastic scattering is defined by

$$I(l) = I_0 \exp(-l/L) \qquad (1.1)$$

Acronym	Technique	Probe particle	Measured particle	Information
AES	Auger-electron spectroscopy[8,9]	Electron	Electron	Composition
HREELS	High-resolution electron energy loss spectroscopy[10]	Electron	Electron	Vibrational modes
LEED	Low energy electron diffraction[11,12]	Electron	Electron	Geometry
RHEED	Reflection high energy electron diffraction[13]	Electron	Electron	Geometry
HEAD	Helium-atom diffraction[14]	Atom	Atom	Surface potential map
INS	Ion neutralization spectroscopy[15]	Ion	Atom	Electronic structure
LEIS	Low energy ion-scattering[16]	Ion	Ion	Atomic positions
RBS	Rutherford back scattering[17]	Ion	Ion	Atomic positions
SIMS	Secondary-ion mass spectroscopy[18]	Ion	Ion	Composition profile
ADPD	Angular-dependent photoelectron diffraction[19]	Photon	Electron	Local structure
EDPD	Energy-dependent photoelectron diffraction[20]	Photon	Electron	Local structure
NEXAFS	Near-edge X-ray absorption fine structure[21]	Photon	Photon, electron	Intramolecular bonding
SEXAFS	Surface extended X-ray absorption fine structure[21,22]	Photon	Photon, electron	Local coordination
UPS	Ultra-violet photoelectron spectroscopy[23]	Photon	Electron	Valence states
XD	X-ray diffraction[24]	Photon	Photon	Long-range structure
XPS	X-ray photoelectron spectroscopy[9]	Photon	Electron	Chemical shifts, quantitative composition

Table 1.1: Adsorbate-sensitive techniques and their characteristics. Individual experimental detail can be found in the references quoted under the technique column.

where I_0 is the incident intensity at a particular energy, and this is attenuated to $I(l)$ after travelling a distance l. Clearly a low value of L corresponds to a high probability for inelastic scattering; correspondingly there will be a high surface sensitivity in experiments in which the electrons are detected at specific energy values.

High-Resolution Electron Energy Loss Spectroscopy (HREELS). Electrons scattering off surfaces can lose energy in various ways. One of these involves excitation of the vibrational modes of atoms and molecules on the surface. With a monochromatized incident beam, at energy from 1 to 10 eV, HREELS measures such vibrational modes. This technique proves to be a powerful tool for hydrocarbon adsorption studies since many other surface techniques cannot detect hydrogen. Unlike optical spectroscopies such as infra-red and Raman spectroscopies, HREELS can measure vibrational modes both perpendicular and parallel to the surface.

Low-Energy Electron Diffraction (LEED). In this technique, the elastically scattered electrons diffract to provide information about the long-range periodicity of the surface structures. The de Broglie wavelength, λ(in Å), of an electron with energy E(in eV) is given by

$$\lambda = \sqrt{(150.4/E)} \qquad (1.2)$$

In the energy range 10 to 500 eV, the electron wavelength varies from 4 to 0.6 Å, and therefore it is generally of the

same order as interatomic and interlayer distances in adlayer structures and metal substrates. The translational symmetry of the surface determines the diffraction pattern; the measured diffracted beam intensities, in conjunction with multiple scattering calculations, can be used to determine interatomic distances.

Reflection High-Energy Electron Diffraction (RHEED). This technique is similar in principle to LEED but utilizes higher incident beam energies(1 to 50 keV). The longer mean free paths associated with higher energies give a reduction in surface sensitivity. In RHEED this is countered by using grazing angles of incidence and emergence. Due to its deeper penetration, RHEED is especially suitable for studies of chemisorption which lead to reaction into the bulk. A similar technique employing incident electron energies between those for LEED and RHEED is called *Medium-Energy Electron Diffraction* (MEED).

Auger Electron Spectroscopy (AES). When an atomic core level is ionized, the subsequent filling of the orbital by an electron from a less-tightly bound level may be accompanied by the emission of a photon or a second electron. This latter electron is termed an Auger electron after P. Auger[26] who first identified the effect in a cloud chamber experiment. The kinetic energy of the Auger electron thus contains information of the energy levels involved. A measurement of the kinetic energies of the Auger electrons from one or more such transitions can then

identify the element(s) present on a surface. Hence AES is routinely used for elemental analysis of surfaces.

Since LEED and AES are the principal techniques used in this laboratory, they will be discussed in depth in the next chapter.

1.2.2 ION OR ATOM SCATTERING TECHNIQUES

Atoms and ions incident on solid surfaces can provide information about the latter through the analysis of (1) the back-scattered primary particles; (2) particles sputtered off from the surface; and (3) electrons emitted from the surface resulting from excitation by the primary beam. These techniques typically use beams of H^+ or He^+ in the energy range of 100 eV to 3 MeV. It is useful to divide the energy into low and high regimes characterized by ion velocities below and above the Bohr velocity of 2.2×10^6 ms^{-1}. In the higher energy regime, the ions cast a very narrow shadow cone of radius about 0.1 Å, and hence have a negligible probability of being neutralized. Consequently, the scattering process can usually be treated kinematically, thus simplifying computations. In the low energy regime, the shadow cone radius is about 1 Å and the probability of neutralization is high. These ions are therefore often used to study the electronic structures of the surface atoms.

Rutherford Back Scattering (RBS). Here a high energy (2-3 MeV) beam of H^+ or He^+ is incident on an ordered surface. These primary ions are scattered by the exposed

surface atoms which 'see' the primary beam directly. If the back-scattered ions are energy analyzed, the atomic weight(s) of the exposed atoms can be determined through simple kinematic calculations. The intensities of these energy peaks identify the number of exposed atoms; further, a measurement of these intensities as a function of incidence angle can reveal the geometrical arrangement of the surface atoms (although careful corrections are required for some parameters, including thermal vibrations).

Secondary-Ion Mass Spectrometry (SIMS). This technique typically uses an ion beam in the energy range 1 to 20 keV. Surface layers are sputtered off as atoms and ions (including clusters), and the ionized fraction is identified in a mass spectrometer. Dynamic SIMS can give surface elemental compositions in the form of depth profiles; however, quantification is difficult due to matrix effects and differential sputtering rates for different elements.

Low-Energy Ion Scattering (LEIS) is similar to RBS, but uses ions of energy about 1 keV. Due to the larger radius of the shadow cone, this technique is sensitive to the exposed atoms only. A version called *Impact Collision Ion Scattering Spectroscopy* (ICISS[27]) measures back-scattered ions at a scattering angle of 180° only. This eliminates blocking effects and allows one to deduce the distance between surface atoms from the shadowing effect alone.

Ion Neutralization Spectroscopy (INS). Lower energy ($\simeq 10^2$ eV) He^+ ions have a high probability of capturing

electrons from the surface atoms and hence becoming neutralized. The subsequent filling of the hole thus created in the surface may result in ejection of a slow electron, as in the Auger process. This gives information on occupied densities of states; however, the insignificant penetration depth of the low-energy ions makes INS extremely surface sensitive.

Helium-Atom Diffraction (HEAD). One can also probe surfaces using low-energy atoms. For example, for He at 10 to 200 meV, the de Broglie wavelength λ (in Å) at energy E (in eV) is given by

$$\lambda = 0.14/\sqrt{E} \qquad (1.3)$$

Thus He atoms with the thermal energy of 200 meV have a wavelength about 1 Å, and so can readily diffract from surfaces. HEAD measures the angular distribution of back-scattered He atoms, thus revealing the 2-dimensional corrugation of the potential between the He atoms and the surface.

1.2.3 PHOTON BEAM TECHNIQUES

Synchrotron sources allow experimenters access to highly collimated and continuous wavelengths of radiation that are not available from other sources. The high intensity of synchrotron radiation gives a higher signal to noise ratio than conventional X-ray generators. By way of

comparison, the most powerful commercially available X-ray generator, a 60-kW rotating-anode tube, delivers 10^8 photons$\cdot s^{-1}$, whereas a synchrotron source can deliver a thousand times that amount.

Surface-Extended X-ray Absorption Fine Structure (SEXAFS) provides one of the most successful applications of synchrotron radiation to surface studies. With an incident beam of soft X-rays of increasing energy, a photoelectron is emitted when the incident photon exceeds the threshold for exciting a core electron of a surface atom. In SEXAFS, those ejected photoelectrons with kinetic energies from 50 to 500 eV are studied. The yield of the ejected electrons from the absorbing atoms is modulated as a function of incident photon energy due to the interference between the outgoing electrons and those backscattered from neighboring atoms. By Fourier analysis of this modulation, the distance between the absorbing atom and its neighbors can be determined. Moreover, if the excitation source is synchrotron radiation (which is polarized), comparison of the amplitude of the interference terms yields information on the adsorption site[28] rather than just the bond length.

Near Edge X-ray Absorption Fine Structure (NEXAFS) is a technique very similar to SEXAFS. However, NEXAFS studies those ejected photoelectrons with kinetic energies near the threshold of excitation (e.g. within 50 eV of the threshold). For molecular adsorption systems, NEXAFS results are dominated by intramolecular resonances[21], which

involve transitions into molecular orbital states, such as σ^* and π^*, whose wavefunctions have amplitudes that are largely localized within the molecule. As a result, NEXAFS is particulary sensitive to the intramolecular bond lengths and the orientation of these bonds relative to the surface.

Energy-Dependent and Angular-Dependent Photoelectron Diffraction (EDPD and ADPD) are techniques closely related to SEXAFS and NEXAFS. Here the number of photoelectrons emitted from a given core level is measured directly as a function of photon beam energy or angle. By measuring the photoelectrons coming from a specific level, the interfering absorption edges seen in SEXAFS can be avoided. Like SEXAFS, these two techniques provide information on local geometrical structure.

Ultraviolet Photoelectron Spectroscopy (UPS) and *X-ray Photoelectron Spectroscopy* (XPS or ESCA). Besides helping develop new surface techniques, synchrotron radiation greatly enhances the effectiveness of several traditional spectroscopies for surface studies. The latter include UPS and XPS. Depending on the incident photon energy, electrons can be ejected from different electronic levels of a surface atom. Both UPS and XPS involve measuring kinetic energies of such emitted photoelectrons. UPS is used to study the valence electronic structure of the surface species; while XPS probes core levels and provides chemical shift information as well as quantitative surface composition.

X-ray Diffraction(XD) is a well-developed technique for studying structure in bulk solids, but applications to surface structure are starting to be developed. Because X-rays penetrate deeply into a solid, the surface signal is necessarily superimposed on a large signal from the bulk, although the former may be maximized with grazing directions of incidence. X-ray diffraction has been used to analyze surface nets with a different periodicity from the bulk. A potential advantage of XD for surface science stems from the application of single (i.e. kinematical) scattering theories.

1.3 SOME BASIC KNOWLEDGE FROM ADSORPTION STUDIES ON METAL SURFACES

The atomic geometry of a surface or interface is, in certain respects, its most fundamental property. From a chemist's standpoint this property determines electronic structure, and ultimately all other properties, including, as one example, reactivity and specificity in catalysis. Studies with LEED, SEXAFS, photoelectron diffraction and ion scattering techniques are starting to provide data on atomic geometrical arrangements for ordered adlayers on well-defined single crystal surfaces. The present situation is that some consistency in structural conclusions can be reached when different techniques are applied to the same surface (e.g. current status for O adsorbed on Al(111)[29] or CO on Ni(100)[30]).

AES, HREELS, INS, thermal desorption[31] and photoemission spectroscopies now offer researchers possibilities to study the nature of the surface chemical bond at the atomic level. This knowledge is essential to the understanding of surface reactivity and reaction mechanism.

Studies of geometrical arrangements for metals adsorbed on surfaces of other metals are so far restricted to LEED analyses, and the total information is very limited. More experimental results in this field are necessary to assist materials scientists to understand the solid-solid interface.

1.3.1 THE STRUCTURAL PARAMETERS

From the overlayer-substrate systems studied so far, some general patterns regarding structural parameters are starting to emerge. One of these is that the adsorbed atoms tend to occupy sites where they are in contact with the maximum number of substrate atoms (largest coordination number). This site is often the one that the bulk atoms would occupy in order to continue the bulk lattice into the overlayer (e.g. bABAB...and cABCABC..., where the lower case letters represent the atom positions for the overlayer). In other words, adsorbed atoms tend to heal broken bonds at a surface. Using ICISS, Aono *et al.*[32] have determined that these sites can correspond to locations of high surface electronic density. The frequently observed contraction of the topmost interlayer spacing at a clean metal surface may

result from electrostatic attractions associated with charge polarizations at the interface.

Sometimes adsorbed layers may affect positions of atoms in the underlying surface. This may involve relaxations, of either vertical or horizontal types, in a basically unreconstructed surface. Alternatively an adsorbed layer may induce reconstruction in an otherwise unreconstructed surface, or may cause the basic surface to revert to the essentially unreconstructed form even though it is reconstructed in the most stable form of the clean surface. The study of surface crystallography has the important objective of providing precise information for all such effects. As well this information can encourage the development of models and understandings specifically for the surface chemical bond.

1.3.2 THE NATURE OF THE SURFACE CHEMICAL BOND

Although a full understanding of the surface chemical bond is not yet possible, several empirical characteristics have been observed with adsorbate-sensitive techniques, such as in particular HREELS, AES, NEXAFS, UPS and XPS. In turn such observations have encouraged mathematical formulations[33,34], but so far the degree of match between theory and experiment is still generally inferior to those currently obtainable for individual molecules or for bulk solids.

With various surface spectroscopies, it has been demonstrated that even on the more atomically homogeneous low-Miller-index surfaces, several binding sites are often distinguishable by their structure and binding strength. As a result, a sequential filling of binding sites may occur with increasing adsorbate coverage. With a particular adsorbate, these binding sites and binding strengths vary with crystal face. These variations add to the complexities which make adsorption studies so challenging.

One novel feature of the surface chemical bond is its dependence on temperature. At low temperature near the boiling points of the adsorbate atoms or molecules, adsorption decreases with increase in temperature at a given pressure. This type of adsorption is known as physical adsorption which is characterized by van der Waals or simple electrostatic interactions and low heats of adsorption (<15 $kcal \cdot mol^{-1}$). For some small molecules such as CO and O_2 on metals, the amount that can be adsorbed starts to rise again as the temperature goes up further. This type of adsorption is generally called chemisorption (or 'activated adsorption' since an energy of activation is required). In the context of the transition from physical adsorption to chemisorption, studies of hydrocarbon molecules adsorbed on some metal surfaces have illustrated sequential bond breaking within the adsorbate molecule with increase in temperature[35,36]. In addition, the details are most varied on heterogeneous surfaces. For example, on stepped surfaces, there is now

abundant evidence[37] that dissociation preferentially occurs at steps or kinks.

Chemisorption involves covalent bond formation. In principle therefore chemisorption bond lengths should relate to those in conventional solid state chemistry. Analyses of surface structural information, from this point of view, have been given by Mitchell and other members of our group[38].

1.4 AIM OF THE THESIS

The work described in this thesis represents a contribution to the development of the subject of LEED crystallography. Specific studies have been made for two types of ordered oxygen adsorption on the (0001) surface of zirconium. The first gives the same number of diffracted beams as the clean Zr(0001) surface; while the second leads to four times as many diffracted beams as the clean surface. A theoretical study which evolved from the (2x2) adsorption was also made.

The motivation for studying the Zr(0001) surface is that structural parameters are generally not well known for adsorbates on hcp(0001) surfaces. In fact, previous LEED studies involving such a surface are restricted mainly to the adsorption of cadmium[39], carbon monoxide[40], and nitrogen[41] on Ti(0001). One interesting result from these studies[41] is the formation of a nitrogen underlayer on Ti(0001). Since both titanium and zirconium belong to group

4† in the periodic table, their chemical properties may be very similar. Adsorption studies on Zr(0001) could therefore shed further light on the phenomenon of underlayer adsorption.

Despite the similarity with titanium, and the fact that zirconium has numerous potential applications[42], studies utilizing the 'clean surface' approach on Zr(0001) are so far very limited. Indeed structural information is restricted to the previous LEED analysis on the clean surface from this laboratory[43]. Factors which have possibly inhibited active study include (1) the high reactivity of zirconium which forms stable oxides, carbides and nitrides in air; (2) the difficulty in obtaining a single crystal of zirconium (not commercially available); and (3) a phase transition from hcp to bcc at a rather low temperature (865°C). The last factor restricts annealing temperatures to below 800°C in practice, and this limits procedure for obtaining ordered surfaces.

Oxygen is a common adsorbate in chemisorption studies, not least because of its important role in fundamental chemical and biological reactions. In addition, the effect of chemisorbed oxygen on single crystal surfaces is being scrutinized closely by the electronics industry because sample wafers are in contact either with air or trace amounts of oxygen constantly in the fabrication process. So far the structural details for oxygen chemisorbed on many

---

†IUPAC notation: 1-18.

well characterized single crystal planes are still unknown in most cases, although several LEED studies have shown that oxygen occupies 'unexpected' sites more often than other gases[44].

Through the study of oxygen chemisorbed on Zr(0001), it is hoped to add to our knowledge about the properties of group 4 metals towards oxygen, and thereby start to generate information about the initial stages of oxidation. More broadly, this should help to elucidate models of the oxidation process of other electropositive elements. Incidentally, one of the most-studied related systems is for oxygen on Al(111)[29].

The layout of the thesis is described as follows.

Chapter 2 outlines the physics of low energy electron diffraction as well as the Auger process. The factors contributing to diffracted beam intensities will be discussed in a semi-quantitative approach.

Chapter 3 discusses the 'combined space' approach in multiple scattering calculations for the diffracted beam intensities, and the important non-geometrical parameters required. A general strategy for setting up an affordable multiple scattering calculation is given.

Chapter 4 examines some general experimental aspects in LEED/AES studies. Topics include UHV, sample preparation, monitoring surface cleanliness by AES, and data acquisition of LEED spot intensities. For the last topic, special attention is focussed on the on-line TV camera method which

is new to this laboratory, and was developed during this work.

Chapter 5 compares the calculated I(E) curves of p(2x1) and p(2x2) surface structures on two hcp(0001) surfaces. Mathematical methods for I(E) curve comparison such as the Zanazzi-Jona and Pendry R-factors are presented. Several approximate schemes of multiple scattering calculation as implied by the results here are discussed.

Chapter 6 reports the adsorption studies of oxygen on Zr(0001) by LEED and AES. Analysis of diffracted beam intensities is performed for both the (1x1) and the (2x2) structures.

CHAPTER 2

PRINCIPLES OF LEED AND AES

2.1 ELECTRON DIFFRACTION FROM ORDERED SURFACES

As mentioned in Section 1.2.1, electrons with wavelengths of the order of interatomic distances in an ordered surface can be diffracted analogously to the much better known X-ray diffraction. The major difference between these two types of diffraction is that X-ray diffraction is basically kinematical whereas electron diffraction involves multiple scattering between the incident electrons and the atoms of the crystal lattice. Nevertheless, the LEED pattern formed by diffracted beams on a collecting screen is a direct consequence of the translational symmetry of the surface region. The diperiodicity of the latter region is conveniently represented by a 2-dimensional net, for which the unit basis vectors are designated here as $\underset{\sim}{s}_1$ and $\underset{\sim}{s}_2$.

2.1.1 CONDITIONS FOR ELASTIC DIFFRACTION

Outside the influence of the crystal, both incident and diffracted electrons normally experience a field free region where they are conveniently represented by plane waves

$$\Psi_{\underset{\sim}{k}}(\underset{\sim}{r}) = \exp(i\,\underset{\sim}{k}\cdot\underset{\sim}{r}). \qquad (2.1)$$

In equation (2.1) the wave vector $\underset{\sim}{k}$ specifies the direction of the beam, and its magnitude ($|\underset{\sim}{k}|=2\pi/\lambda$) relates to energy through

$$E = \hbar^2|\underset{\sim}{k}|^2/(2m), \tag{2.2}$$

where m is the electron's mass and $\hbar$ is Planck's constant divided by 2π. For incident and diffracted beams of wave vectors $\underset{\sim}{k}_o$ and $\underset{\sim}{k}'$ respectively, the differential scattering cross section resulting from the interaction with the solid can be expressed quite generally as

$$d\sigma/d\Omega = (m/2\pi\hbar^2)^2|\langle\underset{\sim}{k}'|\hat{T}|\underset{\sim}{k}_o\rangle|^2, \tag{2.3}$$

where $\hat{T}$ is an appropriate transition operator[45,46]. Furthermore, when the Hamiltonian of the electron is invariant under a symmetry operation $\hat{S}$ applied to the crystal, the matrix elements in (2.3) satisfy[45,46]

$$\langle\underset{\sim}{k}'|\hat{T}|\underset{\sim}{k}_o\rangle = \langle\underset{\sim}{k}'|\hat{S}^{-1}\hat{T}\hat{S}|\underset{\sim}{k}_o\rangle = \langle\hat{S}\underset{\sim}{k}'|\hat{T}|\hat{S}\underset{\sim}{k}_o\rangle. \tag{2.4}$$

If $\hat{S}$ represents translation by a surface net vector $\underset{\sim}{t}$, (2.4) becomes

$$\langle\underset{\sim}{k}'|\hat{T}|\underset{\sim}{k}_o\rangle = \exp[i(\underset{\sim}{k}_o-\underset{\sim}{k}')\cdot\underset{\sim}{t}]\langle\underset{\sim}{k}'|\hat{T}|\underset{\sim}{k}_o\rangle, \tag{2.5}$$

which immediately implies that either the trivial solution

$$\langle\underset{\sim}{k}'|\hat{T}|\underset{\sim}{k}_o\rangle = 0 \tag{2.6}$$

holds, or alternatively the more interesting condition

$$\exp[i(\underset{\sim}{k}_o - \underset{\sim}{k}')\cdot\underset{\sim}{t}] = 1. \tag{2.7}$$

Since the surface net vector $\underset{\sim}{t}$ has the form

$$\underset{\sim}{t} = m\underset{\sim}{s}_1 + n\underset{\sim}{s}_2 \tag{2.8}$$

for integers m and n, equation (2.7) will be satisfied whenever the incident and diffracted wave vectors differ by a vector of the reciprocal net

$$\underset{\sim}{g} = \underset{\sim}{k}_o - \underset{\sim}{k}' = h\underset{\sim}{s}_1^* + k\underset{\sim}{s}_2^*, \tag{2.9}$$

where h and k are integers. The reciprocal net basis vectors $\underset{\sim}{s}_1^*$ and $\underset{\sim}{s}_2^*$ must satisfy the conditions

$$\underset{\sim}{s}_1\cdot\underset{\sim}{s}_1^* = \underset{\sim}{s}_2\cdot\underset{\sim}{s}_2^* = 2\pi, \tag{2.10a}$$

$$\underset{\sim}{s}_1\cdot\underset{\sim}{s}_2^* = \underset{\sim}{s}_2\cdot\underset{\sim}{s}_1^* = 0, \tag{2.10b}$$

and they are related to the unit mesh vectors of the real surface net by

$$\underset{\sim}{s}_1^* = \frac{2\pi}{s_1}\sin^2\phi(\hat{\underset{\sim}{s}}_1 - \hat{\underset{\sim}{s}}_2\cos\phi), \tag{2.11a}$$

$$\underset{\sim}{s}_2^* = \frac{2\pi}{s_2}\sin^2\phi(\hat{\underset{\sim}{s}}_2 - \hat{\underset{\sim}{s}}_1\cos\phi), \tag{2.11b}$$

where the s_i (i=1,2) represent magnitudes of the basis

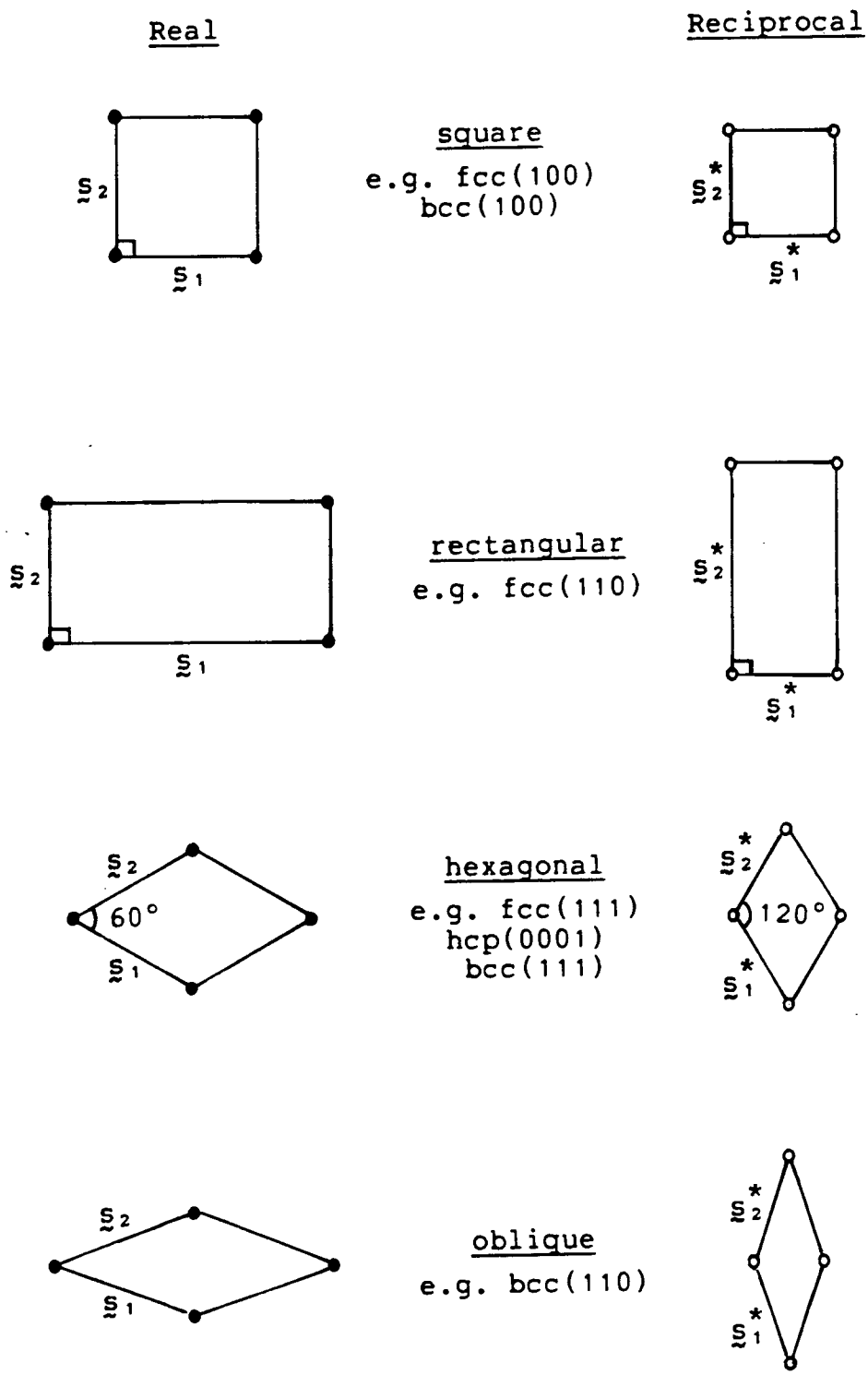

Figure 2.1: Some common real space surface nets and their corresponding reciprocal nets.

vectors $\underset{\sim}{s}_i$, and the $\hat{\underset{\sim}{s}}_i$ equal $\underset{\sim}{s}_i/s_i$ (i.e. represent unit vectors giving the direction of $\underset{\sim}{s}_i$); and ϕ is the angle between $\underset{\sim}{s}_1$ and $\underset{\sim}{s}_2$. With these choices in $\underset{\sim}{s}_1^*$ and $\underset{\sim}{s}_2^*$, it can easily be shown that

$$\underset{\sim}{g}\cdot\underset{\sim}{t} = 2N\pi, \tag{2.12}$$

where N is an integer. Hence, the left hand side of equation (2.7) is also unity. Figure 2.1 shows some common examples of surface nets in real space and their corresponding reciprocal nets.

Conditions for elastic diffraction can now be summarized in terms of conservation of energy

$$|\underset{\sim}{k}_{\underset{\sim}{g}}^-|^2 = |\underset{\sim}{k}_0^+|^2, \tag{2.13}$$

and conservation of momentum parallel to the surface

$$\underset{\sim}{k}_{\underset{\sim}{g}_{||}}^- = \underset{\sim}{k}_{0_{||}}^+ + \underset{\sim}{g}(hk). \tag{2.14}$$

In equations (2.13) and (2.14), the different diffracted beams are distinguished by subscripts which identify appropriate reciprocal net vectors; the superscripts +/- specify the directions into/out of the crystal respectively. No restrictions have been placed on energy, and therefore these conditions apply equally to RHEED.

2.1.2 APPEARANCE OF LEED SPOTS: THE EWALD CONSTRUCTION

The geometrical conditions for the appearance of LEED spots have already been specified by equations (2.13) and (2.14). However, it is often helpful to visualize the situation graphically using an adaptation of the Ewald construction used for X-ray diffraction[47]. For an electron wavelength λ, the magnitude of the incident wavevector $\underset{\sim}{k}_0$ is $2\pi/\lambda$. In the Ewald construction for LEED $\underset{\sim}{k}_0$ is drawn with appropriate magnitude and direction to end at the point chosen as the origin O of the reciprocal lattice. The other end of $\underset{\sim}{k}_0$ defines the center of the Ewald sphere of radius $2\pi/\lambda$ as shown in Figure 2.2. The reciprocal space construction for diperiodic diffraction involves a set of reciprocal rods each of which is perpendicular to the sample surface and passes through a point on the reciprocal net. In Figure 2.2, only a single row of such rods is considered for the sake of clarity (see inset). Each of the reciprocal rods can then be specified by the pair of integral indices (hk) which are used for defining the appropriate reciprocal net point according to equation (2.9). All possible diffracted vectors $\underset{\sim}{k}_g$, which satisfy equations (2.13) and (2.14), originate from the center of the Ewald sphere and terminate at the intersection of the Ewald sphere with a 'reciprocal rod'. In a LEED experiment, only the intersections arising from backscattered $\underset{\sim}{k}_g^-$ can be seen, and then only when they are within the acceptance angle of the apparatus.

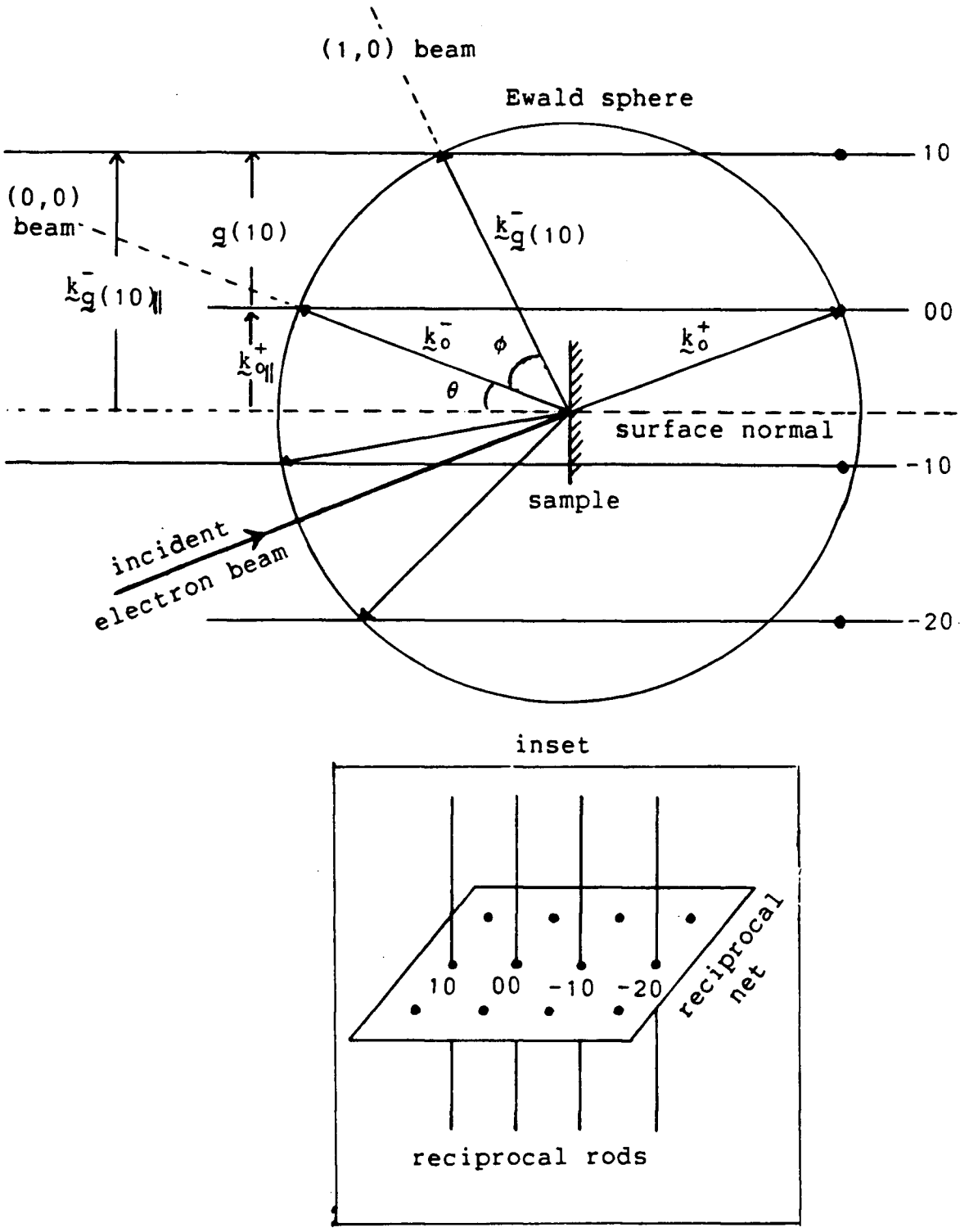

Figure 2.2: Ewald construction for electron diffraction. Only four reciprocal rods are selected from a large number of such rods (inset) for the sake of clarity.

As the energy of the incident electron is increased, λ decreases and therefore the Ewald sphere becomes larger. The first effect is that more spots are observed because more reciprocal rods intersect the surface of the sphere. The second effect is that the angle ϕ between $\underset{\sim}{k}_g^-$ and $\underset{\sim}{k}_o^-$ (Figure 2.2) decreases. Since the specular or (0,0) beam involves no transfer of momentum parallel to the surface, the angle θ is unchanged. Therefore when the energy of the incident beam is continuously increased, the (0,0) beam will remain stationary on the detecting device (provided of course that the electrons move in field free space outside of the crystal); the non-specular beams however will move towards the (0,0) beam. The detecting device of LEED beams is traditionally a hemispherical fluorescent screen whose center of curvature coincides with the sample. Figure 2.3 shows a schematic setup for detecting LEED spots and how the latter are labelled (in this case, for a rectangular reciprocal net).

2.1.3 SUPERLATTICE NOTATION

The LEED pattern as seen on a detecting screen represents the reciprocal space image of the diperiodic translational symmetry of the surface. The presence of ordered adlayers generally adds more translational symmetry to the surface (except when they have the same surface net as the clean surface), the result of which is an increase in diffraction beams in reciprocal space. Such adlayers are

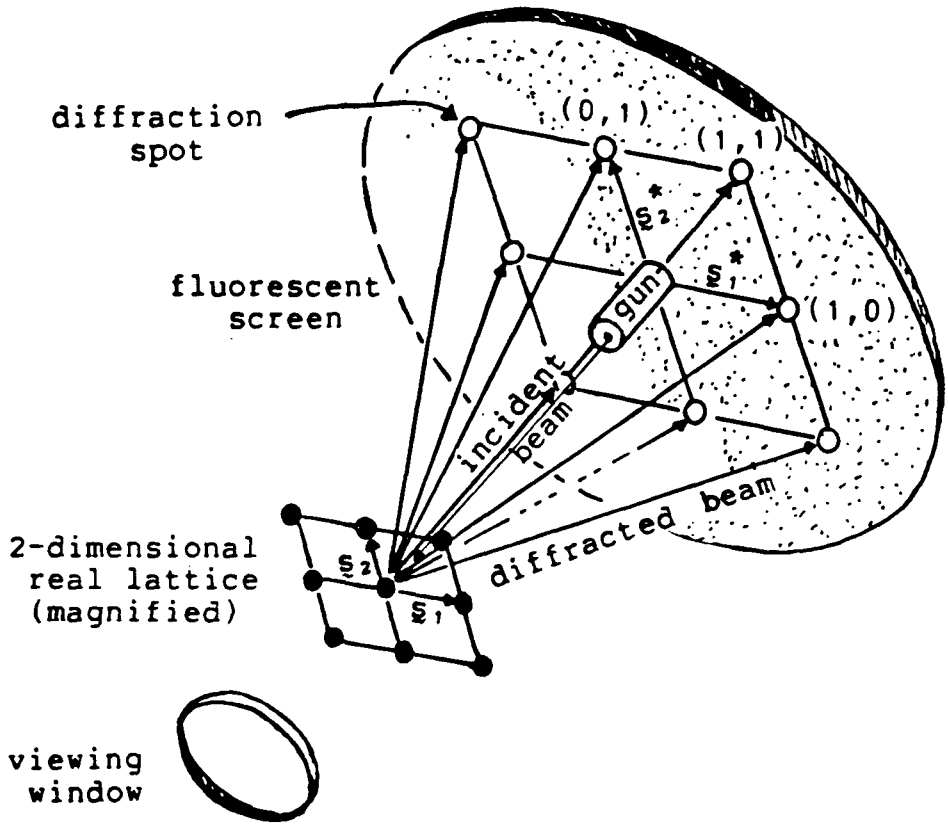

Figure 2.3: Schematic set-up for LEED experiment and the relation between the surface lattice and the diffraction pattern.

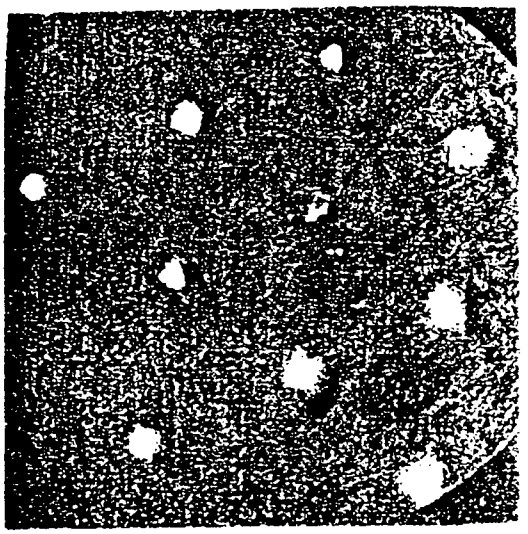

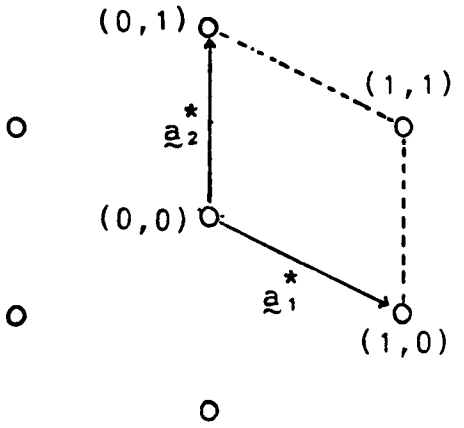

(a)

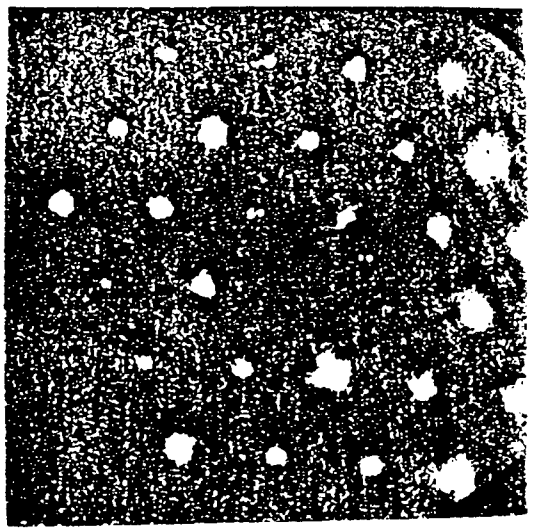

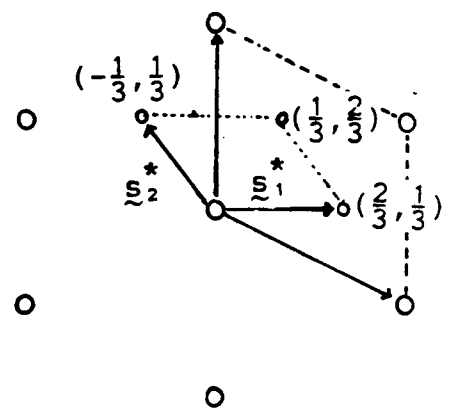

(b)

Figure 2.4: LEED patterns from Rh(111) at 142 eV, normal incidence: (a)Clean surface; (b)After exposure to H_2S. The extra spots are labelled in fractions of the 'clean' reciprocal vectors.

called superlattice structures. Further, they are said to be commensurate if the the positions of the extra beams can be represented by fractional combinations of the substrate reciprocal net vectors, as illustrated by the example shown in Figure 2.4 for the adsorption of sulfur on the surface of Rh(111). In such cases, the extra beams are often referred to as fractional order beams. In short, the size of the reciprocal net of a commensurate superlattice structure is a fraction 1/S (S an integer) of that of the substrate, or alternately the real space surface net of the superlattice is S times as large as that of the substrate.

In LEED crystallography the real space superlattice structures are usually named with the substrate unit cell vectors as reference. Two such systems of nomenclature commonly used are the Wood and the matrix notations.

The Wood notation was originally proposed by Wood[48], which requires that the angle between the adsorbate unit cell vectors $\underset{\sim}{a}_1$ and $\underset{\sim}{a}_2$ be the same as that between the substrate unit cell vectors $\underset{\sim}{s}_1$ and $\underset{\sim}{s}_2$. When this requirement is satisfied, the surface structure is named in the general form p(nxm)Rθ° or c(nxm)Rθ° depending on whether the unit cell of the adsorbate is primitive or centered. θ is the smallest angle which has to be rotated to line up $\underset{\sim}{a}_1$ and $\underset{\sim}{s}_1$ (or $\underset{\sim}{a}_2$ and $\underset{\sim}{s}_2$). n and m are numbers to specify the lengths of $\underset{\sim}{a}_1$ and $\underset{\sim}{a}_2$ in multiples of $\underset{\sim}{s}_1$ and $\underset{\sim}{s}_2$ respectively, that is

$$|\underset{\sim}{a}_1| = n|\underset{\sim}{s}_1|, \qquad (2.15a)$$

$$|\underset{\sim}{a}_2| = m|\underset{\sim}{s}_2|. \qquad (2.15b)$$

When θ is zero, the $R\theta^\circ$ is dropped from the notation. The ratio of the sizes of the unit cell of the superlattice and of the substrate is given by mn if the superlattice is primitive, and mn/2 if the superlattice is centered.

A generalized form of nomenclature is provided by matrix notation. This notation was originally developed by Park and Madden[49], and further discussed by Estrup and McRae[50]. Here, the adlayer basis vectors $\underset{\sim}{a}_1$ and $\underset{\sim}{a}_2$ are expressed as linear combinations of the substrate basis vectors $\underset{\sim}{s}_1$ and $\underset{\sim}{s}_2$ in the form

$$\begin{bmatrix} \underset{\sim}{a}_1 \\ \underset{\sim}{a}_2 \end{bmatrix} = \begin{bmatrix} a_{11} & a_{12} \\ a_{21} & a_{22} \end{bmatrix} \begin{bmatrix} \underset{\sim}{s}_1 \\ \underset{\sim}{s}_2 \end{bmatrix} = \underset{\approx}{A}\underset{\sim}{S}. \qquad (2.16)$$

Superlattice structures are then described by the matrix $\underset{\approx}{A}$. The determinant of $\underset{\approx}{A}$ denotes the ratio of the sizes of the unit cell of the superlattice and of the substrate.

An experimental LEED pattern gives the relationship between the reciprocal net vectors of the substrate and of the adlayer. This relationship can be represented conveniently by a matrix $\underset{\approx}{A}^*$ which is defined by

$$[\underset{\sim}{a}_1 \ \underset{\sim}{a}_2] = [\underset{\sim}{s}_1 \ \underset{\sim}{s}_2]\underset{\approx}{A}^* , \qquad (2.17)$$

where superscript * denotes reciprocal space. The elements

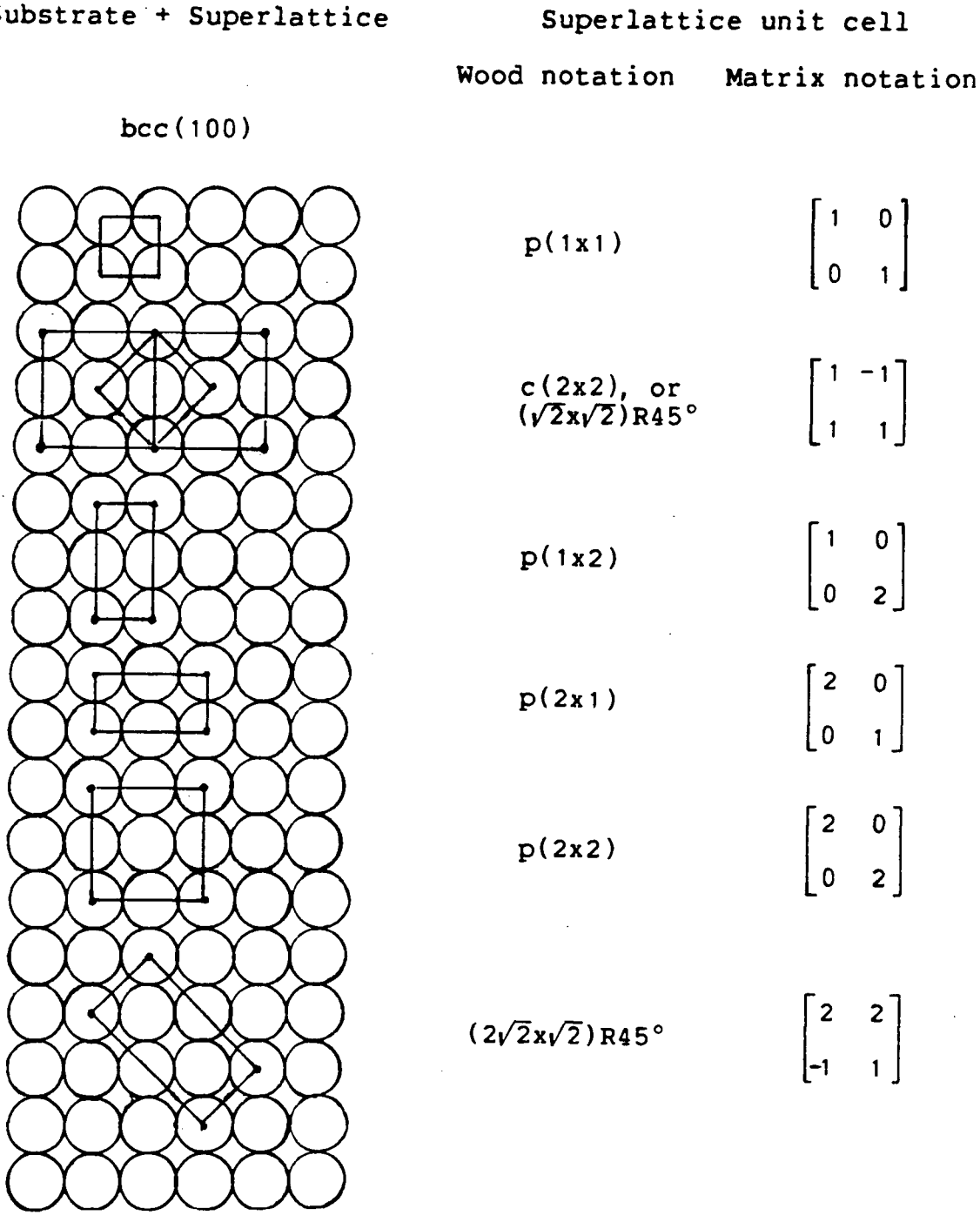

Figure 2.5: Some common superlattice structures on low Miller index surfaces and their nomenclature in both Wood and matrix notations.

fcc(110)

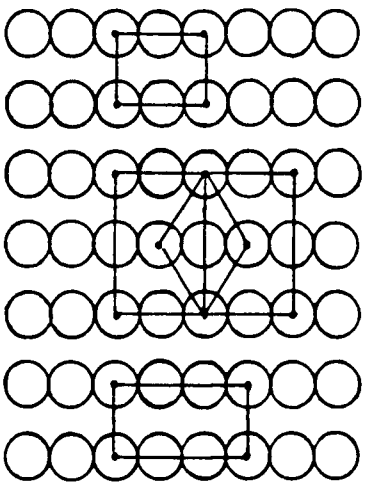

p(2x1) $\begin{bmatrix} 2 & 0 \\ 0 & 1 \end{bmatrix}$

c(2x2) $\begin{bmatrix} 1 & -1 \\ 1 & 1 \end{bmatrix}$

p(3x1) $\begin{bmatrix} 3 & 0 \\ 0 & 1 \end{bmatrix}$

bcc(110)

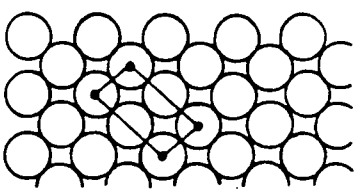

p(2x1) $\begin{bmatrix} 2 & 0 \\ 0 & 1 \end{bmatrix}$

fcc(111), hcp(0001)

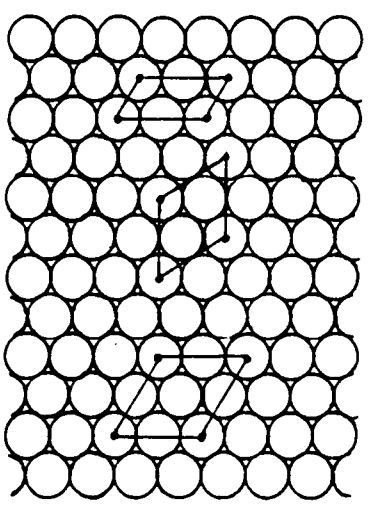

p(2x1) $\begin{bmatrix} 2 & 0 \\ 0 & 1 \end{bmatrix}$

$(\sqrt{3}x\sqrt{3})R30°$ $\begin{bmatrix} 1 & 1 \\ -1 & 2 \end{bmatrix}$

p(2x2) $\begin{bmatrix} 2 & 0 \\ 0 & 2 \end{bmatrix}$

Figure 2.5: (continued)

of the matrix $\underset{\approx}{A}^*$ can be obtained from measurement of the observed LEED pattern. The elements of $\underset{\approx}{A}$ are then calculated by[49]

$$\underset{\approx}{A} = \frac{1}{|\underset{\approx}{A}^*|} \begin{bmatrix} a_{22}^* & -a_{12}^* \\ -a_{21}^* & a_{11}^* \end{bmatrix} \qquad (2.18)$$

where $|\underset{\approx}{A}^*|$ is the determinant of the matrix A^*. Using equation (2.18), the superlattice structure which gives rise to the observed LEED pattern shown in Figure 2.4 can be described as $[\frac{1}{1}\ \frac{1}{2}]$ in matrix notation. The full description of the adsorption system is either Rh(111)-$[\frac{1}{1}\ \frac{1}{2}]$S in matrix notation or Rh(111)-$(\sqrt{3}x\sqrt{3})$R30°-S in the Wood notation. Figure 2.5 shows several common superlattice structures on some low Miller index surfaces and their corresponding nomenclatures in both systems. Although the Wood notation provides an intuitive picture for an ordered adlayer relative to the substrate, its use is limited to simple cases. On the other hand, the matrix notation can be used for any complex patterns. The latter include many hydrocarbon adsorption systems on metal surfaces. One such example is the ordered structure of benzene on Rh(111) surface which is depicted in Figure 2.6.

2.2 LEED SPOT INTENSITY-ENERGY CURVE

The unit mesh vectors for the substrate and for any adsorbate present can usually be obtained by inspection of the LEED pattern from an ordered surface. However, in order

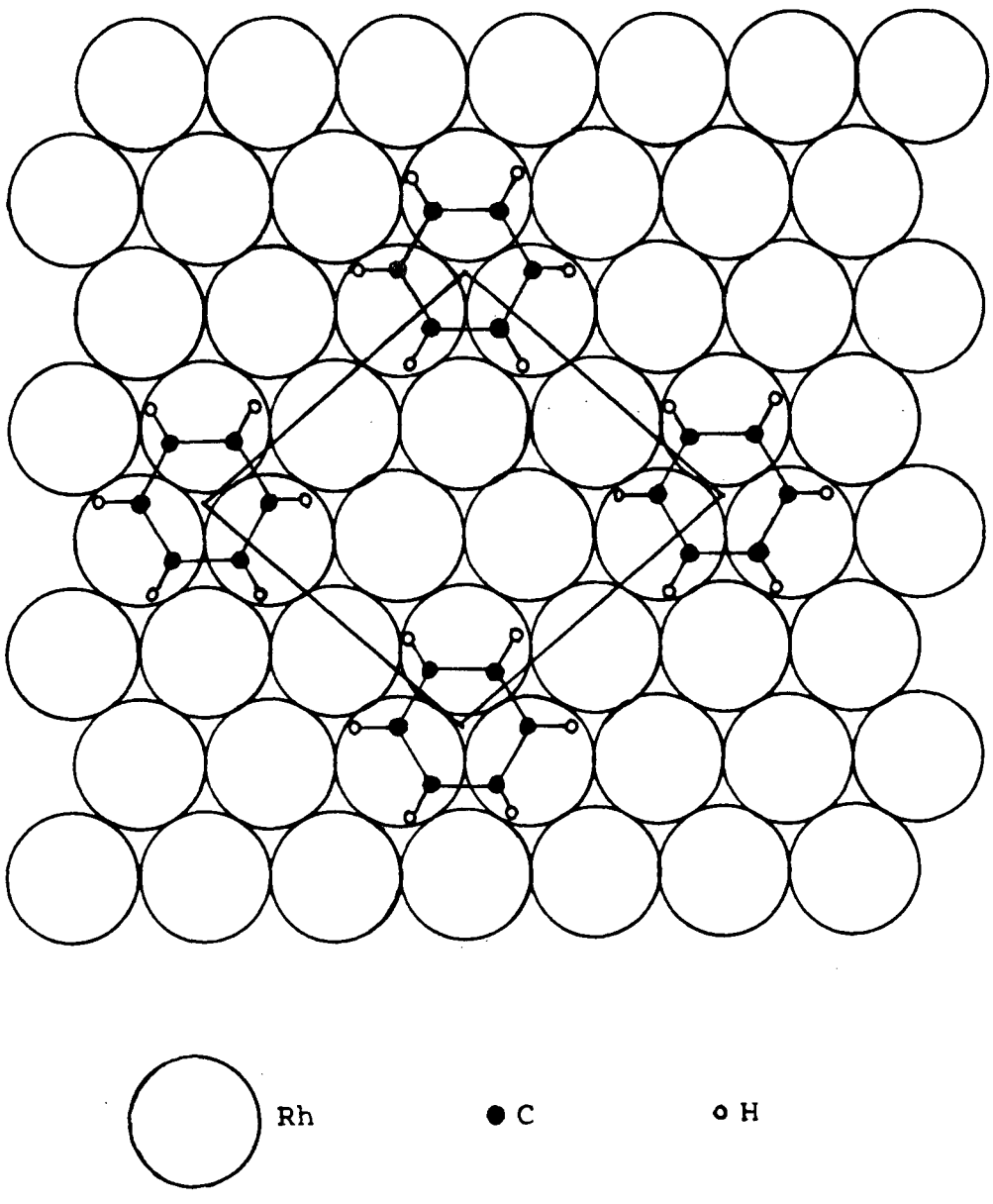

Figure 2.6: Ordered adlayer of benzene on Rh(111). The structure is described as Rh(111)-$\left|\begin{smallmatrix}3 & 1\\ 1 & 3\end{smallmatrix}\right|C_6H_6$ in matrix notation (after Van Hove *et al.*[51]).

to determine atomic positions, the intensities of LEED spots have to be analyzed. For this purpose, the intensities are nearly always measured as a function of incident energy. This method of measurement gives the so-called intensity versus energy, or I(E), curves, an example of which is shown in Figure 2.7. The preference for measuring intensity as a function of incident energy rather than incident angle is due, in large part, to the following factors:

1. Electron energy can be varied and measured straightforwardly, but absolute measurements of angle of incidence are generally harder to accomplish[53],
2. When the incident beam is contained in a symmetry element, especially when perpendicular to the surface, uncertainties in angle measurement can be reduced by averaging nearly-equivalent sets of spots[54], and
3. Multiple scattering calculations are more affordable when the incident beam is chosen to coincide with symmetry element(s) (Section 3.5).

At first glance, experimental I(E) curves appear to be very complicated. The rather simple kinematic formulation for X-ray crystallography often fails to predict the positions of maxima and minima in a typical I(E) curve such as the one shown in Figure 2.7. This is due to the fact that the intensities of the diffracted beams depend not only on the geometrical arrangement of the atoms, but also on the multiple scattering of the LEED electrons by the atoms. The latter is dependent especially on the core potential of the

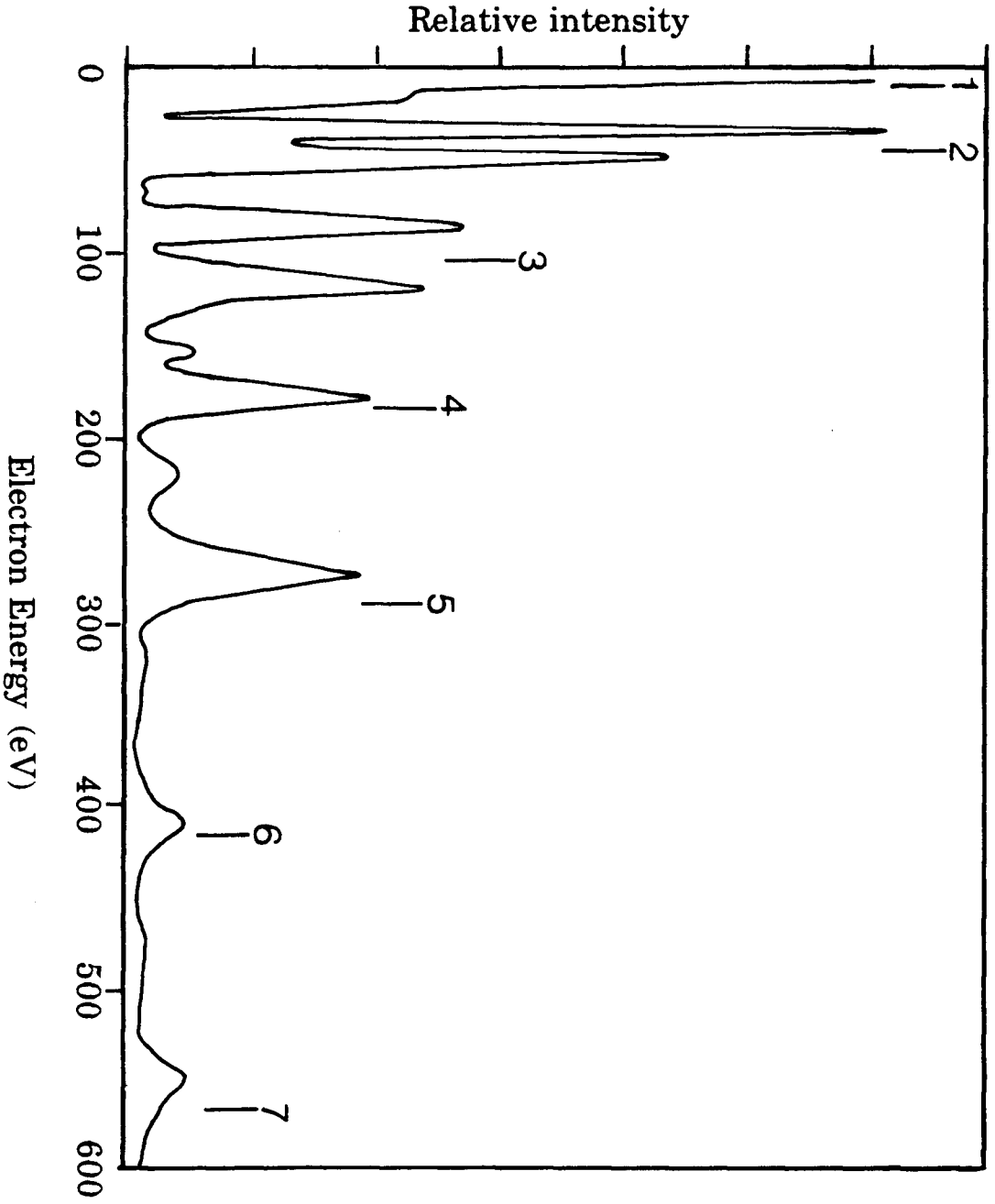

Figure 2.7: I(E) curve for (0,0) beam from Ni(100) at θ=3°. Kinematically expected Bragg peak positions are indicated by vertical bars (after Andersson *et al.*[52]).

atomic species involved. Although numerous mathematical treatments[11,55] of I(E) curve intensities are available in the literature, a semi-quantitative approach taken by Van Hove and Tong[56] to explain the features in an I(E) curve seems helpful to understand the physical processes involved in electron diffraction by a crystal lattice. This simplified approach brings out most of the important ingredients required in a successful multiple scattering calculation. The multiple scattering calculations will be discussed in more detail in the next chapter.

2.2.1 THE DIFFRACTION PEAK POSITIONS

To simplify matters, the discussion will start with a hypothetical 1-dimensional clean crystal with a lattice constant a. It will then be generalized to 3-dimensions, and finally overlayers will be introduced.

In 1-dimension, incident and diffracted electrons can be represented by wavefunctions $\exp(ikx)$ and $\exp(-ikx)$ respectively (where $k^2=2E$ in atomic units). The manner in which individual scatterers of the crystal scatter electrons can be summarized by two complex coefficients: t the amplitude with which a scatterer transmits electrons, and r the amplitude with which a scatterer reflects electrons. Conservation of current, in the absence of damping (inelastic scattering), requires that

$$|t|^2 + |r|^2 = 1. \tag{2.19}$$

Collective scattering of the incident wavefunction $\exp(ikx)$ by an infinite number of identical scatterers of this hypothetical crystal results in a reflected wavefunction whose amplitude is given by[56]

$$R = \sum_{j=0} rt^{2j}\exp(ik2aj) = \frac{r}{1 - t^2\exp(i2ka)}. \tag{2.20}$$

The summation over t^{2j} takes into account that any electron (except the one closest to vacuum) which contributes to the total reflected amplitude has to be transmitted twice at each intervening scatterer: once penetrating into and once emerging out of the crystal. If the transmission coefficient t were real, reflection maxima would occur when the Bragg condition for X-ray diffraction $2ka=n2\pi$ (n integer) is satisfied. However, the use of a complex t generalizes the condition for reflection maxima to

$$2[ka + \arg(t)] = n2\pi, \tag{2.21}$$

where arg(t) represents the argument of the imaginary part (or phase) of the transmission coefficient t. According to equation (2.21), the condition for reflection maxima appears to be independent of the reflection coefficient r, although the latter actually exerts indirect (but generally small) influence through multiple scattering (after all r and t are

related by equation (2.19)). Equation (2.21) is still valid for X-ray diffraction, where $|t| \simeq 1$ and arg(t) vanishes. In electron diffraction, the generally non-zero arg(t) originates from the interaction of the electron with the atomic potential of each scatterer upon transmission, and is responsible for two commonly observed 'anomalies' in I(E) curves. To simplify the discussion, the atomic potential can conceptually be split into two components: a constant potential (inner potential) and a spherically symmetric potential which is largely energy dependent.

For an attractive atomic potential such as the one in metals, the electron is speeded up at each transmission (due largely to the inner potential). Some of the potential energy of the electron is used up in this temporary speeding-up, which results in a shorter k and an accordingly lower E. Therefore, the positions of reflection maxima will be shifted towards lower energy sides of the kinematically expected peaks. This shift is relatively constant for all the reflection maxima (insofar as the slight energy dependence of inner potential is ignored), and is between 5 and 15 eV depending on the type of crystal.

The spherically symmetric potential of an atom in this hypothetical crystal provides a 'potential well' in which an electron with appropriate k can resonate and give rise to standing waves. Constructive interference (or resonance) from this type of atomic scattering often leads to the appearance of 'unexpected' peaks scattered around the

already-shifted Bragg peaks. This effect is most prominent where absorption is weak (e.g. at low energies in LEED). In such instances in real data, it may be difficult to distinguish a Bragg peak from resonance peaks. In a multiple scattering calculation, the effect of atomic scattering is contained in the partial wave 'phase shifts' δ_l.

2.2.2 PEAK WIDTH

The peaks in an experimental I(E) curve almost always show lifetime broadening from finite electron penetration depth (which restricts the number of scatterers an electron 'sees'). The latter is a result of the finite (albeit small) value of $|r|$, which is typically around 0.1 in the energy range considered in LEED. Still assuming no absorption and ignoring the attentuation at each scatterer, conservation of current limits the number of scatterers to approximately $|r|^{-1}$, hence a maximum penetration depth around $a|r|^{-1}$ (where a is the interatomic distance). The actual penetration depth may be even shorter due to inelastic scattering. Diffraction from $|r|^{-1}$ such scatterers will produce diffraction maxima whose widths are given by[57]

$$2\Delta k \simeq \pi|r|/2a \qquad (2.22)$$

in reciprocal space. Differentiation of $k^2=2E$ and substituting the result into equation (2.22) then yields

$$2\Delta E \simeq \pi k|r|/2a, \qquad (2.23)$$

which are the corresponding energy widths of the diffraction maxima. $|r|$ is only slightly energy dependent in the range 30 to several hundred eV, therefore ΔE is mainly determined by k which is proportional to $E^{1/2}$. Not surprisingly, similar results were obtained from electron inelastic mean free path and lifetime consideration by Stern *et al.*[58]. This explains the increasingly broader diffraction maxima at higher energies. ΔE range from 5 to 15 eV in a typical I(E) curve.

At very low energies (typically $E \leq 10$eV), mean free path lengths for inelastic scattering in solids are generally large. Strong elastic scattering may open up wide band gaps, and the electrons have a higher probability of being totally reflected to the vacuum than being absorbed. In other words, $|r|$ becomes appreciable, and the widths of reflection maxima become larger accordingly.

Resonance peaks are generally narrower than Bragg peaks because resonance processes are normally associated with longer natural lifetimes. The latter reduces lifetime broadening to some extent.

2.2.3 THREE-DIMENSIONAL EFFECTS

An immediate consequence of conversion from a 1-dimensional crystal to a 3-dimensional one is the introduction of more beams in which the elastically

diffracted electrons can travel. Each layer may diffract a beam $\underset{\sim}{g}$ into beams $\underset{\sim}{g}'$ with reflection and transmission coefficients $r_{\underset{\sim}{g}\underset{\sim}{g}'}$ and $t_{\underset{\sim}{g}\underset{\sim}{g}'}$ respectively. Each beam will have its own wavevector $\underset{\sim}{k}_{\underset{\sim}{g}}$. Let $\underset{\sim}{k}_{\underset{\sim}{g}\perp}$ denote the component of $\underset{\sim}{k}_{\underset{\sim}{g}}$ perpendicular to the crystal surface, and a the interlayer separation, then equation (2.21) can be modified to[56]

$$\underset{\sim}{k}_{\underset{\sim}{g}\perp}a + \arg(t_{\underset{\sim}{g}\underset{\sim}{g}'}) + \underset{\sim}{k}_{\underset{\sim}{g}'\perp}a + \arg(t_{\underset{\sim}{g}'\underset{\sim}{g}}) = n2\pi \qquad (2.24)$$

as the condition for maximum reflection from beam $\underset{\sim}{g}$ into beam $\underset{\sim}{g}'$. Strictly speaking, equation (2.24) is valid only for single scattering. Nevertheless, it is a very good approximation for multiple scattering as long as the zero-angle forward scattered beam is dominant. It is indeed almost always true for LEED calculations according to Van Hove[57]. Typically the zero-angle forward scattered beam carries as much as 40% of the incident flux while other beams carry only about 1%.

Equation (2.24) again requires peaks in I(E) curves to be shifted from their respective kinematic positions by amounts which are energy-dependent. Here, $\arg(t_{\underset{\sim}{g}\underset{\sim}{g}'})$ and $\arg(t_{\underset{\sim}{g}'\underset{\sim}{g}})$ implicitly contain information on the rather rigid shift of Bragg peaks by the inner potential, and the resonant scattering properties of the spherically symmetric atomic potential.

Intralayer multiple scattering is another new feature in this 3-dimensional crystal. The contribution to

reflection amplitude from intralayer multiple scattering may be small, especially at or near normal electron incidence where at least two large angle scattering events are required for intralayer but just one for interlayer multiple scattering. When absorption is small (e.g. at low energies in LEED) and/or angle of incidence is shallow, intralayer multiple scattering may become important.

2.2.4 OVERLAYER EFFECT

The full 3-dimensional treatment has been given by Andersson and Pendry[59]. Here, the 1-dimensional crystal is invoked again, and the 'clean' crystal can now be visualized as a column with total reflection coefficient R_s. The overlayer is now a point scatterer with transmission and reflection coefficients t_o and r_o respectively, and is assumed to be separated from the substrate by a distance d. An expression similar to equation (2.20) but involving t_o, r_o, R_s and kd can be obtained for the total reflection amplitude for this combined column[57]. Transformation from this expression into the condition for reflection maxima is not straightforward. Nevertheless, a simple expression for the condition for reflection maxima is possible if single scattering is assumed first, and multiple scattering effect is introduced qualitatively in later stages. In this case, reflection maxima occur when

$$2kd + 2\arg(t_o) + \arg(R_s) - \arg(r_o) = n2\pi. \qquad (2.25)$$

The implications of equation (2.25) can be explained as follows. In an overlayer system, the peaks in the I(E) curve originate mainly from Bragg reflections from the substrate (implicitly carried by the term $\arg(R_s)$) because it has sufficient scattering power ($|R_s|$ typically 0.5 to 0.1) available to turn around a substantial number of electrons. Nevertheless, the overlayer exerts its influence by changing the amplitudes of excitation of the wavevectors in the substrate, and by further diffracting beams reflected from the substrate. The term $-\arg(r_o)$ may also cause annihilation of the Bragg condition for reflection maxima. Each of these processes is dependent on details such as the spacing d, and the geometry of the overlayer (in 3-dimensional case). These are the reasons why I(E) curves are so sensitive to the surface layer position.

At very low energies, where absorption is minimal, the term $\arg(r_o)$ becomes appreciable. This has a strong influence on I(E) curves either through interference of the beams directly reflected from the overlayer with those reflected from the substrate, or through the reflection at the internal surface of the overlayer to change the wavefields incident on the substrate. In the event that r_o is comparable to R_s, the electrons can be reflected many times between the overlayer and substrate somewhat as for light in an interferometer. A consequence of this effect is

the appearance of interference fringes around a single strong Bragg peak in the I(E) curve. The positions of these fringes are strongly dependent on the interlayer spacing d.

2.3 DISORDER, DOMAINS AND INSTRUMENTAL RESPONSE

In the discussion of the formation of LEED patterns, two implicit assumptions have been made. The first is that the diffraction takes place from a perfectly ordered surface. The second is that the incident beam and the individual diffracted beams can each be represented by a precisely known single wavevector. In reality, these two assumptions can never be satisfied. The aim of this section is to discuss briefly how the deviations from these assumptions affect the appearance of the LEED pattern and the measured LEED spot intensities.

A perfectly ordered crystal should give rise to infinitesimally narrow reciprocal rods. Therefore a LEED pattern from this ideal surface should consist of 'ideally sharp' spots (i.e. the intensity profiles across these spots could be described by a δ-function[60]). Real surfaces, however, inevitably have defects; the presence of steps, kinks and crystal plane dislocations is well known[61]. Microscopically, a real surface can be represented by a large number of small islands (or domains) of 'ideal surface', each of which possesses the same diperiodicity. The latter still governs the geometrical conditions for diffraction, but the finite sizes of the domains cause a

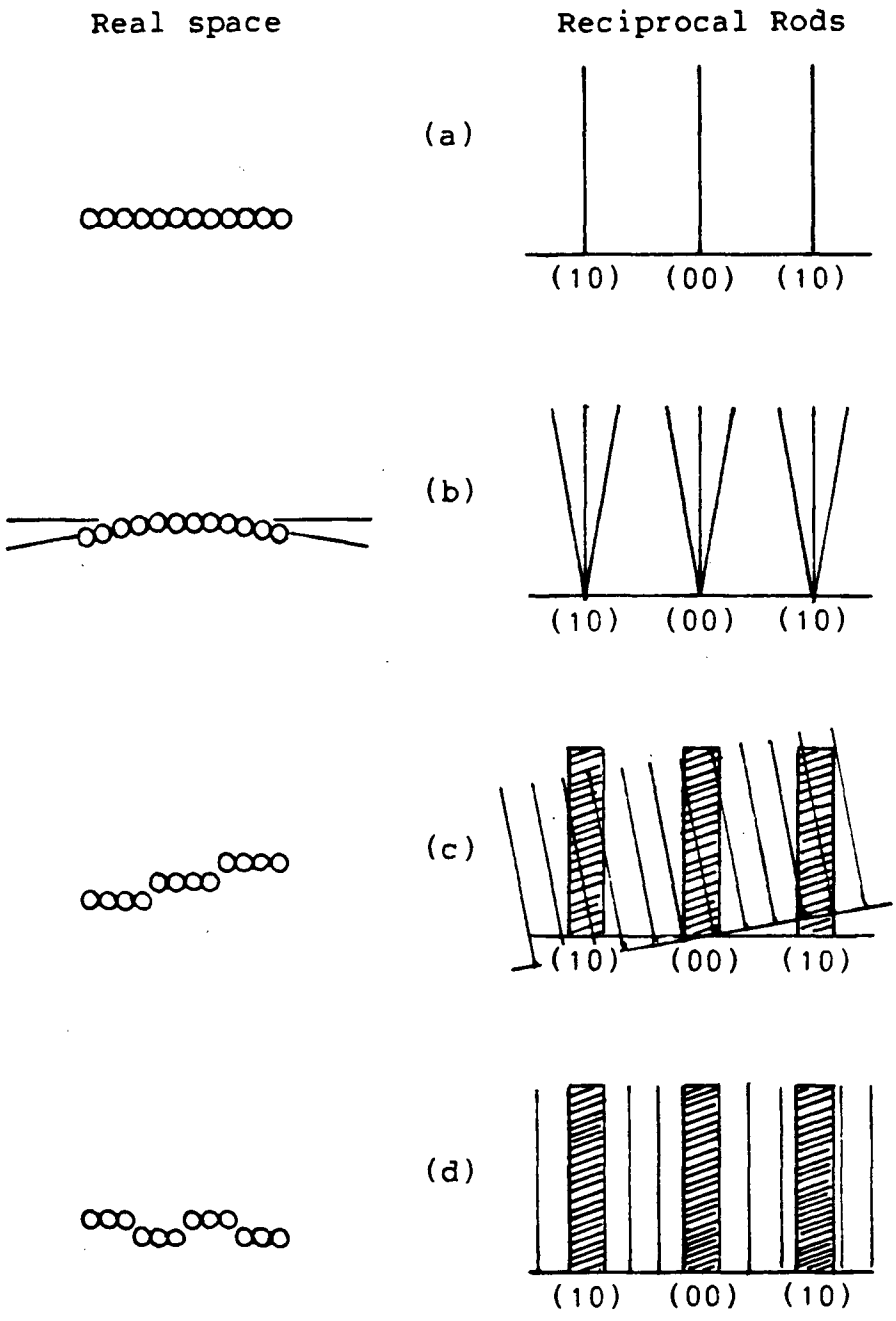

Figure 2.8: Some hypothetical surfaces and their corresponding reciprocal rods. (a)Perfectly ordered surface; (b)Slightly dislocated crystallographic planes; (c)Increasing monatomic steps; and (d)Alternating monatomic steps.

broadening of the reciprocal rods[60]. This is one of the reasons why the observed LEED spots have finite widths. In general, the larger the average domain size, the narrower the spot width. Randomly distributed domains usually give rise to a general background in a LEED pattern. If the domains possess some degree of order among themselves, additional (usually very thin) reciprocal rods can be produced. Several such examples are shown in Figure 2.8. In such cases, the background is modulated due to the non-random distribution[62].

Adlayers can also be treated in the same manner as defects at a clean surface. Adlayer islands are expected if the adsorbed species exercise sufficiently strong attractive interactions, and they may form even at low overall coverages. Generally the LEED spots are broader and more diffuse for small island sizes than for larger islands. In addition, some special effects may occur for adlayers. First, there is a possibility of different adsorption sites in different domains. This is usually a result of slow ordering kinetics in the adlayer itself. For example, an adlayer occupying the 3-fold sites of a fcc(111) surface may form a domain with bABCABC... registry and another domain with cABCABC... registry if the two types of 3-fold adsorption sites are nearly equally favorable energetically (in this notation, the lower and upper cases represent the registries of the adsorbed and substrate layers respectively). Secondly, superlattice structures, whose

rotational symmetry is lower than that of the substrate, invariably show rotationally related domains. An example of this kind is encountered in Chapter 5 for oxygen adsorption on Zr(0001). At low coverage, a p(2x2) LEED pattern is observed, but the same pattern could arise from three sets of p(2x1) domains related by 120° rotations, as depicted in Figure 2.9. Simple visual observation of LEED patterns is not always a good guide to the presence of domains and disorder. For example, some studies have shown that LEED patterns may appear essentially unchanged even as up to 30% of the surface atoms become distributed as random steps[63].

Assuming a perfect instrument for the LEED experiment, the foregoing discussion suggests that information on surface domains and disorder can be obtained rather accurately by analyzing the angular spot profile. However, a real LEED diffractometer puts some restriction on the latter analysis. An electron gun usually produces a beam about 1 mm in diameter, which consists of electrons with slightly differing velocities and directions associated with the finite size and high temperature of the source. Also there are uncertainties in the detection process. Commonly in LEED repelling grids are employed to filter out backscattered electrons which have lost energy on scattering from the crystal. The finite distance that the diffracted electron wave packets have to travel between the sample and the detector inevitably leads to some angular spread of momentum. In short, limitations on the LEED diffractometer

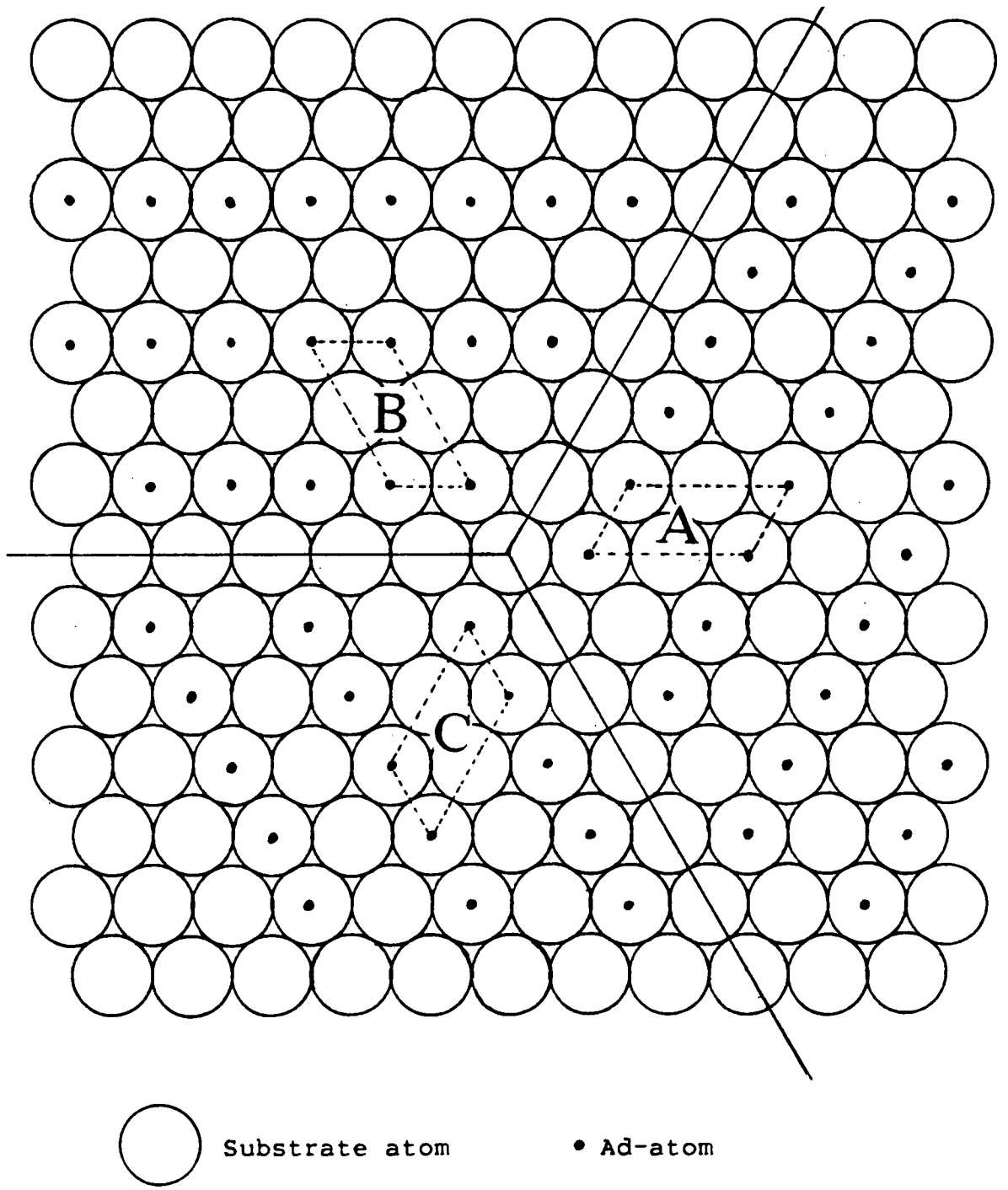

Figure 2.9: Three possible rotational domains (A,B,C) of a p(2x1) superlattice structure on a hexagonal close-packed surface.

inevitably obscure the information that can be obtained from a surface. Assuming an ideal surface, Comsa[64] showed that the total angular broadening by a LEED instrument correlates to a length on the surface, the transfer width, which is around 100 Å. The transfer width corresponds roughly to the largest periodicity of grating which can be resolved straightforwardly. However, Lagally[65] suggested that the size of domains or islands which can be studied by spot angular profile analysis can be larger than the transfer width, and is dependent on experimental setup as well as the the type of islands under investigation. These factors are translated into a function called the resolving power of LEED instrument which is a measure of the size of the domain that can be resolved. The latter ranges from 100 to 500 Å.

As far as I(E) curves are concerned, the large cross sectional area of the incident beam means that inevitably many domains on the surface are sampled. The observed I(E) curves thus contain contributions from these domains. The resulting LEED pattern (and I(E) curves) from the rotational domains shown in Figure 2.9 will therefore indicate a higher symmetry than from any one of the domains alone. In LEED crystallographic studies for such situations, I(E) curves are calculated for individual domains and appropriate beam averages are taken before comparisons are made with the experimental curves.

2.4 AUGER ELECTRON SPECTROSCOPY (AES)

2.4.1 THE AUGER PROCESS

When a core electron is ejected from an atom, the resulting ion is in a highly excited state. A number of possible processes may contribute to reducing the energy of the excited state. One of these processes is the emission of a secondary electron, the process being known as the Auger effect. Auger emission is caused when an electron drops from a higher energy level into the core vacancy, with the excess energy being transferred to an ejected second, or Auger (named after P. Auger[26]) electron. An energy representation of this process is given in Figure 2.10. It has to be emphasized that steps (b) and (c) are separated conceptually only for the sake of clarity. In the actual process the filling of the core hole and the ejection of the Auger electron occur simultaneously; the process arises from a Coulombic rearrangement of these two electrons.

Although Figure 2.10 shows the two electrons concerned in the Auger process as originating in two different atomic levels, this distribution is by no means essential. Other important possibilities are (i) that both electrons come from the same level and (ii) that one or both of them come from the valence levels. A system of nomenclature is clearly needed to identify the different possibilities. The convention accepted by most surface scientists is that electrons originating in the (1s) shell are labelled K, the

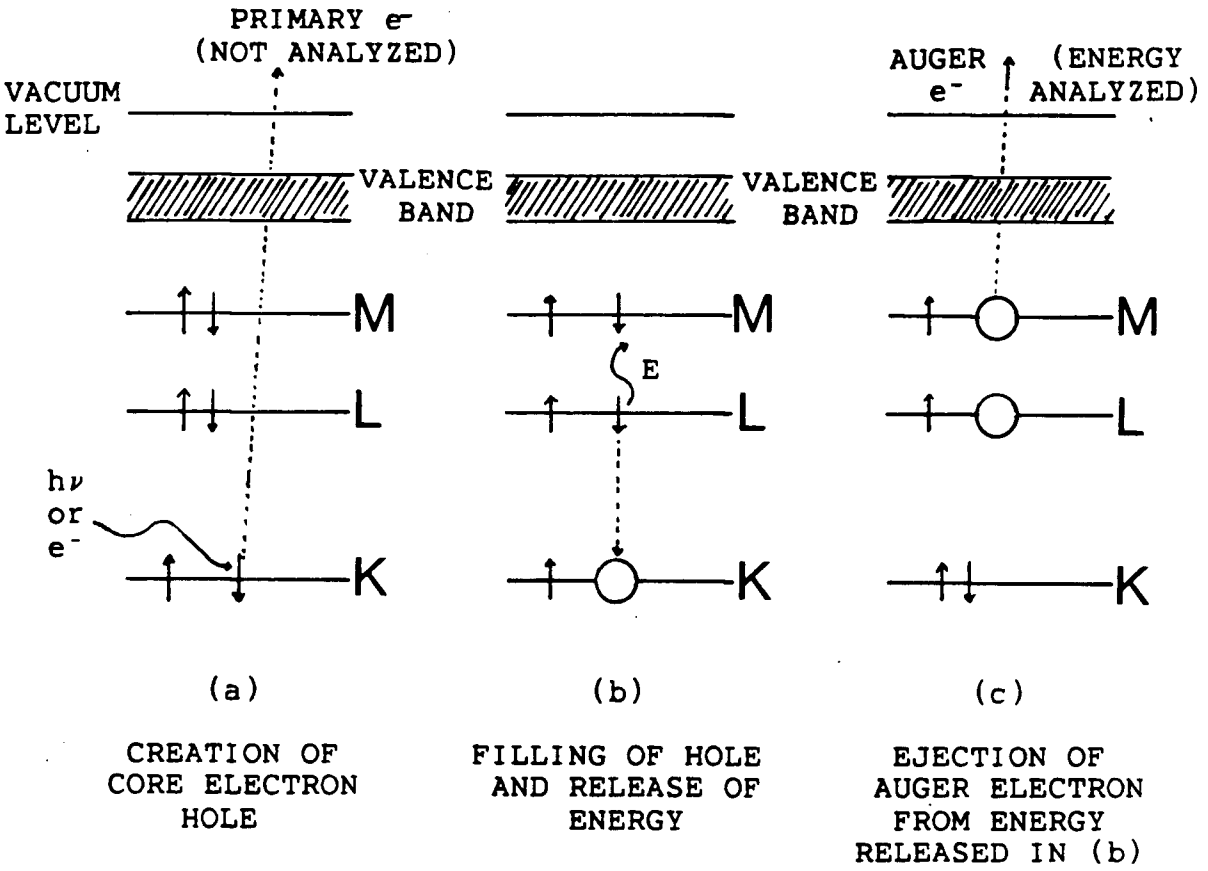

Figure 2.10: Schematic representation of Auger process. K, L and M represent atomic energy levels, and the arrows represent electrons.

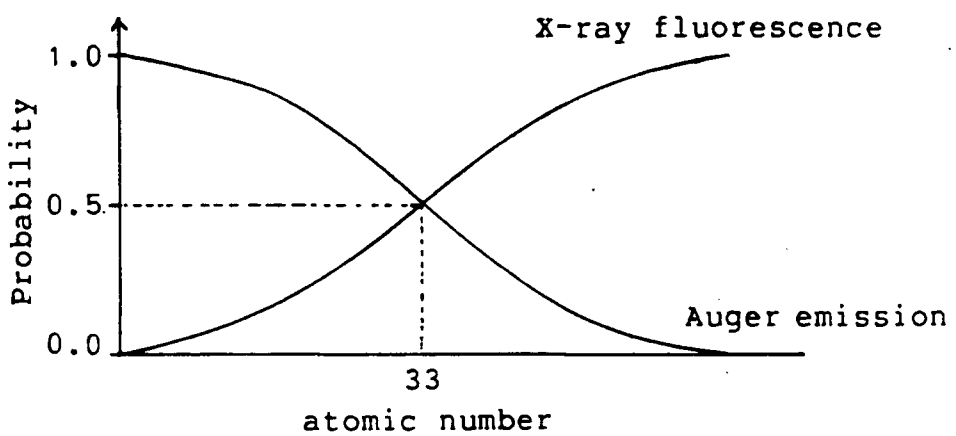

Figure 2.11: Probability of Auger emission and of X-ray fluorescence as a function of atomic number for a K-shell core hole.

(2s) are L_1, the (2p) are L_2 and L_3 and so on. Valence shell electrons are called V. To identify a transition the following sequence of letters is used:

1. the core hole;
2. the hole generated by an electron dropping into the core hole;
3. the hole generated by the ejected electron.

Thus in Figure 2.10 the Auger electron would be designated as (KLM).

A relaxation process which competes with Auger emission is X-ray fluorescence. In this the energy change associated with the descent of the first electron into the core hole is released as a photon of appropriate energy. For a K-shell core hole, the latter process becomes more probable as the atomic number increases, as shown in Figure 2.11. In general, for elements with atomic numbers below 30, Auger emission is more probable than X-ray fluorescence regardless of excitation energy. In heavier elements, Auger emission generally still dominates when the initial excitation energy is less than about 2 keV.

2.4.2 KINETIC ENERGIES OF AUGER ELECTRONS

According to Figure 2.10, the kinetic energy of the ejected electron is given by

$$E_A = E_K - E_L - E_M \qquad (2.26)$$

It can be seen that the kinetic energy of the Auger electron is characteristic of the energy levels of the atom and independent of the energy of the exciting radiation. As a consequence, it is not necessary to monochromatize the radiation source: this is in fact an experimental convenience which makes the electron-excited AES more popular (and more economical) than X-ray-excited AES.

Equation (2.26) only gives a crude approximation to the kinetic energy of an Auger electron because it does not take into account the different degrees of ionization of the atom. Extra energy is required to remove the second electron from a positively charged ion, and Chung and Jenkins[66] proposed the expression

$$E_A(Z) = E_K(Z) - \tfrac{1}{2}[E_L(Z) + E_L(Z+1)] - \tfrac{1}{2}[E_M(Z) + E_M(Z+1)] \qquad (2.27)$$

which depends on the atomic number Z for the atom of interest. The kinetic energies calculated using this formula are accurate to about 5 eV. More detailed corrections are possible, but for our purposes it is sufficient to establish that to within this small uncertainty measured Auger energy values are characteristic of particular atoms.

2.4.3 AES AND SURFACE ANALYSES

When the excitation source is an electron beam, the Auger electrons from surface atoms are obscured by large

numbers of secondary electrons emitted in the same energy range where the Auger transitions occur[67]. This general background emission, which increases slowly with energy, poses a problem for quantitative detection of the Auger electrons. The traditional practice to overcome this problem is to employ the electronic technique of phase sensitive detection (Chapter 4). As a result, Auger peaks are commonly recorded as dN(E)/dE versus E curves. A typical first derivative Auger spectrum is shown in Figure 2.12. It is clear that impurity elements are easily detected by this approach. Indeed, impurity elements on metal surfaces can often be detected at levels of the order of 1% monolayer[68].

As noted before, the energy of an Auger transition is mainly determined by the energy levels of a particular element. Although the chemical environment can sometimes contribute to energy shifts of the order of a few eV[69,70], these are appreciably less than the differences between different elements for a given type of Auger transition. Therefore AES is most suitable for elemental analysis of surfaces. For this purpose, the main interest is in Auger electrons with energies in the approximate range 20-700 eV which are characterized by short mean free path lengths in the solids.

2.4.3.1 Qualitative Analysis

The use of AES in qualitative surface analysis depends on the ability to assign peaks in an Auger

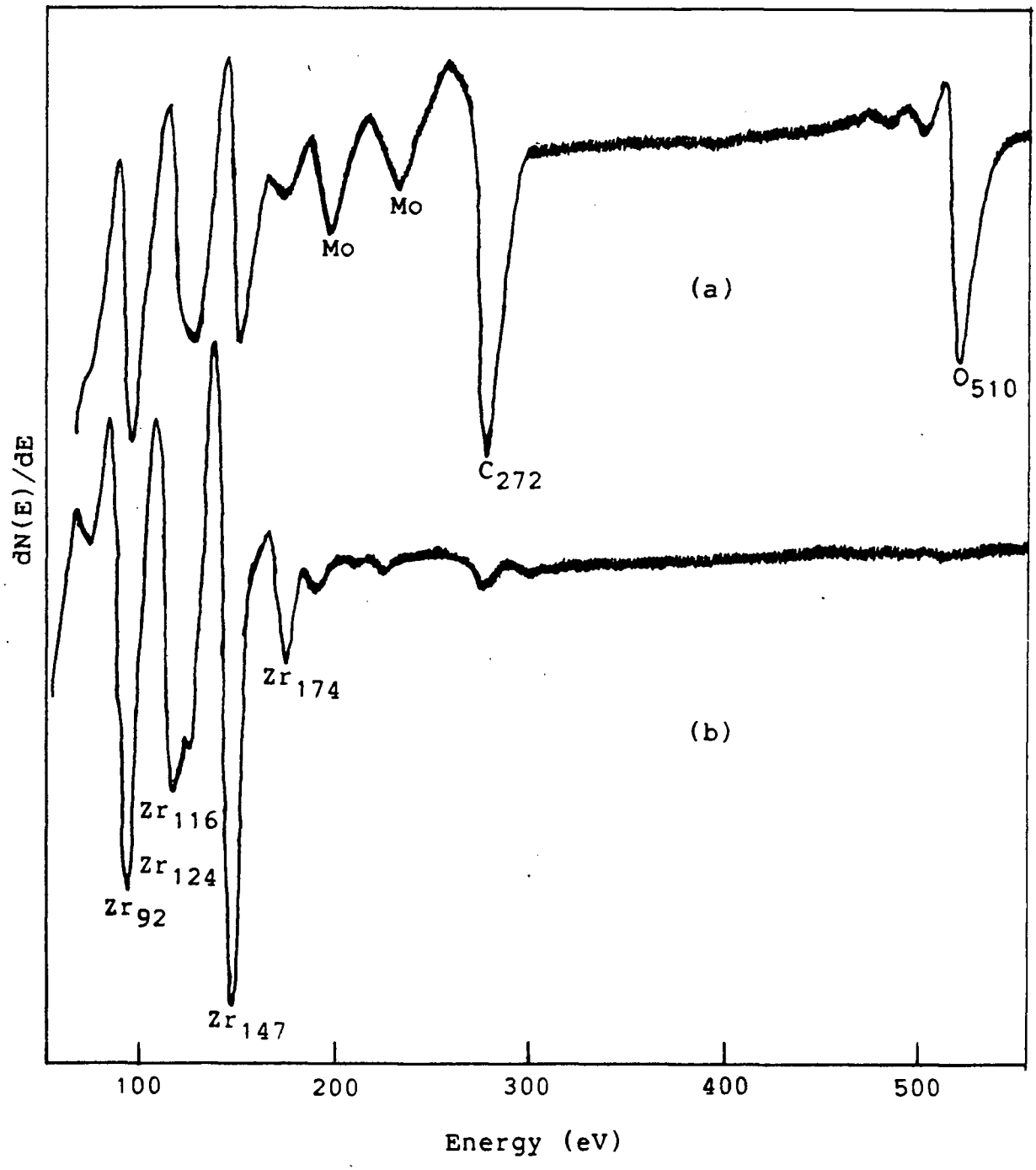

Figure 2.12: Derivative Auger spectra taken from a Zr(0001) surface. (a)Before cleaning; and (b)After ≈50 hours of Ar^+ bombardment.

spectrum to particular elements. Although Auger peaks from different elements do overlap occasionally, the existence of more than one characteristic Auger transition for most elements usually eliminates any ambiguity in assignment. In routine analysis, this is often accomplished by comparing the experimental spectrum with catalogs of reference data[71,72]. This aspect of AES application is most commonly used with LEED for monitoring of surface cleanliness.

2.4.3.2 Quantitative Analysis

Another important application of AES is the quantitative assessment of the atomic density (N) of impurities or structured adlayers on a surface. At a primary beam energy E_0, the Auger emission current $I(E_A,E_0)$ at a characteristic Auger transition energy E_A normalized to primary beam current is a convenient measure of N. In addition, $I(E_A,E_0)$ is a function of several other parameters characteristic of the particular surface atom and its environment. Some of the more important ones include[73] ionization cross section, Auger transition probability, Auger electron escape depth, roughness factor of the surface and instrumental factor. This is by no means an exhaustive list, but it serves to indicate the complexity involved in calculating N directly from measured $I(E_A,E_0)$. Although attempts have been made to calculate some of these parameters from first principles[74], and hence

make direct quantitative analyses, some of the assumptions made are still debatable[75].

Presently, most of the quantitative studies of atomic densities with Auger electron spectroscopy are done in conjunction with calibration methods. The latter includes the use of radioactive counting[76], nuclear microanalysis[77], and measurements of deposition currents[78]. In such studies, the peak-to-peak height of an Auger peak in a derivative spectrum is often taken as proportional to $I(E_A,E_0)$, although this assumption is valid only for Auger peaks which exhibit constant shape in the N(E) versus E spectrum.

If only the atomic fractions, or coverages, of various elements on a surface are of interest to an experimenter, Palmberg's relative atomic sensitivity factors[72] (S_i) can be used. In this scheme I, the peak-to-peak height normalized to primary beam current, is used. The atomic fraction of element i on a surface is defined as

$$\theta_i = (I_i/L_iS_i)/\sum_{\nu} I_\nu/L_\nu S_\nu, \qquad (2.28)$$

where the subscript i denotes the species under investigation, the summation over ν covers all atomic species (including i) present on the surface, and L are the instrumental sensitivity factors.

In association with LEED, a still simpler approach can sometimes be used to estimate the surface coverage of a particular ad-atom. This occurs when the adsorbate gives rise to sharp LEED pattern(s). The Auger peak-to-peak height ratio of the adsorbate and the substrate (I_{ad}/I_{sub}) is taken when the LEED pattern is most well-defined. Insofar as the appearance of a simple LEED pattern corresponds to a definite coverage (e.g. (1x1) for 1 monolayer, p(2x1) for 1/2 monolayer, ($\sqrt{3}$x$\sqrt{3}$) for 1/3 monolayer), the ratio I_{ad}/I_{sub} can thus be used as an internal standard for calibration of coverages. The most favorable condition for this method arises when the same adsorbate gives rise to several of these simple LEED patterns. Then measurements of I_{ad}/I_{sub} for each can give a helpful calibration curve. This approach may become ambiguous when superlattice structures have several atoms per unit mesh[79,80], and therefore it must be used with extreme caution.

CHAPTER 3

MULTIPLE SCATTERING CALCULATIONS

3.1 INTRODUCTION

Detailed descriptions of multiple scattering calculations for LEED include the book by Pendry[11], as well as several other reviews[56,81,82]. The objective of this chapter is therefore to provide an overview and add perspective in relation to the studies undertaken in this work.

A multiple scattering calculation is often referred to as a 'dynamical' calculation because it considers not only the geometry of the crystal lattice and the ad-atoms, but also the interaction of the LEED electron with the vibrating ion cores of the lattice, as well as the multiple scattering events between these ion cores. Thus the potentials within and between these ion cores play important roles in a 'dynamical' calculation. The potential of the solid is usually approximated by the 'muffin-tin' model, where the potential is assumed constant between ion cores but spherically symmetric within atomic regions. The potentials of the latter are described by appropriate sets of phase shifts δ_l. Details of the 'muffin-tin' model are discussed in Section 3.2.

With the known scattering properties of individual ion cores, the scattering by individual planes of atoms (ion cores) can be constructed in angular-momentum, or L-, space by utilizing the spherical symmetry of the ion core potential. To build up the surface region of a solid, isolated planes have to be assembled and the interplanar scattering considered. This step can be done exactly or

perturbationally. Exact methods such as the T-matrix method[81,83] and the Bloch-wave method[84] calculate interplanar scattering to infinite order in the L-space and reciprocal (or K-) space representations respectively. For the case that the individual planes contain just one atom per unit mesh, the T-matrix method involves the inversion of a square matrix of dimension $N(l_{max}+1)^2$, where N is the number of atomic planes required to represent the solid and $(l_{max}+1)$ is the number of phase shifts required to describe the ion core scattering. The Bloch-wave method, on the other hand, has to solve an eigenvalue problem with matrix dimension 2n, where n is the number of plane waves required to represent the wavefield between the atomic planes. This number increases rapidly with decreasing interplanar distance. The exact methods are very demanding on both computing time and storage, and in practice their use is limited to research groups with (essentially) unlimited computing budgets.

To reduce the computing requirements to manageable levels, a perturbational scheme called the 'combined space' method[85] was employed in this work. In this approach, closely-spaced atomic planes (e.g. $\leq$0.5 Å) are grouped together to form a composite layer in L-space (similar to the T-matrix method) while more widely-spaced planes (e.g. $\geq$0.5 Å) are considered as simple (or Bravais lattice) layers. The manner in which each layer scatters plane waves is described by a diffraction matrix $\underset{\approx}{M}^{\pm\pm}$ (Section 3.3). The

interlayer scattering is then treated perturbationally in K-space (Section 3.4). The presence of inelastic scattering ensures that a finite stack of layers will be sufficient to represent the surface scattering. The advantage of the 'combined space' method is that it reduces N to simply the number of subplanes in a composite layer while keeping the number of plane waves for the wavefield expansion between layers to a manageable level (since here the interlayer separation is larger). In general, it is mathematically easier to handle plane waves (in K-space) than spherical waves (in L-space), and symmetry can be used (Section 3.5) to reduce the number of plane waves in practice. Transformation between the wave types has been discussed in detail by Marcus[86].

The final step of a multiple scattering calculation is to compute electron beam reflectivities from the stacked layers. The result may be written as

$$R_{\underset{\sim}{g}} = (k^{-}_{\underset{\sim}{g}\perp} / k^{+}_{\underset{\sim}{o}\perp}) |C_{\underset{\sim}{g}}|^2 \qquad (3.1)$$

where $k^{-}_{\underset{\sim}{g}\perp}$ and $k^{+}_{\underset{\sim}{o}\perp}$ represent the perpendicular components of the diffracted beam and the incident beam respectively and $C_{\underset{\sim}{g}}$ are coefficients in the expansion of the total wavefield outside the crystal, namely,

$$\Psi^{out}(\underset{\sim}{r}) = \exp(i\underset{\sim}{k}^{+}_{o}\cdot\underset{\sim}{r}) + \sum_{\underset{\sim}{g}} C_{\underset{\sim}{g}} \exp(i\underset{\sim}{k}^{-}_{\underset{\sim}{g}}\cdot\underset{\sim}{r}) \qquad (3.2)$$

where superscripts '+/-' denote waves propagating in the +x/-x directions in a left-handed Cartesian co-ordinate system (Figure 3.1) used in the multiple scattering programs. Calculated beam reflectivities correspond to measured beam intensities defined in Section 4.4.

3.2 PHYSICAL PARAMETERS IN LEED CALCULATIONS

Besides a structural model, various non-geometrical parameters are required for the calculation of I(E) curves. Non-geometrical parameters include the crystal potential and the vibration properties of the crystal lattice. The most important part of the crystal potential is the ion core potential which accounts for the multiple scattering experienced by the LEED electrons in a solid. The scattering caused by the valence-electron regions of the solid are responsible for the slight shifts of Bragg peaks and strong electron damping found in LEED. The inelastic scattering of course makes LEED surface sensitive; this damping results in the broadening of peaks in I(E) curves. Temperature also has an effect on beam intensities. The latter decreases as temperature increases. Suitable models must therefore treat the solid as a vibrating lattice.

3.2.1 THE 'MUFFIN-TIN' APPROXIMATION

The 'muffin-tin' model is well established for calculating band structures[87]. It considers the solid as a regular array of hard spheres, each centered on an atom and

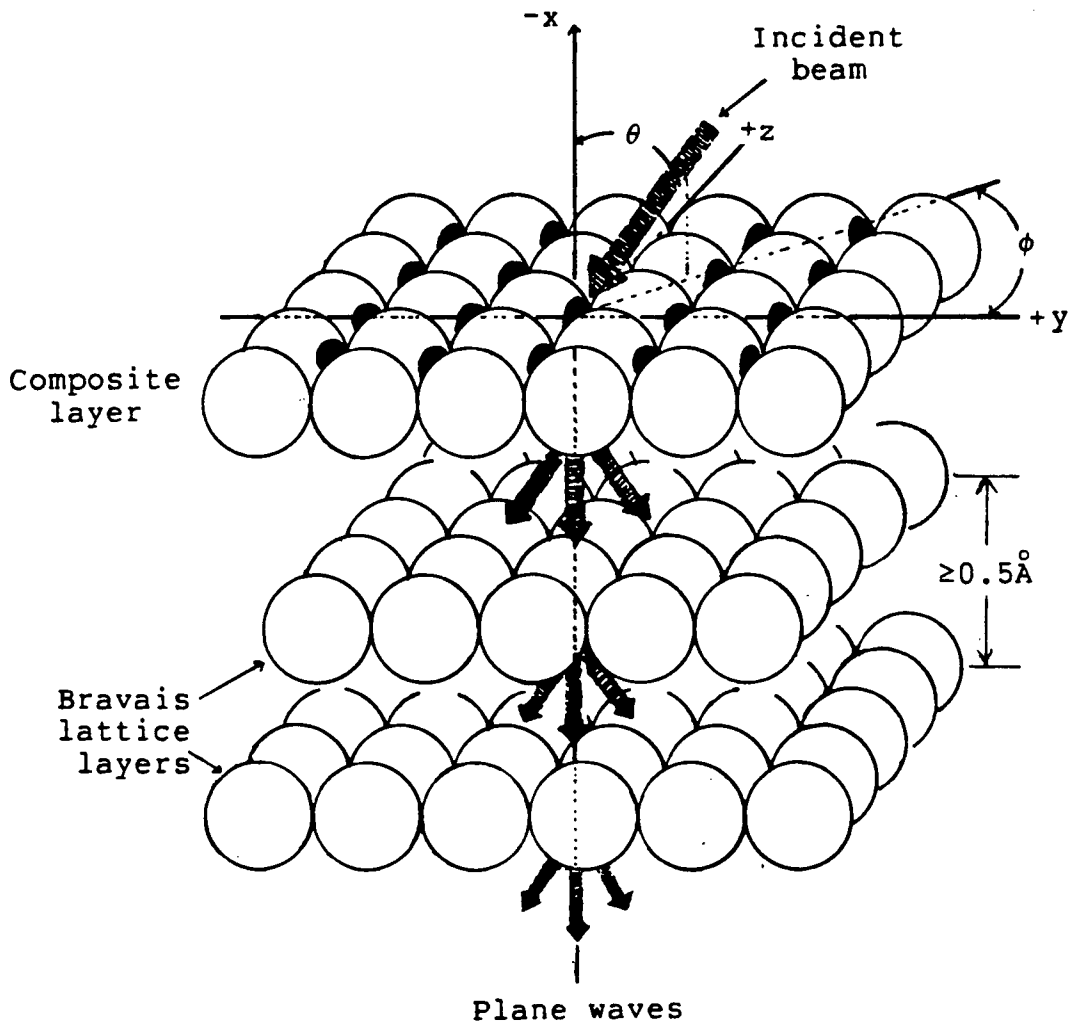

Figure 3.1: Left-handed co-ordinate system used in the 'combined space' multiple scattering calculations. Hollow and solid circles represent substrate and adsorbate atoms respectively. Bravais lattice layers are separated by at least 0.5 Å.

separated from one another by an intersphere region of constant potential V_o (this is sometimes referred to as the 'muffin-tin zero'). Each sphere can be viewed as an ion core within which the potential V_s is spherically symmetric. Figure 3.2 represents a 1-dimensional picture of such a model, with a row of scatterers along the x-axis. Here each scatterer is equivalent to a plane of ion cores in 3-dimensions. To minimize the volume approximated by the constant potential, the radii of the spheres are chosen so that they just touch one another. The scattering by any discontinuities between V_o and V_s at the sphere boundaries must be ignored when comparing calculated I(E) curves with those from experiment.

The potential runs continuously through the surface from vacuum to the solid's interior. Scattering by the surface barrier may occur, although this scattering is not particularly important at the energies used in LEED crystallography†. In practice, surface barrier effects are usually ignored in LEED crystallography, and V_o is set to zero at a distance r_o from the surface-vacuum interface on the vacuum side. In the multiple scattering calculations, r_o is usually chosen as the hard-sphere radius of the atomic species at the topmost surface region (Figure 3.2).

---

†This surface barrier becomes important only at shallow incident angles and/or low incident energies (≤40 eV) where total reflections are possible.

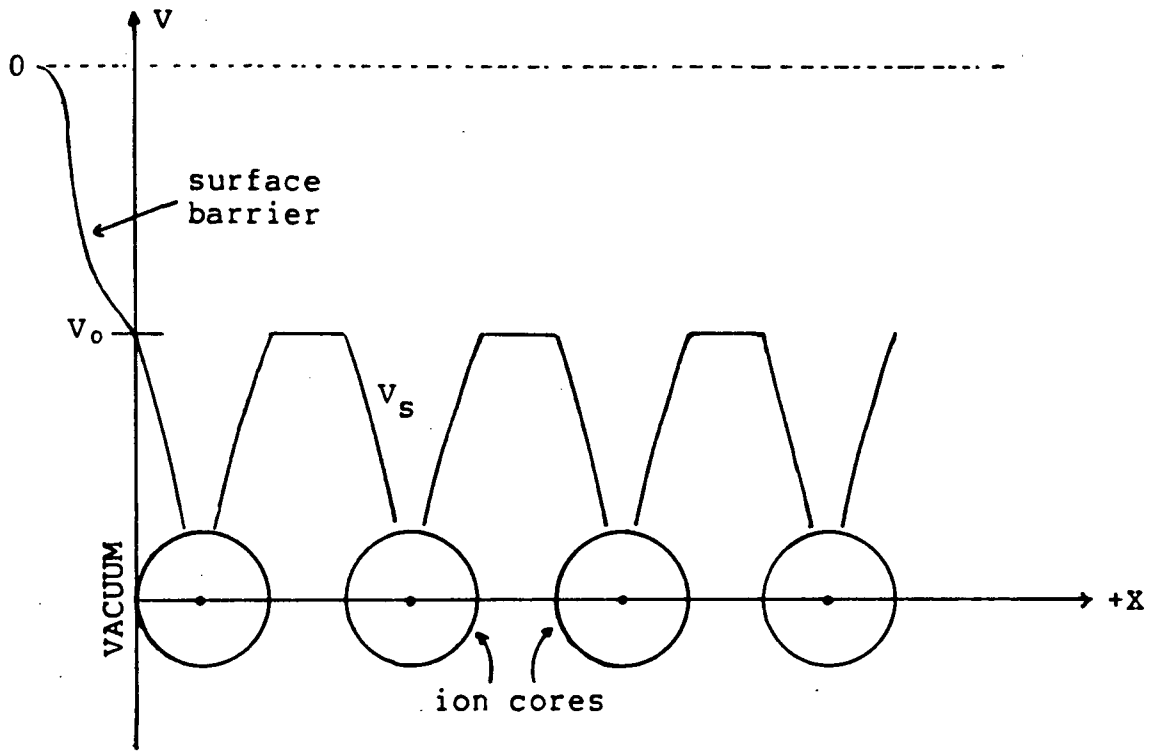

Figure 3.2: 'Muffin-tin' approximation for the potentials of a single row of ion cores along the x-axis.

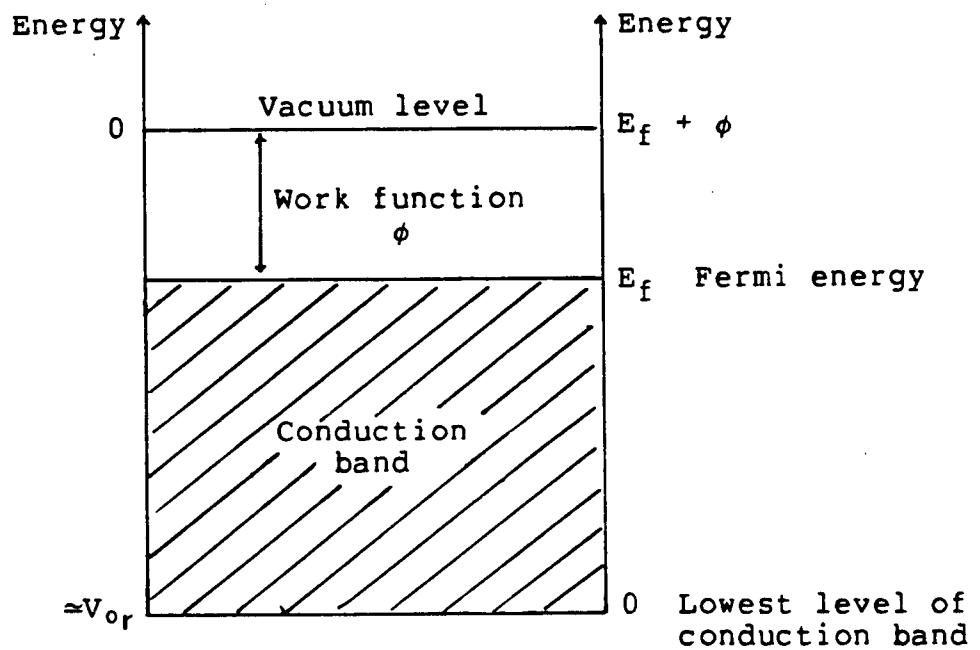

Figure 3.3: Approximation for V_{or} with known quantities of Fermi energy E_f and work function ϕ of metals.

3.2.2 THE CONSTANT POTENTIAL V_0

The main effect of the real part of V_0 is to model the speeding up that an electron experiences on entering the crystal. However, V_0 also requires an imaginary part, V_{0i}, to accommodate the inelastic scattering experienced by the LEED electron. V_0 can thus be written as

$$V_0 = V_{0r} + iV_{0i}, \tag{3.3}$$

where the component V_{0r} corresponds to the 'inner potential', and V_{0i} is defined as a negative number.

3.2.2.1 The Real Potential V_{0r}

Typically V_{0r} is between -5 and -15 eV. Theoretically it is dependent on energy, due to exchange and correlation effects[87], but for LEED crystallographic studies, it can be generally treated as energy-independent[11]. Increasing $|V_{0r}|$ shifts the Bragg peaks to lower energies in calculated I(E) curves (where E corresponds to energy in vacuum).

A first approximation value for V_{0r} is obtained by the sum of the Fermi energy E_f and the work function ϕ. Figure 3.3 schematically shows how V_{0r}, ϕ and E_f are related in metals. In the LEED studies on zirconium, an initial value of -10 eV was used for V_{0r}. However, during comparison with experimental I(E) curves, the calculated I(E) curves are given a rigid shift to provide the best agreement with the former. This enables

a refined value of V_{o_r} to be determined.

3.2.2.2 The Imaginary Potential V_{o_i}

Inelastic scattering is introduced into multiple scattering calculations by the phenomenological approach of giving an imaginary component to V_o. Slater[88] noted for an electron in a region of constant potential with real and imaginary components as in equation (3.3) that intensity decays with time as $\exp(-2V_{o_i}t/\hbar)$. The lifetime, τ, of an electron then relates to V_{o_i} according to

$$\tau = \hbar/2V_{o_i}. \tag{3.4}$$

An increase in V_{o_i} corresponds to a decrease in lifetime and hence to an increase in the inelastic scattering. In general, the shorter the lifetime the greater the uncertainty in energy. Using the Heisenberg uncertainty principle, Pendry[11] derived the relationship between the peak width ΔE_W in an I(E) curve and V_{o_i} as

$$\Delta E_W \geq 2V_{o_i}. \tag{3.5}$$

Therefore, in practice, one examines the peak widths of a series of Bragg peaks in an I(E) curve and correlates the incident energy to V_{o_i}, using the equals sign in equation (3.5). An energy-dependent V_{o_i} has often been used, for example with the functional form[89]

$$V_{oi} = -BE^{1/3}, \qquad (3.6)$$

where E is the incident energy and B is a parameter to be chosen for each material. Although equation (3.6) was used quite successfully in a LEED crystallographic analysis for clean Zr(0001), it was found in the present work that a constant value of -5 eV for V_{oi} was equally favorable. Indeed use of the constant value eliminated some convergence problems which occurred at lower energies when equation (3.6) was used in the multiple scattering calculations.

3.2.3 ION CORE SCATTERING

3.2.3.1 The Ion Core Potential V_s

The spherically symmetrical parts of the 'muffin-tin' potential, V_s, correspond to atomic potentials in a solid and these contributions are primarily responsible for the back scattering in LEED. Ideally V_s should be obtained from a self-consistent energy band calculation for the solid structure of interest[90]. However, such calculations are not generally available for adsorption systems. Also a detailed band structure calculation requires knowledge of the surface geometry, which of course is the objective of a LEED crystallographic study. For first analyses, then, simpler approaches are required to

estimate V_s, and this may be done from charge distributions. In the simplest case these are estimated by a direct summation of individual atomic charge densities, although a preferable approach would involve some sort of molecular orbital investigation. Either way an appropriate structure has to be assumed, and this may be in the form of a cluster[91] or a diperiodic slab[92,93] to mimic the surface system. In general, the spherically symmetrized atomic potential separates into coulombic and exchange contributions such that

$$V_s(r) = V_c(r) + V_{ex}(r). \qquad (3.7)$$

The Coulombic term $V_c(r)$ can be obtained by integrating the Poisson equation with the appropriate ion core charge density distributions[94]. The exchange correlation term $V_{ex}(r)$ can be calculated according to[95]

$$V_{ex}(r) = -3\alpha e^2[3\sigma_{sup}(r)/32\pi^2r^2]^{1/2}, \qquad (3.8)$$

where $\sigma_{sup}(r)$ is the charge density and α depends on the exchange approximation used.

Many investigations indicate that bulk atomic potentials can be adequate for describing surface and near surface atoms in current LEED crystallographic analyses. Band structure atomic potentials for many

metals have been tabulated by Moruzzi *et al.*[96], and a variety of atomic potentials for ad-atoms are available, for example the computer compilation made by Van Hove[97]. Ideally, it is preferable to test several types of V_s, and assess their merits by comparing calculated I(E) curves with those from experiment. It is in this spirit that the crystal lattice method[92,93] was tried for the oxygen adsorption on Zr(0001). Figure 3.4 shows the crystal lattice of zirconium oxide (ZrO) used in this particular method to obtain V_s for oxygen with varying negative charges.

3.2.3.2 The Phase Shifts δ_l

Given the atomic potentials, the wave functions for an electron inside a sphere are obtained by solving the Schrödinger equation

$$[-(\hbar^2/2m)\nabla^2 + V_s]\Psi = E\Psi, \qquad (3.9)$$

where E is the energy with respect to the 'muffin-tin zero'. The asymptotic solution to equation (3.9) has the form

$$\Psi_k(r,\theta_s) = \exp(ikr\cos\theta_s) + t(k,\theta_s)\exp(ikr)/r, \qquad (3.10)$$

where the term $\exp(ikr)/r$ is a spherical wave at a distance r from the center of the ion core and $t(k,\theta_s)$ is the ion core scattering factor which can be expanded

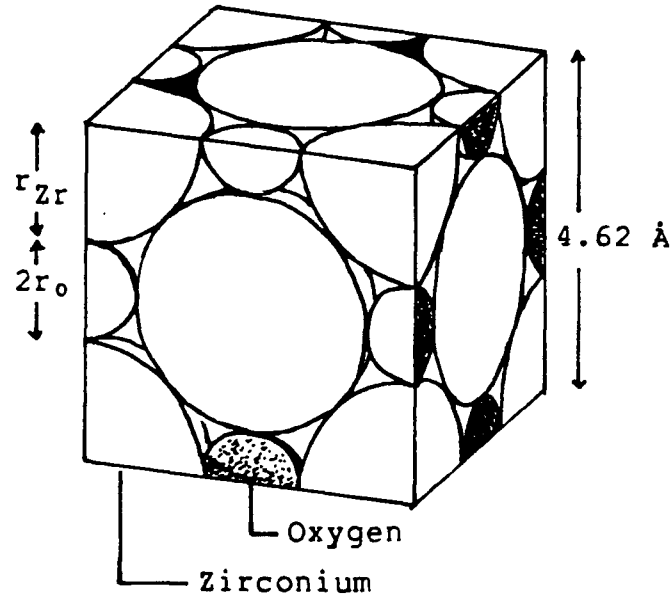

(a)

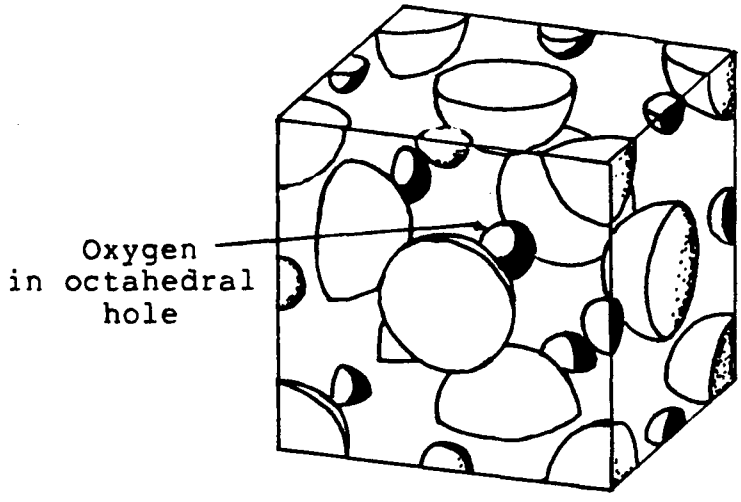

(b)

Figure 3.4: Unit cell of ZrO crystal lattice structure. (a)Unit cell dimensions and respective hard sphere radii for Zr^o and O^o used in the calculations of V_s for both elements. (b)A blown-up to show the local environment of oxygen in the lattice.

as[98]

$$t(k,\theta_s) = 4\pi \sum_{l=0}^{\infty} (2l+1) t_l(k) P_l(\cos\theta_s). \qquad (3.11)$$

In equation (3.11), P_l is the Legendre polynomial associated with the angular momentum quantum number l and the $t_l(k)$ are defined as

$$t_l(k) = (1/2k)\exp(i\delta_l)\sin\delta_l. \qquad (3.12)$$

The quantities δ_l appearing in equation (3.12) are known as atomic phase shifts; they determine the total elastic scattering cross section through

$$\sigma_{el} = (4\pi/k^2) \sum_{l=0}^{\infty} (2l+1)\sin^2\delta_l. \qquad (3.13)$$

Phase shifts for a particular ion core potential V_s are found by solving equation (3.9) inside the atomic sphere and, for each value of l, joining smoothly the asymptotic form of the solution at the boundary of the sphere to the corresponding solution for the outside region[11]. From equation (3.9), it can be understood that phase shifts are dependent on both V_s and the energy of the incident electron. Although, as suggested by equation (3.11), the expansion for the ion core scattering factor requires an infinite number of phase shifts, in practice the expansions can be truncated to a

finite set. For example, for energies less than 250 eV, the use of a maximum of eight phase shifts (i.e. $l_{max}=7$) generally provides a very adequate approximation in order to reduce the computing effort in obtaining the layer diffraction matrices $\underset{\sim}{M}^{\pm\pm}$. Indeed, for weak scatterers, a smaller number of phase shifts may be acceptable. Figure 3.5 compares the phase shifts of oxygen obtained from different V_s while Figure 3.6 does the same for Zr. The computer program used calculates the phase shifts as modulus of π, so discontinuities may appear to be present in a phase shift versus energy plot. This is not a problem for presentation purposes, but such discontinuities are undesirable for the energy interpolation procedures used in a LEED calculation. Therefore, before use, the discontinuities must be removed manually by adding to or subtracting from the calculated phase shifts a value of π.

3.2.4 LATTICE MOTION

So far the ion core scattering factors $t(k,\theta_s)$ have been calculated assuming a rigid lattice. This is true provided the time of interaction of an individual electron with a scattering center is short. Typically in LEED this is around 10^{-16}s, which is considerably smaller than the time for an atomic vibration (10^{-13}s). Nevertheless the set of electrons collected during a LEED intensity measurement inevitably sample positions over the complete range of the

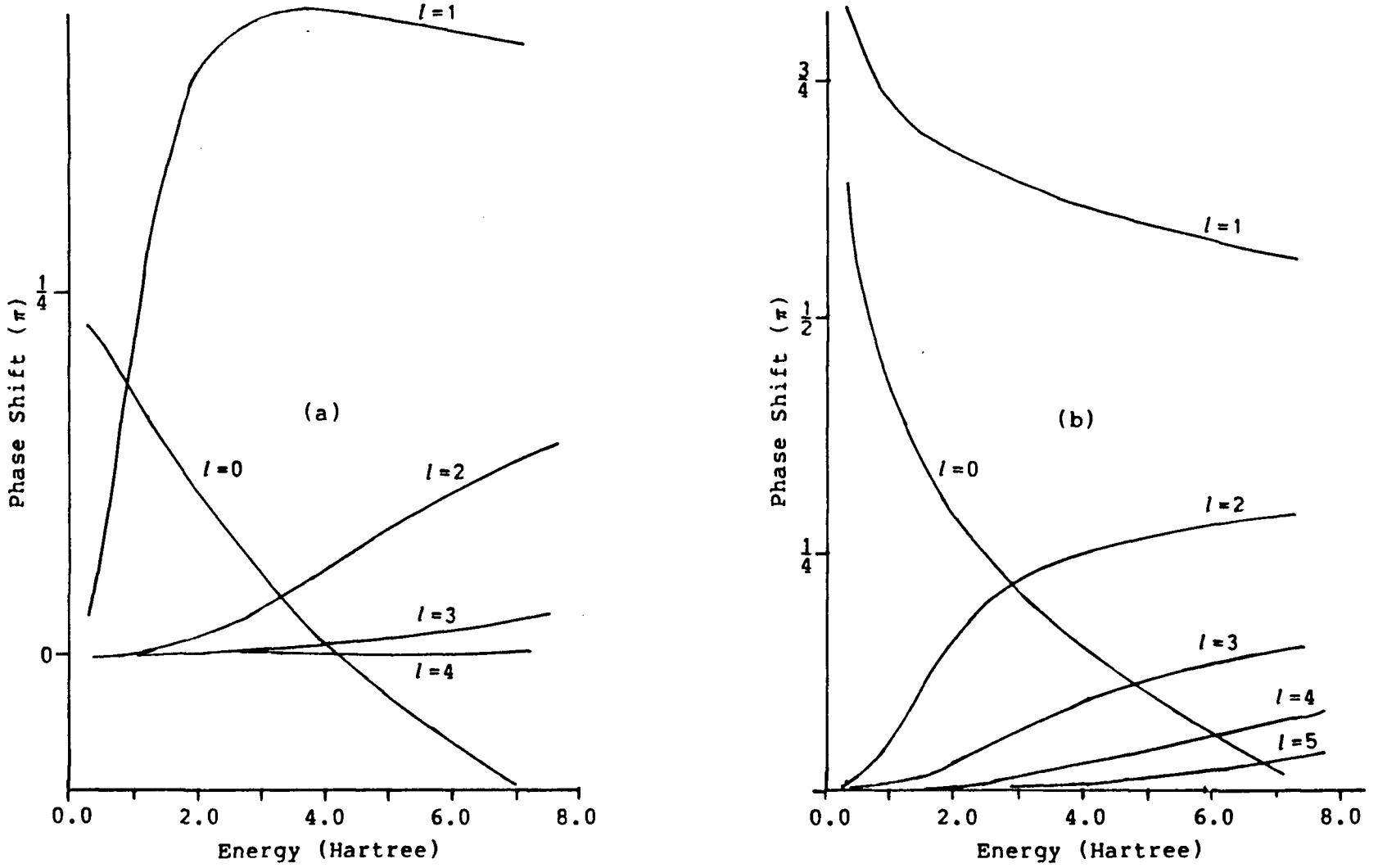

Figure 3.5: Comparison of oxygen phase shifts derived from (a) V_s obtained from ZrO crystal lattice and (b) superposition potentials obtained by Demuth *et al.*[98].

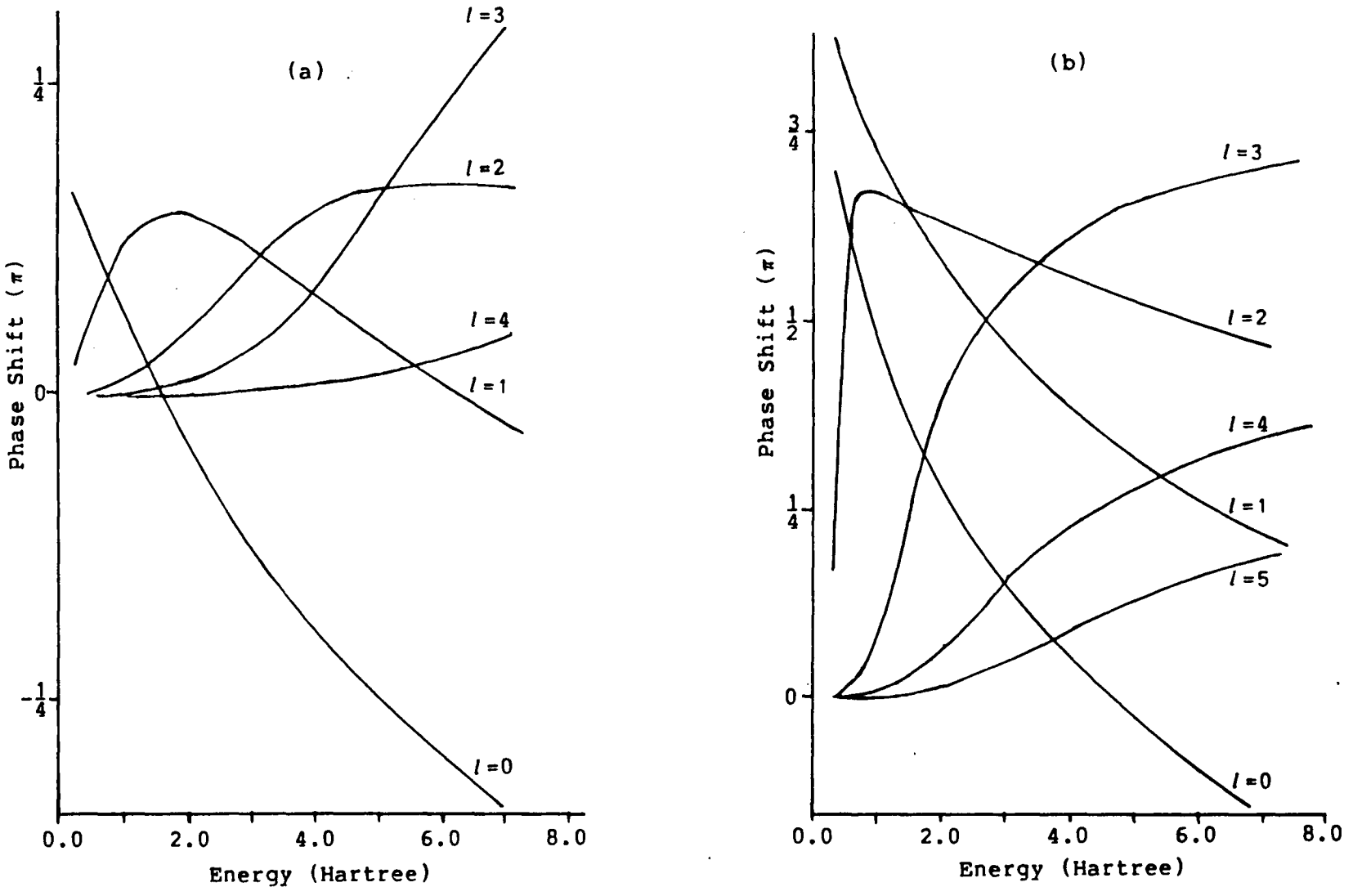

Figure 3.6: Comparison of zirconium phase shifts derived from (a) V_s obtained from ZrO crystal lattice and (b) V_s from band structure calculations[96].

atomic vibrating motions. This suggests the use of scattering factors that are averaged over the motions of the vibrating atom. In other words, the rigid lattice is replaced by a lattice of 'blurred atoms'.

The effect of thermal motions of the atoms in a solid is most generally incorporated into multiple scattering calculations by adding an isotropic Debye-Waller type contribution to the atomic scattering factor. Jepsen *et al.*[99] showed that for isotropic vibrations, and neglecting the correlations between neighboring atoms, the atomic scattering factor $t(k,\theta_s)_T$ for such a vibrating lattice can be related to $t(k,\theta_s)$ by

$$t(k,\theta_s)_T = t(k,\theta_s)\exp(-M), \tag{3.14}$$

where the exponential term is the Debye-Waller factor and M is defined as

$$M = (1/6)|\Delta\underset{\sim}{k}|^2<(\Delta\underset{\sim}{r})^2>_T. \tag{3.15}$$

In equation (3.15), $\Delta\underset{\sim}{k}$ represents the momentum transfer for the diffraction and $<(\Delta\underset{\sim}{r})^2>_T$ represents the mean square vibration amplitude as a function of temperature, which has the following asymptotic forms:

$$<(\Delta\underset{\sim}{r})^2>_{T\to\infty} = 9T/mk_B\theta_D^2; \tag{3.16}$$

and

$$<(\Delta\underset{\sim}{r})^2>_{T\to 0} = (9/mk_B\theta_D)(0.25+1.642T^2/\theta_D^2), \qquad (3.17)$$

where T is the surface temperature, θ_D is the Debye temperature, m is the atomic mass, and k_B is the Boltzmann constant. The first three variables are input parameters in a LEED calculation. Assuming T equal zero in equation (3.17), Van Hove and Tong[56] suggested a single approximate functional form for $<(\Delta\underset{\sim}{r})^2>_T$ such that

$$<(\Delta\underset{\sim}{r})^2>_T = \sqrt{(<(\Delta\underset{\sim}{r})^2>_{T=0})^2 + (<(\Delta\underset{\sim}{r})^2>_{T\to\infty})^2}. \qquad (3.18)$$

The term $<(\Delta\underset{\sim}{r})^2>_{T=0}$ is generally undesirable for most materials (at typical LEED experimental temperatures), and is usually set to zero. However if the user so desires, it can be fed into the calculation through the input list.

With the new ion core scattering factors, a set of temperature-dependent phase shifts δ_{lT} can be derived from

$$t(k,\theta_s)_T = -(\hbar^2/4imk)[\exp(2i\,\delta_{lT})-1]. \qquad (3.19)$$

For the interested readers, the direct relationship between δ_l and δ_{lT} can be found in reference [56]. From equation (3.19), it can be deduced that δ_{lT} are complex quantities. These temperature-dependent phase shifts are used in the calculation of intralayer scattering (Section 3.3), although

for interlayer scattering the effect of thermal motions of atoms can be included by simply multiplying the layer diffraction matrices by exp(-M). Vibrational anisotropy can be introduced into the interlayer scattering by using an anisotropic M formed from different amplitudes for the parallel and perpendicular components of $\Delta\underset{\sim}{k}$ and $\Delta\underset{\sim}{r}$ in equation (3.15). Details on implementation of these concepts in the calculations are discussed in Van Hove and Tong's book[56].

3.3 THE LAYER DIFFRACTION MATRIX

The scattering of plane waves incident on either side of a layer parallel to the surface can be described by the layer diffraction matrix $\underset{\sim}{M}^{\pm\pm}$. A layer in the 'combined space' method is defined as an assembly of one to N parallel subplanes of ion cores each containing only one ion core per unit mesh. When there is only one subplane in the layer, it is called a Bravais lattice layer. When the layer is composed of more than one subplane it is referred to as a composite layer. Examples of these two types of layers are shown in Figure 3.1. Although a composite layer is shown as the top layer in the figure, that is not a necessary condition. In fact the two types of layers can appear in any order parallel to the (yz) plane.

The particular element $M^{\pm\pm}_{\underset{\sim}{g}',\underset{\sim}{g}}$ of the layer diffraction matrix represents the amplitude of the plane wave with a

wavevector $\underset{\sim}{k}_g$, which is scattered from a layer for an incident plane wave of unit amplitude and wavevector $\underset{\sim}{k}_g$. Superscript signs specify the propagation directions of the plane waves: a '+' and a '-' for propagation into and out of the crystal respectively, and they are read from right to left. Figure 3.7 schematically shows the scattering of a set of plane waves by a plane of ion cores with known diffraction matrix $\underset{\approx}{M}^{\pm\pm}$. In general, the layer reflection ($\underset{\approx}{r}$) and transmission ($\underset{\approx}{t}$) matrices can be obtained from $\underset{\approx}{M}^{\pm\pm}$ by the following relationships:

$$\underset{\approx}{r}^{+-} = \underset{\approx}{M}^{+-};\ \underset{\approx}{r}^{-+} = \underset{\approx}{M}^{-+};\ \underset{\approx}{t}^{++} = \underset{\approx}{M}^{++} + \underset{\approx}{I};\ \text{and}\ \underset{\approx}{t}^{--} = \underset{\approx}{M}^{--} + \underset{\approx}{I}, \qquad (3.20)$$

where $\underset{\approx}{I}$ represents a unit matrix. The notations of these matrices are further illustrated diagramatically in Figure 3.8. For a Bravais lattice layer, there is a mirror plane parallel to the layer, bisecting every ion core, hence $\underset{\approx}{r}^{+-} = \underset{\approx}{r}^{-+}$ and $\underset{\approx}{t}^{++} = \underset{\approx}{t}^{--}$.

The evaluation of $\underset{\approx}{M}^{\pm\pm}$ is rather complicated even for the Bravais lattice layer, therefore no attempt will be made here to give the derivation. Detailed mathematical treatments are in the literature[11,56,86]. The important steps involved can be summarized as follows:

1. The plane waves are transformed into spherical waves.
2. The amplitudes of the spherical waves resulting from the scattering by an isolated plane of ion cores are calculated. This information is stored in the planar

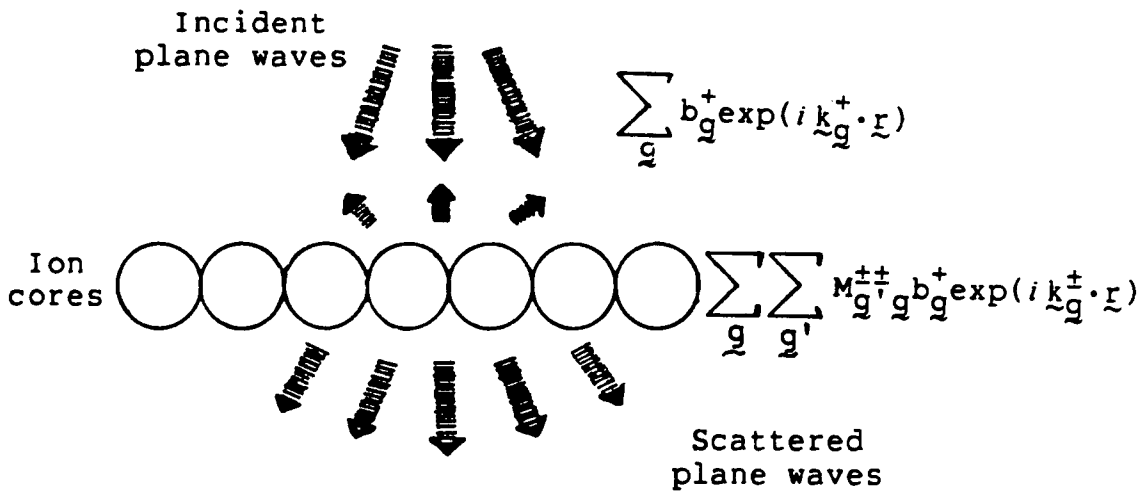

Figure 3.7: Multiple scattering of a set of plane waves by a layer of ion cores with known diffraction matrix $\underset{\approx}{M}^{\pm\pm}$.

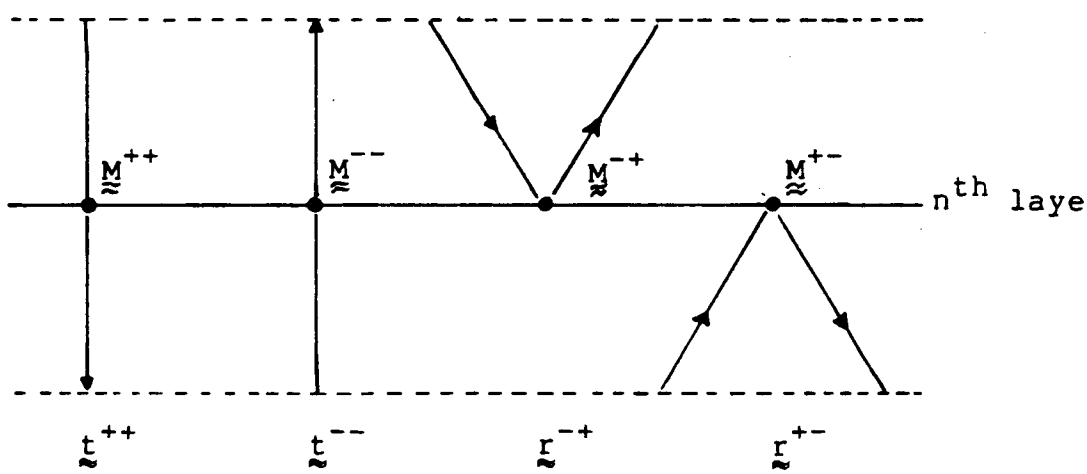

Figure 3.8: Schematic diagram of transmission and reflection matrices at the n^{th} layer. Broken lines are midway between consecutive layers.

scattering matrix $\underset{\sim}{\tau}$.

3. In case of composite layer, the last step is repeated for each subplane in the layer. As a consequence of interplanar scattering, the individual $\underset{\sim}{\tau}^i$ for subplane i is modified to a total planar scattering matrix $\underset{\sim}{T}^i$. The wave amplitudes are then summed from the N subplanes.
4. The spherical waves are transformed into plane waves.

3.3.1 BRAVAIS LATTICE LAYERS

Pendry[11] has detailed the overall treatment which leads to the final expression for the matrix element

$$M^{\pm\pm}_{\underset{\sim}{g}'\underset{\sim}{g}} = \frac{16\pi^2 i}{Ak^{+}_{\underset{\sim}{g}',\perp}} \sum_{LL'} Y_L(\underset{\sim}{k}^{\pm}_{\underset{\sim}{g}})\ \tau_{LL'}(k_0)\ Y^{*}_{L'}(\underset{\sim}{k}^{\pm}_{\underset{\sim}{g}'}), \qquad (3.21)$$

where A is the area of the unit mesh; L and L' represent the pairs of angular momentum quantum numbers (l,m) and (l',m') respectively. Also in equation (3.21), the $Y_L(\underset{\sim}{k})$ are spherical harmonics for the angle between the $\underset{\sim}{k}$ and the surface normal, '*' indicates complex conjugation and $\tau_{LL'}(k_0)$ is the LL' element of the planar scattering matrix $\underset{\sim}{\tau}(k_0)$. The latter matrix is similar to $\underset{\sim}{M}^{\pm\pm}$ except that spherical waves represented by L and L' are considered in angular momentum space, and can be expressed as[81]

$$\underset{\sim}{\tau}(k_0) = \underset{\sim}{t}(k_0)[\underset{\sim}{I} - \underset{\sim}{X}]^{-1}, \qquad (3.22)$$

where $\underset{\approx}{t}(k_0)$ is the diagonal ion core t-matrix whose non-zero elements are given by equation (3.12), the intraplanar scattering matrix $\underset{\approx}{X}$ is the product of a structural factor $\underset{\approx}{G}(\underset{\sim}{k}_0^+)$ and the t-matrix such that

$$\underset{\approx}{X} = \underset{\approx}{G}(\underset{\sim}{k}_0^+)\ \underset{\approx}{t}(k_0). \tag{3.23}$$

$\underset{\approx}{G}$ describes the intraplanar propagators in L-space; these propagators are dependent on damping and the arrangement of the ion cores but independent of the scattering properties of the ion cores. The details in the evaluation of $\underset{\approx}{X}$ have been discussed by Kambe[100] and by Jepsen *et al.*[101].

The expression for $M^{\pm\pm}_{\underset{\sim}{g},\underset{\sim}{g}}$ in equation (3.21) is valid only if the origin of the co-ordinates within the plane is an ion core center. In order to exploit symmetry in K-space (Section 3.5.2), the formula is modified slightly to include a lateral shift such that the origin of the layer can be related to the symmetry element(s) containing the incident electron beam. Also, the temperature effect is accounted for by multiplying $\underset{\sim}{M}^{\pm\pm}$ by a Debye-Waller factor as discussed in Section (3.2.4). The subroutine that computes $\underset{\sim}{M}^{\pm\pm}$ is called MSMF and the details on implementation can be found in Van Hove and Tong's book[56]. All references to specific subroutines in this thesis are either to Van Hove and Tong's book[56] or to the magnetic tape provided by Van Hove[97].

3.3.2 COMPOSITE LAYERS

Here, layers are considered in which there are N (N>1) subplanes of ion cores closely packed together (indeed possibly coplanar). By definition, a subplane contains a single kind of atom, and has just one atom per unit mesh. There is no restriction on the types of subplanes that a composite layer is made up of. Thus, a composite layer can either be atomically homogeneous or otherwise. Two such examples associated with the adsorption studies of oxygen on Zr(0001) are shown in Figure 3.9. Figure 3.9(a) shows a graphitic (2x2) oxygen overlayer on Zr(0001); here the composite layer has two oxygen atoms per unit mesh. Figure 3.9(b) is an example of an atomically heterogeneous composite layer. Specifically a (2x2) oxygen underlayer occupies the tetrahedral holes about 0.4 Å below the first zirconium layer. Therefore this composite layer is made up of four zirconium atoms and one oxygen atom per unit mesh.

In addition to the evaluation of the planar scattering matrix $\underset{\sim}{\tau}^{i}$ for the isolated subplane i, one has to calculate the total scattering matrix $\underset{\sim}{T}^{i}$ for that particular subplane resulting from the multiple scattering with the other (N-1) subplanes inside the composite layer. The general expression for the diffraction matrix element $M^{\pm\pm}_{\underset{\sim}{g}',\underset{\sim}{g}}$ of a composite layer with N subplanes is given by[56,102]

$$M^{\pm\pm}_{\underset{\sim}{g}',\underset{\sim}{g}} = \frac{16\pi^2 i}{Ak^{+}_{\underset{\sim}{g}',\perp}} \sum_{LL'} Y_L(\underset{\sim}{k}^{\pm}_{\underset{\sim}{g}}) Y^{*}_{L'}(\underset{\sim}{k}^{\pm}_{\underset{\sim}{g}'}) \sum_{i=1}^{N} R^{i\pm}_{\underset{\sim}{g}} (R^{i\pm}_{\underset{\sim}{g}'})^{-1} T^{i}_{LL'}. \qquad (3.24)$$

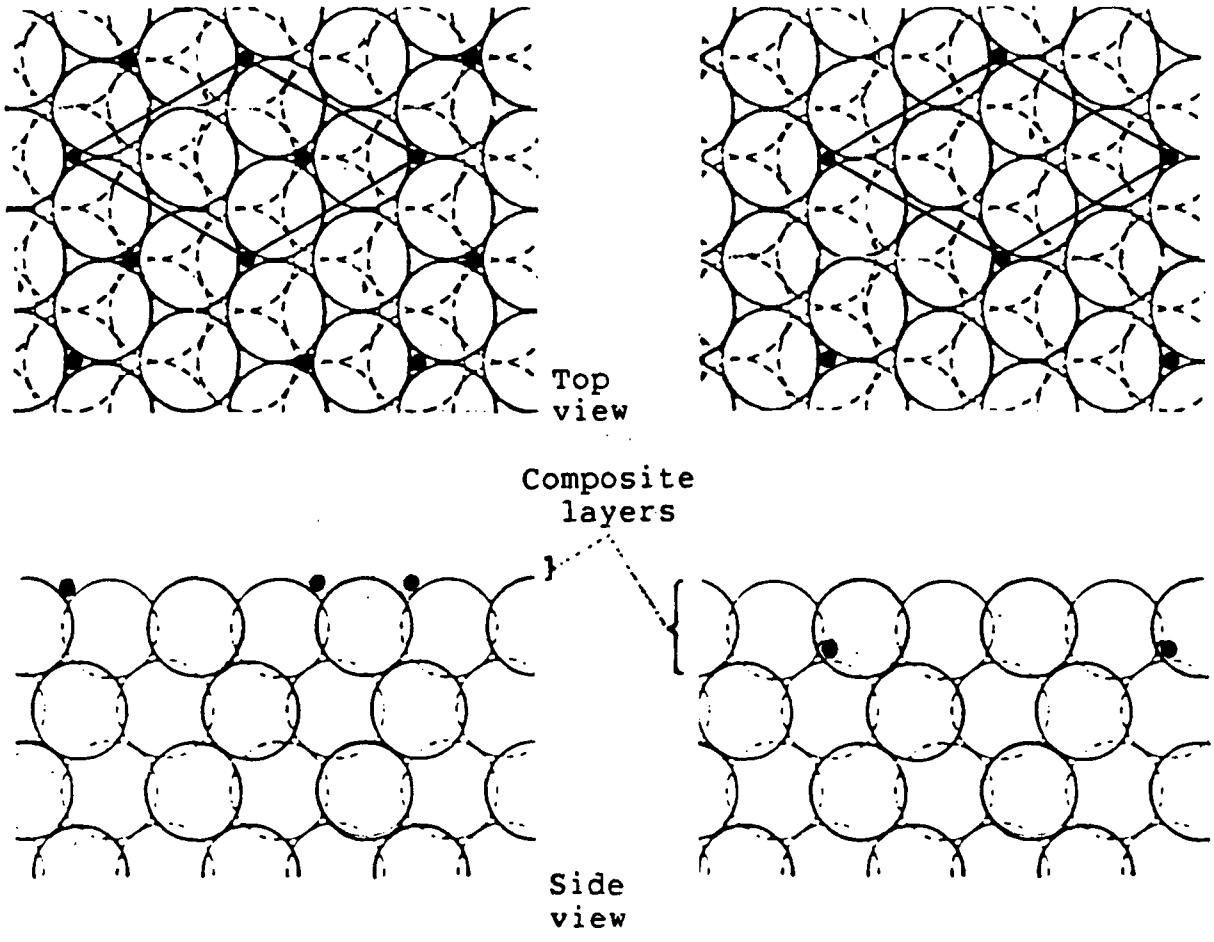

(a) Zr(0001)-(2x2)-2O
graphitic overlayer

(b) Zr(0001)-p(2x2)-O
tetrahedral hole
underlayer

Figure 3.9: Examples of composite layer. (a)Graphitic type oxygen overlayer: 2 oxygen atoms per unit mesh. (b)p(2x2) oxygen underlayer which is separated from the top zirconium layer by ≃0.4 Å: 4 zirconium atoms and 1 oxygen atom per unit mesh.

Most of the symbols in equation (3.24) have been explained in equation (3.21). New symbols appear only after the last summation sign where the index i labels the N subplanes. The origin of each subplane can be defined by the center of any one of the ion cores, which has a position vector $\underset{\sim}{r}_i$ relative to an arbitrary origin of the composite layer. The quantities $R_{\underset{\sim}{g}}^{i\pm}$ are then defined as

$$R_{\underset{\sim}{g}}^{i\pm} = \exp(\pm i \underset{\sim}{k}_{\underset{\sim}{g}}^{\pm} \cdot \underset{\sim}{r}_i). \tag{3.25}$$

The quantities $T^i{}_{LL'}$ (i.e. the LL' elements of the total planar scattering matrix $\underset{\sim}{T}^i$) give the self consistent amplitude of an outgoing spherical wave Y_L leaving an ion core of subplane i due to a spherical wave $Y^*{}_{L'}$ incident on all subplanes of the composite layer.

The evaluation of $M_{\underset{\sim}{g}',\underset{\sim}{g}}^{\pm\pm}$ in equation (3.24) involves the calculation of the total planar scattering matrix $\underset{\sim}{T}^i$ for each subplane. This can be done exactly, as in Beeby's matrix inversion scheme[83], or perturbationally as in the reverse scattering perturbation method[81,103]; in addition a combination of these approaches may be used[56,81]. All of these methods consider the scattering of spherical waves in L-space. The complete mathematical treatments can be found in the references quoted, but the principles involved will be discussed very briefly as follows.

3.3.2.1 Matrix Inversion

In the matrix inversion method, the multiple scattering between any pair of subplanes is treated exactly regardless of magnitudes. Following Beeby[83], the matrices $\underset{\approx}{T}^i$ can be calculated by solving a set of linear equations which can be expressed as

$$\begin{bmatrix} \underset{\sim}{T}^1 \\ \underset{\sim}{T}^2 \\ \cdot \\ \cdot \\ \cdot \\ \underset{\sim}{T}^N \end{bmatrix} = [\underset{\approx}{A}]^{-1} \begin{bmatrix} \underset{\sim}{\tau}^1 \\ \underset{\sim}{\tau}^2 \\ \cdot \\ \cdot \\ \cdot \\ \underset{\sim}{\tau}^N \end{bmatrix} \tag{3.26}$$

The matrix $\underset{\approx}{A}$ in turn consists of N^2 smaller matrices called $\underset{\approx}{A}^{ij}$ which are defined as

$$\underset{\approx}{A}^{ii} = \underset{\approx}{I}, \text{ and } \underset{\approx}{A}^{ij} = -\underset{\sim}{\tau}^i \underset{\approx}{G}^{ij}. \tag{3.27}$$

The square matrix $\underset{\approx}{G}^{ij}$ describes the interplanar propagators from subplane j to subplane i, and has a dimension of $(l_{max}+1)^2$ where l_{max} is the largest value of l included in expressions over angular momentum. The dimension of $\underset{\approx}{A}$, which corresponds to the number of unknowns in equation (3.26), is therefore $N(l_{max}+1)^2$. The computer storage for $\underset{\approx}{A}$, and the computing time required for its inverse limit the number N to about 5

with the computer (Amdahl 470 V8) currently used by this laboratory. For composite layers with strongly scattering ion cores or closely-spaced subplanes, 'matrix inversion' has to be used. One such example is the graphitic oxygen layer depicted in Figure 3.9(a) where two coplanar oxygen subplanes are present.

3.3.2.2 Reverse Scattering Perturbation

In LEED forward scattering is much stronger than back scattering, and this opens the possibility of treating back scattering as a perturbation while forward scattering is considered exactly. The reverse scattering perturbation scheme[56,103] is iterative in nature and is very similar to the renormalized forward scattering method[11] for layer stacking (Section 3.4). The major difference between these two methods is that the former is formulated in L-space while the latter is in K-space.

In the implementation of the reverse scattering perturbation method, the subplanes are ordered according to increasing distance from vacuum. Incident plane waves are transformed into spherical waves which travel back and forth through the composite layer of N subplanes, as shown in Figure 3.10. Specifically, when the waves are propagating into the crystal (+x direction) for the p^{th} time, the total scattering amplitude arriving at plane i (Figure 3.10) will consist of the multiple forward scattering amplitude $F^{i+}(p)$ and the single back scattering amplitude $B^{i+}(p)$

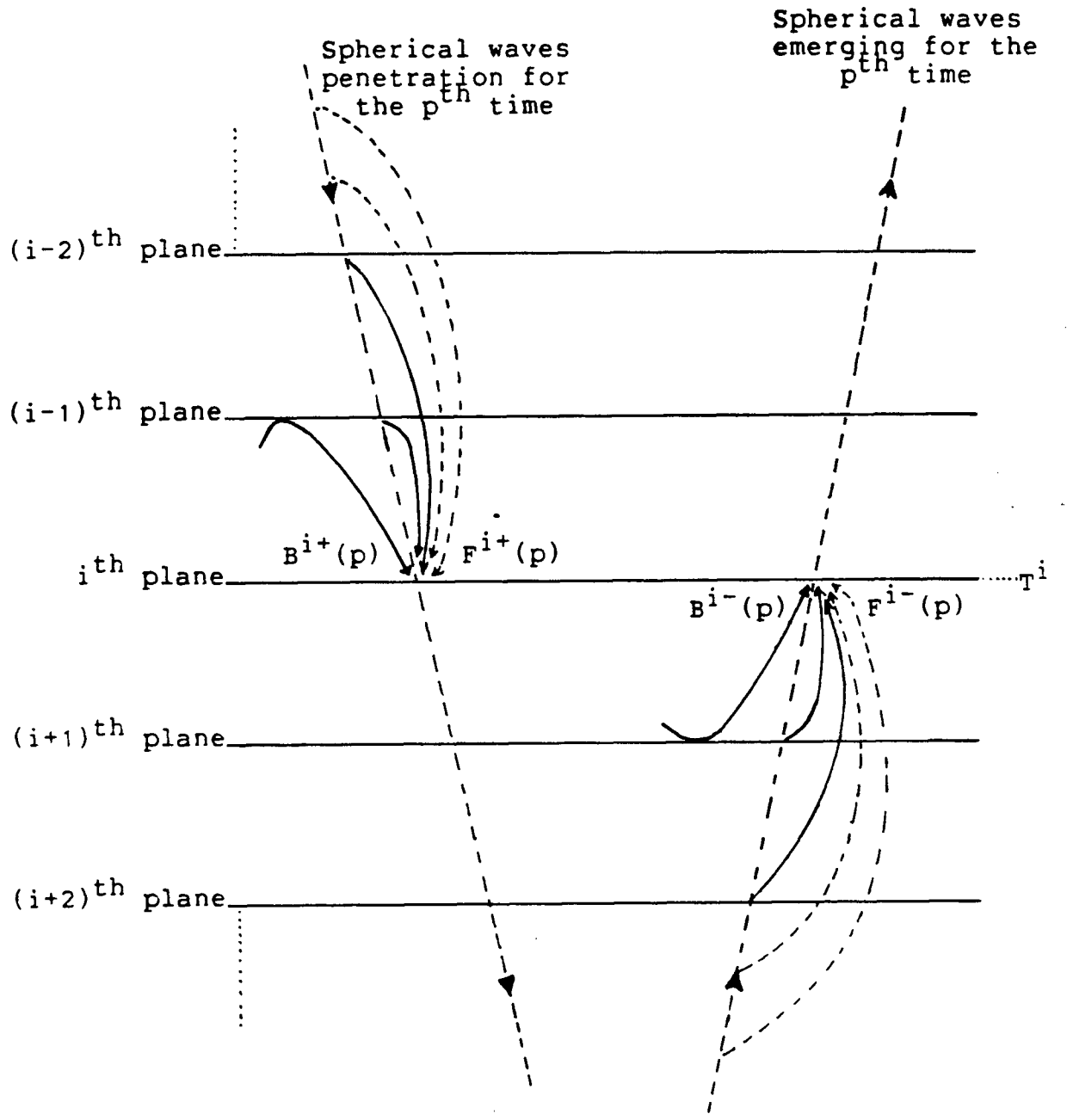

Figure 3.10: Schematic illustration of the contributions of scattering amplitudes to the i^{th} subplane by forward and back scattering. Spherical waves are travelling along $\pm x$ directions for the p^{th} time in the reverse scattering perturbation formalism.

$$T^{i+}(p) = F^{i+}(p) + B^{i+}(p). \tag{3.28}$$

Similarly, when the waves are propagating towards vacuum (-x direction),

$$T^{i-}(p) = F^{i-}(p) + B^{i-}(p). \tag{3.29}$$

The iteration converges when $T^{i-}(p)$ equals $T^{i-}(p-1)$ for all the N subplanes.

Mathematically, the reverse scattering perturbation is equivalent to the Gaussian Seidel-Aitken iterative algorithm for matrix inversion. If one examines equation (3.26) again, the picking up of amplitude from the propagation in the +x direction is similar to solving

$$\underset{\approx}{T}(p) = [\underset{\approx}{A}_{lt}]^{-1} \underset{\approx}{T}(p-1), \tag{3.30}$$

and for propagation in the -x direction. it is similar to solving

$$\underset{\approx}{T}_{new}(p) = [\underset{\approx}{A}_{ut}]^{-1} \underset{\approx}{T}(p), \tag{3.31}$$

where $\underset{\approx}{A}_{lt}$ and $\underset{\approx}{A}_{ut}$ represent the lower and upper triangular matrices of $\underset{\approx}{A}$ respectively. $\underset{\approx}{T}$ is the column of matrices $\underset{\approx}{T}^{i}$, p is the iteration number (i.e. the order of perturbation) and the subscript 'new' identifies the final results after each iteration. To

start the iteration, it is sufficient to note that $\underset{\approx}{T}(0)$ is simply $\underset{\approx}{\tau}$. Calculated $\underset{\approx}{T}(p)$ from the left hand side of equation (3.30) is then substituted into the right hand side of equation (3.31) to obtain $\underset{\approx}{T}_{new}(p)$ for the outward-travelling waves. In the next order of perturbation, $\underset{\approx}{T}_{new}$ is substituted into the right hand side of equation (3.30), and the procedure is repeated until convergence of $\underset{\approx}{T}_{new}$ is achieved.

The inversion of a triangular matrix requires much less computing time than that of inverting the corresponding square matrix. Therefore the reverse scattering perturbation scheme is very efficient especially when the number of iterations required for convergence is small. This occurs when the composite layer is made up of weakly scattering ion cores, or when the distance between subplanes is large (e.g. >0.3 Å). Another advantage of this perturbation scheme is the drastic reduction of computer memory required compared with the matrix inversion method because $\underset{\approx}{T}^i$ can be continuously written over $\underset{\approx}{\tau}^i$.

3.3.2.3 Combining Matrix Inversion and RSP

Some surface models may correspond to composite layers in which one region is composed of closely-spaced planes of strong scatterers while another region has only weakly scattering ion cores. For such layers, matrix inversion has to be employed to calculate a $\underset{\approx}{\tau}^c$ for the former region, and then reverse scattering

perturbation is applied to 'join' it with the rest of the composite layer. Again, the major advantage is the saving of computer core memory. One such example is Zr(0001)-p(2x2)-O depicted in Figure 3.9(b). Here matrix inversion is applied to the four coplanar Zr subplanes, and reverse scattering perturbation is used between the oxygen subplane and the 'composite' zirconium layer.

3.4 LAYER STACKING

This section discusses the stacking of various layers with either the (1x1) type or the superlattice type structures, but with their respective diffraction matrices already calculated by one of the methods mentioned in Section 3.3. In the 'combined space' method employed in this work, only perturbative methods for stacking, namely layer doubling and renormalized forward scattering, are used. These methods expand the total wavefield between layers as plane waves, hence operate in K-space. In general, perturbative methods assume significant inelastic scattering inside the crystal so that the scattering by a surface is well modelled by a maximum of 20 layers.

3.4.1 LAYER DOUBLING

In the layer doubling method[11], the bulk layer periodicity of the crystal is exploited. It is most efficient for the stacking of the bulk region where the layers are either of AAAA... or ABAB... stacking sequence.

In these special cases, two layers of the crystal are considered first, then four, and for each iteration the number of layers is doubled. The minimum interlayer spacing that the layer doubling method can handle is approximately 0.5 Å.

Starting with known reflection and transmission matrices for layer A and layer B from equation (3.20), the corresponding matrices for the composite slab C can be calculated from[56]

$$\begin{aligned}
\underset{\approx}{r}_C^{-+} &= \underset{\approx}{r}_A^{-+} + \underset{\approx}{t}_A^{--}\underset{\approx}{P}^{-}\underset{\approx}{r}_B^{-+}\underset{\approx}{P}^{+}[\underset{\approx}{I} - \underset{\approx}{r}_A^{+-}\underset{\approx}{P}^{-}\underset{\approx}{r}_B^{-+}\underset{\approx}{P}^{+}]^{-1}\underset{\approx}{t}_A^{++}, \\
\underset{\approx}{t}_C^{++} &= \underset{\approx}{t}_B^{++}\underset{\approx}{P}^{+}[\underset{\approx}{I} - \underset{\approx}{r}_A^{+-}\underset{\approx}{P}^{-}\underset{\approx}{r}_B^{-+}\underset{\approx}{P}^{+}]^{-1}\underset{\approx}{t}_A^{++}, \\
\underset{\approx}{r}_C^{+-} &= \underset{\approx}{r}_B^{+-} + \underset{\approx}{t}_B^{++}\underset{\approx}{P}^{+}\underset{\approx}{r}_A^{+-}\underset{\approx}{P}^{-}[\underset{\approx}{I} - \underset{\approx}{r}_B^{-+}\underset{\approx}{P}^{+}\underset{\approx}{r}_A^{+-}\underset{\approx}{P}^{-}]^{-1}\underset{\approx}{t}_B^{--}, \\
\underset{\approx}{t}_C^{--} &= \underset{\approx}{t}_A^{--}\underset{\approx}{P}^{-}[\underset{\approx}{I} - \underset{\approx}{r}_B^{-+}\underset{\approx}{P}^{+}\underset{\approx}{r}_A^{+-}\underset{\approx}{P}^{-}]^{-1}\underset{\approx}{t}_B^{--},
\end{aligned} \tag{3.32}$$

where $\underset{\sim}{I}$ is a unit matrix; $\underset{\sim}{P}^{+}$ and $\underset{\sim}{P}^{-}$ are diagonal matrices which describe plane waves propagating from a reference point in layer A to a reference point in layer B and vice versa. If $\underset{\sim}{r}_{BA}$ represents the vector between the two reference points, then the elements of $\underset{\sim}{P}^{\pm}$ are defined as[56]

$$P_{\underset{\sim}{g}}^{\pm} = \exp(\pm i\,\underset{\sim}{k}_{\underset{\sim}{g}}^{\pm}\cdot\underset{\sim}{r}_{BA}). \tag{3.33}$$

In the next step in the iteration, the matrices calculated on the left hand sides of equation (3.32) can be used as input matrices on the right hand sides to determine

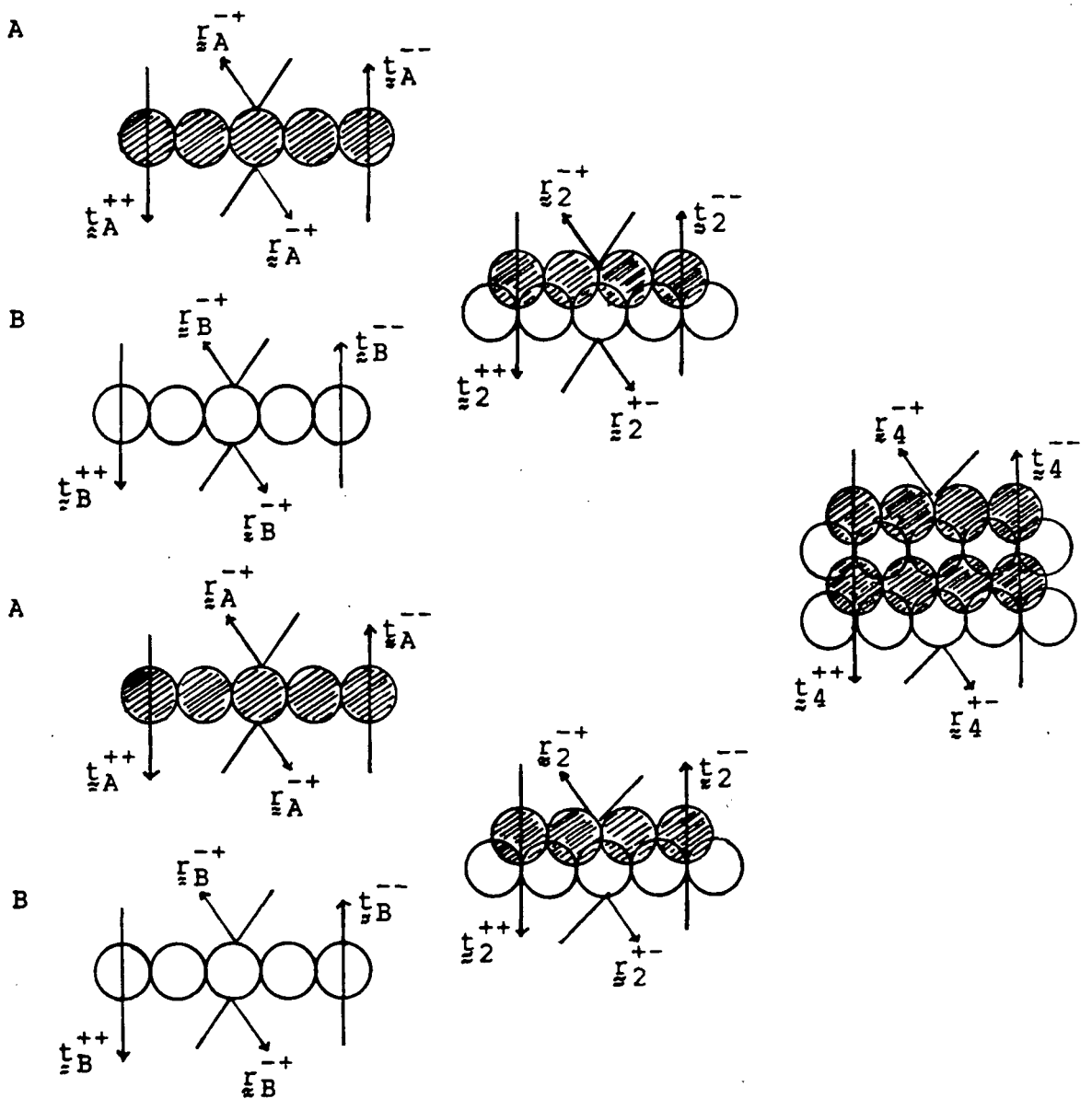

Figure 3.11: Schematic diagram of the layer doubling method used to stack 4 individual layers (with ABAB... registries) into an asymmetric slab of 4 layers (after Tong[81]).

the transmission and reflection matrices for the 4-layer system. The procedure is shown schematically in Figure 3.11. The doubling process is continued until the elements of the matrix $\underset{\approx}{r}^{-+}$ have converged. For most metals convergence is achieved after 3 to 4 iterations. The bulk treatment just mentioned is implemented by the subroutine SUBREF in Van Hove and Tong's programs.

Overlayers can be added onto the 'composite slab' one at a time by calling the subroutine DBG. Alternatively, pairs of overlayers can be combined first using subroutine DBGL, and then added onto the slab. The last step in the layer doubling scheme is to calculate beam reflectivities

$$I_{\underset{\sim}{g}} = (k^{-}_{\underset{\sim}{g}\perp}/k^{+}_{o\perp}) \; |r^{-+}_{\underset{\sim}{g}o}|^2. \tag{3.34}$$

3.4.2 RENORMALIZED FORWARD SCATTERING

The stronger forward scattering compared with back scattering in LEED[57] has already been exploited in the reverse scattering perturbation method for the calculation of diffraction matrices of composite layers in the presence of inelastic scattering. Similarly, for the interlayer scattering, the renormalized forward scattering method treats the forward scattering exactly, but treats back scattering as a perturbation. This method was originally developed by Pendry[104] and discussed further by Tong[81,105] and by Van Hove and Tong[56]. The description

given here follows that of the last authors.

The renormalized forward scattering formalism is an iterative method depicted schematically in Figure 3.12(a). The plane waves generated by the incident beam are forward scattered from layer to layer until they are damped out (i.e. their amplitudes are all less than a predetermined fraction of the incident beam amplitude). Then, starting from the deepest layer reached by the inward-travelling (+x direction) waves, outward-travelling (-x direction) reflected plane waves are allowed to forward scatter by each layer towards the vacuum. The amplitudes of the inward-travelling and outward-travelling plane waves just past the n^{th} layer can be conveniently stored in the column vectors $\underset{\sim}{a}_i^+(n)$ and $\underset{\sim}{a}_i^-(n)$ respectively, where the subscript i stands for the i^{th} iteration. As shown in Figure 3.12(b), the components in $\underset{\sim}{a}_i^+(n)$ represent amplitudes of plane waves between the n^{th} and $(n+1)^{th}$ layers, whereas those in $\underset{\sim}{a}_i^-(n)$ represent amplitudes between the n^{th} and $(n-1)^{th}$ layers. With these notations, the amplitudes of the incident beam in vacuum is defined as

$$\underset{\sim}{a}_1^+(0) = \begin{bmatrix} 1 \\ 0 \\ 0 \\ \vdots \\ \vdots \\ \vdots \end{bmatrix} \qquad (3.35)$$

where 1 at the top of the column vector on the right stands

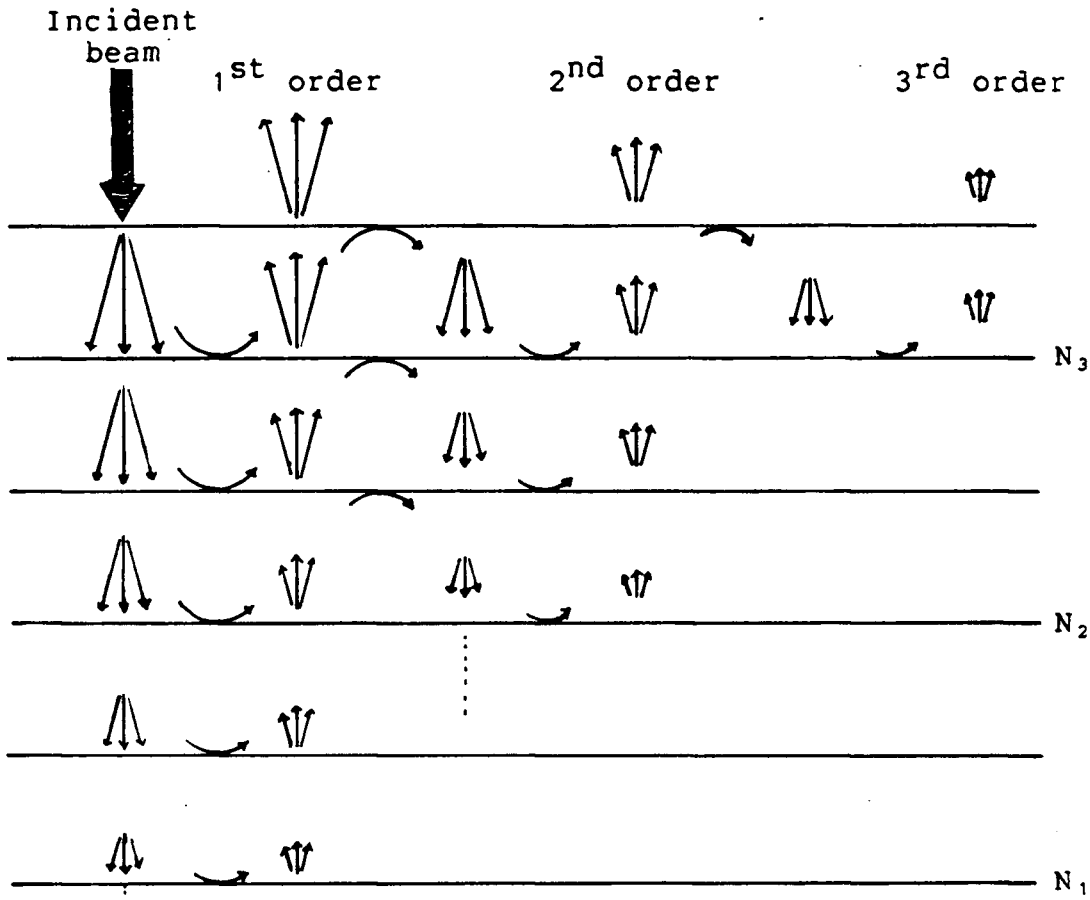

(a) N_1, N_2, and N_3 denote the deepest layer reached in the 1st, 2nd, and 3rd penetration, respectively.

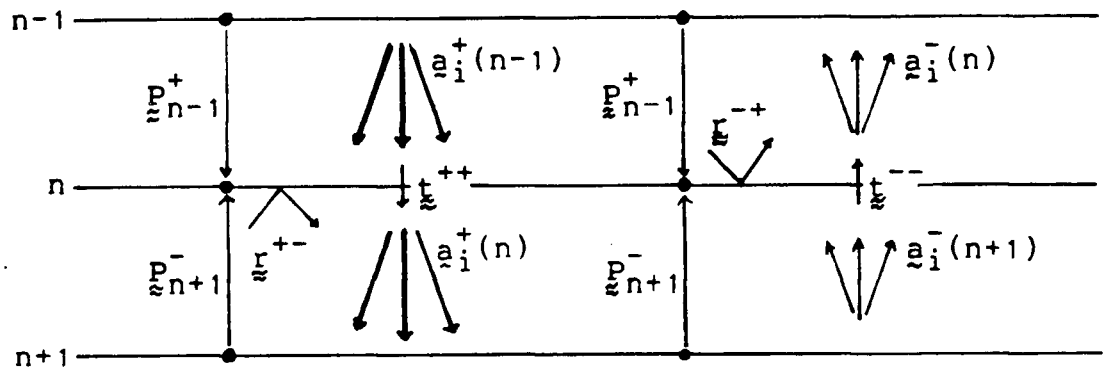

(b) Amplitudes of the inward-travelling waves ($\underset{\sim}{a}_i^{+}$) and outward-travelling waves ($\underset{\sim}{a}_i^{-}$).

Figure 3.12: Schematic diagram of the renormalized forward scattering method. (a)Each triplet of arrows represents the complete set of plane waves that travel from layer to layer. (b)Illustration of the vectors which store the amplitudes of the inward- and outward-travelling waves (after Van Hove and Tong[56]).

for the unit amplitude of the (0,0) beam. All other $\underset{\sim}{a}_i^+(0)$ ($i>1$) are necessarily null vectors since there can be no incident beams for the higher order of iteration.

The inward-travelling wave amplitudes just past the n^{th} layer arise from transmission of inward-travelling waves and reflection of the outward-travelling waves at layer n, and can be expressed as

$$\underset{\sim}{a}_i^+(n) = \underset{\approx}{t}^{++}\underset{\approx}{P}^+(n-1)\underset{\sim}{a}_i^+(n-1) + \underset{\approx}{r}^{+-}\underset{\approx}{P}^-(n+1)\underset{\sim}{a}_i^-(n) \qquad (3.36)$$

for plane waves penetrating the crystal for the i^{th} time. Here n runs from 1 to N_i, where N_i represents the deepest layer reached in the i^{th} iteration. A similar expression can be obtained for the emerging wave amplitudes, namely

$$\underset{\sim}{a}_i^-(n) = \underset{\approx}{t}^{--}\underset{\approx}{P}^-(n+1)\underset{\sim}{a}_i^-(n+1) + \underset{\approx}{r}^{-+}\underset{\approx}{P}^+(n-1)\underset{\sim}{a}_i^+(n), \qquad (3.37)$$

where n runs from (N_i-1) to 0. The $\underset{\approx}{P}^{\pm}$ are plane wave propagators between appropriate reference points in neighboring layers. The definitions of these propagators have been given in (3.33) and are also illustrated diagramatically in Figure 3.12(b).

The iteration starts with the input of $\underset{\sim}{a}_1^+(0)$ into equation (3.36). From Figure 3.12(a) for the first penetration, the $\underset{\sim}{a}_1^-(n)$ are simply column vectors of zero's because there are no emerging waves yet. When the plane waves reach the deepest layer, namely N_1 for the first

penetration, the calculated value of $\underset{\sim}{a}_1^+(N_1)$ is substituted into the right hand side of equation (3.37) to obtain $\underset{\sim}{a}_1^-(n)$. After the first iteration, the reflected wave amplitudes into vacuum are stored in the $\underset{\sim}{a}_1^-(0)$. This procedure is repeated to obtain the higher orders $\underset{\sim}{a}_i^-(0)$, and then the total reflected amplitudes can be expressed as

$$\underset{\sim}{A}^- = \underset{\sim}{a}_1^-(0) + \underset{\sim}{a}_2^-(0) + \underset{\sim}{a}_3^-(0) + \cdots \qquad (3.38)$$

Typically, $\underset{\sim}{A}^-$ converges after about 3 or 4 orders of iteration. Some 12 to 15 layers are usually required for the first penetration, but N_i decreases with increasing order of iteration. However, in the presence of closely-spaced layers, non-convergence may occur. The experience with Zr is that a minimum separation of 1.1 Å is required for the renormalized forward scattering method to work effectively. At convergence, the beam reflectivities are given by

$$I_g = (k_{g\perp}^-/k_{0\perp}^+)\ |A_g^-|^2. \qquad (3.39)$$

Convergence problems may occur occasionally in the renormalized forward scattering, and the topic has been discussed by other authors[106]. When these poor convergences are found only at isolated energies, the most convenient solution in practice is to perform the calculation again at neighboring energy points and then interpolate the results to the desired energy. If they

appear at several consecutive energies, then layer doubling can be used to re-calculate them. In the event that even layer doubling fails to rectify the situation, composite layer calculations must be carried out.

3.4.2.1 Subroutine RFSG

The latest version of the renormalized forward scattering scheme is implemented by the subroutine RFSG (Van Hove[97],1983). This subroutine has been generalized to handle a wide variety of stacking sequences, and it receives special mention here because it was used extensively in the later stages of this work. In this regard, Figure 3.13 refers to examples for Zr(0001)-p(2x2)-O with two oxygen underlayers occupying octahedral holes.

In RFSG, the surface is conceptually divided into two regions, which are periodic or non-periodic in the perpendicular direction; the latter is therefore the region closest to the vacuum interface. Each region may be composed of any combination of layers which conform to the superlattice or the primitive (1x1) type structures; these layers have known reflection and transmission matrices. A new feature of RFSG requires that the elements of these matrices be stored as 1-dimension vectors. In general, there are four such vectors to describe both types of layers, namely, $\underset{\sim}{r}^{+-}_{sup}$,

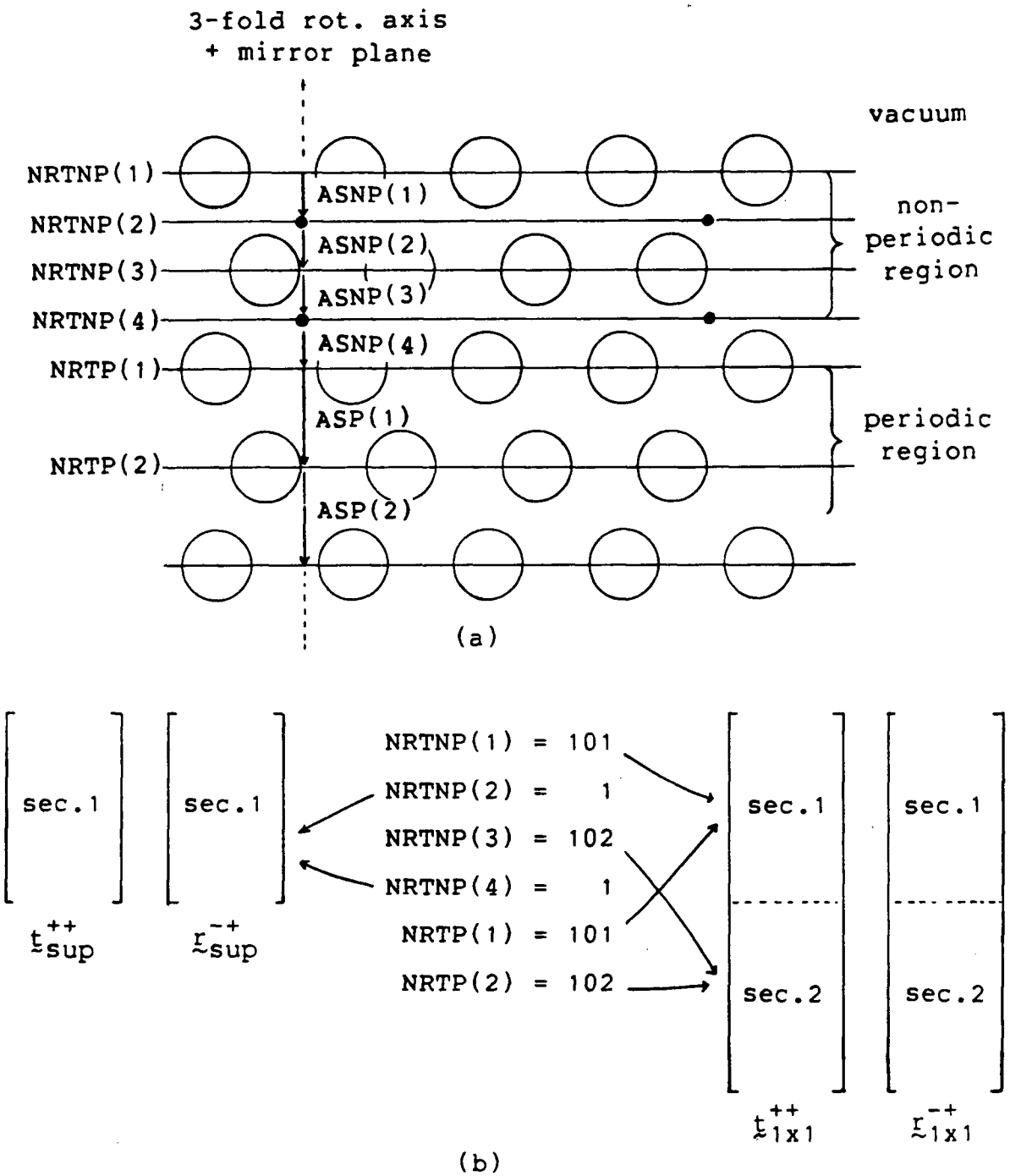

Figure 3.13: Schematic illustration of some important input parameters in subroutine (RFSG) for the adsorption system Zr(0001)-p(2x2)-O with 2 oxygen underlayers occupying octahedral holes. (a)Side view of the layer arrangement of the surface region. (b)Selection of appropriate diffraction matrices with coding vectors NRTNP and NRTP.

$\underset{\sim}{t}^{++}_{sup}$, $\underset{\sim}{r}^{-+}_{sup}$ and $\underset{\sim}{t}^{--}_{sup}$ for the superlattice type; and $\underset{\sim}{r}^{+-}_{1x1}$, $\underset{\sim}{t}^{++}_{1x1}$, $\underset{\sim}{r}^{-+}_{1x1}$ and $\underset{\sim}{t}^{--}_{1x1}$ for the (1x1) type layers. The corresponding transmission and reflection matrices of all the required (but non-equivalent) layers of the system investigated are transferred into consecutive sections of these vectors. In the stacking procedure, the diffraction properties of the layers in the non-periodic and periodic regions are retrieved from the appropriate sections of these vectors by two coding vectors NRTNP and NRTP respectively (Figure 3.13(b)). A code number over 100 signals (1x1) type layer while a code number under 100 denotes a superlattice type layer; the last digit of the code number refers to the section number of the appropriate reflection and transmission vectors. The interlayer vectors for the non-periodic region are stored in ASNP while those for the periodic region are in ASP. The user has to set up all the mentioned vectors in the main program before calling RFSG. The example in Figure 3.13 is intended to clarify the usage of these vectors. Since the two oxygen and all zirconium layers are of Bravais lattice type, $\underset{\sim}{r}^{+-} = \underset{\sim}{r}^{-+}$ and $\underset{\sim}{t}^{--} = \underset{\sim}{t}^{++}$. Further, a 3-fold rotational symmetry is available for this particular calculation, and all the interlayer vectors are contained in the rotational axis. The origins of both oxygen layers are chosen to coincide with the rotational axis so that only one registry shift

(hence only one section each in $\underset{\sim}{r}^{-+}_{sup}$ and $\underset{\sim}{t}^{++}_{sup}$) is required.

3.5 GENERAL CONSIDERATIONS IN 'COMBINED SPACE' METHOD

3.5.1 TOTAL BEAM REQUIREMENT IN K-SPACE

In the layer doubling and renormalized forward scattering methods, layer scattering is described by square matrices $\underset{\sim}{M}^{\pm\pm}$ whose dimension equals the number of components in the beam expansion. As a minimum, such expansions should include all the propagating plane waves and the first few evanescent waves. However, with small interlayer distances, such as for the adsorption of small atoms deep into hollow sites of metal surfaces, a substantially increased number of evanescent waves is required for convergence. By considering the decay factor associated with an evanescent wave, such that the amplitude decays to a fraction t over distance d, the estimated number of plane waves required in a K-space calculation for a minimum interlayer distance of d_{min} is given by Van Hove and Tong[56] as

$$n_g = (A/4\pi)[2(E-V_0) + (\log(t)/d_{min})^2], \qquad (3.40)$$

where A is the appropriate unit mesh area and $(E-V_0)$ is the electron energy inside the crystal (in atomic units). The decay factor t is user-selected. A reasonable value is about

Energy(eV)	d_{min}(Å)		
	0.90	0.70	0.50
50	187	271	493
100	211	313	511
150	253	349	553
200	301	373	577
250	337	413	619

(a)

Energy(eV)	d_{min}(Å)		
	0.90	0.70	0.50
50	39	54	93
100	43	62	97
150	51	68	104
200	60	72	108
250	66	79	116

(b)

Table 3.1: The variation of the number of plane waves required with incident energy and the shortest interlayer distance (d_{min}) for the multiple scattering calculation of Zr(0001)-p(2x2)-O; t=0.002. (a) Unsymmetrized beams; and (b) Beams symmetrized with respect to a 3-fold rotation axis and mirror plane(xz) symmetry operations.

0.002; for this value Table 3.1(a) shows the variation n_g with both energy and d_{min} for the adsorption system Zr(0001)-p(2x2)-O.

Although n_g is a function of A, E and d_{min}, the last parameter can dominate because of the dependence on d_{min}^{-2}. Thus n_g increases rapidly with decreasing interlayer distance. For example, if d_{min} = 0.3 Å, over 200 plane waves are required at a starting energy of 50 eV and a relatively small unit mesh area A of 10 Å^2. Normally, once the dimensions of $\underset{\approx}{M}^{\pm\pm}$ go beyond the 10^2 range, the K-space methods become very time-consuming and numerically unstable. In this work, effective limits of d_{min} are set at 0.5 Å. For smaller d_{min}, composite layer calculations in L-space were used.

3.5.2 USE OF SYMMETRY AND BEAM SETS

The number of plane waves required in K-space calculations can be reduced if the incident electron beam coincides with one or more symmetry elements of the surface. Under such conditions, individual beams related by the symmetry elements can be represented by a symmetrized wavefunction. In the adsorption system quoted in Table 3.1, there is a 3-fold rotational and a mirror plane(xz) symmetry at normal incidence. The beams related by such symmetry operations are indicated by the same labels in the reciprocal lattice as shown in Figure 3.14(a). In the calculation, only one of these symmetry-related beams needs

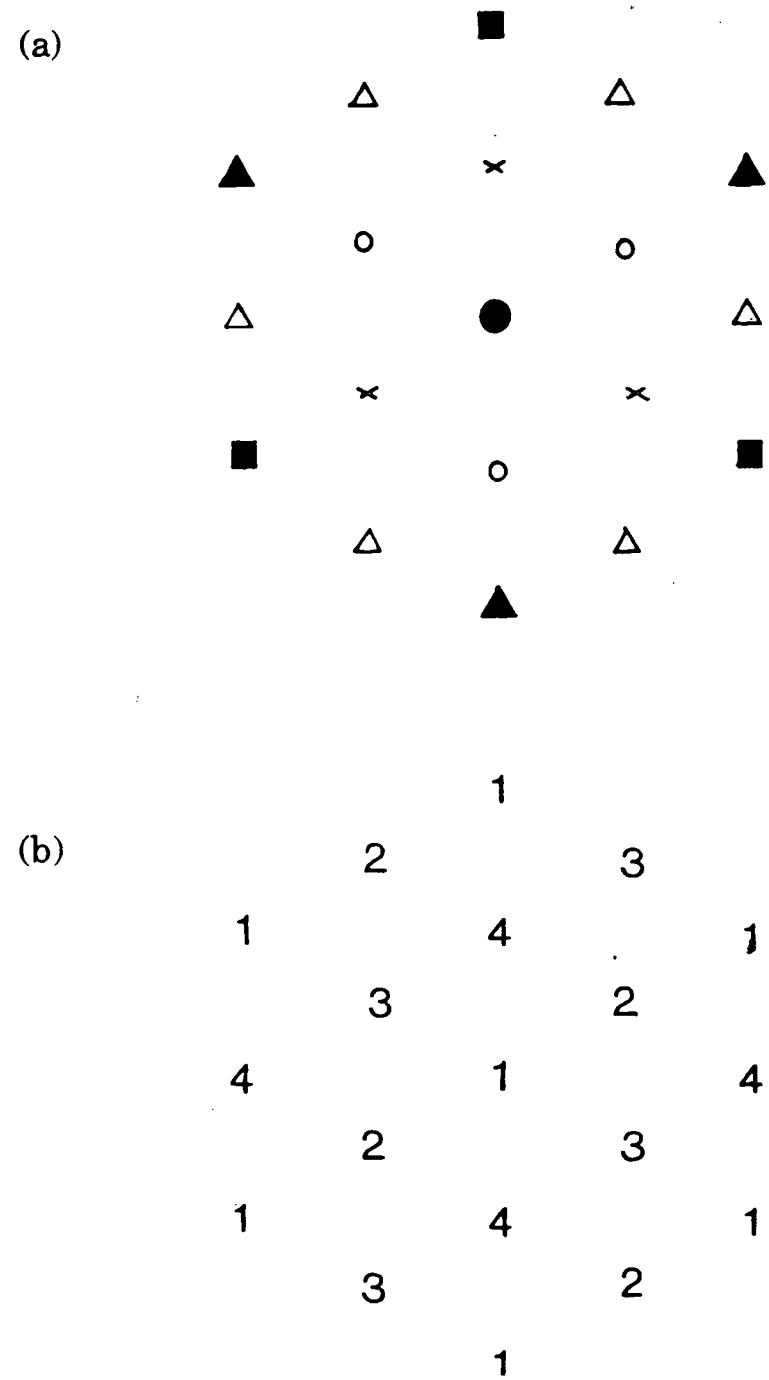

Figure 3.14: LEED pattern from Zr(0001)-p(2x2)-O. (a)Symmetry-related beams are indicated by the same symbols (at normal incidence). (b)Beams belonging to the same beam set are indicated by the same number (independent of angle of incidence).

to be input. The corresponding number of symmetrized wavefunctions used at various energies are listed in Table 3.1(b), and a comparison with Table 3.1(a) demonstrates the appreciable reduction in the number of beams required when symmetry is utilized.

The presence of an adsorbed layer with a unit mesh area S times that of the substrate produces S times as many diffracted beams as the substrate at a given energy. Since the multiple scattering programs used here cannot deal with incommensurate superlattices, S is assumed to be an integer. Thus, with an adsorbed layer, it would appear that $\underset{\approx}{M}^{\pm\pm}_{ad}$ and $\underset{\approx}{M}^{\pm\pm}_{sub}$ with dimensions S times that of the clean substrate have to be calculated for the adlayer and the substrate respectively. This is indeed the case for $\underset{\approx}{M}^{\pm\pm}_{ad}$. However, for the substrate layer, one can separate the beams into S sets such that within each set all beams are interrelated by the (1x1) type reciprocal lattice vectors. One such example is shown in Figure 3.14(b). An important property of these beam sets is that the substrate layers, with their (1x1) periodicity, cannot diffract a beam from one beam set into a beam in another beam set[56]. As a result, $\underset{\approx}{M}^{\pm\pm}_{sub}$ block diagonalizes according to

$$\underset{\approx}{M}^{\pm\pm}_{sub} = \begin{bmatrix} \underset{\approx}{M}^{\pm\pm}_{in} & & & \\ & \underset{\approx}{M}^{\pm\pm}_{f_1} & 0 & \\ & & \ddots & \\ & 0 & & \underset{\approx}{M}^{\pm\pm}_{f_{S-1}} \end{bmatrix}, \qquad (3.41)$$

where the subscript "in" refers to the integral beam set from the substrate atoms, and "f_i" refers to the i^{th} fractional beam set. The calculations of the smaller matrices $\underset{\approx}{M}^{\pm\pm}$ on the right hand side of equation (3.41) are simple compared to that of $\underset{\approx}{M}^{\pm\pm}_{ad}$. Furthermore, with the use of symmetry, some of the fractional beam sets may merge into a single set. One example can be found in Figure 3.14(b), where the three fractional beam sets (labelled 2, 3 and 4 in the figure) cannot be distinguished under a 3-fold rotational and a mirror plane symmetry operations. So in the multiple scattering calculation for that particular system, only one of these three sets is input together with the integral beam set.

3.5.3 SELECTION OF METHODS

Before setting up a multiple scattering calculation, one has to consider its feasibility, computing cost and flexibility. The last two factors become important when many adsorption models require testing on a 'trial and error'

basis.

Feasibility in the 'combined space' method is mainly determined by the perturbative (K-space) part of the calculation. When the number of beams, N, required after symmetrization is over 100, convergence may not be assured. This situation can occur with large unit cell mesh areas or with small interlayer spacings. The latter may be countered by constructing composite layers, which lead to the inversion of matrices of dimensions PL^2 where P is the number of subplanes and L is the number of phase shifts. However if PL^2 exceeds about 200, the inversion step is numerically unstable. This limit can be slightly higher when computations are made in double precision. Currently in this laboratory, we are limited to models with $N \leq 100$ or $PL^2 \leq 200$.

The building blocks of the 'combined space' method consist of the construction of layer diffraction matrices and the subsequent stacking of these layers. The computing effort for the former depends on N, P and L, while, for the latter, the important parameters are N and the number of layers (M) required to mimic a surface region for a LEED calculation. Van Hove and Tong[56] have scaled the computing times for different methods within each building block and they are summarized in Table 3.2 together with their characteristics.

In general, the most computationally expensive step is the evaluation of the layer diffraction matrix for a composite layer. Priority is therefore given to Bravais

Building block	Method	Computing time scale	Comments
Layer diffraction matrix:	Bravais lattice layer	L^3N^2	$d_{min} \geq 0.5\text{Å}$
	Composite layer by matrix inversion(mi)	$L^3P^3N^2$	Exact, large core size required if $P \geq 4$
	Composite layer by reverse scattering perturbation(rsp)	$L^2P^2N^2$	Possible convergence problem; smaller core size than (mi)
	Composite layer by combining (mi) and (rsp)	Between (mi) and (rsp)	core size comparable to (mi)
Layer stacking:	Renormalized forward scattering	N^2M	$d_{min} \geq 1.0\text{Å}$; versatile subroutine (RFSG)
	Layer doubling	$N^3 \ln M$	$d_{min} \geq 0.5\text{Å}$; many working matrices required.

N = number of beams after symmetrization (if any)
L = number of phase shifts
P = number of subplanes in the composite layer
M = number of layers considered in the surface scattering

Table 3.2: Relative computing times for the building blocks in the 'combined space' multiple scattering calculations (After Van Hove and Tong[56]).

lattice layers whenever the minimum interlayer spacing d_{min} is ≥ 0.5 Å, although cases can be identified where a composite layer calculation is considered even when the Bravais lattice layer calculation is possible.

Perturbative multiple scattering calculations between layers are generally less computationally demanding than the calculations of the layer diffraction matrices. However if many adsorption models involving different interlayer spacings between the adsorbate and the substrate have to be tested, which is true for LEED crystallography, the cost of stacking becomes important. In this regard the fastest method, namely renormalized forward scattering, is preferred whenever the interlayer spacings are above 1.1 Å. Also the subroutine RFSG provides more flexibility on the layer periodicity. Layer doubling, on the other hand, has to be used to stack layers with interlayer spacings from 0.5 to 1.0 Å. However, the present layer doubling subroutine SUBREF can only stack bulk layers with 1- or 2-layer periodicities. 4-layer periodicity (ABCDABCD....) can be handled by first combining AB and CD with subroutine DBGL, and then stacking the two 'composite' layers with SUBREF. 3-layer periodicity, such as shown by the fcc(111) surface, poses a problem in the layer doubling scheme. A solution involves excluding all symmetry except for one mirror plane. In this case, the surface can be visualized as having 1-layer periodicity with the same sloping interlayer vector (contained in the mirror plane) linking atomic centers in

consecutive layers. If the smaller interlayer spacing occurs only between the adsorbate and the top substrate layer, then the symmetries can be preserved either by doing a composite layer calculation as mentioned in the preceding paragraph, or by layer doubling the two layers with the subroutine DBGL and stacking them with the faster RFSG subroutine.

Convergence problems occur on occasion with perturbation methods for cases of strong multiple scattering. Obvious non-convergence can usually be indicated by the appearance of spurious peaks in several I(E) curves from the same calculation. This is largely due to the lack of conservation of electron current in perturbation methods. These problems can be avoided by increasing the damping and/or increasing the lattice vibrational amplitude which effectively reduces the ion core scattering factor. Although these two procedures affect the relative intensities of reflection maxima slightly, the peak positions are almost unchanged[106]; these results are acceptable for structural determinations in LEED crystallography. For identifying the less obvious convergence problems, Moore *et al.*[107] suggested plotting the sum of the emergent beam intensities versus the topmost interlayer spacing at a particular energy; any non-convergence would lead to a sum displaced from an otherwise smooth curve. The problem is then rectified by careful reselection of input beams.

The 'combined space' approach has especially been employed in the studies of oxygen adsorption on Zr(0001)

(Chapter 6), and in the theoretical study of the stability of fractional order beam intensities from superlattices. With careful set-up of the main program and monitoring of occasional convergence problems, this approach provides an affordable alternative to exact calculations. Equally important is the consistency obtained from this approach; different subroutines applied to the same adsorption system have yielded almost identical results. Table 3.3 summarizes the functions of some important subroutines frequently used in this work.

Subroutine	Function
ADREF1	adds an overlayer onto a substrate, by layer doubling, producing a vector of reflected amplitudes.
DBG	combines 2 layers by layer doubling, producing 1 reflection matrix (usually as the 'new' substrate).
DBLG	combines 2 layers by layer doubling, producing all reflection and transmission matrices.
MPERTI	generates diffraction matrices by reverse scattering perturbation and partial matrix inversion if requested.
MTINV	generates diffraction matrices by matrix inversion for composite layers.
MSMF	generates diffraction matrices for Bravais lattice type layers.
RFSG	stacks layers by renormalized forward scattering, producing a vector of reflected amplitudes.
RINT	produces beam intensities from beam amplitudes.
SUBREF	stacks bulk layers with 1- or 2-layer periodicity by layer doubling, producing a reflection matrix only.

Table 3.3: Functions of several important and frequently used subroutines in the 'combined space' multiple scattering calculations provided by Van Hove and Tong[56,97].

CHAPTER 4

GENERAL EXPERIMENTAL ASPECTS

4.1 THE UHV CHAMBER

The success of the 'clean-surface approach' to surface studies has been brought about, to a large extent, by the commercial availability of ultra-high vacuum (UHV) facilities. The need for using UHV can be appreciated by reference to a result from the kinetic theory of gases. The number of molecules striking a unit area of a surface in unit time is given by[107]

$$n = 3.52\times10^{22}(MT)^{-1/2}P \text{ molecule cm}^{-2}\text{ s}^{-1}, \qquad (4.1)$$

where P is the pressure in torr, M is the molecular weight of the gaseous molecule, and T is the temperature in K. A typical low Miller-index metal surface has approximately 10^{15} adsorption sites per cm^2, so a gas such as O_2 at room temperature can fill up all the adsorption sites in about one second at 10^{-6} torr, assuming a constant sticking coefficient of one. However, at a pressure of 10^{-10} torr, a monolayer is formed in $\simeq$160 minutes. Although the sticking coefficients for most gases are below unity, the above comparison does indicate how important UHV is to keep a surface in a well-defined state for the duration of an experiment.

The work in this thesis was carried out in a Varian FC12 vacuum chamber. This particular chamber is made of demagnetized stainless steel and is equipped with numerous ports utilizing conflat flanges. Figure 4.1 shows the layout

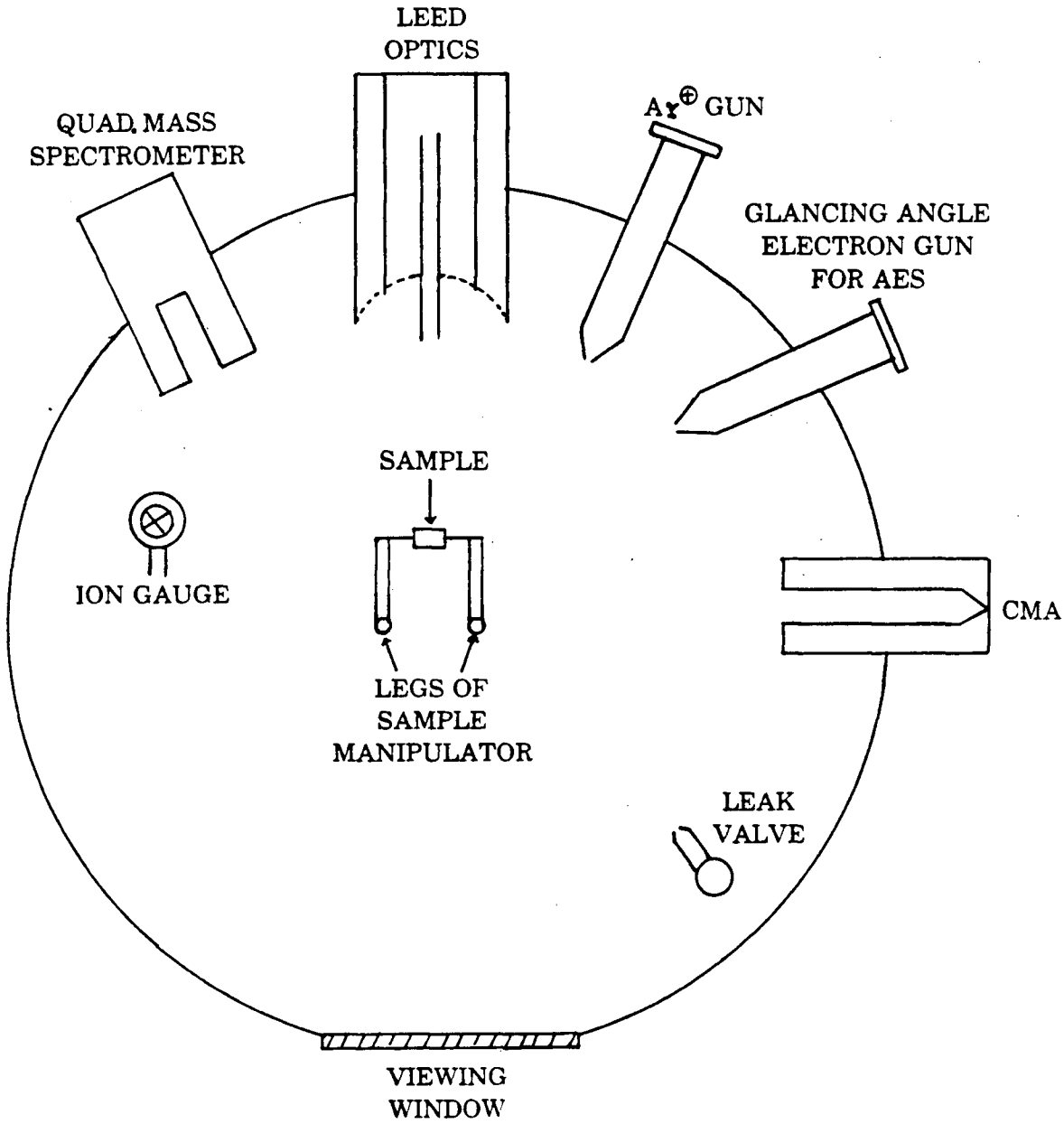

Figure 4.1: Schematic diagram of the FC12 UHV chamber and some of its important assessories. AES = Auger electron spectroscopy; CMA = cylindrical mirror analyzer.

of the UHV chamber and the major analytical tools available. The accompanying pumping system for the FC12 chamber and the facilities for start-up pumping are schematically outlined in Figure 4.2. The total pumping system consists of four types of pumps which include two sorption pumps, a diffusion pump, an auxiliary titanium sublimation pump, a central ion pump (200 Ls^{-1}) and a small ion pump (20 Ls^{-1}) for the gas inlet line.

A sorption pump consists of zeolite in a container cooled by liquid nitrogen. The zeolite has large effective surface area and it can physically absorb large amounts of gas, thereby reducing the pressure of the chamber to the 10^{-3} torr range from atmospheric pressure very quickly. A diffusion pump works by entrainment of gaseous species near the pump inlet by high velocity streams of vapor of a non-volatile liquid (e.g. polyphenyl ether) ejected from a boiler. The streams of vapor later condense on water-cooled walls and flow back down to the boiler while the gaseous species are pumped away by a rotary pump. A liquid nitrogen cold trap is usually connected between the UHV chamber and the diffusion pump to prevent any possible back diffusion of the non-volatile liquid. Both the ion and titanium sublimation pumps are examples of 'getter type' pumps. Ion pumps depend on a discharge to produce ions from the gas to be pumped. These ions are then trapped by magnetic fields and directed on to reactive 'getter' plates made of titanium which remove the ions by the formation of stable solid

compounds. Noble gases are pumped by burial, although that mechanism is not very effective. Titanium sublimation pumps, on the other hand, simply evaporate films of titanium which have very high adsorption rates for reactive gases. The burial route is again slow. Thus 'getter type' pumps are generally not used directly after argon bombardment (Section 4.2.2), but instead the diffusion pump is used to 'rough out' the system until the pressure is down to a level (e.g. 10^{-7} torr) which the ion pump can handle.

In the start-up procedure, the initial pumping is performed by one or both sorption pumps to reduce the pressure of the chamber to the 10^{-3} torr range. At this stage the well-trapped (liquid nitrogen) diffusion pump is used to pump the chamber down to around 10^{-7} torr. Finally the central ion pump is switched on and the chamber is baked at 200-250°C for 12-15 hours. The chamber is then allowed to cool to room temperature, and in the absence of leaks, the pressure should reach the 10^{-10} torr range. Degassing all the filaments and switching on the titanium sublimation pump for about half an hour should reduce the pressure further, even to the mid-10^{-11} torr range.

Although it does not occur very often, leaks can occur between the seals. When the leak results in a pressure $\geq 10^{-7}$ torr, it can usually be detected by a helium detector (Varian 925-40). Smaller leaks can be detected by squirting methanol on to the slit between the flanges where the leak is suspected; a sudden drop in pressure resulting from a

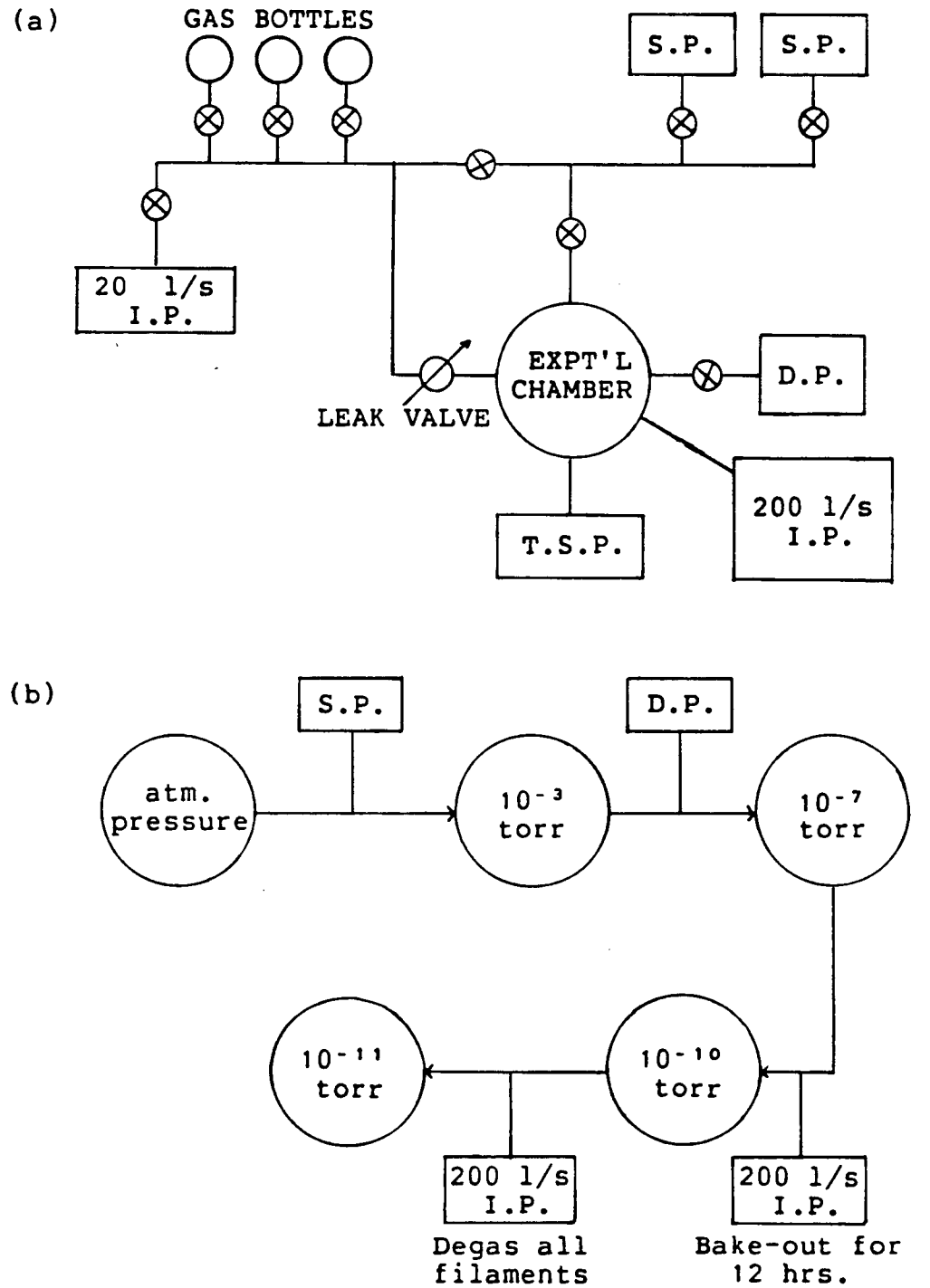

Figure 4.2: (a)Pumping system associated with the FC12 UHV chamber. (b)Start-up procedure for pump-down from atmospheric pressure to UHV.

temporary freezing of the methanol would indicate the presence of a leak. Detailed information on pumping methods, measurements of pressure and related topics are given in several reviews on UHV techniques[108-110].

The following facilities are also available in the FC12 chamber: a set of 4-grid LEED optics (Varian 981-0127); a single pass cylindrical mirror analyzer (Varian 981-2607); a glass viewport directly opposite to the fluorescent LEED screen; an ion gun (Varian 981-2043) for cleaning by ion bombardment; a glancing incidence electron gun (Varian 981-2454) gun for Auger electron spectroscopy; a molydenum sample holder with a resistive heating block mounted on a sample manipulator (Varian 981-2530) which allows (x,y,z) linear translation and two degrees of rotational freedom (since the FC12 chamber is built for multi-technique analysis, the sample is held on the manipulator $2\frac{1}{2}$" off the vertical axis); a quadruple mass spectrometer (EAI 150A) to monitor the composition of the residual gases; a variable leak valve for letting in gases; and a nude ion gauge for pressure measurement.

Magnetic fields in the chamber are annulled by three orthogonal sets of Helmoltz coils, using a Hall probe to set zero field at the sample position. Zero field can further be checked by observing the specular beam in the LEED experiment: the position of the (0,0) beam will not change, even at the lowest energies, if the region between the sample and the LEED screen is field-free.

4.2 SAMPLE PREPARATION AND CLEANING

4.2.1 CRYSTALLOGRAPHIC PLANE ORIENTATION

The surface studied with LEED in this laboratory is usually in the form of a thin circular disk with diameter around 5 mm and thickness between 1 and 2 mm. The following procedure is taken to obtain a desired crystallographic plane. A high-purity single crystal is mounted on a goniometer with plastic cement and aluminum powder. The purpose of the latter is to make electrical contact between the crystal and the goniometer for the spark erosion step after orientation. Better electrical contact can be achieved by tying the crystal with a copper wire, one end of which is wrapped to the base of the goniometer. The crystal is oriented to the desired plane using back reflection Laué X-ray diffractography[111]. This involves analyzing a pre-oriented diffraction photograph and subsequently correcting the angle through the manipulation of the goniometer micrometers[112].

After orientation, slices of the desired plane are cut from the rod using the spark erosion technique ('Agietron', Agie, Switzerland). The crystal disk is then mounted in an acrylic resin ('Quickmount', Fulton Metallurgical Products), and glued to a polishing jig[113], which has alignment micrometers that allow the sample orientation to be adjusted. The whole assembly can be fitted on to the track of the X-ray diffractometer enabling minor adjustments to be

made to compensate for the errors in alignment introduced during the cutting stage (typically ≤2°). After re-adjustment, the jig is put on to a planetary lapping system (DU 172, Canadian Thin Films Ltd.) for polishing. The crystal is mechanically polished with progressively finer diamond paste, starting usually at 9 μ and finishing at 1 μ. The polishing from 3 μ down is done manually with artificial deer skin (Microcloth, Buehler 40-7218) to minimize damage to the surface. After the 1-μ polish, the surface is normally smooth enough for an optical face alignment by back reflection of a Ne/He laser fixed on an optical bench as shown in Figure 4.3. When the reflected laser beam makes an angle less than half a degree with the incident beam, the polishing is considered satisfactory. The whole assembly is then moved back to the X-ray diffractometer, and a Laué photograph taken to ensure that the optical face coincides with the desired crystallographic plane to within $\frac{1}{2}$°.

At this stage the crystal is retrieved from the resin by dissolving the latter in acetone. Any smearing introduced by the 1-μ polish can be smoothed out by gentle polishing with 0.05 μ alumina on typing paper for 30 to 60 seconds. The crystal is then rinsed with de-ionized water in an ultrasonic bath, and thoroughly degreased with trichloroethylene. The crystal is often acid-etched or electropolished to yield a shiny surface.

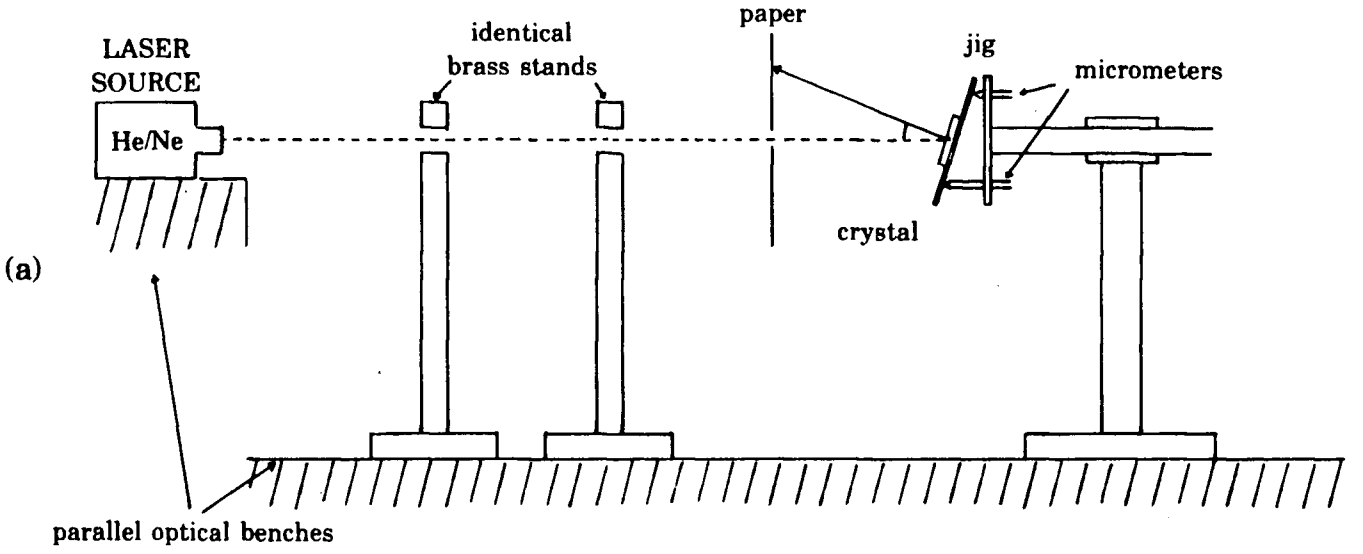

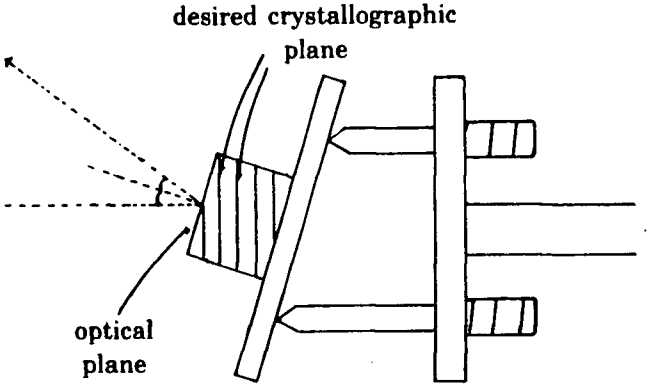

Figure 4.3: (a)Schematic diagram of laser alignment of optical and crystallographic planes of a single crystal. (b)A blow-up to show the relationship between the optical and crystallographic planes. Alignment is acceptable when $\theta \leq \frac{1}{2}°$.

4.2.2 SURFACE CLEANING IN UHV CHAMBER

Argon ion bombardment is the most common method for cleaning a crystal surface under UHV. The damage done by bombardment is relieved by annealing. When the crystal is first placed in the chamber, the most abundant impurities on the surface are frequently oxygen and carbon. These can be removed by Ar^+ bombardment, preferably at room temperature to avoid their possible diffusion into the bulk[114] at elevated temperatures. Argon ions with energies in the range of 1 to 2 keV are used for the bombardment. In the early stages, the high energy end of the range is used to sputter off the impurities; this may take as long as 30-50 hours, depending on the type of crystal and its process history. Whenever possible low energy ions are preferred to minimize damage or profiling of the surface. To carry out the Ar^+ bombardment, the central ion pump is switched off and argon gas is leaked into the chamber until the pressure is in the mid-10^{-5} torr range. The ion current on the surface should be around 4 to 6 μA. During the bombardment, the sublimation pump is kept switched on. Since the sublimation pump is not effective in removing argon via the burial route, it essentially pumps away impurities knocked off from the surface of the sample in a differential manner. After several hours of bombardment, the sample should be checked to assess progress in cleaning. For this the whole chamber must be pumped down, first with the diffusion pump and then with the ion pump. At this stage an Auger spectrum is taken

to assess surface cleanliness. If impurity levels are still high, Ar^+ bombardment is repeated using fresh argon gas.

Eventually when the Auger spectrum indicates an essentially clean surface, the sample can be heated to drive impurities from the bulk to the surface, and to anneal out damage to the surface caused by the ion bombardment procedures. These are repeated cyclically until no appreciable impurities can be detected by Auger electron spectroscopy and the surface is sufficiently well-ordered to show a sharp LEED pattern. If the bulk impurities were not effectively driven out in the preliminary stages of cleaning they would likely appear during the annealing steps prior to the first investigations with LEED. A resistive heater (Varian 981-2058) with tantalum clips is used for annealing and heating of the sample. The sample temperature is measured with a 0.005" alumel-chromel thermocouple spot-welded to the edge of the crystal disk. It is important to know the melting point and any phase transition temperature of the particular crystal before any heating procedure is undertaken.

Residual hydrocarbon impurities knocked off from the sample may not be pumped quickly by the ion or sublimation pumps. However, it is found that leaking oxygen into the chamber at 10^{-8} torr for several minutes can reduce the amount of these residual gases, presumably by cracking them down into some reactive forms.

4.2.3 SURFACE COMPOSITION BY AUGER ELECTRON SPECTROSCOPY

Surfaces studied with LEED can be conveniently assessed with Auger electron spectroscopy. The latter, as already mentioned in Section 2.3.4, is useful not only for detecting and identifying impurities, but also for estimating the relative coverages of adlayers under investigation. In this laboratory, electron beams are employed as the excitation source for Auger electron spectroscopy. As a result, weak Auger electron signals are superimposed on a much larger general background[67,115]. Two electrostatic analyzers of the retarding field and dispersive types[116] are available for the detection of the Auger signals.

A retarding field analyzer uses the hemispherical grids of the conventional LEED display system as shown in Figure 4.4. In such a set-up, the electron gun, the sample, and the grids G1 and G4 are all earthed, while the screen is biased at +300V to collect electrons emitted from the sample. The electron gun delivers an electron beam with a typical energy ≃2 keV and a current of ≃20 μA. A variable retarding voltage V_r is applied to grids G2 and G3. This voltage is ramped by a multi-channel analyzer (Fabritek 1062) linked to a programmable power supply (Kepco OPS 2000). The total current collected from the screen is a function of V_r. A derivative spectrum can be obtained by superimposing on V_r a small modulation $V_m \sin\omega t$ (frequency $\omega \simeq 1$ kHz). Provided that V_m is small (e.g. <10 V), the amplitude of the component of the collector current at the modulating

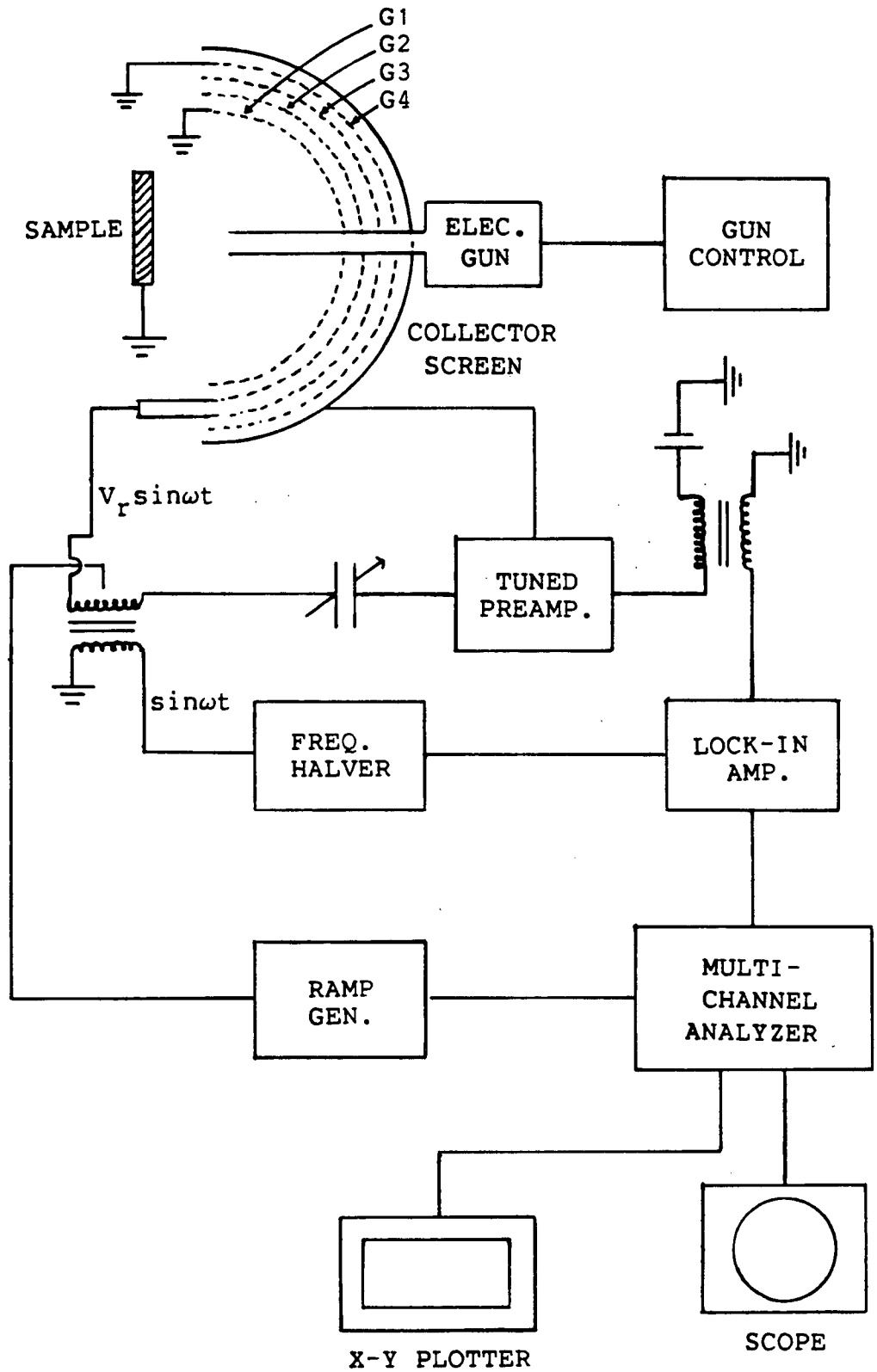

Figure 4.4: Schematic diagram of LEED optics used as a retarding field analyzer for AES.

frequency is $V_m(dI/dV_r)$, and the amplitude at the second harmonic is $-0.25V_m^2(d^2I/dV_r^2)$[117]. Therefore, by detecting with a lock-in amplifier (PAR HR8) the current received by the collector screen at the appropriate frequencies, the derivatives (dI/dV_r) and (d^2I/dV_r^2) are readily obtained as a function of V_r. The second derivative essentially eliminates the slowly varying background current and gives a spectrum with prominent Auger peaks as shown in Figure 2.12. The output from the lock-in amplifier after each sweep can be stored in the Fabritek and signal averaged until the signal to noise ratio is satisfatory. A typical spectrum requires about 10 scans, and takes 3-5 minutes. A tuned pre-amplifier based on the design by Nathan and Hopkins[118] is used to isolate the high voltage applied to the collector screen. The use of two retarding grids (G2,G3) provides better energy resolution in general. The earthed grid (G4) is used here to remove the capacitance between the retarding grids and the collector screen which would otherwise generate unwanted signals.

The retarding field analyzer has been popular because it directly uses a 4-grid LEED optics. In addition, it has a very high collector efficiency: between 10-20% of the Auger electrons emitted from the sample can reach the screen. The major disadvantage of a retarding field analyzer is that its sensitivity is restricted by high 'shot noise'. The latter is proportional to $\sqrt{I_{E+}}$, where I_{E+} represents the total collected current contributed by electrons having energies

greater than E, the Auger energy of interest. The high 'shot noise' reduces the signal to noise ratio because the latter is dependent on $I_{\Delta E}/\sqrt{I_{E+}}$ (where $I_{\Delta E}$ is the current from those electrons with energies $E\pm\Delta E$†).

The signal to noise ratio can be enhanced by up to 10^2 by using a dispersive type analyzer, which operates via velocity selection. With such an analyzer, only electrons within a narrow energy spread ΔE are collected. The signal to noise ratio now scales as $I_{\Delta E}/\sqrt{I_{\Delta E}}$, and is clearly much more favorable than that for a retarding field analyzer.

The dispersive type analyzer used in this laboratory is a cylindrical mirror analyzer (CMA). The CMA is used in conjunction with a glancing incidence primary beam which can improve the surface sensitivity. Figure 4.5 shows a schematic experimental set-up for Auger electron spectroscopy using the CMA and the glancing angle electron gun. A typical primary beam here has an energy around 2-3 keV, a current of 100-200 μA, and a cross-sectional area ≤ 1 mm^2. The CMA consists basically of two co-axial cylinders of radii r_1(inner) and r_2(outer) (Figure 4.5), with entrance and exit grids cut in the inner cylinder[119]. The inner cylinder is grounded while a variable repulsive voltage V_r is applied to the outer cylinder. Only a narrow band of electrons with mean energy E have trajectories which can pass through the exit grids and be detected by the channel electron multiplier. The rest will collide with the walls of

---

†ΔE is determined by the instrumental resolution.

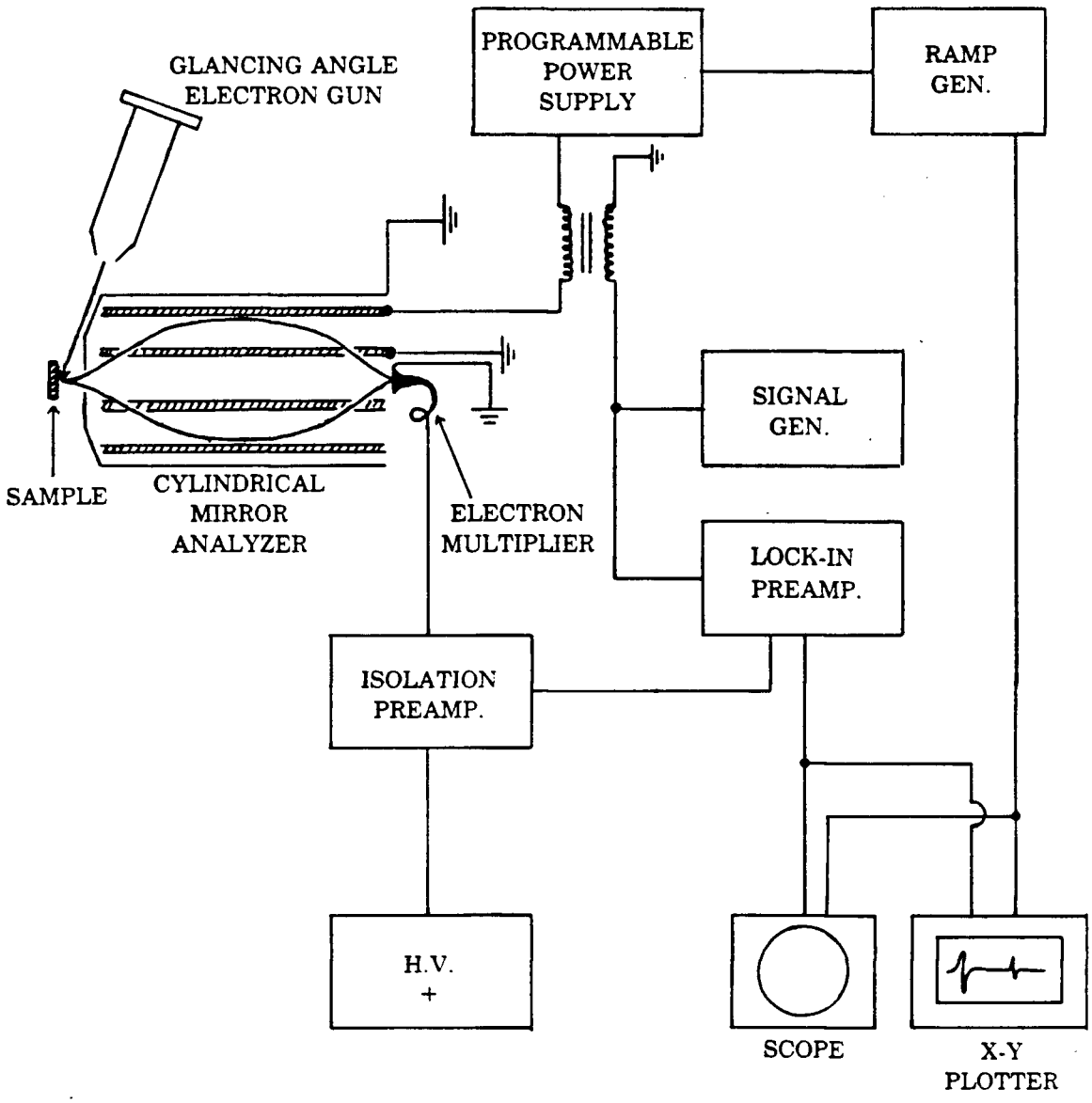

Figure 4.5: Schematic diagram of the experimental set-up for AES using a cylindrical mirror analyzer and glancing incidence electron gun.

the cylinders and eventually die out. The front end of the electron multiplier is usually earthed, but is set to a potential +300V when electrons with kinetic energies less than 50 eV are to be detected. A pre-amplifier is used to isolate the higher voltage (2-2.5 kV) on the electron multiplier[120]. In order to obtain a derivative spectrum of the type shown in Figure 2.12, a small modulation voltage $V_m \sin\omega t$ ($\simeq$3V at 5-10 kHz) is superimposed on V_r. In contrast to the RFA, the output from the lock-in amplifier with the CMA is set at the modulation frequency[67], and it yields directly derivative Auger spectra as shown in Figure 2.12. Due to the improved signal to noise ratio, a single scan is able to give a spectrum, in less than 30 seconds, which is superior to those obtained with the retarding field analyzer. The increased speed enables the experimenter to scan different parts of the sample surface quickly. In adsorption studies, the increasing adlayer coverage in an adsorbate uptake curve can be continuously monitored by the growth of an Auger peak.

4.3 THE LEED EXPERIMENT

4.3.1 LEED OPTICS

Figure 4.6 shows the electron optics used in the FC12 chamber. There are two main parts, namely the electron gun, which directs electrons with variable energies on to the sample, and the detector, which energy-analyzes the back

scattered electrons. Details on LEED optics and quantitative measurement of LEED beam intensities can be found in a review by Lagally and Martin[12].

The electron gun (Varian 981-2125) produces an electron beam by thermionic emission from a tungsten cathode; these electrons are accelerated and focussed through anode plates. When the gun is well-tuned, it gives a collimated beam with a cross-sectional diameter ≤ 0.75 mm in the energy range between 10 and 300 eV. The energy spread of the electrons is determined mainly by the filament temperature T. For a Maxwellian distribution, the width at half-maximum is given by

$$\Delta E = 2.54kT, \tag{4.2}$$

where k is the Boltzmann constant. Although filament materials with low operating temperatures can be used for LEED guns, considerations of chemical stability and lifetime have encouraged the use of tungsten filaments. These filaments operate at around 2300K, thus giving a ΔE of approximately 0.5 eV. The beam current increases almost linearly with energy below about 100 eV, and then levels off. This variation has to be recorded for normalizing measured LEED spot intensities (otherwise the intensities would appear artificially reduced at low energies).

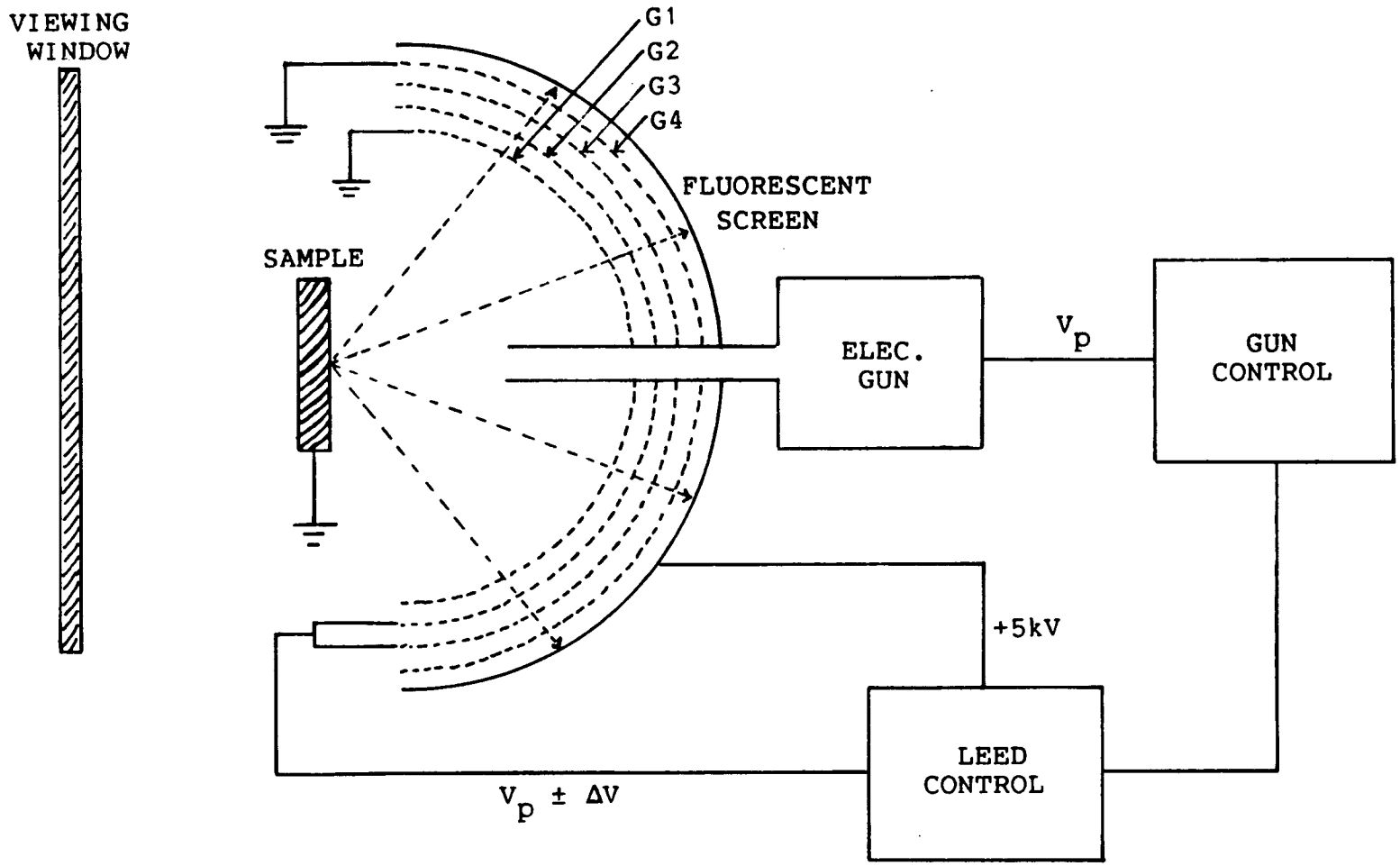

Figure 4.6: Schematic diagram of the electron optics used for LEED experiments.

4.3.2 DISPLAY OF THE LEED PATTERN

The electrons back scattered from the crystal surface are traditionally displayed on a fluorescent screen which is situated behind the 4-grid system. The latter can also be used for the detection of Auger electrons (Section 4.2.3). In a LEED experiment, the sample is positioned at the common center of curvature of the concentric grids and fluorescent screen. The final anode plate of the electron gun, G1, G4 and the sample are usually grounded to ensure that both the incident and reflected electrons travel in an electrostatically field-free space.

The accelerating voltage V_p for the electron gun is variable, while the potential for both G2 and G3 (the repelling grids) is set to $-V_p+\Delta V$, where ΔV is a small positive voltage. With such a repelling potential, only the elastically scattered electrons and a small fraction of inelastically scattered electrons, which have lost an amount of energy less than $e\Delta V$, can pass through the grids. The latter lead to a general background on the fluorescent LEED screen. The background intensity can be reduced by setting the repelling potential at V_p, but it results in much larger diffracted beam widths[121]. Since typical grids have an electron transparency of about 80%, the use of two repelling grids reduces the number of electrons reaching the screen. However the advantage of 4-grid optics, over a 3-grid system with one repelling grid, is especially apparent when used as a retarding field analyzer for Auger electron spectroscopy.

Nevertheless for LEED also, the two repelling grids do offer better energy resolution which enhances the contrast in diffraction patterns.

Visual display of a LEED pattern is accomplished for the electrons which pass through G4. They are accelerated by a positive potential of about 5 keV on to a phosphor-coated metal screen. Thus each elastically diffracted beam produces a spot on the screen, and the whole pattern can be observed through a glass window directly opposite to the screen. Part of the LEED pattern will be blocked by the legs of the manipulator and the large sample holder in this traditional set-up. One solution involves using an inclined mirror[122] to view the image of the pattern through a side viewport. Alternatively, de Bersuder[123] reduced this problem by viewing the LEED pattern from the rear of a glass phosphor screen; rear-viewing systems are now commercially available.

4.4 QUANTITATIVE MEASUREMENT OF LEED SPOT INTENSITIES

Diffracted beam intensity is conveniently defined as the elastic reflectivity

$$I = i/i_0, \tag{4.3}$$

where i and i_0 are the diffracted and incident beam currents respectively. To obtain an I(E) curve for a particular beam, I is measured over a range of energy at a fixed direction of incidence.

In early LEED studies, the diffracted beam current i was often measured directly by using a movable Faraday cup collector[1,124]. This method of measurement is very accurate and provides high sensitivity (detectable current $\simeq 10^{-14}$ A, which is several orders lower than that of 4-grid and screen system). The major disadvantage of this approach is that it is slow, especially for the non-specular beams whose directions vary as the energy of the incident beam is changed.

With hemispherical grid systems[125], a variety of methods have been developed for estimating I from the brightness of the spots on the fluorescent screen[12]. These indirect methods assume in general that the luminance is linearly proportional to the electron current striking the screen. The brightness of the spots can be measured directly with an external spot photometer[126], or indirectly from a photographic plate[127] containing the negative image of the spots. The latter technique was modified by Frost *et al.*[128] who used a computer-controlled Vidicon camera to digitize the darkness of the negative image of the spot. The data acquisition time in the spot photometer technique is comparable to the Faraday Cup method. The photographic methods, on the other hand, can cut down the actual LEED experimental time dramatically. Records can be taken at 2 eV intervals from 40 to 300 eV in just a few minutes, thereby greatly reducing possibilities for contamination or beam effects occurring while the surface is being studied.

However this method is inconvenient from another point of view. The developing of the films, and the subsequent analysis, can take a day or so. That means in practice that the experimenter would not learn until perhaps two days later of whether the data were satisfactory, or whether, for example, errors in orientation had occurred to render the whole exercise meaningless.

Recent advances in low-light-level TV cameras, and faster microprocessors, had opened new possibilities for direct scanning and digitization of the brightness distribution on the LEED screen through the viewing window. Such on-line methods can accumulate data in a minute or so, and produce I(E) curves shortly after via an oscilloscope or a printer. These shorter experimental times are very significant for limiting the effects of beam-surface interactions.

In this work both the photographic method described by Frost *et al.*[128] and an on-line TV camera method were used. They are discussed in the following sections.

4.4.1 PHOTOGRAPHIC METHOD

This method uses a Nikon F2 camera (85 mm-f1.8 with K2 extension ring) placed in front of the viewport. Kodak Tri-X 35 mm black/white film (ASA 500) is used. The aperture of the lens is normally set at f1.8 or f2.8 with exposure time varying from 1 to 4 seconds depending on the brightness of the spots. The shorter exposure time is usually adequate for

LEED patterns from clean metal surfaces. With overlayers, the intensities of the spots may be reduced, so that longer exposure times are required.

When the screen is photographed at 2 eV intervals from 40 to 300 eV, the total time required is less than 10 minutes even with 4-second exposures. The procedure requires recording of incident beam current at each energy point for later normalization of the measured intensities. The film is developed in a tank using Acufine developer for 5 to 10 minutes at 75° to 80°C with gentle agitation. Some experimentation with time and temperature is needed for different LEED patterns. However, over-long developing times will lead to saturation of the LEED spot images. After fixing (Kodak rapid Fixer, ≃5 min.), the film is immersed in distilled water at room temperature for about 10 minutes and then dried. This provides a permanent record of the diffraction patterns.

The digitization of the LEED spots involves placing the photographic negative on a light table and scanning with the Vidicon camera. The position of each spot is identified by the co-ordinates of a cursor displayed on the TV monitor; the cursor can be moved by the user via a joystick. The circular region with a user-selected diameter centering on each spot is digitized (Vidicon and Digitizer, Spatial Data System, Galena, California) and the density values are integrated subject to a background subtraction†. The summed

---

†Background subtraction will be discussed in Section 4.4.3.

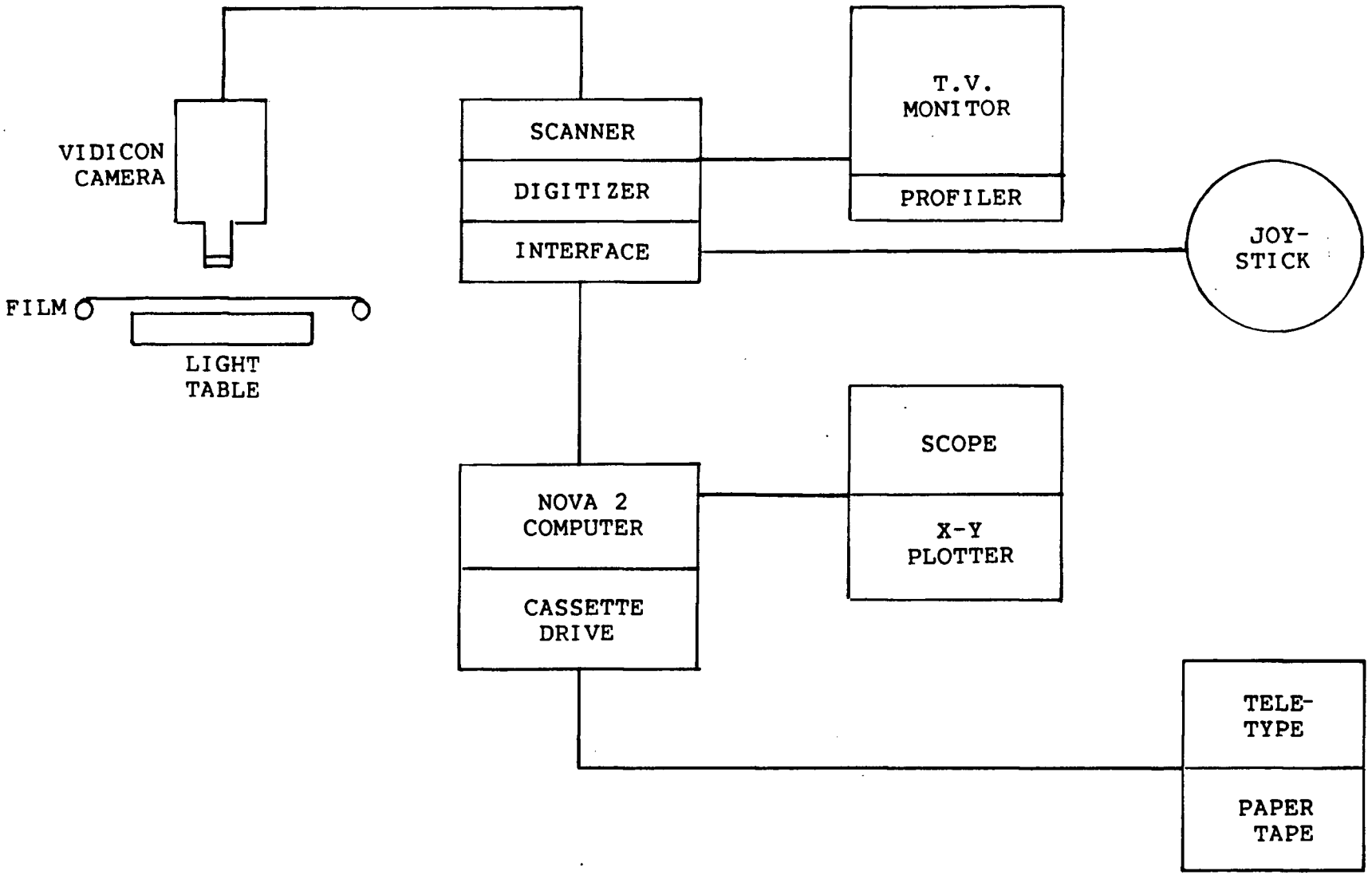

Figure 4.7: Schematic diagram of the computer-controlled analysis of photographic negatives of LEED patterns.

intensities at each energy are divided by the appropriate incident beam current. An optional grid transparency correction[129,130] can be done off-line. The I(E) curves are usually smoothed by a 3-point smooth routine. A schematic diagram for the arrangement of the computer-controlled digitization process is shown in Figure 4.7. The integrated intensities are then stored on cassette tape and can be transferred to the mainframe computer (Amdahl 470 V8) via paper tape.

The applicability of the photographic method depends on two general assumptions:

1. the optical density for a spot on the film negative is proportional to the amount of light that causes the darkening; and
2. the intensity of a spot on the fluorescent screen is proportional to the impinging electron flux.

Spots with comparable maximum intensity in the energy range considered are analyzed with the same settings of black and maximum levels. The analysis procedure is therefore faster, but it is also important that individual spots span as much as possible of the grey scale; this will yield better peak-and-valley resolution in the subsequent I(E) curves.

4.4.2 TV CAMERA METHOD

The TV camera method to measure relative intensities directly from a LEED screen was first introduced by Heilmann *et al.*[131]. Since then various modifications involving

video recording[132] and closed-circuit TV[133] have been described. The tape recording method is fast, requiring only several seconds to store a hundred 'frames' of LEED pattern which can be analyzed later. However, the quality and resolution of reasonably-priced commercially available video recorders and tapes set a major limitation on the applicability of this approach. In recent years, A/D converters and microprocessors have improved so much that Heilmann *et al.*[134] have described the scanning and digitization of particular LEED beams at some 500 data points in only about 10 seconds. This can truly be said to define an on-line method. The need for faster LEED data acquisition arises both from the need to minimize beam-surface interactions, and to be able to test experimental settings quickly prior to making measurements (i.e. to overcome the serious problems noted above for the photographic method).

I was working on the development of a video recorder type system for this laboratory when we became aware of a commercial video LEED analyzer (Data-Quire Corp., Stony Brook, N.Y.). Funds were then obtained to purchase the latter which was incorporated into our new TV system. The LEED measurement facilities based on this VLA is shown schematically in Figure 4.8. The most important part of the system is a 32K microprocessor (Motorola 6800). This digitizes the video signals from the camera via an A/D converter and also controls the LEED gun voltage via a D/A

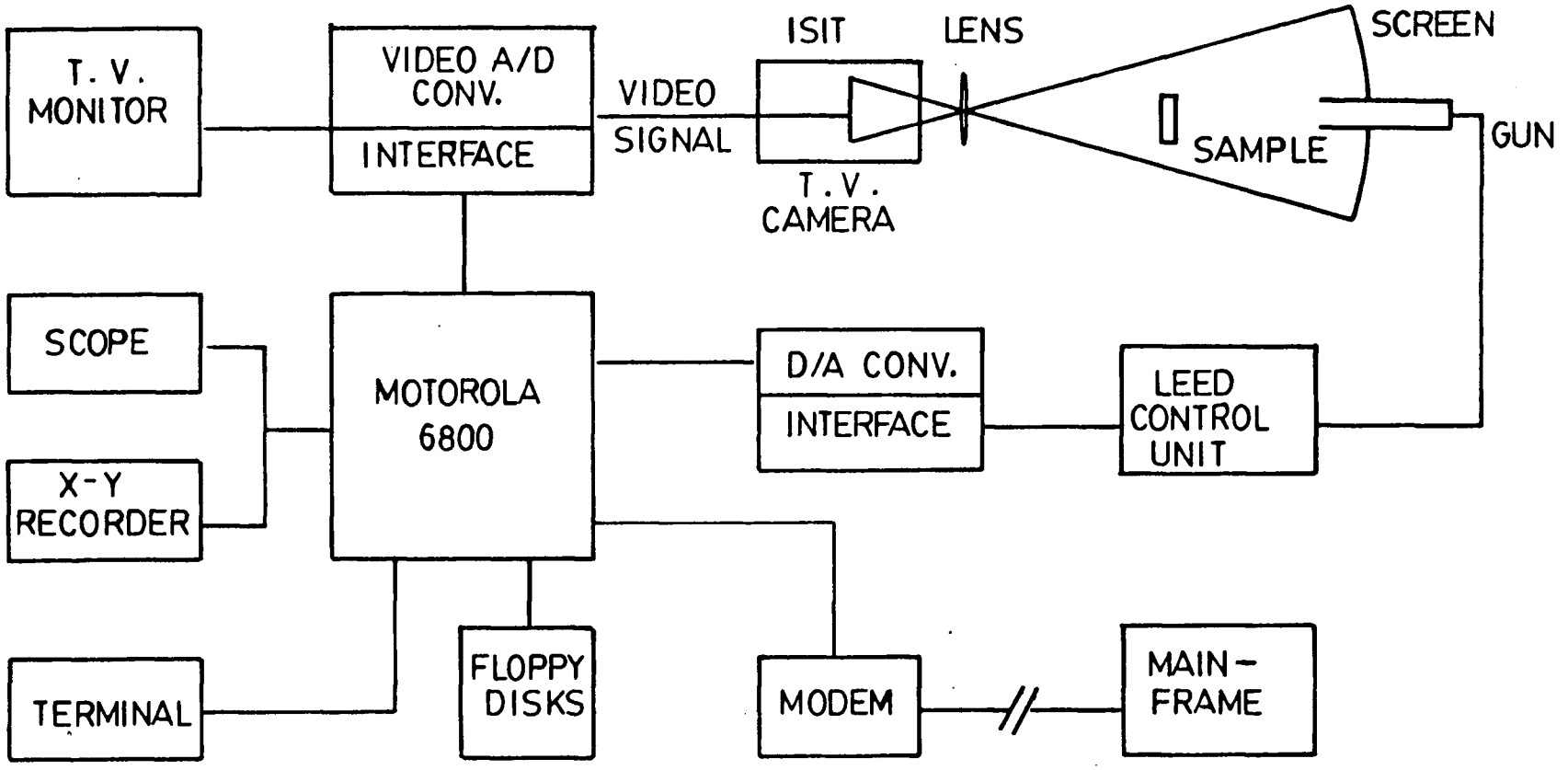

Figure 4.8: Schematic diagram of the real-time LEED spot intensity analysis using a video LEED analyzer (VLA, Data-Quire).

converter.

The TV camera used is of the intensified silicon intensifier target type (COHU 4410/ISIT). An ISIT camera basically consists of a photocathode tube and a silicon target. When light passes through the camera lens on to the photocathode tube, electrons are produced. In conventional Vidicon cameras, the current from these electrons is a measure of the light intensity. In an ISIT camera these electrons are further accelerated on to the silicon target, where more secondary electrons are produced, thereby resulting in higher currents for given conditions than can be obtained with a Vidicon camera. Consequently, an ISIT camera is some 10^3 times more sensitive than a conventional Vidicon camera. This enables the incident current to be kept to low levels to minimize any heating or electron stimulated desorption effects[135-137].

In a LEED experiment the TV camera is positioned in front of the LEED fluorescent screen in such a way that it gives a picture of the LEED pattern that covers approximately the whole area of the video monitor screen. For fixed values of the incident beam (energy, direction of incidence) and for fixed conditions of the surface, the latter picture is defined as a frame. Such a frame consists of 256x256 picture elements (or pixels). The intensity of each pixel can be digitized in a grey scale of 0-255. In North America, only 1/60 second is required for a single scan of all 65,536 pixels of each frame. The scan starts at

the upper left corner and moves left to right first along the topmost horizontal line exactly one pixel wide, and then continues down to scan all 256 horizontal lines in order. It is possible, at least in principle, to digitize the desired LEED spots within the time taken to scan the whole frame. This is indeed the case in the latest system used by Heilmann *et al.*[134]. However, the digitization rate of the central processor unit of our VLA is much lower than the scanning rate, so a slightly different approach is taken to 'buy time' for the digitization process. The digitization is done columnwise: only one of the 256 pixels on the same horizontal line is digitized in a single scan. In other words, it takes as many scans as number of pixels to digitize a row of such pixels, whereas only one scan is required to digitize a column of (any number of) pixels in each frame. A frame can therefore be viewed as being made up of 256 columns of pixels, and the complete digitization of the latter requires 256/60 seconds.

To further reduce the data acquisition time, only the user-selected 10x10 pixel windows superimposed on desirable LEED spots observed on the video monitor screen are digitized. For an isolated window, 10 scans (because there are 10 columns of pixels), which will be called a pass (10/60 seconds), are required to digitize the 100 pixels inside. In general n such passes, or n/6 seconds, are required to digitize n selected windows on the TV monitor. However, due to the columnwise digitization, windows not

lying on the same horizontal scanning path (10 pixel wide) can be digitized in the same pass. Thus to speed up the digitization procedure, it is sometimes necessary to rotate the TV camera in such a way that the desired windows lie on non-overlapping horizontal paths. Figure 4.9 illustrates how eight windows on a square net can be measured in one pass with the appropriate rotation instead of three passes otherwise. On average, the data acquisition time for n spots would be $167\sqrt{n}$ msec. The time-saving routine is particularly useful when multiple scanning is desired to enhance the signal to noise ratio. Comparing to the system used by Heilmann *et al.*[134], the measurement of a single spot by the VLA takes almost 10 times as long. The former system, however, measures only a maximum of 4 spots per run; whereas the VLA can measure up to 49 spots per run. So when measurements are required from a LEED pattern of 25 spots, the VLA takes only about twice the time in data acquisition as does Heilmann *et al.*'s system.

At each pass, the position of the pixel with the maximum intensity I_{max} inside each window is noted together with the value of I_{max}. The sum of the intensities of the 100 pixels are stored as the 'hundred sum' or HSUM. In addition, the computer also stores the number (N) of those pixels which have intensities higher than a user-selected fraction of I_{max}, and the summed intensity of these pixels is called the NSUM. The quantities I_{max}, HSUM, NSUM and N are further illustrated in Figure 4.10. The HSUM's are

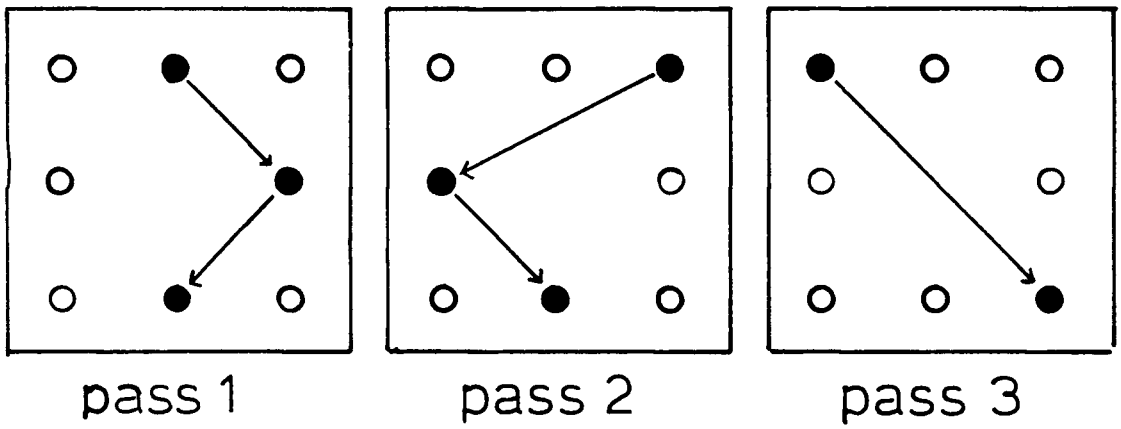

(a) 3 passes required for the digitization of 8 LEED spots on a 'perfect' square net. The particular routes chosen by the computer tend to optimize the time-delay between digitization of each spot.

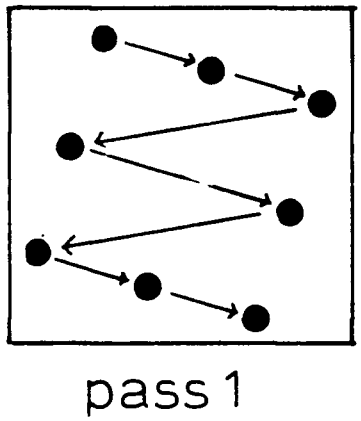

(b) 1 pass required for the digitization of the same spots as in (a) with a slight rotation of the TV camera.

Figure 4.9: Schematic illustration of the number of passes required for digitization of 8 LEED spots in a square net.

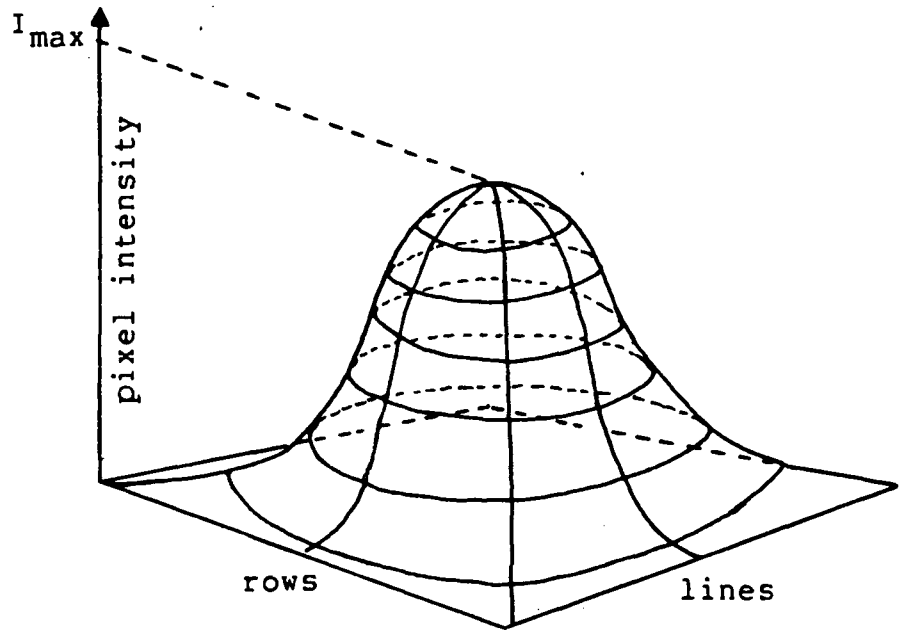

(a) The total volume under the 'dome' represents HSUM which corresponds to the integrated intensity of 100 pixels.

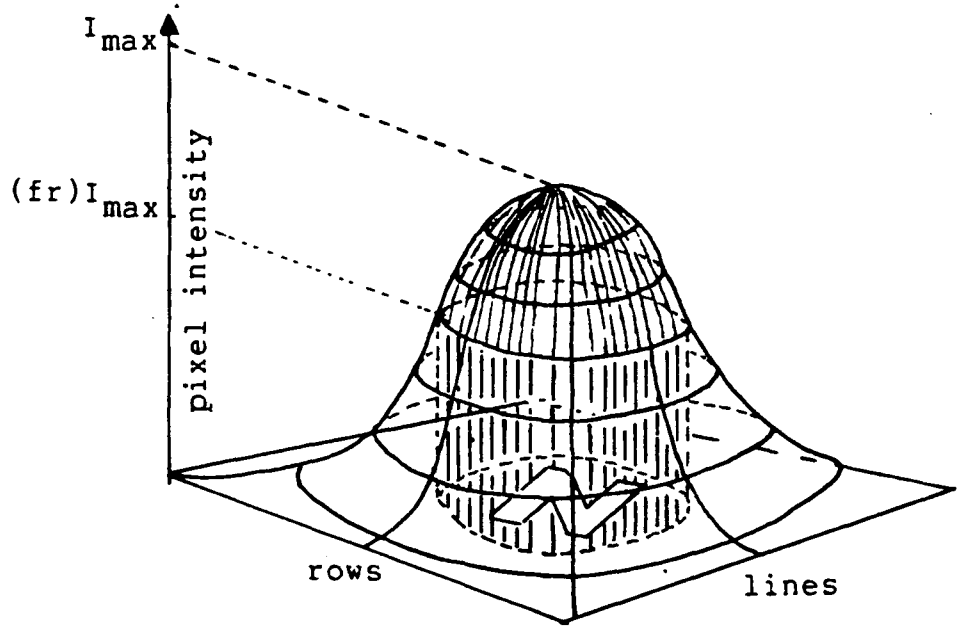

(b) The volume of the 'bullet-shaped' structure represents NSUM. This is the integrated intensity of N pixels each of which has an intensity $\geq(fr)I_{max}$ (where (fr) may be 1/2, 1/4, 1/8,....).

Figure 4.10: 3-dimensional diagrams of two types of integrated LEED spot intensity in a (10-pixel x 10-pixel) window. (a)Hundred sum (or HSUM). (b)N-sum (or NSUM).

usually used to represent the relative intensities in I(E) curves. With a careful preset fraction, the NSUM's and the N's can be utilized to estimate suitable background corrections. This procedure will be discussed in Section 4.4.3.

Once a frame is digitized, one of the parameters of a LEED experiment is changed to give the next frame. In this work, the interest is especially in I(E) curves, so the normal procedure is to change the energy of the incident beam (e.g. by 1 or 2 eV). The change can either be positive or negative, but spot positions in the new frame will have changed slightly from the preceding frame (assuming of course that the change in energy is small). The VLA provides two tracking modes for the spots, which are available at the user's discretion. One of these is the computer-controlled mode: the new spot positions on the screen are calculated by the computer from information on unit mesh dimensions and directions entered by the user at the beginning of the run. The other tracking mode is referred to as the 'dynamic correction' mode; it uses the positions of those pixels with I_{max} in the preceding frame as the centers of the new windows. There is a user-selectable threshold intensity value to trigger 'dynamic correction'; when I_{max} is below this threshold intensity, the calculated mode must be used exclusively. The 'dynamic correction' mode should be used with caution when either the LEED pattern is generally weak, or when bright spots arising from fluorescent screen burns

are present. In the first case, the feedback tracking may be distracted by the general background light, while in the second the cursor may latch on to the bright spots when the actual LEED spots are close to the former.

Subsequent treatments of data for normalization, grid transparency correction and 3-point smoothing are done off-line.

4.4.3 BACKGROUND SUBTRACTION

In the photographic method, as traditionally used in this laboratory, a fairly elaborate background subtraction scheme could be included because analysis time is not a crucial factor in this approach. Here a circular LEED spot is assumed to have a radius r which is user-selectable but is constant for all the spots in the same run. The background intensity is then estimated as the average of the intensities of all the pixels lying on a thin annulus with width Δr and mean radius $(r+\Delta r/2)$. The product of this background density and the area of the spot is subtracted from the spot's integrated intensity to give a 'background free' value.

Somewhat similarly in the on-line system described by Heilmann *et al.*[134], a window of nxn pixels is assumed. A hardware adder sums the intensities of n pixels on each parallel line in the window, and stores the line-sum L_i (for the i^{th} line). The procedure is repeated for n lines in the window, and the total intensity is then the sum of L_i

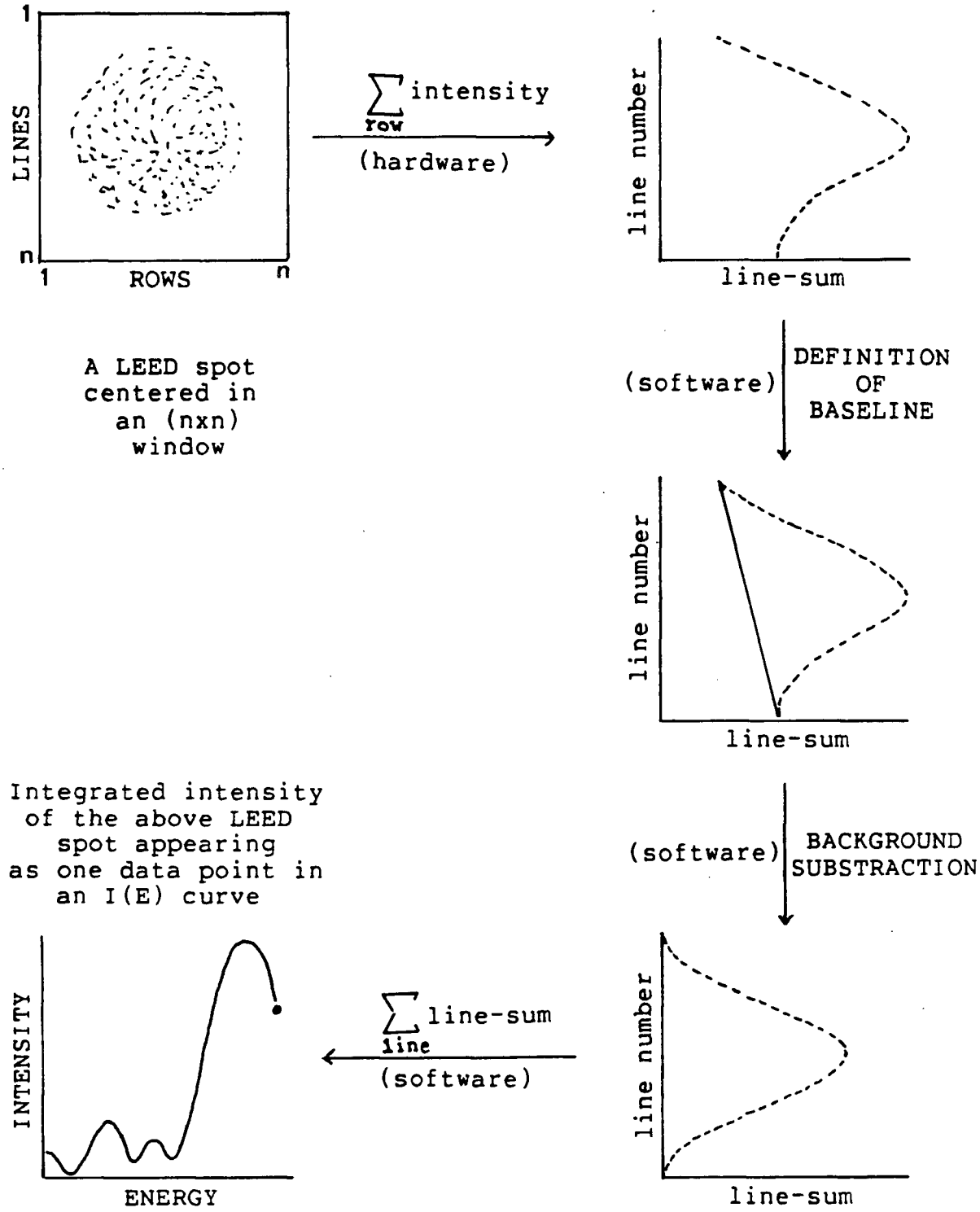

Figure 4.11: Schematic diagram of the real-time background subtraction with the aid of a hardware adder (after Heilmann *et al.* [134]).

through L_n. The background is defined as $n(L_1 + L_n)/2$ and is subtracted from the total intensity. The above procedure is represented schematically in Figure 4.11. With the use of the hardware adder, the time required for the background subtraction step is relatively short. The above procedure assumes that the spot is well-centered in the window, which can be achieved by calculated and/or dynamic tracking modes.

Due to the comparatively low digitization rate and the lack of a hardware adder, this procedure is not available with our video LEED analyzer. Although profiling of a spot can be done by software, background subtraction with Heilmann *et al.*'s scheme would inevitably put a severe strain on both the speed and the core space of the central processor when the VLA is used for multi-beam analysis. Currently two rather simple methods, which were originally proposed by Strozier and Jona[138], are used with our VLA for estimating background corrections. The philosophy of approach partly takes note of the fact that there is no universal definition of background intensity in LEED. In any event, for both the methods we currently use, the subtraction step is done off-line.

The first approach used with our VLA defines the background B as the intensity of the area between two neighboring LEED spots. In its implementation, the windows are moved (initially by the user, then by the calculated tracking mode) to these areas after the digitization of the LEED spots of interest for the appropriate energy range.

HSUM of these windows is taken as B. To reduce the time spent on acquisition of background intensities, only a few representative areas need be scanned. Figure 4.12(a) illustrates how two such areas may be selected for a nine spot LEED pattern. In this example, X and Y represent background between strong/weak and weak/weak pairs of LEED spots respectively. Thus only one background intensity is recorded for each type of related pairs of beams. In this approach, it is preferable to select areas not lying on the same horizontal path; this is to exploit the columnwise digitization process.

An unsatisfactory feature of this approach arises when two neighboring spots have very markedly different intensities. In such cases, the initially-determined background correction B, such as from the area marked X in Figure 4.12(a), will be dominated by the brighter spot as shown in Figure 4.12(b). Weighted backgrounds, such as

$$b_1 = BI_1/(I_1+I_2) \text{ and } b_2 = BI_2/(I_1+I_2) \qquad (4.4)$$

may then be more appropriate. In equation (4.4), I_1 and I_2 are the total intensities of the two LEED spots, and b_1 and b_2 are the corrected background values. This simple method has the limitation that when the spots are very close together, there may not be enough room to accommodate the window for measuring B. When that occurs, another method can be used.

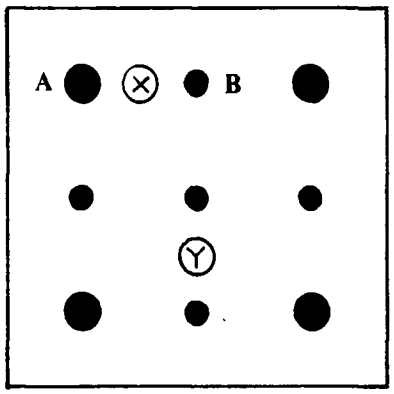

(a) X represents background between bright and weak spots.
Y represents background between weak spots.

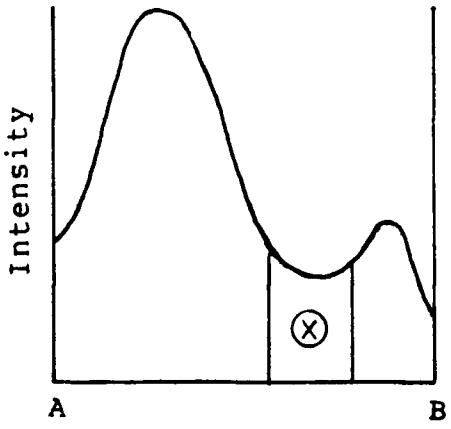

(b) Intensity profile from A to B. Intensity of the region X is made up largely of the 'tail' of the bright spot.

Figure 4.12: LEED spot background intensity approximated by HSUM of a window between neighboring spots.

The second method uses the NSUM and N introduced in Section 4.4.2. While HSUM represents the total integrated intensity of the 100 pixels in a window, NSUM gives only the sum of the intensities of those N pixels whose intensities are greater than a pre-determined fraction of the maximum pixel intensity (I_{max}) in the window. The background for a LEED spot with these sums and N is defined as

$$B = (HSUM - NSUM)/(100-N). \qquad (4.5)$$

The numerator in equation (4.5) corresponds to the shaded areas in Figures 4.13(a) and 4.13(b). The denominator represents the number of pixels in the shaded area. In effect, B gives an approximation to the averaged intensity in the 'tails' of the intensity distribution curves shown in Figure 4.13. It is evident from the same figure, that the applicability of this method depends on the choice of an optimum fraction for NSUM. The latter is user-selected and has values of 1/2, 1/4, 1/8,..... Before any data acquisition, the user should scan the whole LEED energy range to determine the appropriate value for the NSUM if background subtraction with equation (4.5) is desired. The value of B is unstable when N is very close to 100. This occurs when the selected fraction is a low value such as 1/16 or 1/8. To avoid this, a value of 1/2 is generally used. However, some 'injustice' will be done to the sharper spots such as the one shown in Figure 4.13(a). Here, the

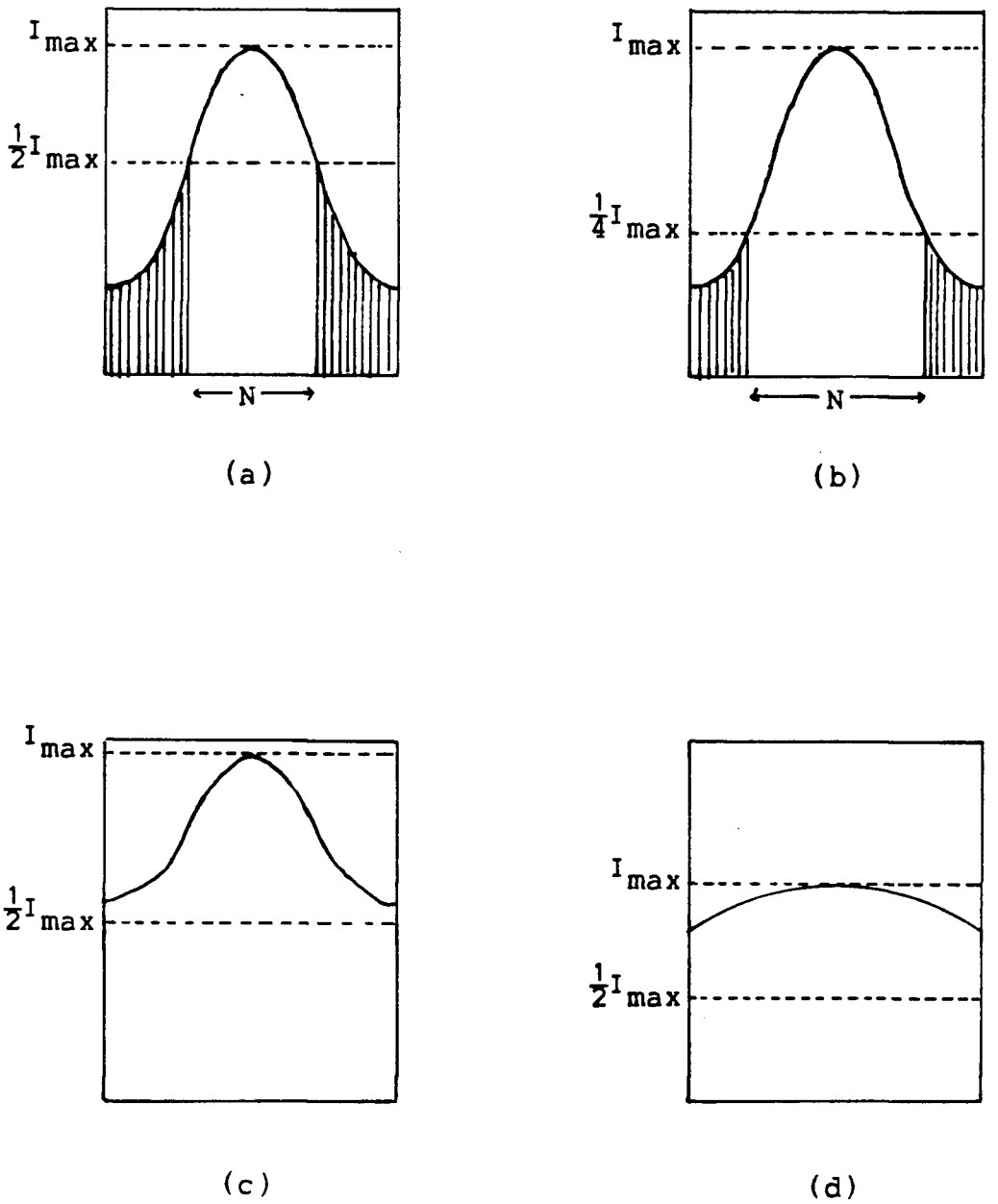

Figure 4.13: Schematic illustration of the use of HSUM and NSUM for the estimation of background. The shaded 'tails' in (a) and (b) represent the difference (HSUM-NSUM). The average background is defined as this difference divided by the number of pixels that make up the tails. (c) and (d) represent two types of spot where HSUM=NSUM, and equation (4.5) is not applicable.

spot would have an apparently low intensity since a significant part of its 'real' intensity is taken as the tail. Equation (4.5) is not applicable when N equals 100. This is the case when the spot is either extremely bright (Figure 4.13(c)) or has a relatively flat intensity distribution curve (Figure 4.12(d)). Bright spots can be avoided by lowering the gain of the ISIT camera. Unfortunately, this will lead to an across-the-board reduction in LEED spot intensities. As a result some weaker spots may be lost. At the present time, there is no good solution for the 'flat-top' spots, although the latter were rarely observed in this work.

Figure 4.14 compares the (0,1) beam from a clean surface of Rh(111) obtained by the VLA, with and without background corrections. Smoothing is deliberately omitted so that any abnormal features resulting from the two simple background correction schemes may be observed. In general, background correction according to equation (4.4) levels the base lines of I(E) curves satisfactorily; but it does not greatly affect the positions and shapes of peaks. Background subtraction utilizing NSUM enhances the sharpness of peaks appreciably; but this scheme may lead to unexpected appearance of peaks and valleys, possibly due to 'unfair' subtraction from very bright spots. One such subtraction is evident at the 150 eV peak in Figure 4.14 (curve c), where the large peak turns into a small dip. Therefore caution has to be taken when using NSUM for estimating background

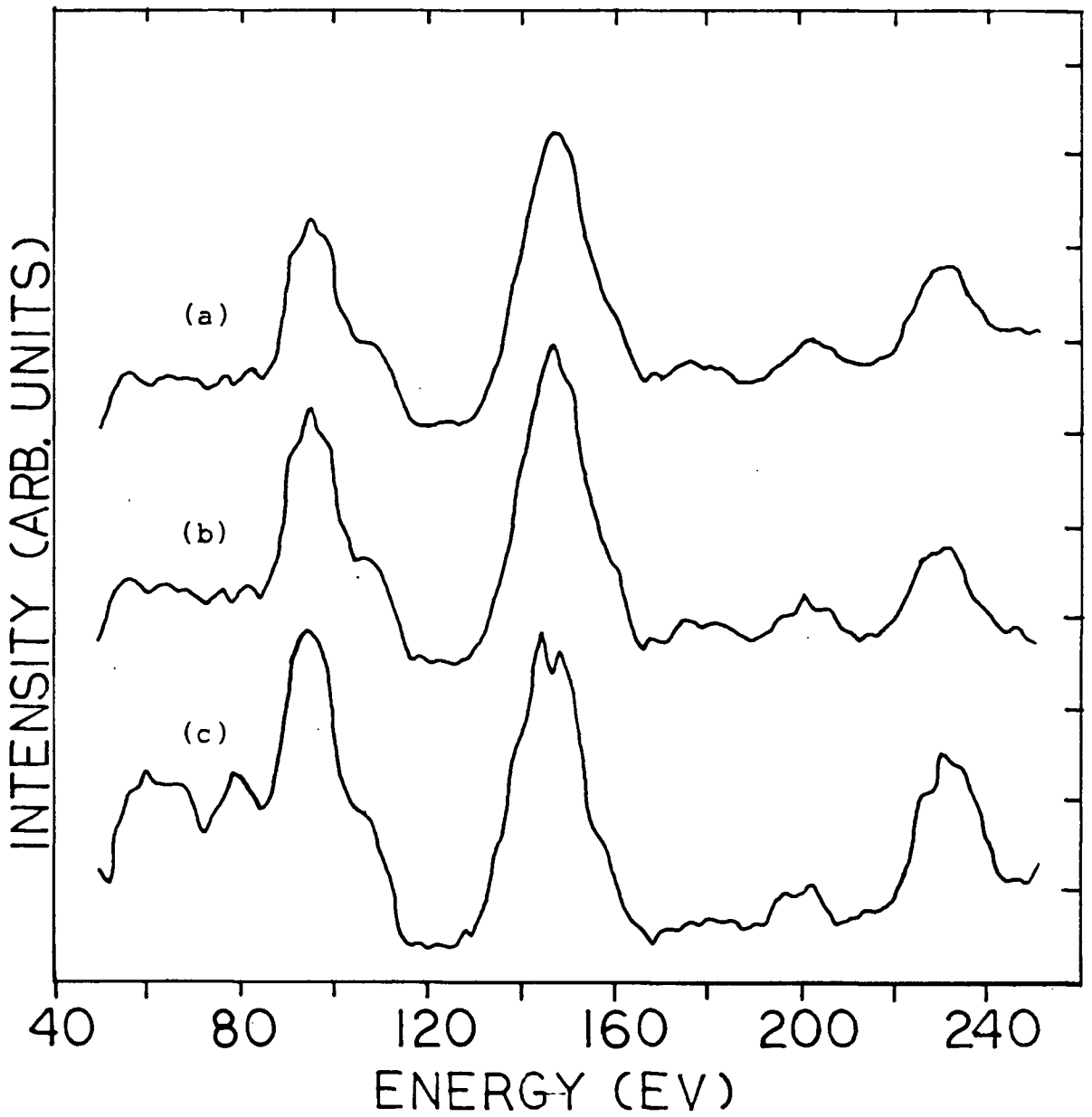

Figure 4.14: Experimental I(E) curves for (0,1) beam of clean Rh(111) surface (θ=0°, no smoothing). (a)No background subtraction. (b)Background subtraction using equation (4.4). (c)Background subtraction using equation (4.5).

corrections.

CHAPTER 5

STABILITY OF LEED FRACTIONAL ORDER BEAM INTENSITIES

5.1 INTRODUCTION

While making multiple scattering LEED intensity calculations for O adsorbed on the Zr(0001) surface, I observed a strong tendency for corresponding fractional order beam I(E) curves to be closely constant with changing adlayer coverage, specifically from quarter monolayer (2x2) structures to half monolayer (2x1) structures. This appears as an interesting observation which apparently contrasted with an indication by Shih *et al.*[40] that these translational symmetries could be distinguished by LEED crystallography for models of dissociated CO on the (0001) surface of titanium. Nevertheless the observation here reinforces and extends similar observations by Yang *et al.*[139], and it further provides support for some approximate schemes of multiple scattering calculation such as the quasi-dynamical method[140,141], diagonal dominant method[142], unit cell reduction method[139,143] and beam set neglect method[51]. The last method, which was introduced by Van Hove *et al.*, is especially useful in making tractable the calculation of LEED intensities from surface structures with large unit meshes.

When I(E) curves for related fractional order beams are closely independent of coverage, for constant adsorption site, there is an implied insensitivity of the LEED technique to surface coverage. In one sense this may be seen as a disadvantage, but equally, insofar as these beams are independent of the unit mesh area, multiple scattering

calculations may be made with smaller unit mesh areas. The latter would reduce the beam requirement in K-space. Yang *et al.*[139] concluded that the stability in the fractional order I(E) curves with changing coverage requires a constant substrate environment around each adsorbed atom and negligible scattering between the adsorbed atoms.

Given a potential usefulness for the stability in fractional order beam intensities as discussed by Yang *et al.*[139], further investigation of the range of its applicability appears useful. This requires consideration of the effects of changing scattering strengths for the adsorbate and substrate atoms. In general the closer the adsorbate atoms are to one another, the more important should be the scattering within the adsorbed layer[106], and therefore according to Yang *et al.*[139] the greater are likely to be the differences in corresponding I(E) curves with changing coverages. This brings out the importance of new observations for the adsorption of O on Zr(0001) surface, since for three-domain p(2x1) models neighboring O atoms are then relatively close (i.e. separated by just the substrate interatomic distance), and therefore larger multiple scattering contributions may be anticipated. Thus further comparisons between p(2x1) and p(2x2) structures should be helpful for illuminating the range of applicability of the fractional order beam stability first discussed by Yang *et al.*[139].

Comparisons between sets of calculated intensity curves can be assessed with the methods developed for comparing experimental and calculated I(E) curves in LEED crystallography. Therefore the next section reviews the LEED reliability indices which are used in this chapter, as well as in the next for structural analyses for oxygen adsorbed at the Zr(0001) surface.

5.2 COMPARISON OF I(E) CURVES: THE RELIABILITY INDICES

In LEED crystallography, I(E) curves calculated with different models are compared with the corresponding experimental I(E) curves until a 'best fit' is obtained. Traditionally such comparisons were made by visual inspections, but this approach becomes increasingly unwieldy in general. The need for some mathematical functions which can systematically make these comparisons is well documented[144]. The reliability indices (or R-factors) proposed by Zanazzi and Jona[145] and by Pendry[146] are described in the following.

5.2.1 ZANAZZI-JONA R-FACTOR

Zanazzi and Jona[145] have proposed a mathematical index which compares I(E) curves with regard to all features which seem important from the experience of visual comparisons. For a single beam, these authors used

$$r = \frac{\int w(E)\,|I_e' - cI_t'|\,dE}{\int I_e\,dE}, \qquad (5.1)$$

where I_e and I_t refer to experimental and theoretical intensities respectively; the primes indicate first derivatives. The integrals are over the energy range where the experimental and theoretical data overlap, and the function w(E) is defined as

$$w(E) = \frac{|I_e'' - cI_t''|}{|I_e'| + |I_e'|_{max}}. \qquad (5.2)$$

Here double primes indicate second derivatives, $|I_e'|_{max}$ is the maximum value of $|I_e'|$, and c is a scaling factor which is taken as the ratio of the mean experimental and calculated intensities such that

$$c = \frac{\int I_e\,dE}{\int I_t\,dE}. \qquad (5.3)$$

For a single beam, the function r in equation (5.1) has the property that the lower its value, the better is the match between the experimental and calculated I(E) curves.

The use of the scaling factor c makes r independent of the absolute value of intensities of the I(E) curves. However, r is not dimensionless, and because of this Zanazzi and Jona proposed the reduced index

$$r_{zj} = r/r_o, \tag{5.4}$$

where r_o has been given the numerical value of 0.027, which represents an average from a set of random curves. For comparing intensity curves from several diffracted beams, one R-factor discussed by Zanazzi and Jona is

$$R_{zj} = \sum_i \Delta E^i r^i_{zj} / \sum_i \Delta E^i, \tag{5.5}$$

where i runs over over all the individual beams. This represents an average of the r_{zj} values of the individual beams, weighted according to the energy range (ΔE) over which the comparison with experiment has been made.

5.2.2 PENDRY R-FACTOR

Pendry[146] proposed an alternative multi-beam R-factor which avoids the use of second derivatives, and apparently has a clearer significance for high values. This is

$$R_p = \sum_i \int (Y^i_e - Y^i_t)^2 dE / \sum_i \int [(Y^i_e)^2 + (Y^i_t)^2] dE, \tag{5.6}$$

where again the summations are over the different beams i. The Y are functions of energy formed from the I(E) curves, and they are defined as

$$Y = L/(1 + L^2 V_{oi}), \tag{5.7}$$

where the L are logarithmic derivatives

$$L(E) = d\ln I/dE \tag{5.8}$$

for both Y_e^i and Y_t^i, respectively derived from the experimental and theoretical I(E) curves. In (5.7), V_{oi} is the imaginary part of the constant 'muffin-tin' potential used in the multiple scattering calculations.

A comparison of identical sets of I(E) curves would yield a value of R_p equal to zero, but the denominator in equation (5.7) tends to restrict R_p to about one when a comparison of random sets of I(E) curves are made (assuming the product $Y_e^i Y_t^i$ have random signs and magnitudes). R_p emphasizes the positions of peaks and troughs in the curves being compared; moreover all maxima and minima receive essentially equal weights in the comparison.

5.2.3 NORMALIZATION OF R-FACTORS

R_{zj} and R_p have the property that the smaller their value, the better the agreement between two sets of I(E) curves; in case of identical sets, the R-factors would be zero. Van Hove and Koestner[146] discussed several other (simpler) reliability indices for LEED, but, for all, these authors introduced normalization constants to ensure that the indices generally fall between 0 and 1. Van Hove and

Koestner proposed that a normalization constant of 1/2 is appropriate for R_{zj} and R_p, and R-factors reported in this work have all been normalized with this additional factor.

5.3 (2X1) VERSUS (2X2)

During the LEED study of oxygen adsorption on Zr(0001), a diffraction pattern corresponding to a (2x2) surface structure was observed. The LEED pattern (and the I(E) curves) exhibited an apparent 6-fold symmetry at normal incidence; this is due to the existence of two sets of domains arising from either the A or B termination characteristic of a hcp(0001) surface (Figure 5.1). Figure 5.2 details that the observed (2x2) diffraction pattern may arise from a (2x2) surface structure or from a superposition of patterns from the three types of rotationally related (2x1) domains which may be present simultaneously on the surface (models in real space are specified in Figure 2.9).

In order to assess whether LEED crystallography alone is likely to be able to distinguish (2x1) and (2x2) structures on a hcp(0001) surface, a series of multiple scattering calculations were performed for the adsorption of several atomic species on the Ti(0001) and Zr(0001) surfaces.

5.3.1 THE CALCULATIONS

I(E) curves were calculated for surface models with Bravais lattice layers (Section 3.3.1) of adsorbate and

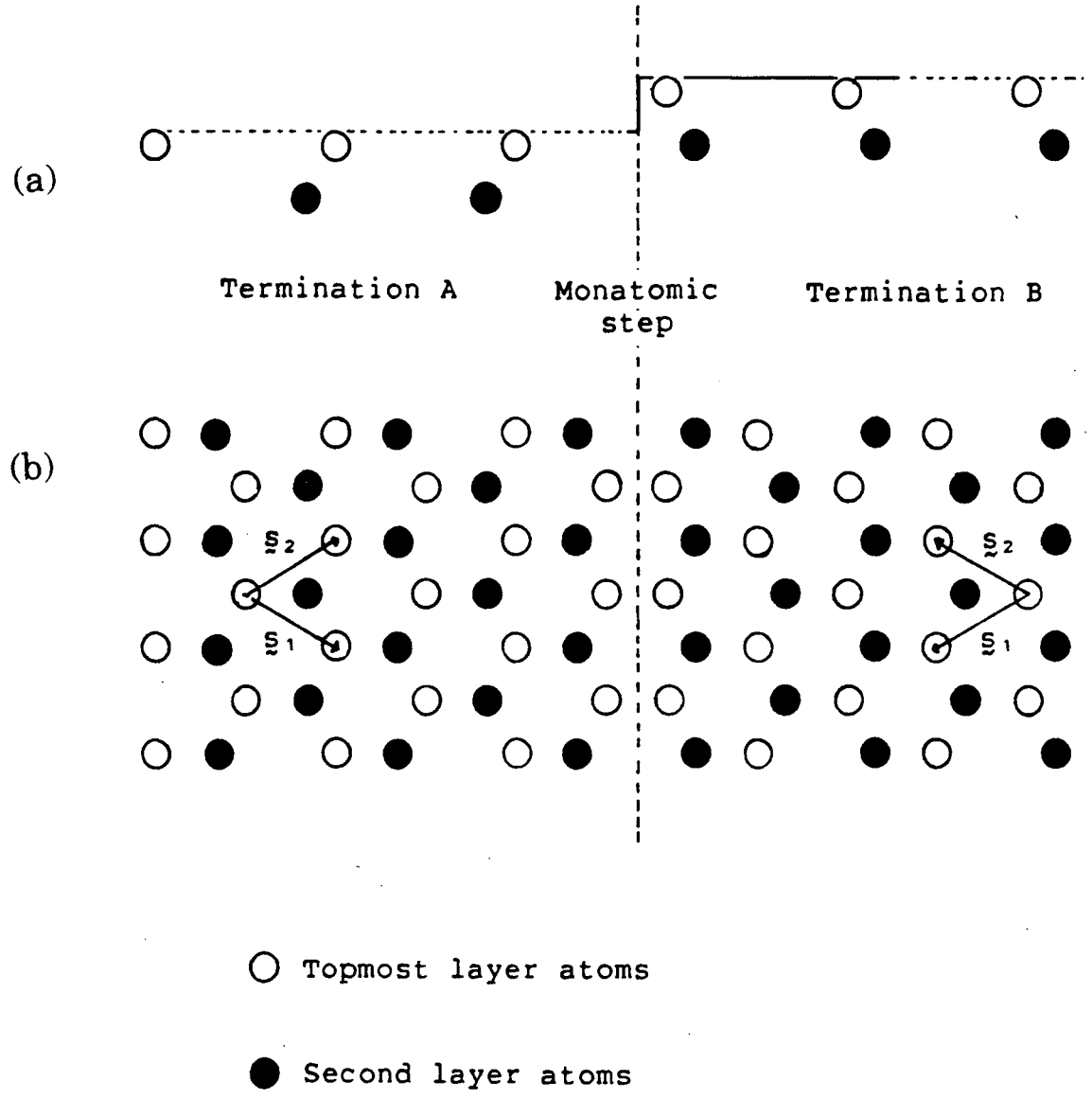

Figure 5.1: (a)Side view and (b)top view of the two possible domains resulting from the truncation of the bulk structure of a hcp(0001) surface. The two domains are related to each other by a 180° rotation.

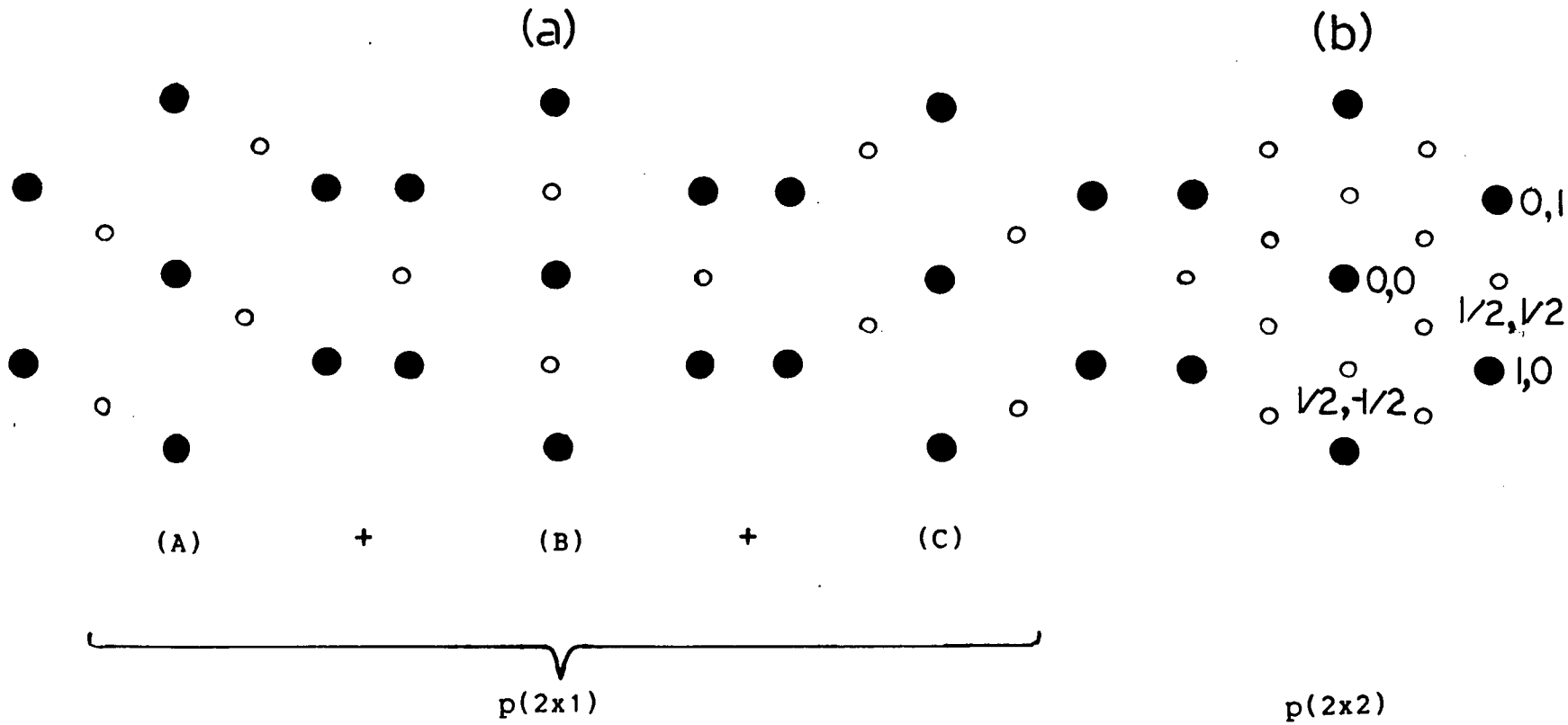

Figure 5.2: Superposition of the (2x1) reciprocal lattices in (a) from the three possible rotational domains of a (2x1) structure on a hcp(0001) or fcc(111) surface to form an apparent (2x2) reciprocal lattice in (b). Solid and hollow circles represent integral- and fractional-order beams respectively.

substrate atoms, and the layers were stacked by the renormalized forward scattering method (Section 3.4.2). Normal incidence was used in all cases. Thus a 3-fold rotational and a mirror plane(xz) symmetry could be assumed for the (2x2) models, and just a mirror plane(xz) symmetry for the (2x1) models (beam labelling is detailed in Figure 5.2). For (2x1) structures, a calculation for just one domain is sufficient at normal incidence; the diffracted beams of the other two domains can be obtained by 120° rotations. In both (2x2) and (2x1) calculations, diffracted beams which are related by a 180° rotation were averaged with equal weightings to correspond to the situation that real hcp(0001) surfaces generally consist of equal populations of domains with A and B terminations.

The adsorption systems studied included

1. oxygen on Ti(0001);
2. titanium on Ti(0001);
3. tellurium on Ti(0001);
4. oxygen on Zr(0001); and
5. zirconium on Zr(0001).

Two adsorption sites (3h and 3f) were considered for each adsorption system; an additional site (6u) was considered for system (1). The adsorption site labels 3h and 3f identify sites of 3-fold coordination (3h/3f distinguishes whether each adsorbed atom is directly above an atom in the second substrate layer/an octahedral hole in the substrate), while 6u corresponds to the model in which the adsorbed

atoms incorporate into the octahedral holes between the first and second substrate layers. The interlayer spacings used were Zr-Zr 2.57 Å, Zr-O 1.30 Å, Ti-Ti 2.34 Å, Ti-O 1.30 Å, Ti-Te 2.07 Å; phase shifts (to l=7) for titanium and zirconium were deduced from band structure atomic potentials[96], whereas those for oxygen and tellurium were from Demuth *et al.*[98]. The imaginary part of the 'muffin-tin' potential (V_{0_i}) was given a constant value of -5 eV for all systems.

5.3.2 R-FACTOR ANALYSES AND DISCUSSION

Calculated I(E) curves for four integral order beams ((0,0), (1,0), (1,1) and (2,0)) and seven fractional order beams ((1/2,-1/2), (1/2,1/2), (3/2,-1/2), (3/2,-3/2), (3/2,1/2), (5/2,-3/2) and (5/2,-1/2)) for the corresponding (2x1) and (2x2) structures were compared with the normalized versions of R_{zj} and R_p[144]. The results for comparisons of corresponding (2x1) and (2x2) I(E) curves for seven surface structures and their total energy ranges of the I(E) data are summarized in Table 5.1.

For comparing the I(E) curves from corresponding (2x1) and (2x2) models, the Zanazzi-Jona R-factor (R_{zj}) may be most suitable since it attempts to compare I(E) curves with regard to all significant features. The comparisons in Table 5.1 indicate very low values for R_{zj}, and hence close similarity between corresponding I(E) curves from the (2x1) and (2x2) models. This statement holds true for different

Surface	Integral beams			Fractional-order beams		
	ΔE	R_{zj}	R_p	ΔE	R_{zj}	R_p
Ti(0001)-O (3h)	714	0.020	0.105	952	0.010	0.025
Ti(0001)-O (6u)	714	0.011	0.046	978	0.012	0.036
Ti(0001)-Ti (3h)	352	0.007	0.060	492	0.009	0.049
Ti(0001)-Te (3h)	710	0.026	0.126	868	0.051	0.119
Ti(0001)-Te (3f)	710	0.041	0.135	868	0.047	0.143
Zr(0001)-O (3h)	364	0.028	0.120	508	0.005	0.033
Zr(0001)-Zr (3h)	364	0.013	0.122	508	0.019	0.130

Table 5.1: Comparisons of calculated I(E) curves for integral and fractional-order beams for surface structures with (2x1) and (2x2) translational symmetries on hcp(0001) surfaces according to the reliability indices of Zanazzi-Jona (R_{zj}) and Pendry (R_p). The energy range of I(E) data for each comparison is identified by ΔE (in eV).

structural arrangements and for a variety of ion core scattering factors. Nevertheless, there is a general tendency for the fractional order beam R-factors to increase with the scattering strength of the adsorbed species. This trend is demonstrated by the series of O, Ti and Te adsorbed on the 3h site of Ti(0001) surface. Inspection of the fractional order beam I(E) curves (Figures 5.3 to 5.6) of corresponding (2x1) and (2x2) structures indicates increasing, albeit small, differences from oxygen to tellurium. Since the ion core scattering shows a general increase with atomic number, tellurium is assumed to have the highest scattering strength in this series of ad-atoms. The fact that tellurium has a hard sphere radius slightly larger than that of titanium suggests that neighboring Te atoms are too close together for a real (2x1) structure to be formed; nevertheless appreciable multiple scattering in the adsorbed layer may be expected from a model calculation.

For integral beams the situation is slightly different. For the (2x1) and (2x2) models of Ti (or Zr) on the (0001) surface of Ti (or Zr) (with the appropriate bulk topmost interlayer spacing), the I(E) curves of integral order beams become very similar to the corresponding beams from the (1x1) bulk-like surface. As a result, for example, R_{zj} decreases for the integral beams on replacing O on Ti(0001) by Ti or replacing O on Zr(0001) by Zr. Figure 5.7 shows the (2x1) versus (2x2) comparison for the (1,1) beam from O on Zr(0001), and from Zr on Zr(0001). The latter pair of I(E)

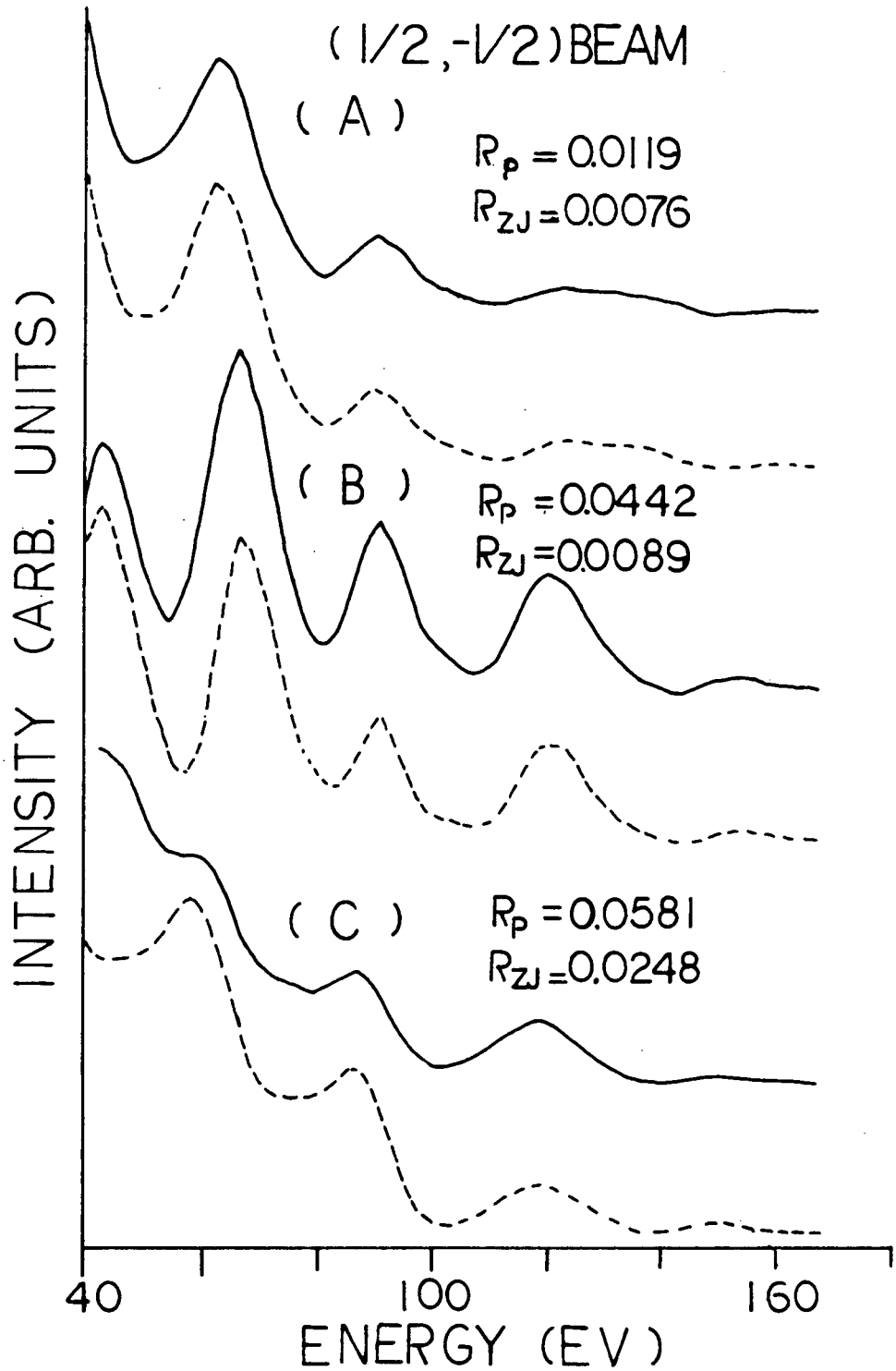

Figure 5.3: Comparison of calculated I(E) curves for the (1/2,-1/2) beam for the corresponding (2x1) (dotted line) and (2x2) (solid line) structures for adsorption of (A) O, (B) Ti and (C) Te, at the 3h site on the Ti(0001) surface. Single beam R_p and R_{zj} are indicated for each pair of I(E) curves.

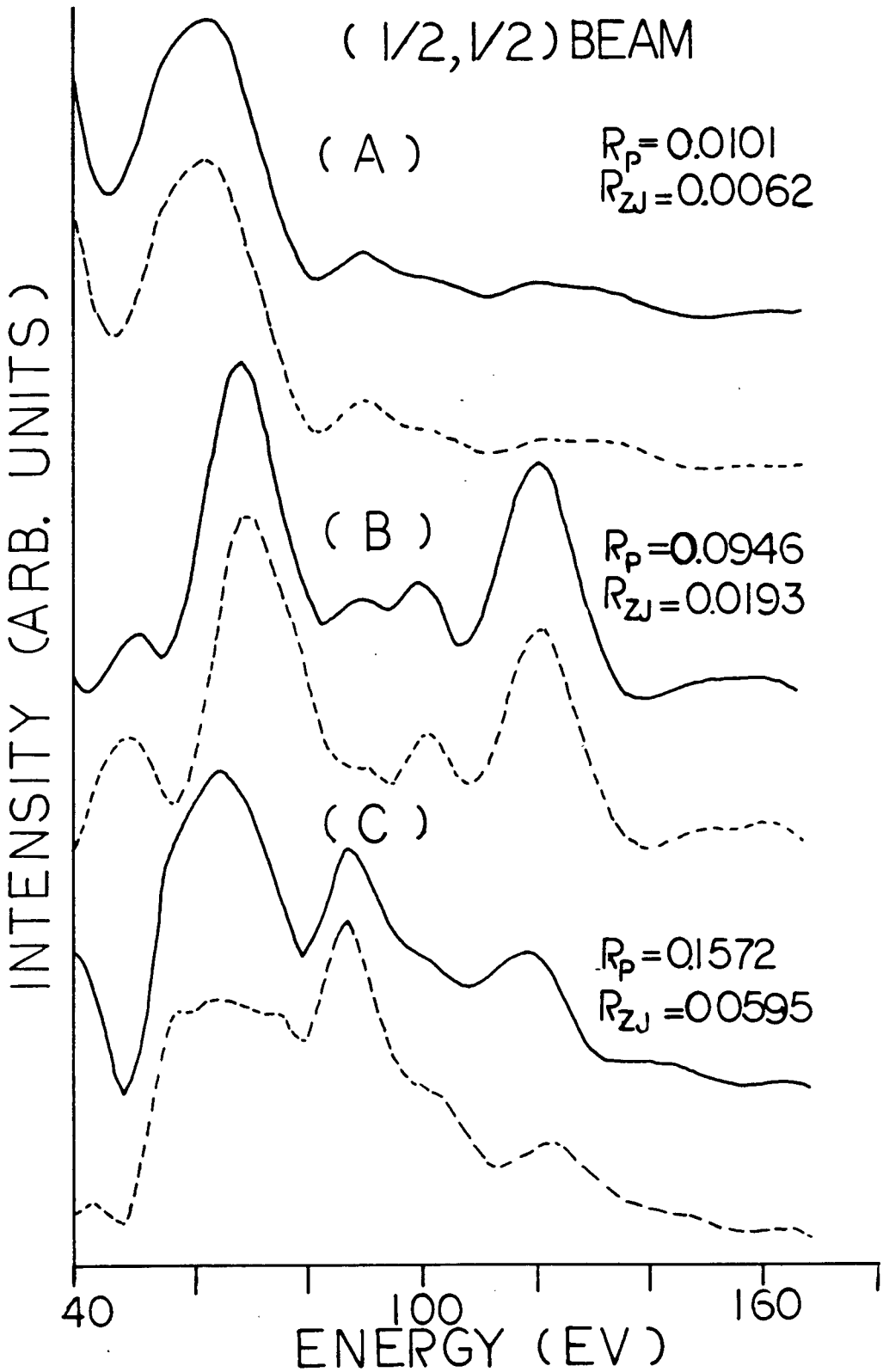

Figure 5.4: Same as Figure 5.3, except for the (1/2,1/2) beam.

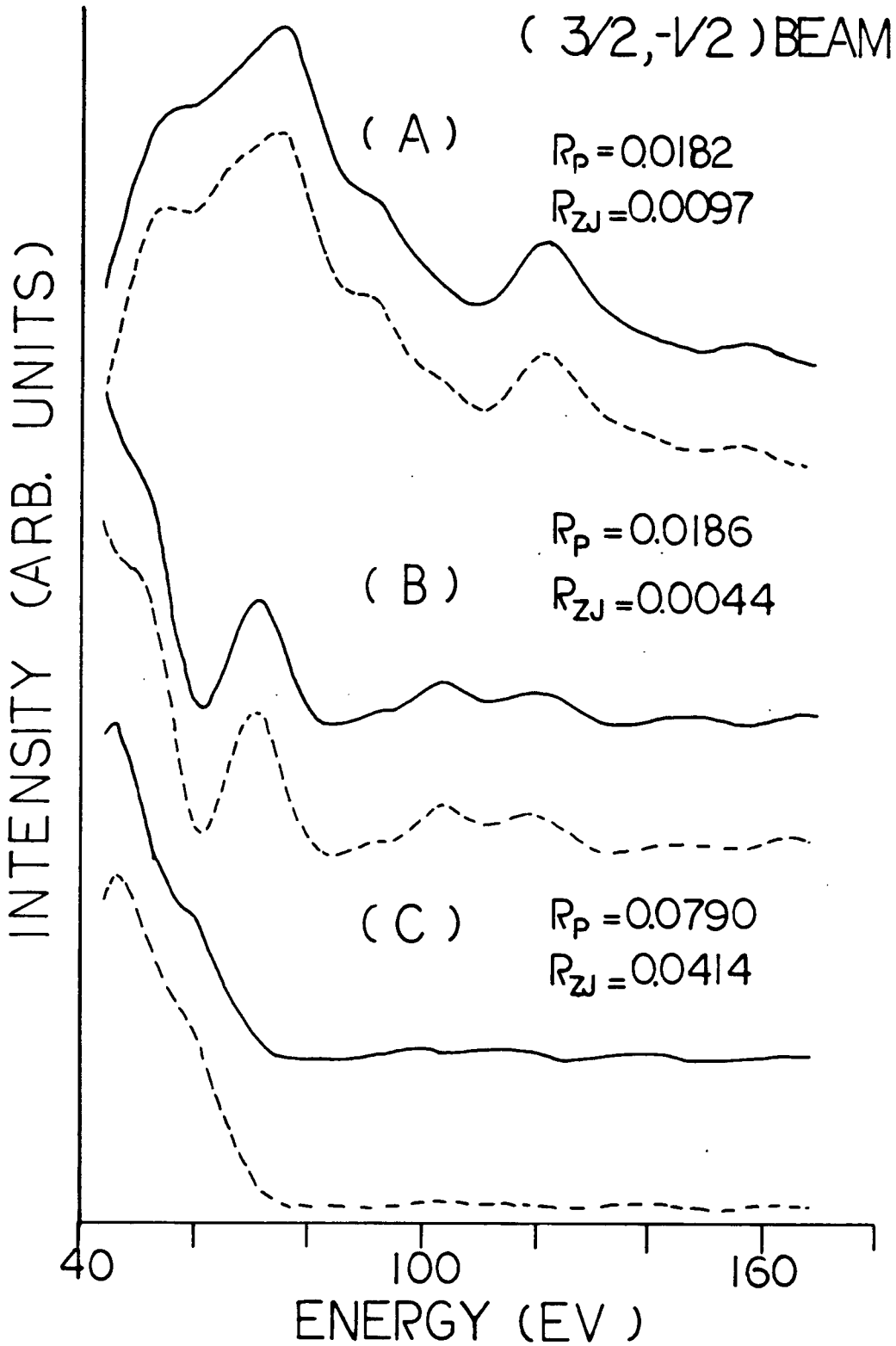

Figure 5.5: Same as Figure 5.3, except for the (3/2,-1/2) beam.

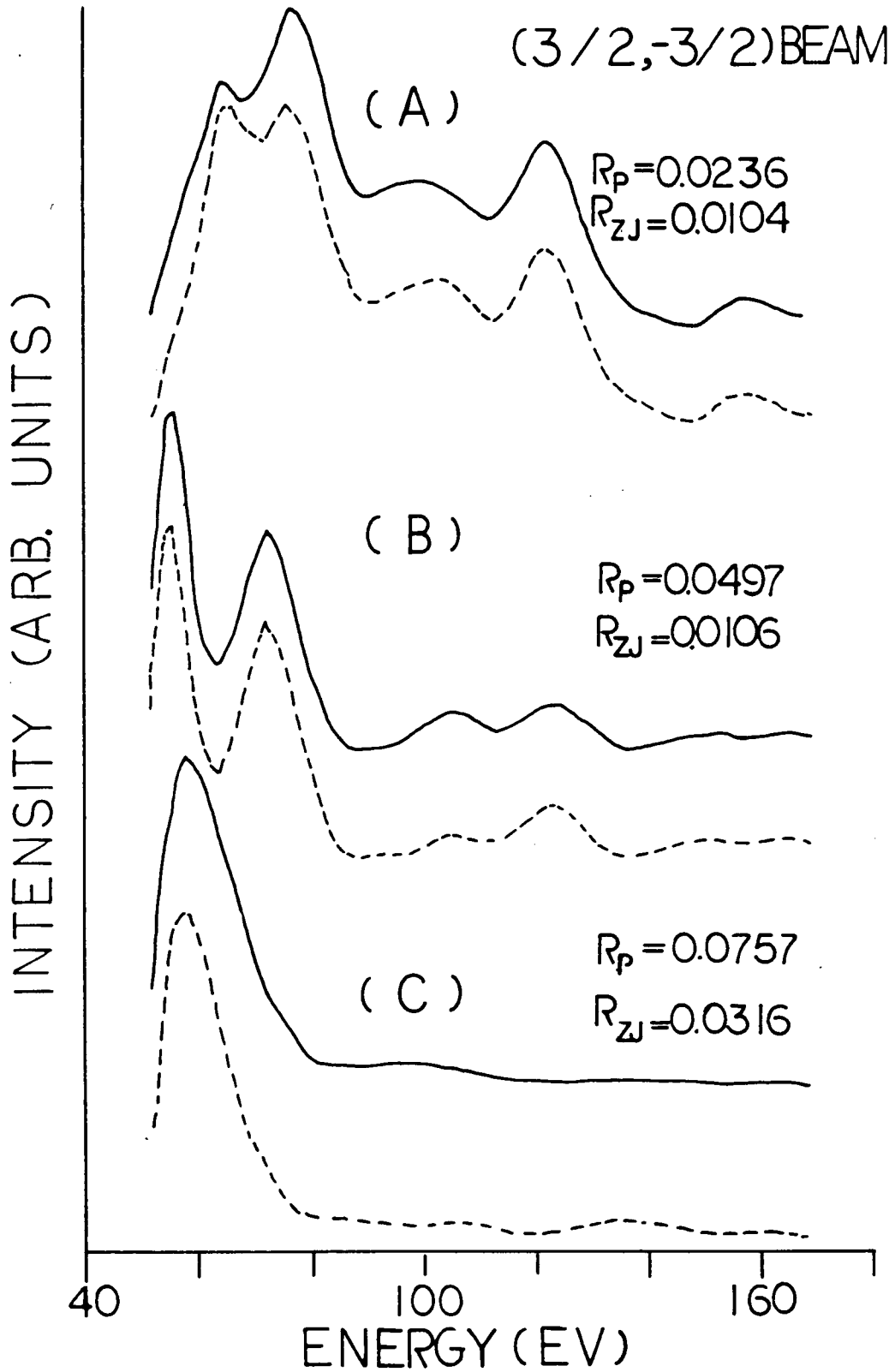

Figure 5.6: Same as Figure 5.3, except for the (3/2,-3/2) beam.

curves are almost visually indistinguishable, which is also indicated so by a very low value of R_{zj}.

Pendry's R-factor (R_p) emphasizes positions of peaks and troughs, and its values tend to be considerably larger than the corresponding values of R_{zj}; apparently R_p can exaggerate the effect of small differences in I(E) curves because unlike R_{zj} it does not put extra weights on prominent peaks. This is most evident from Figure 5.7. Here R_{zj} increases almost 10 times while R_p is only doubled, from a pair of nearly visually indistinguishable curves to a pair of curves showing easily detectable differences in shape. That suggests R_{zj} is more useful for comparing I(E) curves which match comparatively well (e.g. for refinement stages of a LEED analysis) whereas R_p is better for the initial stages of a surface crystallographic study.

This work developed from a LEED crystallographic investigation for oxygen adsorbed at a Zr(0001) surface (Chapter 6). It was found that with normal incidence experimental intensity data for seven (3 integral and 4 fractional order) diffracted beams multiple scattering calculations were unable to distinguish between the (2x1) and (2x2) translational symmetries for a variety of local coordination models, although an early report by Shih *et al.*[40] did suggest that there may be sufficient differences in calculated I(E) curves for the (2x2) and (2x1) models of dissociated CO on Ti(0001) to distinguish between such models. This is interesting since C is not

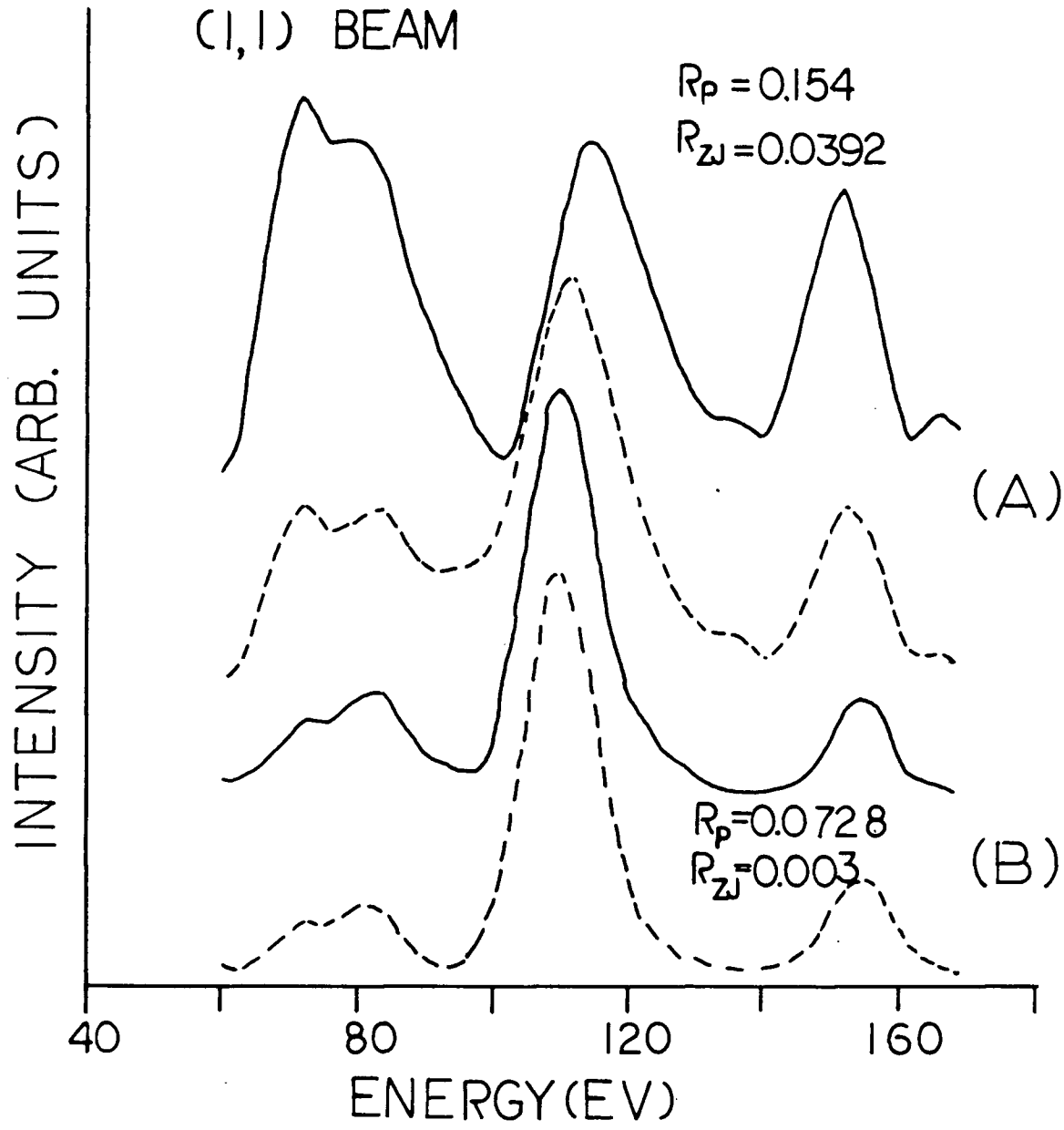

Figure 5.7: Comparison of calculated I(E) curves for the (1,1) beam for the corresponding (2x1) (dotted line) and (2x2) (solid line) structures for adsorption of (A) O and (B) Zr, at the 3h site on the Zr(0001) surface. Single beam R_p and R_{zj} are indicated for each pair of I(E) curves.

likely to be a stronger scatterer than O; however small differences may accumulate with a more extensive set of intensity data. Therefore the observation of Shih *et al.* may have been possible because of the relatively large amount of experimental data that they had available (specifically, 10 beams over 2 directions of incidence). Further study could be useful to assess whether resulting differences in R-factor values (for comparisons between experimental and the corresponding calculated I(E) curves from each coverage) could be large enough to distinguish between the two coverages. It is possible that the similarity of I(E) curves from the (2x1) and (2x2) structures may be most pronounced at normal incidence where the multiple scattering within the overlayers is small; this is because atomic scattering factors for scattering angles close to 90° are generally small. This suggests a strategy for LEED analyses for such systems. First use normal incidence data to determine the local adsorption site for the ad-atom, then use data for shallow angles of incidence to determine the unit mesh of the adlayer.

5.4 APPROXIMATE SCHEMES FOR MULTIPLE SCATTERING CALCULATIONS

The stability of the fractional order beam I(E) curves with different adsorbate coverages implies that (1) intralayer multiple scattering (at least in the adlayer) is weak compared to interlayer scattering, and (2) the unit mesh area of the adlayer can be reduced, but so as to keep

an appreciable number of beams in common with the situation for the original structure. These two aspects have been used in various attempts to simplify multiple scattering calculations for more complex systems.

5.4.1 APPROXIMATIONS IN L-SPACE

At or near normal incidence, intralayer multiple scattering can often be relatively weak because such processes require at least two large-angle (≥90°) scattering events[139], whereas only one such event (back scattering) need occur with interlayer multiple scattering. Thus the effect of intralayer scattering may, to a reasonable approximation, be treated kinematically. The latter treatment yields a diagonal intralayer scattering matrix $\underset{\approx}{X}$ (equation (3.23)), which restricts angular momentum mixing between neighboring atoms to the same (lm) pair (l and m are the angular momentum quantum numbers for characterizing spherical waves). One of the most time-consuming steps in the calculation of the diffraction matrix $\underset{\approx}{M}^{\pm\pm}$ involves the inversion of the matrix $[\underset{\approx}{I}-\underset{\approx}{X}]$ (see equations (3.22) and (3.23)); but the kinematical treatment leads to just the trivial inversion of a diagonal matrix. In the *quasi-dynamical method* (QDM)[140,141], a stronger assumption is made that intralayer multiple scattering can be neglected in all layers. Indeed for moderately weakly scattering crystals, such as Si and Ge, the quasi-dynamical and full dynamical methods give similar intensity curves[147]. For

strongly scattering atoms in more-compact structures, this approximation is less satisfactory[148]. The results of this work suggest that QDM may be more generally applicable if the neglect of intralayer multiple scattering is restricted to the adsorbed layers, regardless of scattering strengths. A higher order approximation of intralayer multiple scattering is considered in the *diagonal dominant method* (DDM), which was proposed by Shih and Tam[142]. In this method, angular momentum mixing between two atoms is allowed only when m=m'; it therefore gives rise to a sparse (but banded) intralayer scattering matrix $\underset{\sim}{X}$. The inversion of the latter is computationally much less demanding than the corresponding full matrix. Shih and Tam have shown that the results from DDM for several ionic crystals agree very well with exact calculations, although the comparison has been limited to normal incidence calculations.

5.4.2 APPROXIMATIONS IN K-SPACE

The similarity between the calculated I(E) curves for the corresponding (2x1) and (2x2) structures immediately shows that the area of the unit mesh of the adsorbed layer can be halved without significantly affecting the results of the calculations. A very useful consequence of this fact is the reduction in the number of beams required in a multiple scattering calculation, because the number of beams required is directly proportional to the unit mesh area in a particular adsorption system (equation (3.40)). In this work

normal incidence is assumed, and therefore the scattering problem for the (2x2) structure can utilize a higher surface symmetry (namely a 3-fold rotation and a mirror plane) which leads to fewer symmetrized beams compared to the (2x1) calculation. In general, however, a smaller unit mesh area is more favorable when off-normal incidence is considered.

The unit mesh size reduction method has been further tested in this laboratory for the system Cu(100)-p(2x2)-S[149]. Preliminary results have indicated that even at off-normal incidence (θ=14°) I(E) curves for fractional order beams from p(1x2), p(2x1) and c(2x2) (for constant local structure) are almost identical to the corresponding I(E) curves from the full p(2x2) calculation.

From a physical standpoint, the unit mesh size reduction method essentially breaks the surface structure into smaller adsorption nets; and the reciprocal lattices of the latter then combine to mimic that of the original surface structure. From a computational standpoint, this procedure is equivalent to ignoring all but two sets of diffracted beams (the concept of beam sets has been discussed in Section 3.5.2) in the multiple scattering calculation for beam intensities.

More broadly, the full beam sets are required to define the long range 2-dimensional periodicity of the adsorbed layer, but they are less important insofar as beam intensities are concerned. The latter have been shown[51,139] (and further supported by this work) to be

determined primarily by short-range order (i.e. local atomic environment). For a commensurate (pxq) superlattice, pq beam sets are formally required for the calculation of its layer diffraction matrix (Section 4.5.2) in an exact multiple scattering calculation, thereby taking into account all the possible scattering paths between pairs of diffracted beams. By restricting the number of non-zero-angle scattering events to just one or two, Van Hove *et al.*[51] noted that an emergent integral order beam is not affected by any fractional order beams; whereas an emergent fractional order beam is affected only by beams which belong to its own beam set or to the integral order beam set. This is the basis for their proposed *beam set neglect* (BSN) method for the calculation of the diffraction matrix $\underset{\approx}{M}^{\pm\pm}$ for the superlattice. In this method, a fractional order beam set is coupled with the integral order beam set to form a mini-diffraction matrix for the adlayer. The subsequent stacking of layers to obtain diffracted beam intensities for this particular set of fractional order beams is the same as the full dynamical treatment. This procedure can be repeated for all the other fractional order beam sets. The p(2x1) calculations in this work thus represent a special case of this generalized scheme; the diffraction matrix for the p(2x1) structure can be taken as one of the mini-diffraction matrices of the p(2x2) structure, but because of symmetry, only one such matrix is required. In general, for a (pxq) superlattice structure, instead of calculating a

superlattice diffraction matrix of dimension pqn (where n is the average number of beams in each beam set), the beam set neglect method simply calculates (pq-1) smaller matrices of dimension 2n. The savings in computing effort is significant, especially in LEED studies involving a very large superlattice, and for off-normal incidence where symmetrization of beam sets is minimal. This method has been applied satisfactorily to a LEED analysis of benzene adsorbed on the Rh(111) surface[51], although more tests are needed to assess its general applicability.

5.5 CONCLUSION

This work has extended an observation of Yang *et al.*[139], and shown that corresponding I(E) curves for surface structures with (2x1) and (2x2) translational symmetries on hcp(0001) surfaces can be remarkably similar. For a (2x1) structure, atoms in the adsorbed layer are separated by just the substrate interatomic distance, but the previous statement is found to hold closely even over a range of scattering strengths. Overall this study adds further support to several approximate schemes for simplifying multiple scattering calculations, at least for the exploratory investigations of systems with long repeat distances. Since the comparisons here are made for curves which are basically rather similar, the Zanazzi-Jona and Pendry R-factor procedures could be compared in ways that

rarely have been tried before (for example, the values of R_{zj} are low compared with the more usual comparisons between experimental and calculated I(E) curves). Finally this work emphasized again[150] that an appreciable number of LEED I(E) curves are still required when the objective is to distinguish between fine differences in a structural analysis (and this includes distinguishing (2x1) and (2x2) structures on hcp(0001) and fcc(111) surfaces).

CHAPTER 6

OXYGEN ADSORPTION ON ZR(0001)

6.1 INTRODUCTION

Zirconium ranks twelfth among the elements in abundance. It has found applications in construction for nuclear reactors because it has a low absorption cross section for neutrons as well as a high resistance to the corrosive environments inside a reactor. The outstanding corrosion resistance of zirconium and its alloys is due to the formation of a protective but very thin film of oxide on the metal surface. In fact the ease of oxide formation makes zirconium a useful getter material for oxygen, which is widely used in the electronics industry. The generally high reactivity of zirconium toward gaseous species also makes it an important constituent of many catalytic alloys[151]. There is a growing interest in the adsorption properties of zirconium due to its technological applications. Several studies of the chemisorption of small gaseous molecules on zirconium surfaces under UHV environments have been reported[69,152-158], but most of these are concerned either with polycrystalline zirconium or with thick films of oxide.

Structural information of adsorbates on metal surfaces represents a fundamental requirement for developing atomistic models both for simple chemisorption and ultimately for surface reactivity with the adsorbing species. Despite the numerous technological applications of zirconium metal and its alloys, no structural data are currently available for adsorption systems that involve surfaces of zirconium. This may be attributed in part to the

difficulties in obtaining a well characterized zirconium surface (Section 1.4). The present LEED crystallographic study aims to reveal the atomic geometry of oxygen adsorption on the (0001) surface of zirconium at relatively low oxygen coverages. Specifically the intensities of LEED beams from Zr(0001)-(2x2)-O and from Zr(0001)-(1x1)-O were measured and analyzed. This study is potentially challenging, not only because of the difficulties of working with zirconium, but also because some uncommon structural results may be expected following studies by Shih *et al.*[41] for nitrogen adsorption on the (0001) surface of another group 4 hcp metal, namely titanium. The latter study suggested that N atoms form an underlayer structure by occupying all octahedral hole sites between the first and second Ti layers. Then the first three layers of the surface region correspond closely to three successive (111) layers of TiN. Since ZrO has the same NaCl type crystal lattice as TiN, it is logical to ask whether oxygen adsorption on Zr(0001) surfaces would yield the same phenomenon of underlayer formation, and this is one of the motivations for the present LEED crystallographic study.

The present work was initiated by observations made by Moore[130] at the end of his Ph.D. thesis, where several I(E) curves were reported from the (2x2) and (1x1) LEED patterns. However, initial calculated I(E) curves obtained in the early stages of this work yielded poor agreement with Moore's measured I(E) curves. I then undertook a re-analysis

of Moore's photographic record of the LEED patterns. That confirmed the original I(E) curves, except for the (3/2,-3/2) beam (see Figure 5.2 for beam notation) for the (2x2) pattern, where the energies were 40 eV higher than the correct values. With the corrected measured I(E) curves, only slightly better agreement with calculated curves was achieved.

Similar LEED patterns to those formed with oxygen adsorption on Zr(0001) have been reported for oxygen on Ti(0001)[159], but no structural results have yet been published. Indeed once my work was at an advanced stage, we learned that Shih and Jona[159,160] had been unable to complete a LEED crystallographic analysis for O on Ti(0001). The latter system has since been studied by a wide variety of surface techniques[161], yet so far there has been no consensus on the question of oxygen overlayer versus underlayer, let alone structural data. From the results reported for oxygen adsorption on titanium and on aluminum[162], it can be concluded that the initial stages of oxidation of electropositive metal surfaces may not be straightforward, but that only makes the present studies more worthwhile.

In this work separate LEED experiments and several AES studies were carried out with an independent zirconium sample to establish that the experimental data are reproducible. The I(E) curves for the (1x1) pattern were also measured with the new TV camera method while this

thesis was being written, and they show a high degree of reproducibility with the previously measured data. The latest version of the multiple scattering calculations computer programs provided by Van Hove[97] in 1983 facilitated model calculations for many complicated surface models, some of which have been found to give better agreement with experimental intensities from the Zr(0001)-(2x2)-O structure.

6.2 EXPERIMENTAL

6.2.1 SAMPLE PREPARATION AND CLEANING

Initial zirconium specimens were cut by spark erosion from 99.97% purity single crystal rods (grown by A. Akhtar, Dept. of Metallurgy, U.B.C.) of $\frac{1}{4}$" diameter. The normal to the cutting plane was oriented to within 1° of the (0001) direction in the crystal. After cutting, the samples were mechanically polished with increasingly finer diamond paste (9-1 μ), and finally with 0.025 μ alumina paste for about 1 minute. The samples were degreased thoroughly with trichloroethylene, and then chemically etched in acid (45% HNO_3, 50% H_2O_2, 5% HF, by volume[163]) for 30-60 seconds. This procedure resulted in a shiny surface without obvious smearing when viewed with a 10X magnifier. The crystal slice was mounted on a Varian resistive heater and a chromel-alumel thermocouple was spot-welded to the sample edge.

Figure 2.12(a) shows an Auger spectrum measured with the cylindrical mirror analyzer (16 kHz modulation frequency) from a Zr(0001) surface on entering the FC12 chamber. Large quantities of C and O were indicated by the Auger peaks at 272 eV (C_{272}) and 510 eV (O_{510}) respectively. The Mo peaks came from the sample holder cup, which is sometimes struck by a small part of the electron beam from the glancing incidence gun. Argon ion bombardment (0.8-1.2 keV, 4-5 μA) was then carried out at room temperature until impurities other than C were reduced to below the detectable amounts. At this stage, the sample was annealed at about 600°C for 30 minutes to drive most of the bulk carbon and also sulfur to the surface. This was followed by several cycles of Ar^+ bombardment (with decreasing primary energies to minimize damage to the surface) and annealing until both C and S were at their minimum coverages. Sulfur cannot be detected directly by AES with the present resolution because the sulfur Auger peak at 150 eV (or S_{150}) overlaps with the zirconium Auger peak at 147 eV (Zr_{147}). However the presence of sulfur can be detected indirectly by monitoring the peak ratio of Zr_{147}/Zr_{92}. The use of the Zr_{92} peak as a reference was prompted by my observation that it was unattenuated when the Zr(0001) surface was exposed to large doses of H_2S. After a total of about 50 hours of Ar^+ bombardment, the peak ratio Zr_{147}/Zr_{92} reached a limiting value of approximately 1.35, which compared well with published data for a cleaned zirconium surface[164]. Carbon contamination could not be

removed to undetectable levels, and the minimum C_{272}/Zr_{174} peak ratio obtained was about 0.1, which is believed to correspond to carbon coverage of less than 3% monolayer (discussed further in Section 6.5).

6.2.2 MEASUREMENTS OF I(E) CURVES

Exposure of a clean Zr(0001) surface to research grade oxygen (Matheson 99.99% purity) at a pressure of approximately $5x10^{-9}$ torr at temperatures below 100°C gave rise first to the formation of a faint (2x2) LEED pattern with diffuse diffraction spots, after an exposure of about 1 Langmuir (1 L = 10^{-6} torr s). However the spots became brighter and sharper when the sample was annealed at about 250°C for 2-3 minutes. Annealing at temperatures above 400°C for a few minutes resulted in a depletion of oxygen, which is presumably due to diffusion of oxygen into the bulk as has been observed in adsorption studies on polycrystalline zirconium[157]. With increasing oxygen exposure, the (2x2) pattern became fainter and eventually a (1x1) pattern appeared, whose diffracted beam I(E) curves were different from those of the clean surface. For even greater oxygen exposures, the LEED pattern remained (1x1) but became diffuse with an increasing background. The latter stage possibly signaled multi-layer adsorption, as has been proposed for reactive adsorbates on surfaces of electropositive transition metals such as titanium and zirconium[165].

The sharpest (2x2) LEED pattern was obtained after the sample was annealed at 250°C for 5 minutes, and then cooled to room temperature. The Auger peak ratio O_{510}/Zr_{174} was then about 0.9, and this corresponds to 0.37 monolayer O coverage, according to a calibration method with CO (Section 6.5). For the sharp (1x1) pattern, after the sample was annealed at 250°C for about 3 minutes, the ratio O_{510}/Zr_{174} was 2.0, which corresponds to 0.8 monolayer oxygen coverage.

Diffracted beam intensities for both oxygen structures were measured at normal incidence by the photographic method at 2 eV intervals. Before the introduction of the TV camera method to this laboratory, normal incidence was established by adjusting the sample manipulator micrometers until, by visual inspection, the appearance and disappearance of the supposedly symmetrically equivalent beams were synchronized as the incident energies were varied. Figure 6.1 shows the I(E) curves of the six 'equivalent' (1,0) beams, as well as the average of these curves for Zr(0001)-(2x2)-O, at normal incidence adjusted by the above visual method. With experience, this method works reasonably well, and an assessment is made in Figure 6.1 by reporting values of R_p and R_{zj} for the individual beams in comparison with the averaged beam. In the later stages of this work, the normal incidence adjustment could be made more objective with the use of the video LEED analyzer; I(E) curves of equivalent beams were then compared on-line to assess the accuracy of normal incidence. With the photographic method, I

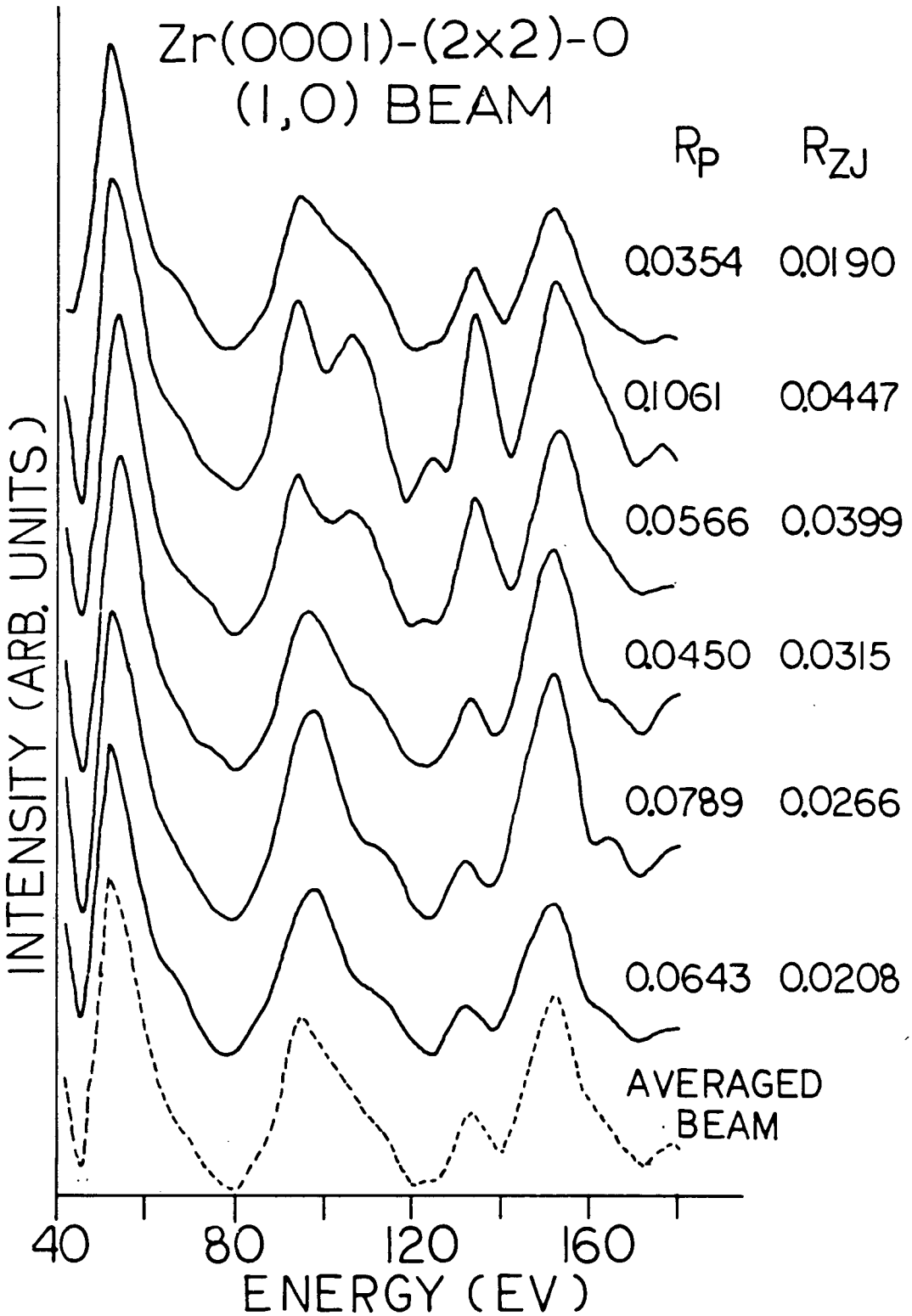

Figure 6.1: Comparison of experimental I(E) curves of six 'equivalent' (1,0) beams (solid lines) obtained at normal incidence for Zr(0001)-(2x2)-O with the averaged curve (dotted line). Single-beam R_p and R_{zj} are also given for such comparisons.

re-measured I(E) curves for seven diffracted beams designated (1,0), (1,1), (2,0), (1/2,-1/2), (1/2,1/2), (3/2,-1/2) and (3/2,-3/2) for the (2x2) structure, and for the two diffracted beams designated (1,0) and (1,1) for the normal incidence (1x1) structure (beam notation follows that of Figure 5.2). Measured I(E) curves from different beams which are expected to be equivalent from symmetry and for equal populations of the possible rotationally related domains (Figure 5.1) were averaged to take up minor deficiencies in alignment[54], but all essential structure was apparent in the individual beams. My data agreed closely with those of Moore; the high reliability of the experimental data is suggested by the representative comparison in Figure 6.2 for I(E) curves of the (3/2,-1/2) beam measured in this work and by Moore for the Zr(0001)-(2x2)-O diffraction pattern.

During the writing of this thesis, I(E) curves for the two diffracted beams of the (1x1) pattern were again measured in a collaborative project on a different zirconium single crystal†. I prepared the new Zr(0001) surface, and P. Wong completed the LEED measurements with the VLA; the resulting intensity data compare well with previous measurements. Figure 6.3 shows I(E) curves for the (1,1) beam measured by the two methods. The positions of major peaks and valleys compare rather favorably, which is

---

† The single crystal was kindly provided by P.R. Norton, AECL, Chalk River Nuclear Laboratories.

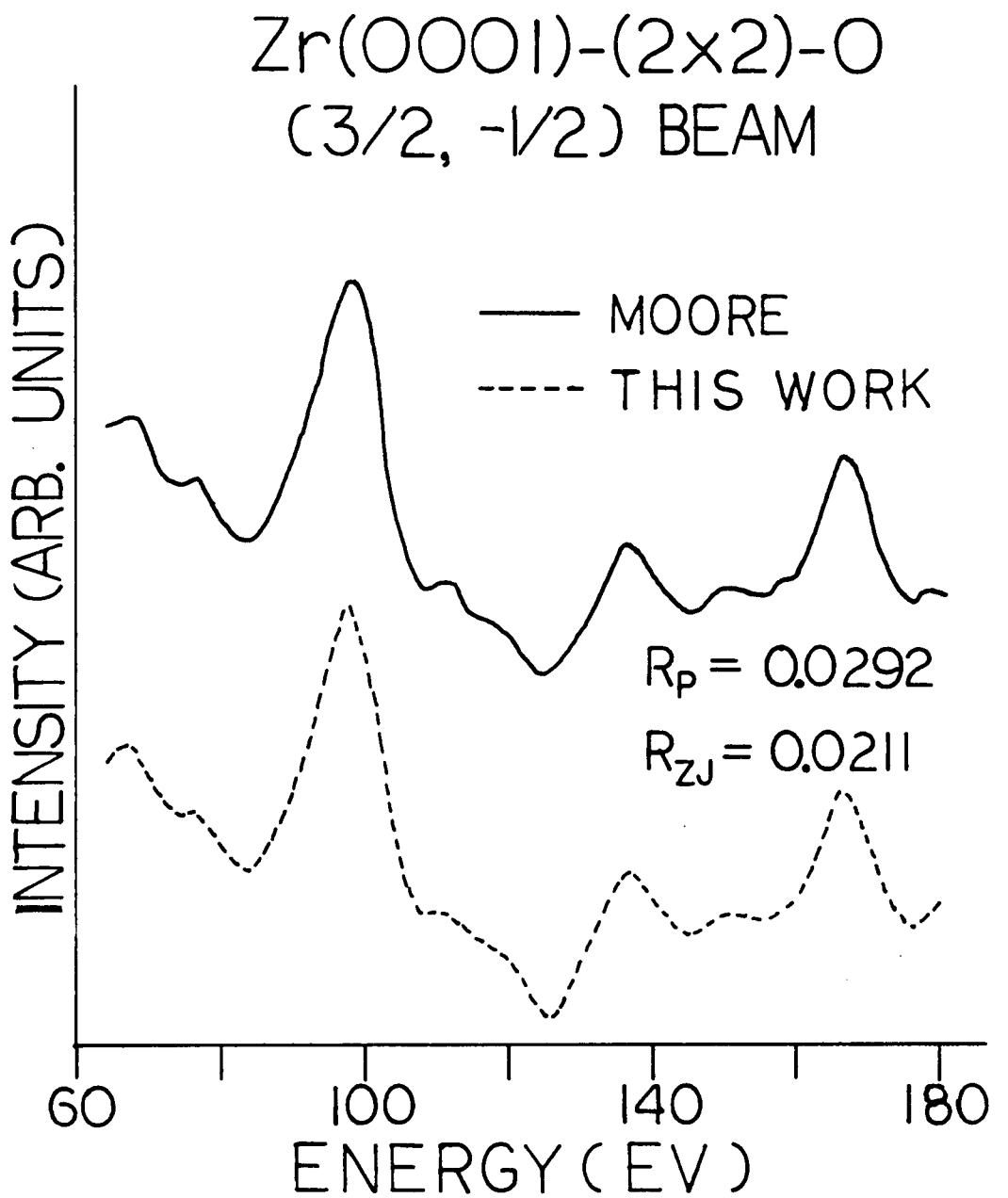

Figure 6.2: Comparison of experimental I(E) curves measured by Moore[130] (solid line) and by this work (dotted line) for the (3/2,-1/2) beam for Zr(0001)-(2x2)-O at normal incidence.

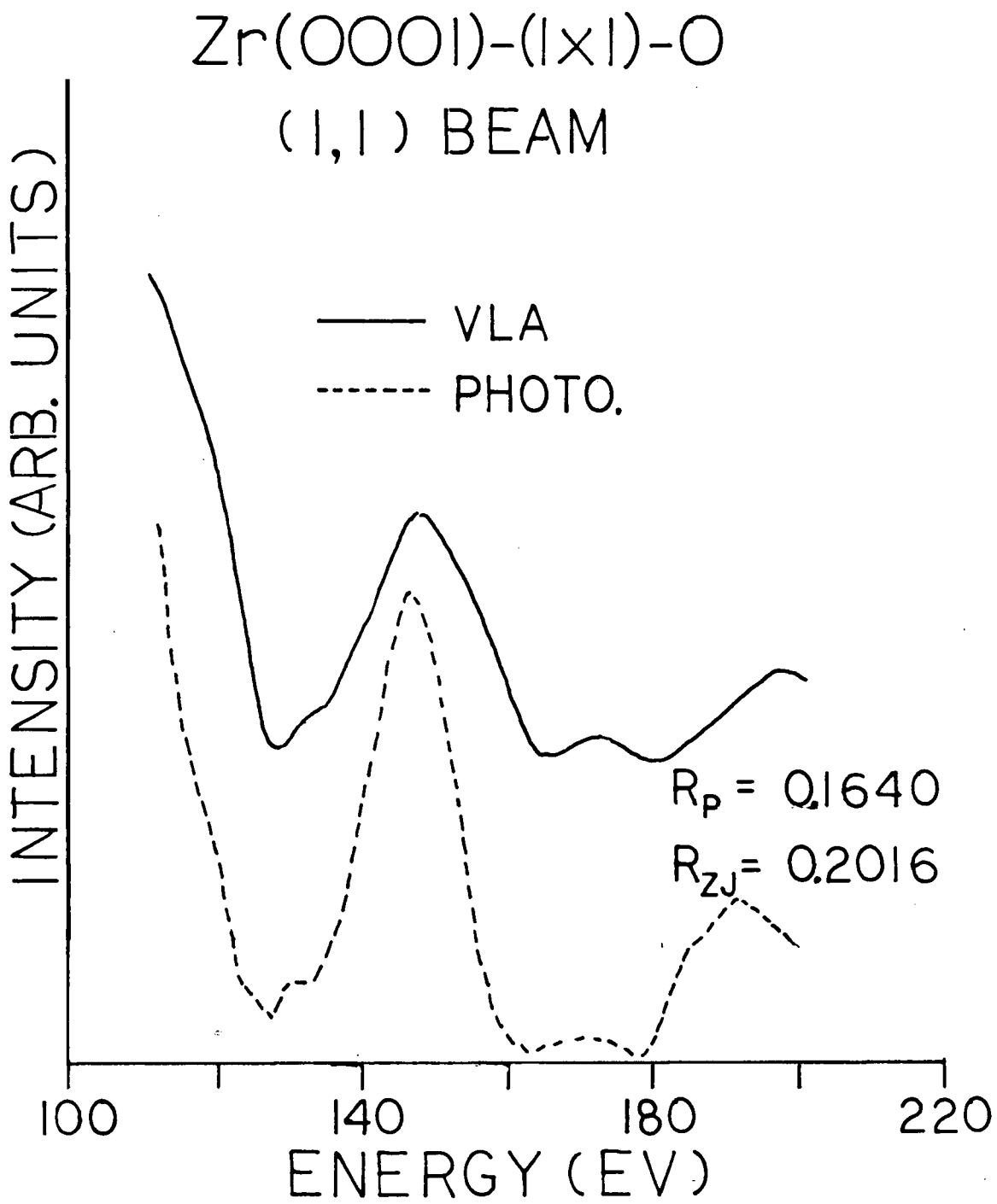

Figure 6.3: Comparison of experimental I(E) curves measured with the VLA (solid line) and with the photographic method (dotted line) for the (1,1) beam for Zr(0001)-(1x1)-O at normal incidence.

supported by a reasonably low value of R_p. The slightly higher value of R_{zj} is a result of differences in peak shape; I(E) curves measured by the VLA tend to yield broader peaks and valleys. This may be a consequence of the rather simple background subtraction scheme employed in the VLA method; specifically the intensity of the areas between neighboring spots were used for background estimation.

6.3 STRUCTURE ANALYSIS OF ZR(0001)-(2X2)-O

6.3.1 MULTIPLE SCATTERING CALCULATIONS

I(E) curves for an extensive set of adsorption models were obtained using the 'combined space' approach to multiple scattering calculations. The specific methods used for different categories of surface models are discussed below. The following details the non-structural parameters which were kept constant for all surface models considered. The potential was expressed in the usual 'muffin-tin' form. The real part of the constant potential (V_{o_r}) between the atomic spheres was set initially at -10.0 eV, and the imaginary potential (V_{o_i}) was fixed at -5.0 eV. For atomic potentials, zirconium was characterized by phase shifts (δ_l, up to l=7) derived from a band structure potential[96], and for oxygen the superposition potential obtained by Demuth *et al.*[98] was used. The Debye temperature (θ_D) used for zirconium was 270K (an average value from the compilation by Schneider[166]), and for oxygen 843K (a value suggested by

other LEED analyses involving oxygen adsorption on metal surfaces[56,97]). The experimental temperature was estimated at 300K.

The dramatic increase in sticking probability for oxygen molecules on polycrystalline zirconium surfaces from room temperature to temperatures even below 100°C observed by Hoflund *et al.*[152], and the appreciable charge transfer from zirconium to adsorbed oxygen reported by Tapping[156] are indicative of dissociative chemisorption[167]. The LEED patterns observed in this work are believed to involve atomic adsorption, and no molecular models were tested in the multiple scattering calculations. Figure 6.4 shows several possible adsorption sites for oxygen atoms on top of or underneath the topmost layer of a Zr(0001) surface conforming to the hcp structure or the reconstructed fcc structure. The surface models considered in the calculations included oxygen overlayer (Zr-O interlayer spacing from 1.4 to 0.0 Å), single oxygen tetrahedral underlayer (both a_t and b_t in Figure 6.4, with the shorter Zr-O interlayer distance being varied from 0.7 to 0.4 Å), as well as single, double and infinite (i.e. bulk) oxygen octahedral underlayers.

Due to the large number of adsorption models tested, they cannot be described adequately by simple designations such as those used in Chapter 5. A generalized nomenclature for surface models included in this work is explained as follows. The symbols A, B, C (with reference to Figure 6.4) identify close-packed zirconium layers which are laterally

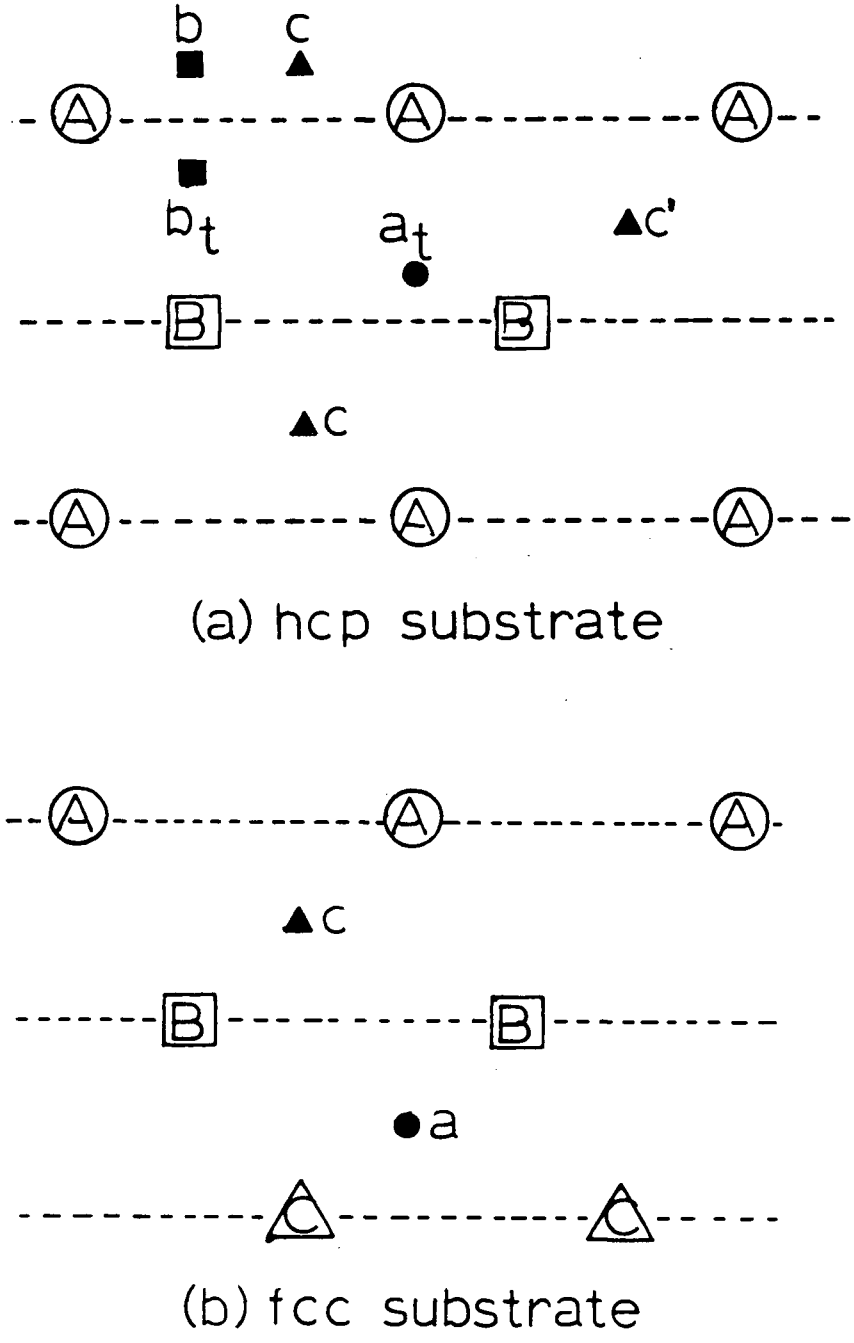

Figure 6.4: Side view of the Zr(0001) surface with (a) hcp and (b) reconstructed fcc stacking sequences to show some possible oxygen adsorption sites. Upper and lower case letters represent the registries of Zr and O layers respectively. Except for b_t and a_t, all underlayer O atoms occupy octahedral holes.

displaced so that the hcp and fcc structures follow respectively the familiar stacking sequences ABABAB.. and ABCABC... Lower case symbols in parentheses have analogous meaning for oxygen, except that the calculations are made for O layers which have (2x2) or (2x1) translational symmetry with respect to the zirconium substrate; (c), (c') indicate two such layers which are displaced laterally from one another by the vector sum of the substrate unit translational vectors parallel to Zr(0001). A sequence of layers from vacuum to the bulk is specified by listing the appropriate symbols from left to right. The bulk layer periodicity is indicated by the number of dots trailing the list: if there are n such dots, the last n symbols are to be repeated infinitely to represent the bulk.

Using this system of nomenclature, the surface models (3h, 3f and 6u) of Chapter 5 are described as (b)AB.., (c)AB.. and A(c)BA.. respectively, and the surface model which involves oxygen underlayers occupying octahedral holes in the bulk of a fcc lattice is written as A(c)B(a)C(b)..... and so on. Unless otherwise stated, the neighboring Zr-Zr interlayer spacing is held at the value for zirconium metal (2.57 Å). An oxygen underlayer occupying octahedral holes of the lattice is assumed to be midway between two successive Zr layers. For a tetrahedral-hole oxygen underlayer, there are two different Zr-O interlayer spacings; the shorter one was varied from 0.4 to 0.6 Å, while the longer one takes a value which gives the metallic

Zr-Zr spacing when combined with the shorter one.

The close similarity of corresponding I(E) curves for the (2x2) and (2x1) models (with constant local environment for the oxygen atoms as discussed in Chapter 5) was exploited in the multiple scattering calculations. In each case, the translational symmetry which leads to the more economical calculations was used. The general guidelines for choosing between the (2x2) and (2x1) models are as follows.

1. For composite layer calculations which involve both Zr and O in the same composite layer, the oxygen adlayers are assigned a (2x1) translational symmetry. Such a choice limits the number of subplanes in the composite layer to two (compared to five if a (2x2) translational symmetry is assumed for oxygen).
2. For calculations which involve only Bravais lattice layers, the (2x2) translational symmetry is assumed for oxygen whenever the resulting surface model preserves the 3-fold rotational axis and mirror plane symmetry of the clean surface at normal incidence; otherwise the calculations assume the (2x1) translational symmetry for oxygen, where the highest possible symmetry for the surface region is just a mirror plane.

Therefore, calculations for surface models with two or more layers of oxygen were done with the (2x1) model except when the successive oxygen layers possess the same registry (e.g. in A(c)B(c)....). The input beams for the (2x1) and (2x2) calculations followed the beam labels of domain (B) for

Figure 5.2(a) and Figure 5.2(b) respectively.

The stacking of layers was performed by the renormalized forward scattering method for Zr-O interlayer spacings (d_{Zr-O}) greater than 1.15 Å, and by the layer doubling method for d_{Zr-O} less than 1.10 Å. Calculated I(E) curves of beams which are related by a 180° rotation about the normal were averaged with equal weightings to take into account the effects of domains due to the two terminations of the bulk (Figure 5.1).

6.3.2 RESULTS AND DISCUSSIONS

Figure 6.5 compares the experimental I(E) curve of the (1/2,1/2) beam with the corresponding I(E) curves from representative model calculations. The latter are arranged according to the extent of oxygen incorporation into the bulk. The overall agreement between calculated and experimental I(E) curves is not very good; this is especially true for the overlayer models. More structure in calculated I(E) curves is observed for models which involve underlayer oxygen, and these structures become more pronounced as the number of oxygen underlayers is increased; this is presumably due to more multiple scattering of the LEED electrons by oxygen atoms. These statements are generally true for the other beams.

Comparisons of the complete set of experimental I(E) curves (four fractional and three integral order) with the corresponding set from each surface model calculation were

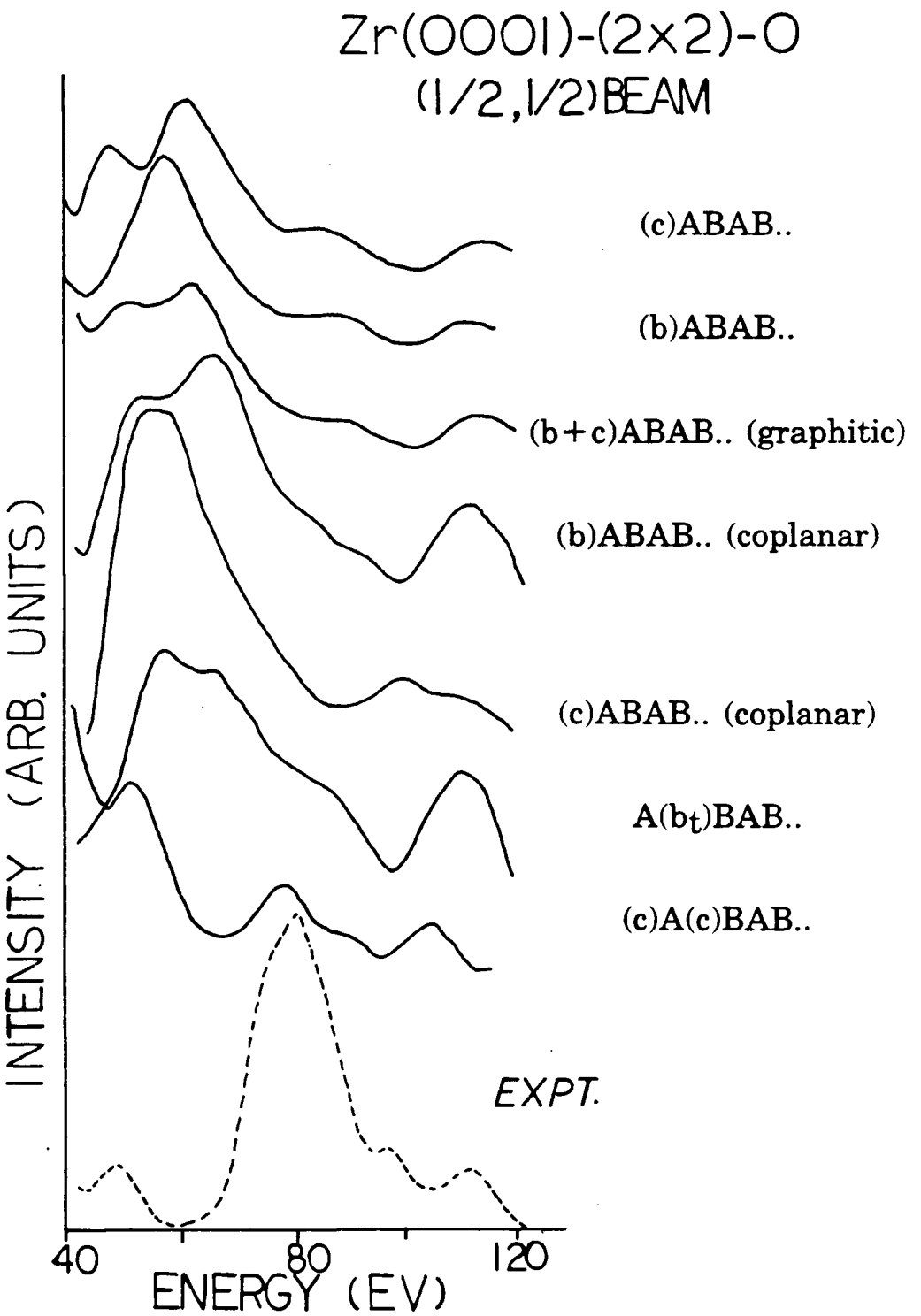

Figure 6.5: Comparison of the experimental I(E) curve of the (1/2,1/2) beam with the 'best' curves from selected model calculations for Zr(0001)-(2x2)-O at normal incidence.

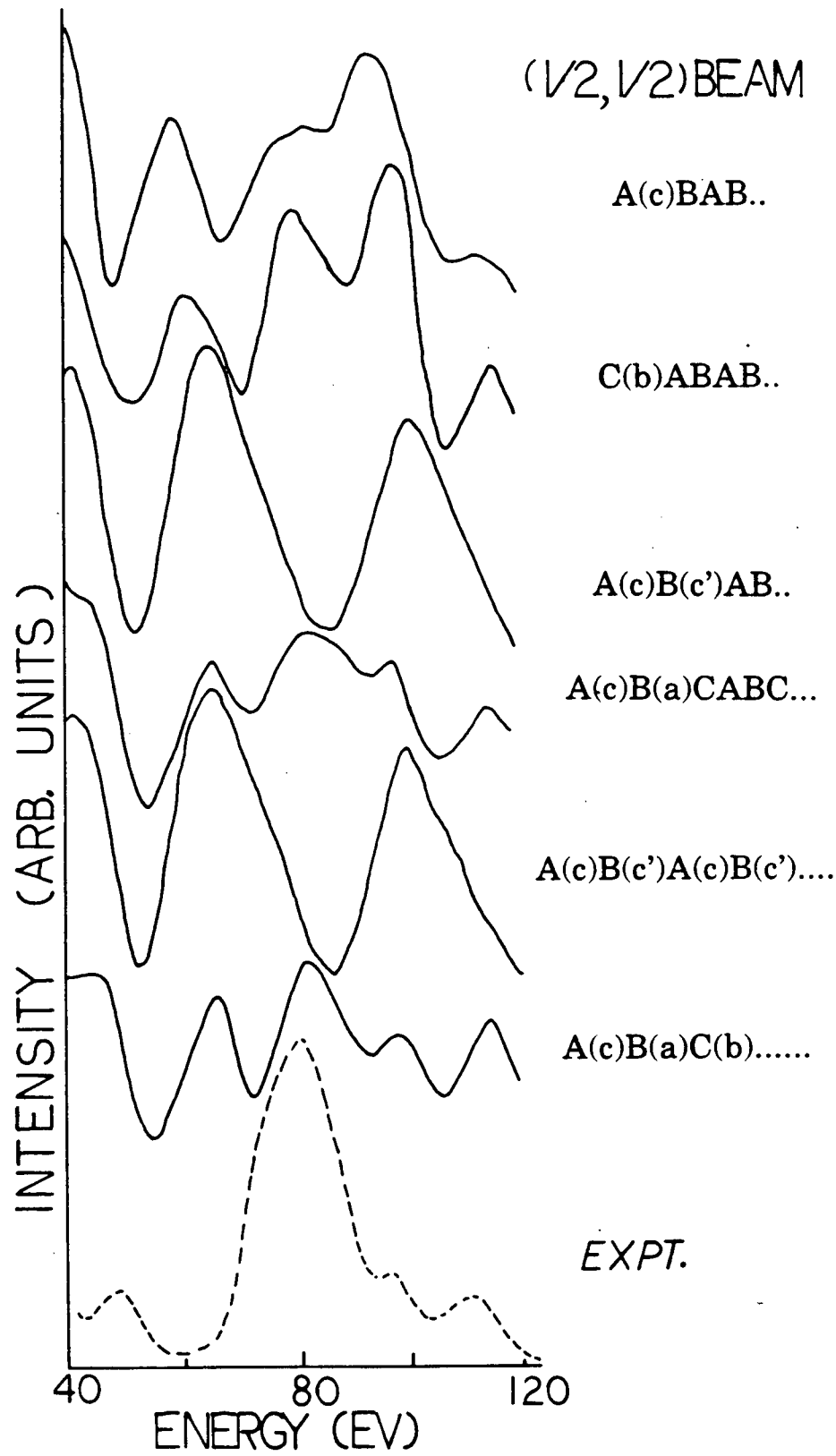

Figure 6.5: (continued)

performed using the reliability index (R_p) proposed by Pendry[145] multiplied with a normalization constant of 1/2 proposed by Van Hove and Koestner[146]. For a particular surface model, several sets of I(E) curves corresponding to different Zr-O interlayer spacings (d_{Zr-O}) were calculated. Each set of these I(E) curves was compared with corresponding curves from experiment, with rigid shifts of the calculated curves with energy (in steps of 2 eV) for fine-tuning the value of the real part of the constant potential V_{o_r} between the atomic spheres. To obtain the minimum value of R_p for a particular surface model, the values of R_p at various d_{Zr-O} and V_{o_r} combinations were interpolated and plotted as contour lines; these lines therefore represent discrete values of R_p as a function of both d_{Zr-O} and V_{o_r}. Figures 6.6-6.8 show such contour plots for surface models which involve one, two and bulk underlayers. Table 6.1 reports minimum values of R_p obtained from contour plots, and the corresponding d_{Zr-O} and V_{o_r}, for a series of model calculations in which the incident energy is varied from 40 to 180 eV. Surface models for very short d_{Zr-O} (including O atoms coplanar with Zr) and the tetrahedral underlayer models were tested for a restricted energy range, and the calculated I(E) curves appear very unfavorable, hence these models are not included in the R-factor analysis presented in Table 6.1.

The models investigated in Table 6.1 can be categorized as: (i) O overlayer, (ii) single O underlayer, (iii) double

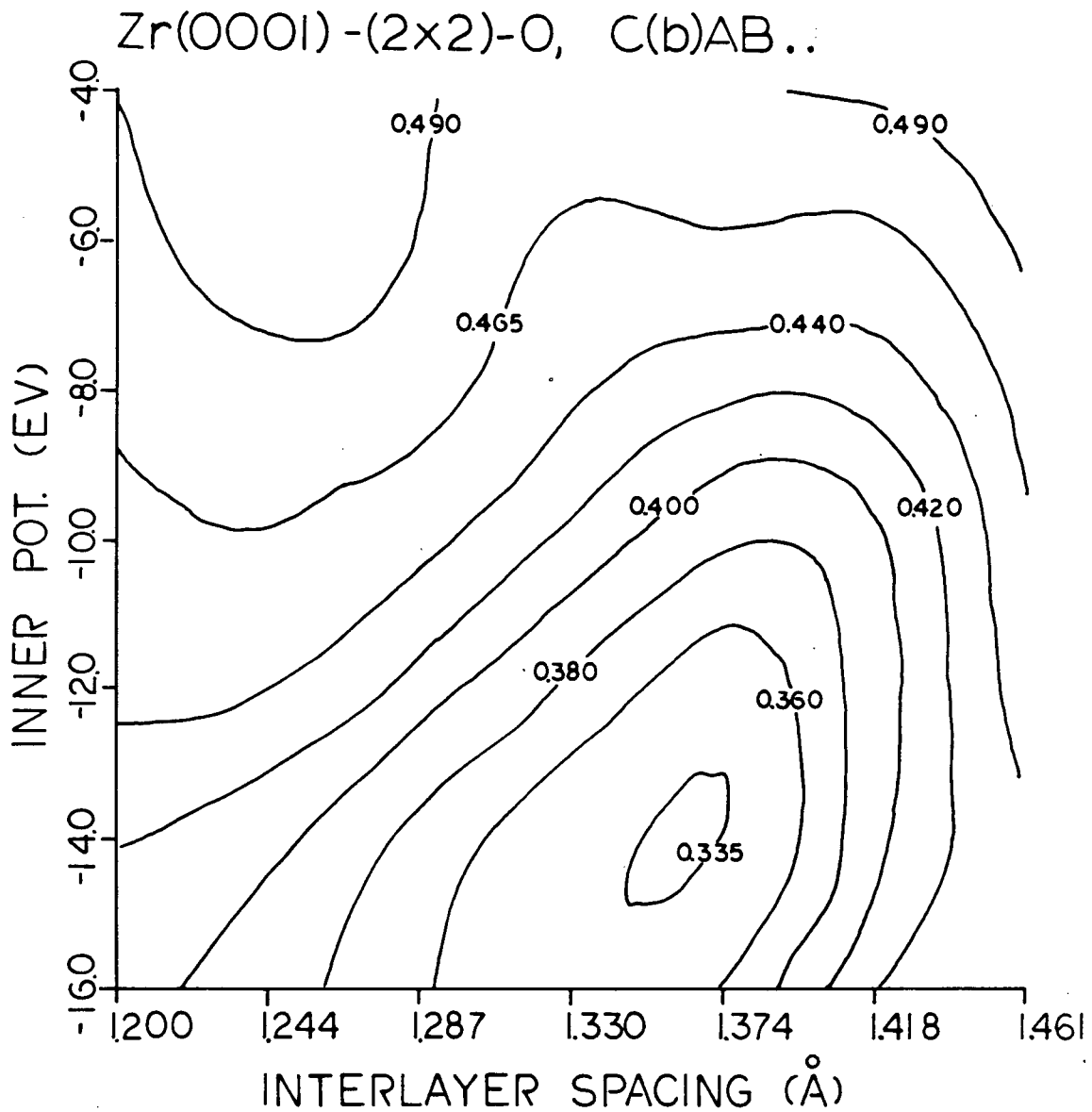

Figure 6.6: Contour plot of multi-beam R_p for Zr(0001)-(2x2)-O versus V_{o_r} and Zr-O interlayer spacing for the adsorption model designated C(b)AB.. at normal incidence.

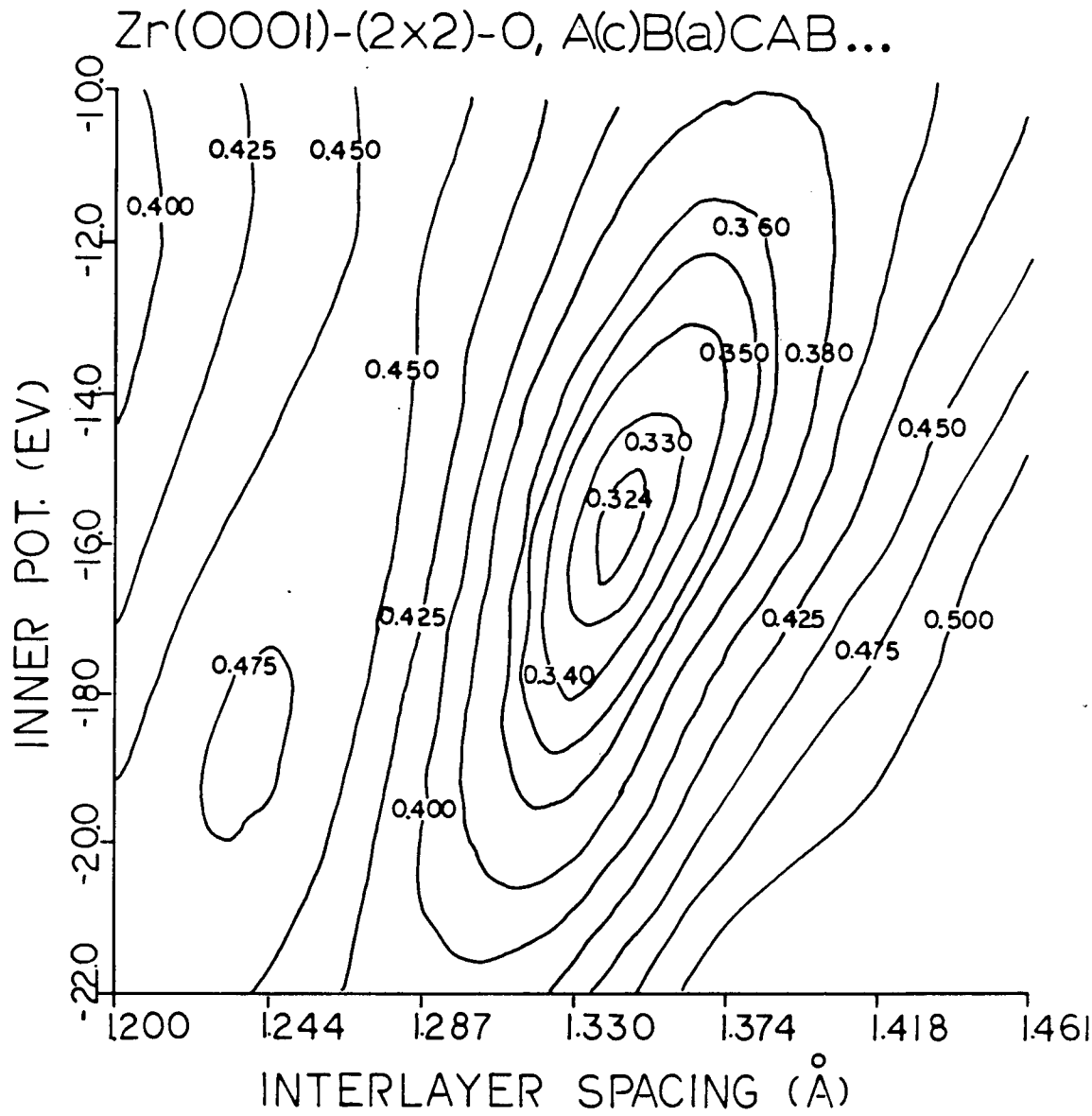

Figure 6.7: Contour plot of multi-beam R_p for Zr(0001)-(2x2)-O versus V_{o_r} and Zr-O interlayer spacing for the adsorption model designated A(c)B(a)CAB... at normal incidence.

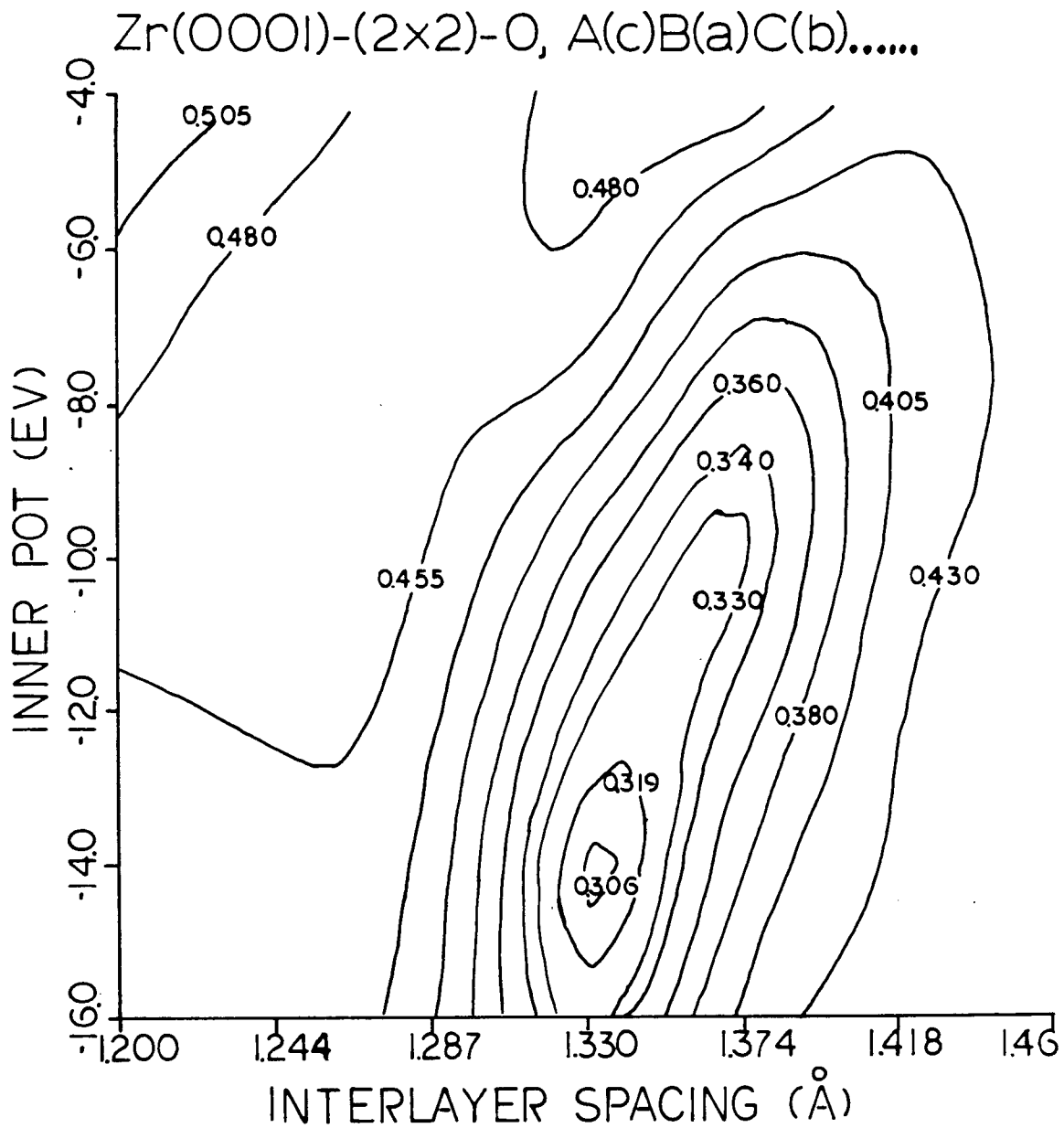

Figure 6.8: Contour plot of multi-beam R_p for Zr(0001)-(2x2)-O versus V_{o_r} and Zr-O interlayer spacing for the adsorption model designated A(c)B(a)C(b)..... at normal incidence.

Surface	R_p	d_{Zr-O}(Å)	V_{or}(eV)
(b)AB..(hcp)	0.410	0.99	-16.0
(c)AB..(hcp)	0.380	1.03	-13.9
(b+c)AB..(hcp)	0.365	1.10	-9.5
(c)A(c)BA..(hcp)	0.373	1.25	-18.6
A(c)BA..(hcp)	0.360	1.35	-14.5
C(b)AB..(hcp)	0.332	1.36	-14.0
A(b)CAB..(hcp)	0.360	1.26	-13.4
A(c)BCA...(fcc)	0.363	1.36	-14.2
A(c)B(c)AB..(hcp)	0.350	1.37	-14.5
A(c)B(c')AB..(hcp)	0.352	1.28	-14.8
C(b)A(b')CAB..(hcp)	0.350	1.27	-16.0
B(c)A(b)CAB..(hcp)	0.337	1.33	-13.6
C(a)B(c)AB..(hcp)	0.332	1.34	-12.4
A(c)B(a)CAB...(fcc)	0.324	1.34	-16.0
A(c)B(c)....(hcp)	0.350	1.35	-10.4
A(c)B(c')....(hcp)	0.328	1.29	-14.0
A(c)B(a)C(b).....(fcc)	0.306	1.33	-14.0

Table 6.1: Minimum values of multi-beam R_p with the corresponding Zr-O interlayer spacings (d_{Zr-O}) and V_{or} obtained from the comparisons of experimental and calculated I(E) curves based on oxygen adsorption models listed in the first column for Zr(0001)-(2x2)-O at normal incidence.

O underlayer, and (iv) bulk O structures. In principle O adsorption in octahedral holes may occur within the unreconstructed hcp structure for zirconium (i.e. ABAB.. stacking sequence), within a reconstructed hcp structure (i.e. ACABAB..), or within structures which include varying degrees of fcc reconstruction (e.g. from top layer reconstruction CABAB.. through to the complete fcc structure). The examples in Table 6.1 give some possibilities for each category, and three interesting trends appear: (a) overlayer models yield very high values of minimum R_p; the smallest value is 0.365, which is greater than the largest values in the other groups; (b) the average values of minimum R_p decrease with increasing numbers of O underlayers, the values being 0.354 for category (ii), 0.340 for category (iii) and 0.328 for (iv); (c) within categories (ii)-(iv) the lowest value of R_p occurs for the simplest fcc type reconstruction which spans the depth of O atoms, that is C(b)AB.. for category (ii), A(c)B(a)CAB... for (iii) and A(c)B(a)C(b)..... for (iv). The high values of R_p for all the overlayer models support the view that chemisorption occurs via some form of O underlayers; this is consistent with a conclusion for oxygen adsorption on polycrystalline titanium[161].

The lowest value of R_p found so far for the Zr(0001)-(2x2)-O surface structure is 0.306 for the model in which O atoms occupy octahedral holes within the fcc reconstructed form of zirconium. Figure 6.9 compares the set

of I(E) curves calculated from the surface model A(c)B(a)C(b)..... (with the optimum d_{Zr-O} and V_{o_r}) with the corresponding curves from experiment. The calculation assumes a bulk-like structure, although in practice LEED provides information on just a restricted number of Zr layers (e.g. 3-5); in any event, from the initial exposure given, substantial O incorporation seems unlikely to extend significantly deeper than the depth probed by LEED. Although Figure 6.9 reports the best correspondence found to date between experiment and calculation for the Zr(0001)-(2x2)-O structure, the match-up is still less than ideal. Nevertheless the favored model does have some reasonable features. For example, the reported value of d_{Zr-O} equal to 1.33 Å seems quite plausible, since it suggests that the interstitial O atoms expand the Zr-Zr interlayer spacing by just 3.5% from that in zirconium metal. Further, the resulting LEED-determined Zr-O bond distance of 2.29 Å agrees closely with the value 2.31 Å given by X-ray diffraction for bulk ZrO[168]. Incidentally the latter compound has the sodium chloride lattice structure, and therefore (i) O atoms in ZrO have the same local coordination as indicated by LEED for the interstitial Zr(0001)-(2x2)-O surface structure; and (ii) the Zr atoms in ZrO form the fcc arrangement.

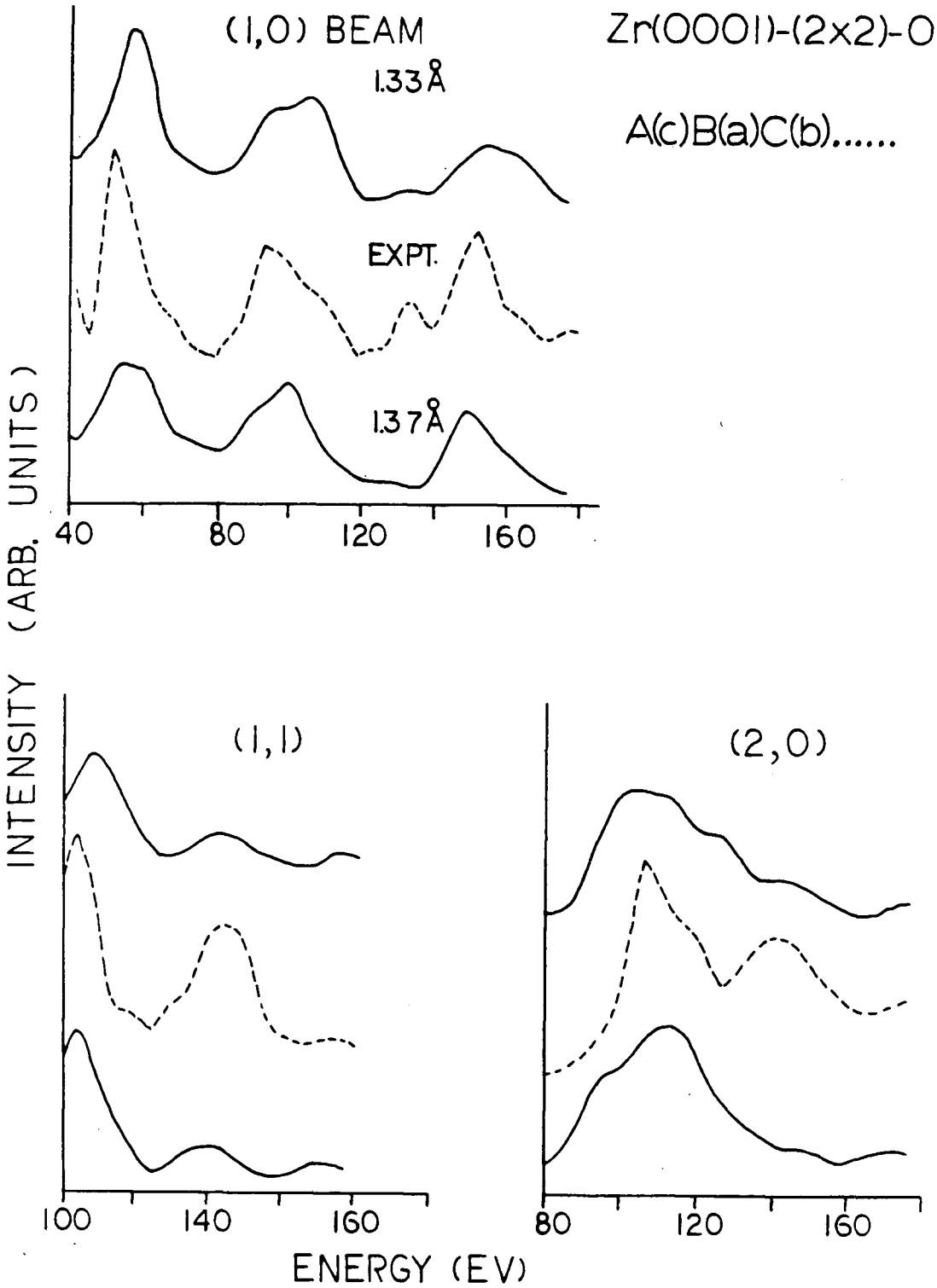

Figure 6.9: Comparison of experimental I(E) curves (dotted lines) for three integral and four fractional order beams from Zr(0001)-(2x2)-O with the corresponding I(E) curves calculated for the adsorption model A(c)B(a)C(b)..... at normal incidence with d_{Zr-O} at either 1.33 or 1.37 Å.

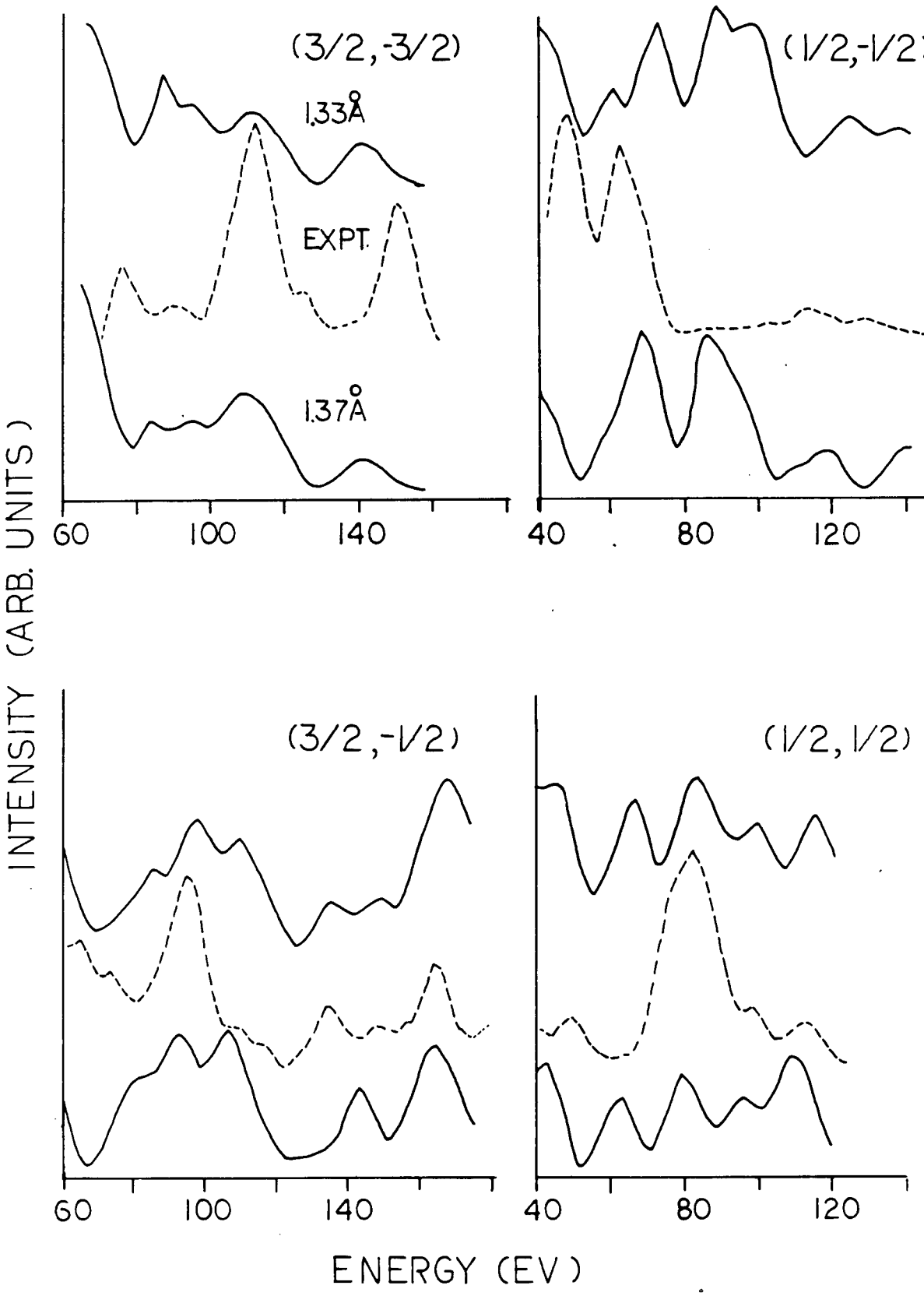

Figure 6.9: (continued)

6.3.3 STRUCTURAL REFINEMENT

Although the LEED analysis reported here apparently has some consistency with other structural information, the discrepancies in LEED intensities (particularly for the (1/2,-1/2) beam where so far no adsorption models tested yield a satisfactory match-up with the experimental curve) still make this a challenging surface structure. Some ingredients required for structural refinement are discussed in the following. The trend of better correspondence with increasing number of oxygen layers opens the possibility that the original atomic scattering factor used for oxygen may not be adequate, and that this deficiency is artificially compensated for by the presence of more oxygen layers in the model calculations. Since the LEED analysis indicates a bulk-like oxide structure, that may suggest it would be more appropriate to use an atomic potential for negatively charged O, derived from self-consistent crystal lattice or cluster structure. A preliminary investigation of this was undertaken in the analysis of the Zr(0001)-(1x1)-O structure (Section 6.4.2). Even if the surface structure used for Figure 6.9 is basically correct, some warping of Zr layers would be likely in the presence of (2x2) O layers. That would introduce both an extra parameter, and a complication in the multiple scattering calculations. Nevertheless it is a refinement that should be considered in future work. With incorporation of O into the bulk it seems inevitable that there would be some degree of random

occupation of O in the octahedral holes. A final refinement is to consider the possibility of variation of structure in different surface domains, perhaps with different levels of fcc reconstruction.

Although the first two ingredients for refinement listed above (i.e. negatively charged O and Zr layer warping) can be investigated with further multiple scattering calculations, assessments of the other two ingredients (disorder, different domains) will apparently require analysis with the LEED fine-beam angular spot profile technique[65]. That the fourth ingredient may be relevant is perhaps tentatively suggested by the close correspondence (as judged by optimal values of R_p) for the different models considered in Table 6.1. Incidentally all the models optimize R_p with Zr-O interlayer spacings in the range 1.28 to 1.37 Å; the corresponding set of Zr-O bond lengths match the interatomic distance in bulk ZrO to within about 2%.

6.4 STRUCTURE ANALYSIS OF ZR(0001)-(1X1)-O

6.4.1 MULTIPLE SCATTERING CALCULATIONS

The nomenclature of surface models follows the convention for the (2x2) analysis, except that it is now understood that the oxygen adlayers have (1x1) translational symmetry. The non-geometrical parameters used in the (1x1) calculations were exactly the same as those used for the

(2x2) analysis.

The bulk Zr-Zr interlayer spacing used was 2.57 Å. For oxygen underlayers occupying octahedral holes in the bulk, each O layer was assumed to be midway between two successive Zr layers, unless otherwise stated. For surface models with both O overlayer and O underlayer (e.g. (b)A(c)BA.. and (c)A(c)BA..), d_{Zr-O} for the O underlayer was fixed at 1.35 Å (an average value from the (2x2) analysis), while that for the overlayer was varied from 0.7 to 1.4 Å. For the tetrahedral underlayer calculations, the shorter Zr-O spacing was varied from 0.6 to 1.1 Å, while the longer Zr-O spacing was varied from 2.1 to 1.6 Å in such a way that the maximum spacing between the two topmost Zr layers did not exceed 2.7 Å.

The same criteria for selection of either the renormalized forward scattering or the layer doubling method described in Section 6.3.1 were applicable. The notation for input beams follows that of the integral beams of the (2x2) reciprocal lattice depicted in Figure 5.2(b). I(E) curves were calculated at normal incidence, and were domain-averaged before comparing to experimental curves.

6.4.2 RESULTS AND DISCUSSION

Figure 6.10 compares the experimental I(E) curve for the (1,0) beam with the corresponding curves calculated from surface models ranging from O overlayer to bulk O underlayers. The first observation is that I(E) curves

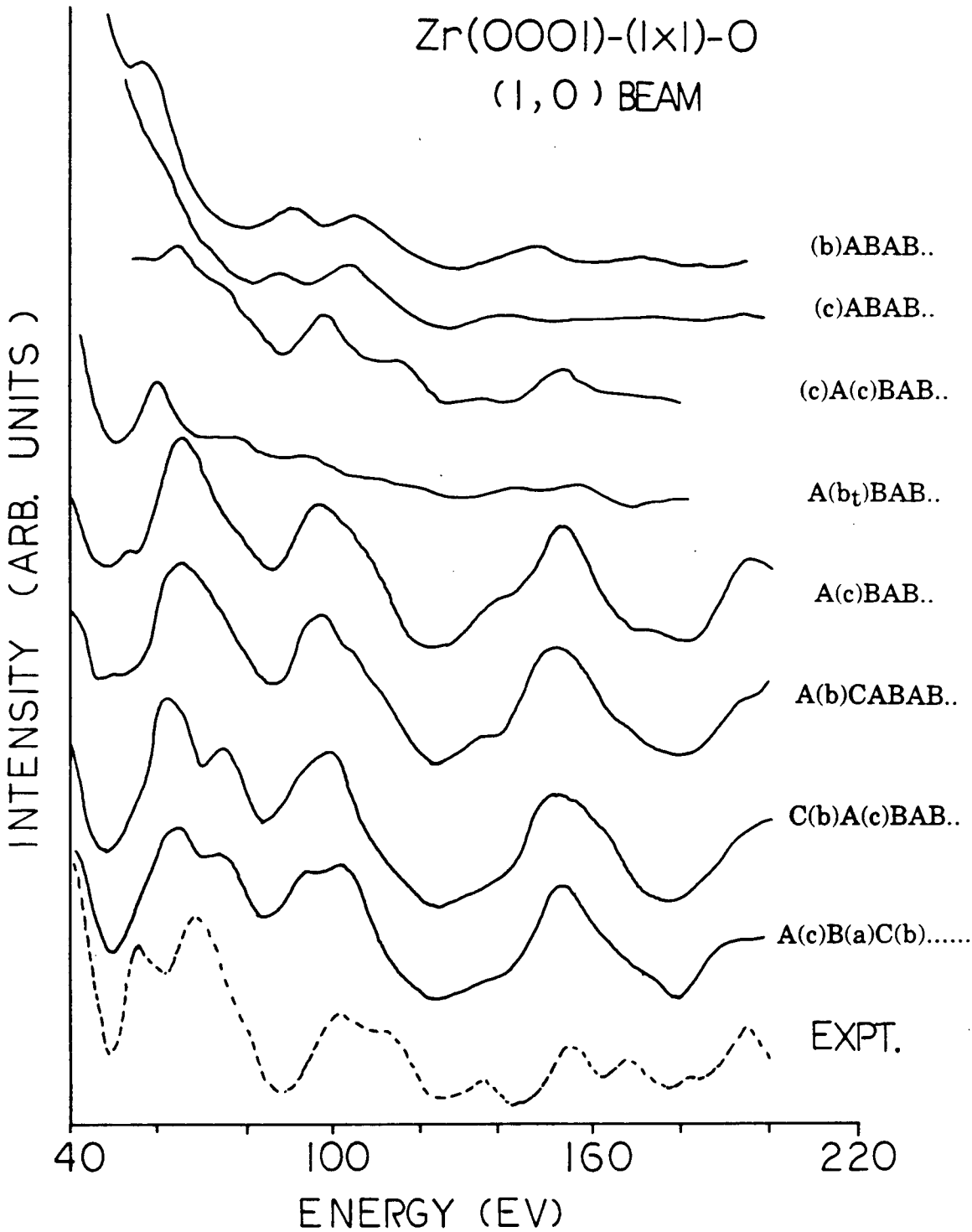

Figure 6.10: Comparison of the experimental I(E) curve of the (1,0) beam with the 'best' curves from selected model calculations for Zr(0001)-(1x1)-O at normal incidence.

calculated from models in which an O overlayer is present show little structure in the energy range of comparison. The same observation has been reported for fractional beams in the (2x2) analysis. The second observation is that I(E) curves calculated from models with single, double, or infinite (i.e. bulk) O layers occupying octahedral holes appear to be visually similar almost regardless of the number of O layers. This suggests that the calculated beam intensities for integral beams are mostly contributed by the substrate Zr atoms, which is presumably the result of the greater scattering strength of Zr compared with O. The latter group of I(E) curves also indicate better correspondence with the experimental curve, although the 'match' is less than ideal.

Table 6.2 reports the minimum values of R_p and their corresponding d_{Zr-O} and V_{or} obtained from the comparisons of experimental I(E) curves (for (1,0) and (1,1) beams) with those from model calculations. These values were derived from contour plots, which are described in Section 6.3.2. The models investigated in Table 6.2 can again be categorized as: (i) overlayer, or combinations of overlayer and a single underlayer,(ii) single underlayer, and (iii) multi-underlayers. Category (i) has high average R_p values, which tend to support the conclusion that O overlayers do not form on Zr(0001) at low exposures, thereby showing some consistency with observations from different techniques for studies of oxygen chemisorption on the Ti(0001)

Surface	R_p	d_{Zr-O}(Å)	V_{o_r}(eV)
(b)AB..(hcp)	0.388	1.30	-14.0
(c)AB..(hcp)	0.332	1.47	-10.0
A(b_t)BA..(hcp)	0.365	0.70[1],2.00[2]	-8.0
(b)A(c)BA..(hcp)	0.330	1.40[3],1.35[4]	-8.0
(c)A(c)BA..(hcp)	0.294	1.00[3],1.35[4]	-8.2
A(c)BA..(hcp)	0.264	1.38	-7.4
C(b)AB..(hcp)	0.265	1.39	-7.0
A(b)CAB..(hcp)	0.240	1.37	-7.4
A(c)B(c)AB..(hcp)	0.280	1.37	-6.2
A(c)B(c)AB..(hcp)	0.283	1.37	-6.2
C(b)A(c)BA..(hcp)	0.300	1.37	-8.3
A(b)C(a)BA..(hcp)	0.300	1.37	-8.6
A(c)B(a)C(b).....(fcc)	0.306	1.33	-14.0

[1]Top Zr layer to O layer; [2]O layer to second Zr layer; [3]For O overlayer; [4]For O underlayer.

Table 6.2: Minimum values of multi-beam R_p with the corresponding Zr-O interlayer spacings (d_{Zr-O}) and V_{o_r} obtained from the comparisons of experimental and calculated I(E) curves based on oxygen adsorption models listed in the first column for Zr(0001)-(1x1)-O at normal incidence.

surface[162]. Unlike the (2x2) analysis, the smallest values of R_p fall in the group of single O underlayer in which O atoms occupy the octahedral holes between the first two Zr layers. However not much weight should be given to this conclusion considering the fact that the experimental I(E) data are only available for two beams. Nevertheless information at this stage is still useful since it sets limitations on possible models for further analyses.

The lowest value of R_p found so far for the Zr(0001)-(1x1)-O surface structure is 0.240 for the surface model A(b)CAB.., in which the O atoms occupy octahedral holes between the first two Zr layers, while the registry of the second layer is shifted so that the second, third and fourth Zr layers resemble three fcc(111) layers. The latter shift of registry again indicates that some degree of fcc reconstruction is favored for the incorporation of oxygen into the bulk of zirconium. Figure 6.11 compares the two experimental I(E) curves with the corresponding curves calculated from A(b)CAB.., while the R-factor contour plot for this model is depicted in Figure 6.12. Although the value of R_p for this model calculation is quite satisfactory, this study only yields preliminary results for the Zr(0001)-(1x1)-O system since a very limited beam set was available. For a complete analysis, more experimental data (e.g. off-normal incidence I(E) curves) are required. Nevertheless for the favored model, the first three atomic layers correspond to the (111) layers of ZrO, which is

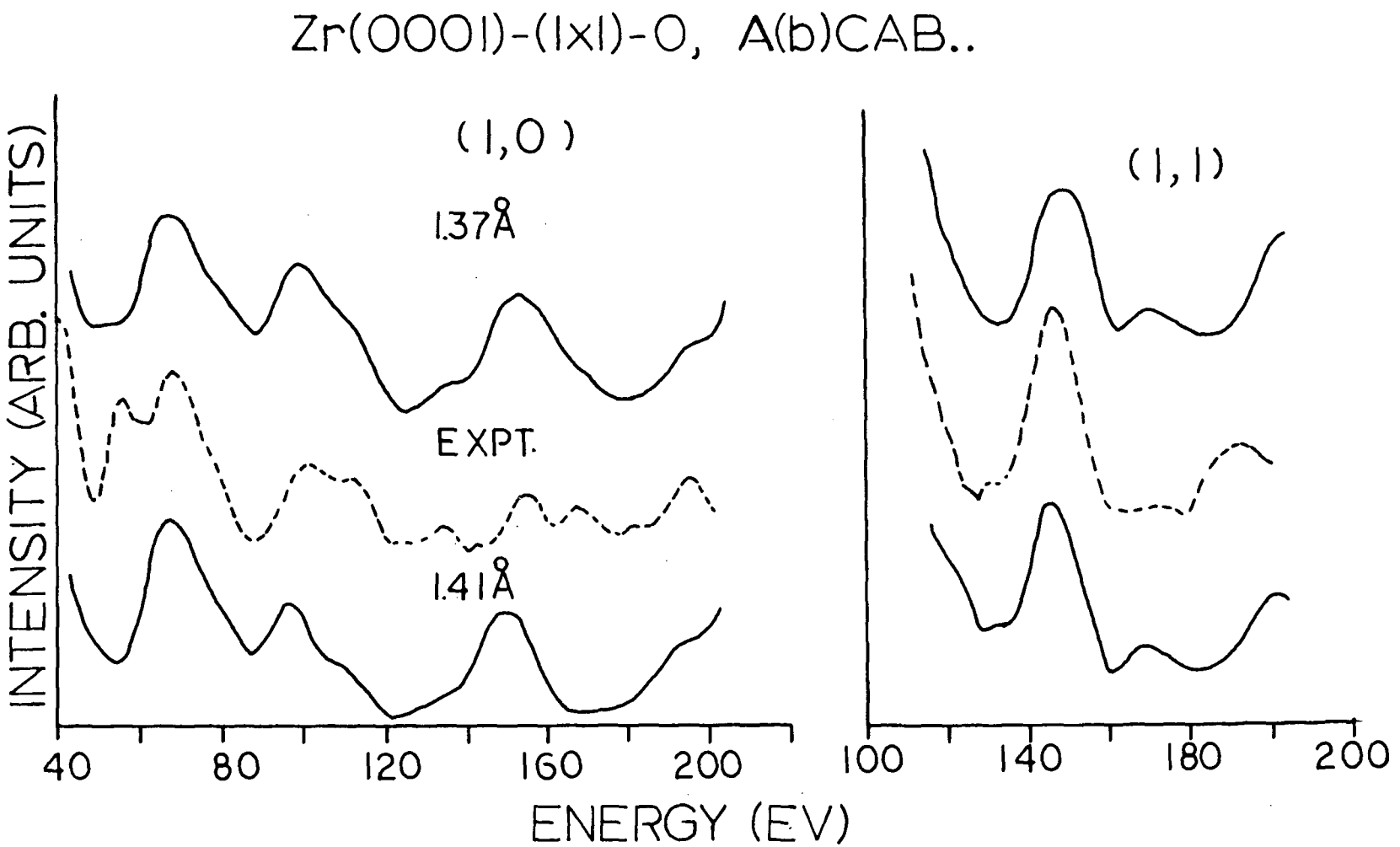

Figure 6.11: Comparison of experimental I(E) curves (dotted lines) for two diffracted beams from Zr(0001)-(1x1)-O with the corresponding I(E) curves calculated for the adsorption model A(c)CAB.. at normal incidence with d_{Zr-O} at either 1.37 or 1.41 Å.

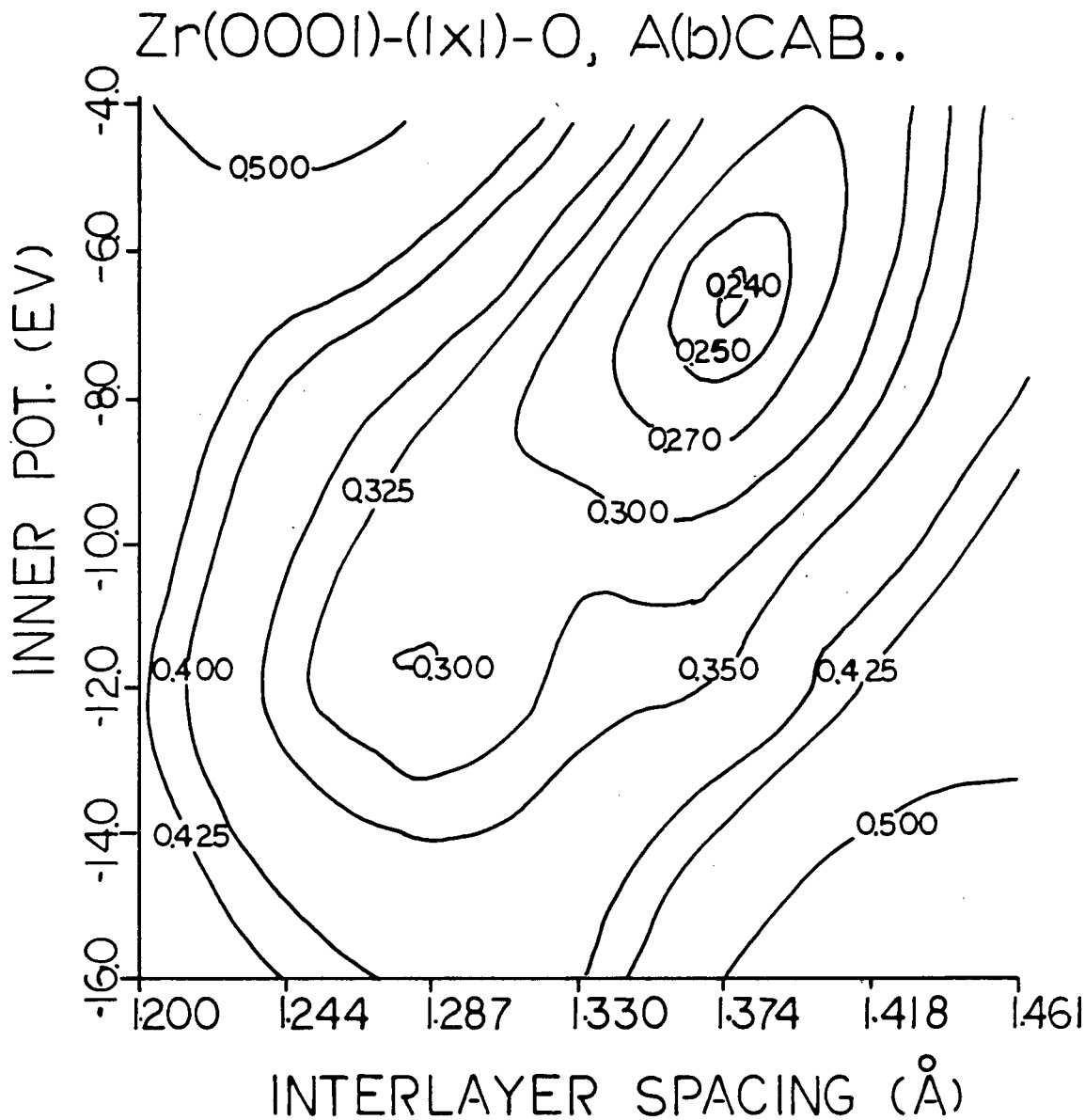

Figure 6.12: Contour plot of multi-beam R_p for Zr(0001)-(1x1)-O versus V_{or} and Zr-O interlayer spacing for the adsorption model designated A(b)CAB.. at normal incidence.

consistent with the conclusion for Ti(0001)-(1x1)N reported by Shih *et al.*[41]. Moreover, the reported value of d_{Zr-O} equal to 1.37 Å seems quite plausible. This value suggests that the interstitial O atoms expand the Zr-Zr interlayer spacing by 6.6% from that in zirconium metal. The resulting LEED-determined Zr-O bond distance of 2.31 Å agrees exactly with the value given by X-ray diffraction for bulk ZrO[168].

6.4.3 VARIATION OF PHASE SHIFTS

With the preliminary knowledge of the possible formation of ZrO (at least in the top three layers), it seems appropriate to assign some negative charge to oxygen and to repeat the multiple scattering calculations for the surface models A(c)BA.., C(b)AB.. and A(b)CAB.. to see if any improvement can be obtained. For this purpose, five additional sets of phase shifts were considered for O and Zr corresponding to ionic charges of 0.00, 0.50, 1.00, 1.50 and 2.00 (here it is understood that the charge is positive for Zr and negative for O). The ion core potentials for each of these species were derived following Matheiss[93] for a sodium chloride type ZrO lattice (Figure 3.4), in which O has the same local environment as in the adsorption model; the input wavefunctions for atomic Zr and O were obtained from Clementi and Roetti[169], and the exchange terms (α) used were 0.70 and 0.74 for Zr and O respectively. The 'muffin-tin' radii for Zr (r_{Zr}) and O (r_O) were estimated by matching the radial distributions of the potentials for Zr

Charge	r_O(Å)	r_{Zr}(Å)	Potential (eV)
0.00	1.01	1.30	-13.12
0.50	1.05	1.26	-11.12
1.00	1.09	1.22	-9.06
1.50	1.11	1.20	-6.14
2.00	1.13	1.18	-4.78

Table 6.3: Variation of 'muffin-tin' radii for O (r_O) and Zr (r_{Zr}) with ionic charge on O (negative) and Zr (positive) respectively from calculations of ion core potentials for the two species in a ZrO crystal lattice. The values of the potential at hte 'muffin-tin' radii for each ZrO lattice with the specified ionic character for the two species are also given.

Surface	R_p	d_{Zr-O}(Å)	V_{or}(eV)
(i) O^0			
A(c)BA..(hcp)	0.330	1.41	-6.0
C(b)AB..(hcp)	0.360	1.39	-4.5
A(b)CAB..(hcp)	0.340	1.39	-6.0
(ii) O^{-1}			
A(c)BA..(hcp)	0.316	1.20	-5.0
C(b)AB..(hcp)	0.326	1.38	-6.0
A(b)CAB..(hcp)	0.307	1.38	-5.5
(iii) O^{-2}			
A(c)BA..(hcp)	0.330	1.15	-5.0
C(b)AB..(hcp)	0.300	1.20	-8.0
A(b)CAB..(hcp)	0.360	1.39	-5.0

Table 6.4: Minimum values of multi-beam R_p for Zr(0001)-(1x1)-O at normal incidence. The corresponding values of d_{Zr-O} and V_{or} were obtained from the comparisons of experimental and calculated I(E) curves, for adsorption models in which the three topmost layers correspond to the three (111) layers of ZrO lattice. O phase shifts used were derived from ion core potentials of (i) O^0, (ii) O^{-1} and (iii) O^{-2} in a ZrO lattice.

and O. The nuclei of these species were fixed at 2.31 Å apart, and the distribution curves of potentials were drawn in opposite directions until they crossed each other. The latter crossing point to the respective centers of the two species then defined the 'muffin-tin' radii. Table 6.3 summarizes values so obtained for the 'muffin-tin' radii and the associated potential (in each case the latter may be seen as a first approximation for V_{0r}).

Multi-beam minimum R_p resulting from multiple scattering calculations utilizing three sets of these new phase shifts for O are given in Table 6.4. Although no improvement on minimum R_p is indicated in this study, the trend in the average value of minimum R_p for the three surface models suggests that some partial negative charge on O may be more favorable. The 'muffin-tin' radii for O given in Table 6.3 appear unusually large. In future studies it may be preferable to calculate the ion core potentials in clusters with some self-consistent charge adjustment.

6.5 INTERPRETATION OF ADSORBATE COVERAGES

In order to determine the oxygen uptake characteristics of the Zr(0001) surface, research grade oxygen (Matheson 99.99% purity) was leaked into the FC12 chamber through a leak valve (with both the titanium sublimation pump and the main ion pump operating) at room temperature, at a pressure of 5×10^{-9} torr indicated by an ionization gauge in the chamber. No detectable changes were observed in the mass

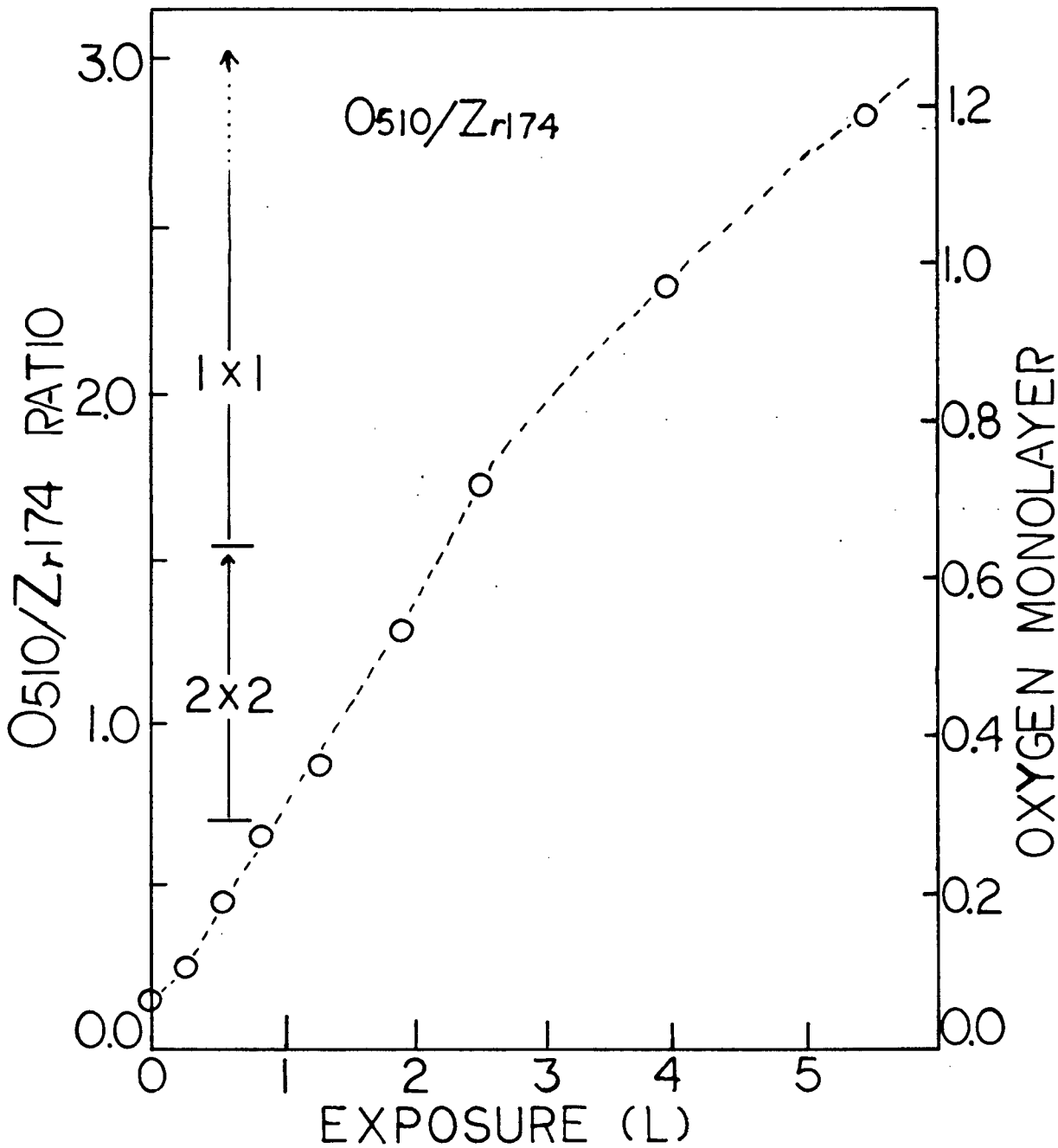

Figure 6.13: A plot of Auger peak ratio O_{510}/Zr_{174} and estimated oxygen monolayer as a function of O_2 exposure (in Langmuir, 1 L = 10^{-6} torr s) to the (0001) surface of zirconium. The oxygen coverages for the appearance of the (2x2) and (1x1) patterns are also given.

spectra, or in surface contamination levels as indicated by AES. The Auger peak height ratio O_{510}/Zr_{174} was measured as a function of oxygen exposure, as shown in Figure 6.13. No breaks were apparent in this curve around the coverages that correspond to the (2x2) and (1x1) LEED patterns. The other observation (not shown in the figure) was that the curve did not level off even at the high oxygen exposure ($\simeq$20 L) considered in the experiment, although the slope did decrease. This behavior may be attributed to the ease of formation of oxygen multi-overlayers on group 4 metal surfaces[164], or to the fact that the Zr_{174} peak (which corresponds to an MVV Auger transition) is attenuated with high oxygen coverages[157].

The lack of apparent breaks in the oxygen uptake curve means that there are no reference coverages for calibration of the O_{510}/Zr_{174} ratio. The fractional monolayer oxygen coverages given in Figure 6.13 were actually calibrated using CO uptake data of Moore[130], which are shown in Figure 6.14. Here C_{272}/Zr_{174} and O_{510}/Zr_{174} Auger peak height ratios are plotted against CO exposure. In contrast to the oxygen exposure experiment, the uptake curve of CO shows a sharp break at saturation coverage, where a (1x1) LEED pattern appears†. The same uptake behavior was also observed for heteronuclear molecules (e.g. CO, NO and N_2O) on polycrystalline zirconium surfaces by Foord *et al.*[157].

---

†This pattern was also observed in this work, and some preliminary I(E) data were collected at normal incidence. It is hoped that analysis can be done in the future when the oxygen problem is fully solved.

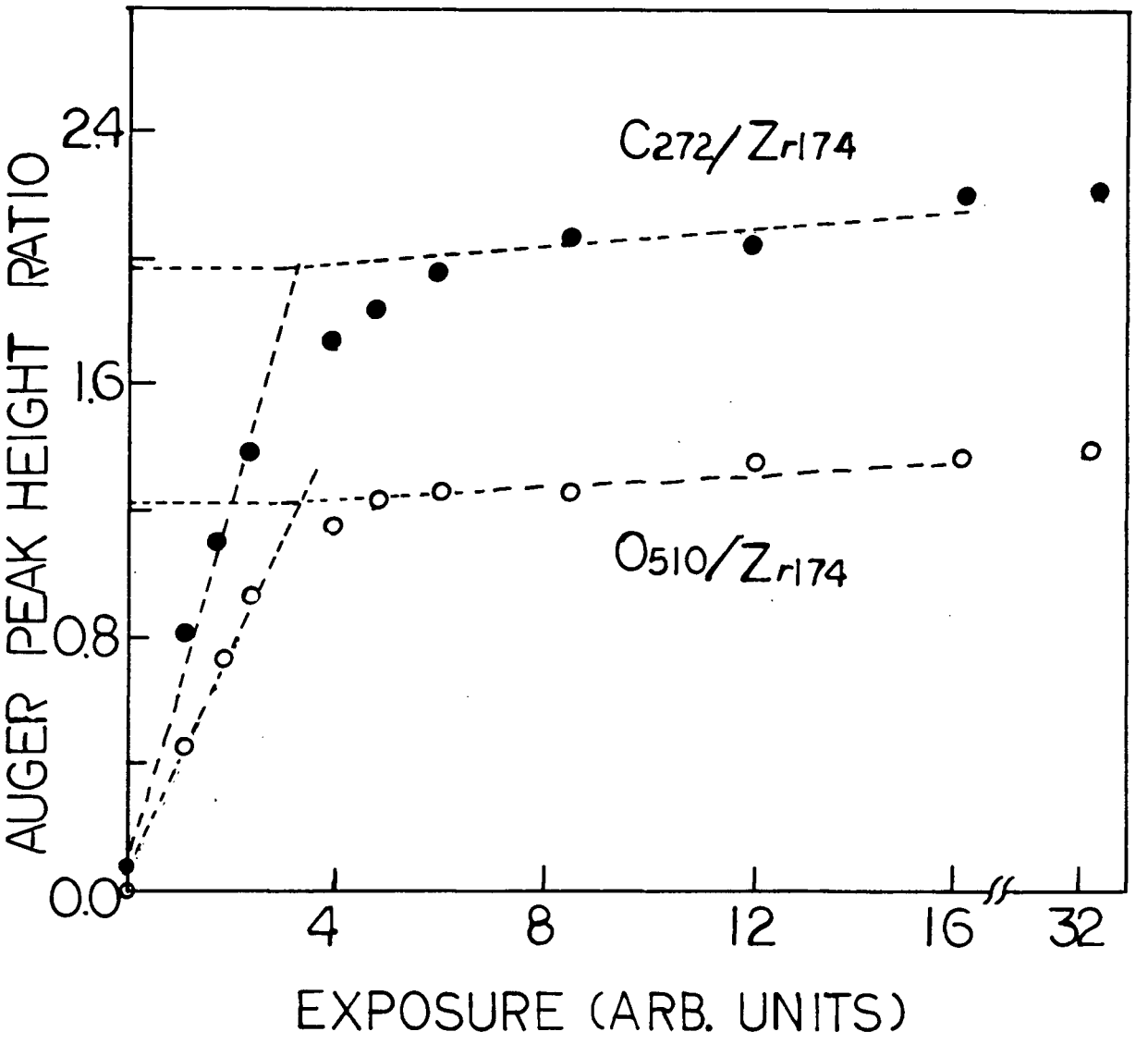

Figure 6.14: A plot of Auger peak ratios O_{510}/Zr_{174} and C_{272}/Zr_{174} as a function of CO exposure to the (0001) surface of zirconium. The values of O_{510}/Zr_{174} and C_{272}/Zr_{174} at the intersections of the tangents of the steep part and of the flat part of the curves are used as reference for half monolayer each of O and C respectively (after Moore[130]).

These authors suggested that these molecules chemisorb dissociatively on the metal surface, probably with an initial 'head-on' physisorption at specific sites; once these sites are occupied (e.g. by a monolayer of CO) subsequent chemisorption is slow. If an additional assumption is made that C and O atoms are in the same plane (which is suggested by the preliminary, but incomplete, LEED analysis of Ti(0001)-(2x2)-CO[40]), then the saturation coverage corresponds to half monolayer each of C and O atoms†. By extrapolation of the tangent of the rapidly rising part and of the relatively leveled part of the uptake curve (Figure 6.14), saturation Auger peak ratios for C_{272}/Zr_{174} and O_{510}/Zr_{174} are found to be approximately 1.9 and 1.2 respectively.

The level of carbon contamination for a cleaned Zr(0001) surface (Section 6.2.1) was estimated by dividing the minimum recorded value of C_{272}/Zr_{174} (about 0.1) by 3.8, which gives the approximately 3% of a monolayer referred to earlier.

Using O_{510}/Zr_{174}=1.2 to indicate a half monolayer of O, the peak height ratios for oxygen uptake curve in Figure 6.13 were all divided by 2.4 to yield the fractional monolayer coverage on the right hand y-axis. The (2x2)-O pattern was observed for oxygen coverages between 0.3 and 0.65 monolayer, while the (1x1) pattern was observed from

---

† In principle C could form an overlayer while O forms an underlayer, in which case the saturation coverage corresponds to one monolayer each of C and O.

0.65 to greater than monolayer oxygen coverages. The sharpest (1x1) LEED pattern was obtained at about 0.8 monolayer coverage, and therefore that is apparently consistent with a single underlayer of O atoms conforming to the (1x1) translational symmetry. The Auger data for the (2x2) pattern are not as clear cut as those for (1x1). Here the sharpest pattern was observed for oxygen coverage around 0.37 monolayer. With this value alone, it is difficult to decide whether O atoms conform to the (2x2) or (2x1) translational symmetries, which correspond to 0.25 and 0.5 monolayer of O atoms respectively. Perhaps the (2x2) translational symmetry is favored, however, since then it is possible to form almost two underlayers of O atoms in relatively fully occupied domains.

6.6 CONCLUSIONS AND FUTURE WORK

This study has yielded preliminary structural data for the Zr(0001)-(2x2)-O and Zr(0001)-(1x1)-O surfaces. This represents the first surface structural information available for oxygen chemisorption on a hcp metal. In both structures considered here O atoms are indicated to occupy octahedral holes between Zr layers which in turn reconstruct to show fcc packing. Although the favored models have some consistency with the bond length in bulk ZrO, and with the previously reported underlayer formation in Ti(0001)-(1x1)-N, the surface structures for O on Zr(0001) still appear challenging.

Now that the geometrical structures for these two oxygen adsorption structures have become clearer, it seems appropriate to have further experimental I(E) curves (e.g. measurements carried out at off-normal incidence) to enable more detailed comparisons with calculated I(E) curves to refine both geometrical and physical parameters. To resolve the problem of (2x2) versus (2x1) translational symmetry for adsorbed oxygen, experimental I(E) curves collected at shallow angles of incidence should be especially useful. In this regard, it will also be helpful to measure the angular spot profiles of fractional order beams as a function of oxygen exposure. The full width at half maximum (FWHM) of the profiles is expected to increase as the degree of order decreases; correspondingly a (2x2) to (2x1) transition should be indicated by a rise in the FWHM. A preliminary study of this is currently being undertaken with our VLA[170], but a fine-beam spot profile analyzer (SPA) would be very helpful to probe aspects of disorder and domain structure over greater dimensions than we can do currently. As to the extent of O incorporation into the bulk, the oxygen signal from XPS can be monitored as a function of incidence angles of the X-ray beam. The number of layers probed by the primary beam will increase as the incidence direction moves towards the normal. Such studies should give a semi-quantitative depth profile for oxygen.

The calibration of oxygen coverage using the CO uptake data (Section 6.5) can still be improved. To answer whether

the O and C atoms are in the same plane, the C_{272}/O_{510} Auger peak ratio could be measured as a function of Ar^+ bombardment of the Zr(0001) surface that gives a (1x1)-CO pattern. A decrease of the ratio would presumably indicate C overlayer and O underlayer (assuming C and O have similar sputtering yields). The use of nuclear microanalysis and Rutherford backscattering should be particularly helpful for clarifying coverages and structural conclusions proposed in this work.

REFERENCES

1. C.J. Davisson and L.H. Germer, Phys. Rev. 30, 705(1927).

2. T. Rhodin and S.Y.Tong, Phys. Today, p23, Oct(1975).

3. J.E. Inglesfield, Prog. Surf. Sci. 20, 105(1985).

4. See the compilations by (a) G.A. Somorjai, "Chemistry in Two Dimensions: Surfaces", Cornell Univ. Press, 1981; and (b) K.A.R. Mitchell, "Low Energy Electron Diffraction", to be published.

5. See, for example, (a) R.J. Koestner, M.A. Van Hove and G.A. Somorjai, J. Phys. Chem. 87, 203(1983); and (b) L.L. Kesmodel, L.H. Dubois and G.A. Somorjai, J. Chem Phys. 70, 2180(1979).

6. See, for example, (a) C.B. Duke, A. Paton, R.J. Meyer, L.J. Brillson, A. Kahn, D. Kanani, J. Carrelli, J.L. Yeh, G. Margaritondo and A.D. Katnani, Phys. Rev. Lett. 46, 440(1981); and (b) A.Kahn, D. Kanani, J. Carrelli, J.L. Yeh, C.B. Duke, R.J. Meyer, A. Paton and L.J. Brillson, J. Vac. Sci. Technol. 18, 792(1981).

7. R.M. Flemming, D.B. McWham, A.C. Gossard, W. Wiegmann and R.A. Logan, J. Appl. Phys. 51, 357(1980).

8. G. Ertl and J. Kuppers, "Low Energy Electrons and Surface Chemistry", Verlag Chemie(1974).

9. T.A. Carlson, "Photoelectron and Auger Spectroscopy", Plenum, N.Y.(1975).

10. H. Ibach and D.L. Mills, "Electron Energy Loss Spectroscopy and Surface Vibrations", Academic Press, N.Y.(1982).

11. J.B. Pendry, "Low Energy Electron Diffraction", Academic Press, N.Y.(1974).

12. M.G. Lagally and J.A. Martin, Rev. Sci. Inst. 54, 1273(1983).

13. J.M. Van Hove, C.S. Lent, P.R. Pukite and P.I. Cohen, J. Vac. Sci. Technol. B1, 741(1983).

14. M.J. Cardillo and G.E. Becker, Phys. Rev. B21, 1497(1980).

15. E. Taglauer, Appl. Phys. A38, 161(1985).

16. R.A. Baragiola, in "Inelastic Particle-Surface

Collisions", eds. E. Taglauer and W. Heiland, Springer Ser. Chem. Phys. 17, 38(1981).

17. G. de Roos, J.M. Fluit, J.H.W. deWit and J.W. Geus, Surf. Interface Anal. 3, 229(1981).

18. W. Heiland and E. Taglauer, Methods Expt. Phys. 22, 299(1985).

19. C.S. Fadley, Prog. Surf. Sci. 16, 275(1984).

20. D.H. Rosenblatt, J.G. Tobin, M.G. Mason, R.F. Davis, S.D. Kevan, D.A. Shirley, C.H. Li and S.Y. Tong, Phys. Rev. B23, 3829(1981).

21. J. Stohr, in "X-ray Absorption: Principles, Applications, Techniques of EXAFS, SEXAFS, XANES", eds. R. Prins and D. Koningberger, Wiley, N.Y.(1985).

22. P. Eisenberger, P. Citrin, R. Hewitt and B. Kincaid, Crit. Rev. Solid State and Material Sci. 10(2), 191(1981).

23. F.J. Himpsel, Adv. Phys. 32, 1(1983).

24. M. Nielsen, J. Als-Nielsen, J. Bohr and J.P. McTaque, Phys. Rev. Lett. 47, 582(1981).

25. M.P. Seah and P. Dench, Surf. Interface Anal. 1, 1(1979).

26. P. Auger, J. Phys. Radium 6, 205(1925).

27. M. Aono, Nucl. Inst. Methods Phys. Res. B2, 374(1984).

28. P.H. Citrin, P.Eisenberger and R.C. Hewitt, J. Vac. Sci. Technol. 15, 449(1978).

29. J.P. Batra and L. Kleiman, J. Elec. Spec. Rel. Phenom. 33, 175(1984), and references therein.

30. S.D. Kevan, R.F. Davis, D.H. Rosenblatt, J.G. Tobin, M.G. Mason, D.A. Shirley, C.H. Li and S.Y. Tong, Phys. Rev. Lett. 46, 1629(1981), and references therein.

31. J.T. Yates, Jr., Methods Expt. Phys. 22, 425(1985).

32. M. Aono, C. Oshima, S. Zaima, S. Otani and Y. Ishizawa, Jpn. J. Appl. Phys. 20, L829(1981).

33. T.N. Rhodin and J.W. Gadzuk, in "The Nature of The Surface Chemical Bond", eds. T.N. Rhodin and G. Ertl, North-Holland Pub. Co. Amsterdam (1979).

34. R.P. Messmer, Surface Sci. 158, 40(1985).

35. T.N. Rhodin, C. Brucner and A. Anderson, J. Phys. Chem. 82, 894(1978).

36. G.A. Somorjai, Acc. Chem. Res. 9, 248(1976).

37. G.A. Somorjai and F. Zaera, J. Phys. Chem. 86, 3070(1982).

38. (a)K.A.R. Mitchell, Surface Sci. 149, 93(1985); (b)K.A.R. Mitchell, S.A. Schlatter and R.N.S. Sodhi, Can. J. Chem., in press.

39. H.D. Shih, F. Jona, D.W. Jepsen and P.M. Marcus, Phys. Rev. B15, 5550(1977).

40. H.D. Shih, F. Jona, D.W. Jepsen and P.M. Marcus, J. Vac. Sci. Technol. 15, 596(1978).

41. H.D. Shih, F. Jona, D.W. Jepsen and P.M. Marcus, Surface Sci. 60, 445(1976).

42. J.H. Scheml and H.S. Rosenbaum, "Zirconium in Nuclear Applications", Am. Soc. for Testing and Materials, Special Tech. Publn. 551, Philadelphia(1973).

43. W.T. Moore, P.R. Watson, D.C. Frost and K.A.R. Mitchell, J. Phys. C12, L887(1979).

44. (a) M.A. Van Hove and S.Y. Tong, Phys. Rev. Lett. 35, 1092(1975); and (b) C.M. Chan, K.L. Luke, M.A. Van Hove, W.H. Weinberg and S.P. Withrow, Surface Sci. 78, 386(1978).

45. A. Messiah, "Quantum Mechanics Vol. 2", North-Holland Pub. Co. Amsterdam(1961).

46. E. Merzbacher, "Quantum Mechanics", John Wiley and Sons, N.Y.(1961).

47. N.W. Ashcroft and N.D. Mermin, "Solid State Physics", Holt, Rinehart and Winston, 1976.

48. E.A. Wood, J. Appl. Phys. 35, 1306(1964)

49. R.L. Park and H.H. Madden, Surface Sci. 11, 188(1968).

50. P.J. Estrup and E.J. McRae, Surface Sci. 25, 1(1971).

51. M.A. Van Hove, Rongfu Lin and G.A. Somorjai, Phys. Rev. Lett. 51, 778(1983).

52. S. Andersson and B. Kasemo, Surface Sci. 25, 273(1971).

53. J.R. Noonan and H.L. Davis, Surface Sci. 99, L424(1980).

54. H.L. Davis and J.R. Noonan, Surface Sci. 115, L75(1982).

55. (a)E.G. McRae, Surface, 42, 413(1974); (b)E.G. McRae, Surface Sci. 42, 427(1974); (c)E.G. McRae and C. Gaubert, Surface Sci. 42, 404(1974).

56. M.A. Van Hove and S.Y. Tong, "Surface Crystallography by LEED", Springer Verlag, Berlin(1979).

57. M.A. Van Hove, Surface Sci. 49, 181(1975).

58. R. M. Stern and F. Balibar, Phys. Rev. Lett. 25, 1338(1970).

59. S. Andersson and J.B. Pendry, J. Phys. C6, 60(1973).

60. M.G. Lagally, Methods Expt. Phys. 22, 237(1985).

61. J.M. Blakely, "Introduction to the Properties of Crytstal Surfaces", Pergamon Press, N.Y.(1973).

62. M. Henzler, Surface Sci. 152/153, 963(1985).

63. P.O. Hahn and M. Henzler, J. Appl. Phys. 52, 4122(1981), and references therein.

64. G. Comsa, Surface Sci. 81, 57(1979).

65. M.G. Lagally, Springer Ser. Chem. Phys. 20, 281(1982), and T.M. Lu and M.G. Lagally, Surface Sci. 99, 695(1980).

66. M.P. Chung and L.H. Jenkins, Surface Sci. 22, 479(1970).

67. D. Roy and J.D. Carette, "Electron Spectroscopies for Surface analysis", p13, ed. H. Ibach, Springer Verlag, Berlin(1977).

68. C.C. Chang, Surface Sci. 25, 53(1971).

69. M.Y. Zhou, R.H. Milne, M.A. Karolewski, D.C. Frost and K.A.R. Mitchell, Surface Sci. 139, L181(1984).

70. C.D. Wagner, Disc. Faraday Soc. 60, 291(1975).

71. Y. Strausser and J.J. Uebbing, "Varian Chart of Auger Electron Energies", Varian Corp. Palo Alto(1970).

72. P.W. Palmberg, G.E. Riach, R.E. Weber and N.C. MacDonald, "Handbook of Auger Electron Spectroscopy", Phys. Elec. Ind., Edima, Minnesota(1972).

73. C.C. Chang, in "Characteristics of Solid Surfaces",

eds. P.F. Kane and G.B. Larrakee, Plenum, N.Y.(1975).

74. S. Mroczkowski and D. Lichtman, Surface Sci. 131, 159(1983), and 127, 119(1983).

75. J. Ferron, L.S. de Bernardez and R.H. Buitrago, Surface Sci. 145, L501(1984).

76. M. Perdereau, Surface Sci. 24, 239(1971).

77. J.A. Davies and P.R. Norton, Nucl. Inst. Methods, 168, 611(1980).

78. R.E. Weber, A.L. Johnson, J. Appl. Phys. 40, 314(1969).

79. M.A. Van Hove, R.J. Koestner, J.C. Frost and G.A. Somorjai, Surface Sci. 129, 482(1983).

80. W. Erley, Surface Sci. 94, 281(1980).

81. S.Y. Tong, Prog. Surf. Sci. 7, 1(1975).

82. C.B. Duke, Adv. Chem. Phys. 27, 1(1974)

83. J.L. Beeby, J. Phys. C1, 82(1968).

84. (a)E.G. McRae, J. Chem. Phys. 45, 3258(1966); (b)E.G. McRae, Surf. Sci. 11, 479(1968).

85. M.A. Van Hove and S.Y. Tong, in "Determination of Surface Structure by LEED", eds. P.M. Marcus and F. Jona, Plenum Press, N.Y.(1984).

86. P.M. Marcus, in "Determination of Surface Structure by LEED", eds. P.M. Marcus and F. Jona, Plenum Press, N.Y.(1984).

87. J.C. Slater, in "Methods in Computational Physics, Vol. 8", eds. B. Alder, S. Fernbach and M. Roternberg, Academic Press, N.Y.(1968).

88. J.C. Slater, Phys. Rev. 51, 840(1937).

89. D.W. Jepsen, P.M. Marcus and F. Jona, Phys. Rev. B8, 5523(1973).

90. P.J. Feibelman, C.B. Duke and A. Bagchi, Phys. Rev. B5, 2436(1972).

91. S.Y. Tong, J.B. Pendry and L.L. Kesmodel, Surface Sci. 54, 21(1976).

92. T.L. Loucks, "Augmented Plane Wave Method", Benjamin, N.Y.(1967).

93. L.F. Matheiss, Phys. Rev. 133, A1399(1964).

94. F. Herman and S. Skillman, "Atomic Structure Calculations", Prentice Hall, Englewood Cliffs(1963).

95. E. Clementi, IBM J. Res. Develop. 9, 2(1965).

96. V.L. Moruzzi,J.F. Janak and A.R. Williams, "Calculated Electronic Properties of Metals", Pergamon Press, N.Y.(1978).

97. A magnetic tape provided by M.A. Van Hove, 1983.

98. J.E. Demuth, D.W. Jepsen and P.M. Marcus, Surface Sci. 45, 733(1974).

99. D.W. Jepsen, P.M. Marcus and F. Jona, Phys. Rev. B5, 3933(1972).

100. K. Kambe, Z. Naturforsch, A22, 322(1967); and A23, 1280(1968).

101. D.W. Jepsen, H.D. Shih, F. Jona and P.M. Marcus, Phys. Rev. B22, 814(1980).

102. S.Y. Tong and M.A. Van Hove, Phys. Rev. B16, 1459(1977).

103. B.W. Holland and D.P. Woodruff, in "Determination of Surface Structure by LEED", eds. P.M. Marcus and F. Jona, Plenum Press, N.Y.(1984).

104. J.B. Pendry, Phys. Rev. Lett. 27, 856(1971).

105. S.Y. Tong, Solid State Comm. 16, 91(1975).

106. M.A. Van Hove and G.A. Somorjai, Surface Sci. 114, 171(1982).

107. W.T. Moore, S.J. White, D.C. Frost and K.A.R. Mitchell, Surface Sci. 116, 253(1982).

108. J.P. Hobson, J. Vac. Sci. Technol. A2, 144(1984).

109. G.L. Weissler and R.W. Carlson, "Vacuum Physics and Technology", Academic Press, N.Y.(1979).

110. J.H. Lech, Contemp. Phys. 20, 401(1979).

111. N.F.M. Henry, H. Lipson and W.A. Wooster, "The Interpretation of X-Ray Diffraction Photographs", MacMillan, London(1960).

112. G.L. Price, Rev. Sci. Instrum. 51, 1000(1980).

113. G.A. Bennett and R.B. Wilson, J. Sci. Instrum. 43, 669(1966).

114. J.S. Foord, P.J. Goddard and R.M. Lambert, Surface Sci. 94, 339(1980).

115. N.J. Taylor, in "Techniques of Metals Research, Vol. 7", ed. R.F. Bunshah, Interscience, N.Y.(1972).

116. J. Landau, J.C. Helmer and J. Uebbing, Rev. Sci. Instrum. 44, 265(1973).

117. N.J. Taylor, Rev. Sci. Instrum. 40, 792(1969).

118. R. Nathan and B.J. Hopkins, J. Phys. E6, 1040(1973).

119. P.W. Palmberg, G.K. Bohn and J.C. Tracy, Appl. Phys. Lett. 15, 254(1969).

120. J. Adams and B.W. Manley, Electron Eng. 37, 180(1965).

121. D.G. Welkie and M.G. Lagally, Appl. Surf. Sci. 3, 272(1979).

122. M.D. Chinn and S.C. Fain, Jr., J. Vac. Sci. Technol. 14, 314(1977).

123. L. de Bersuder, Rev. Sci. Instrum. 45, 1569(1974).

124. H.E. Farnsworth, Phys. Rev. 34, 679(1929).

125. J.J. Lander, J. Morrison and F. Unterwald, Rev. Sci. Instrum. 33, 782(1962).

126. L. McDonnell and D.P. Woodruff, Surface Sci. 46, 505(1974).

127. P.C. Stair, T.J. Kaminska, L.L. Kesmodel and G.A. Somorjai, Phys. Rev. B11, 623(1975).

128. D.C. Frost, K.A.R. Mitchell, F.R. Shepherd and P.R. Watson, J. Vac. Sci. Technol. 13, 1196(1976).

129. K.O. Legg, M. Prutton and C. Kinniburgh, J. Phys. C7, 4236(1974).

130. W.T. Moore, Ph.D. thesis, Univ. British Columbia, 1981.

131. P. Heilmann, E. Lang, K. Heinz and K. Müller, Appl. Phys. 9, 247(1976).

132. E. Lang, P. Heilmann, G. Hanke, K. Heinz and K. Müller, Appl. Phys. 19, 287(1979).

133. H. Leonhard, A. Gutmann and K. Hayck, J. Phys. E13,

298(1980).

134. P. Heilmann, E. Lang, K. Heinz and K. Müller, in "Determination of Surface Structure by LEED", eds. P.M. Marcus and F. Jona, Plenum Press, N.Y.(1984).

135. H. H. Madden and G. Ertl, Surface Sci. 35, 211(1973).

136. R.M. Lambert and C.M. Comrie, Surface Sci. 38, 197(1973).

137. R.G. Musket, Surface Sci. 21, 440(1970).

138. J.A. Strozier, Jr. and F. Jona, private communication.

139. W.S. Yang, F. Jona and P.M. Marcus, Phys. Rev. B27, 1394(1983).

140. S.Y. Tong, M.A. Van Hove and B.J. Mrstik, in "Proceedings of the Seventh International Vacuum Congress and the Third International Conference on Solid Surfaces, Vienna, 1977", eds. R. Dobrozemsky *et al.*, F. Berger, Sohne, Vienna(1977).

141. S.Y. Tong and A.L. Maldonado, Surface Sci. 78, 459(1978).

142. H.D. Shih and S.W. Tam, in "Determination of Surface Structure by LEED", eds. P.M. Marcus and F. Jona, Plenum Press, N.Y.(1984).

143. M.A. Van Hove, R.F. Lin, R.J. Koestner and G.A. Somorjai, Bull. Am. Phys. Soc. 28, 538,(1983).

144. E. Zanazzi and F. Jona, Surface Sci. 62, 61(1977).

145. J.B. Pendry, J. Phys. C13, 937(1980).

146. M.A. Van Hove and R.J. Koestner, in "Determination of Surface Structure by LEED", eds. P.M. Marcus and F. Jona, Plenum Press, N.Y.(1984).

147. F. Jona, H.D. Shih, D.W. Jepsen and P.M. Marcus, J. Phys. C12, L455(1979).

148. S. Hengrasmee, Ph.D. thesis, Univ. British Columbia(1980).

149. H.C. Zeng, unpublished work.

150. F. Jona, J.A. Strozier, Jr. and W.S. Yang, Rep. Prog. Phys. 45, 527(1982).

151. U. Bardi, P.N. Ross and G.A. Somorjai, J. Vac. Sci. Technol. A2, 40(1984).

152. G.B. Hoflund, D.A. Asbury, D.F. Cox and R.E. Gilbert, Surface Sci. 22/23, 252(1985).

153. J.M. Lin and R.E. Gilbert, Appl. Surf. Sci. 18, 315(1984).

154. G.B. Hoflund, D.F. Cox and R.E. Gilbert, J. Vac. Sci. Technol. A1, 1837(1983).

155. L.R. Danielson, J. Vac. Sci. Technol. 20, 86(1982).

156. R.L. Tapping, J. Nucl. Mat. 107, 151(1982).

157. J.S. Foord, P.J. Goddard and R.M. Lambert, Surface Sci. 94, 339(1980).

158. B.W. Veal, D.J. Lam and D.G. Westlake, Phys. Rev. B19, 2856(1979).

159. H.D. Shih, K.O. Legg and F. Jona, Surface Sci. 54, 355(1976).

160. F. Jona, private communication with K.A.R. Mitchell.

161. M.J. Pellin, C.E. Young, D.M. Gruen, Y. Aratono and A.B. Dewald, Surface Sci. 151, 477(1985), and references therein.

162. R.L. Strong and J.L. Erskine, J. Vac. Sci. Technol. A3, 1428(1985).

163. F.M. Cain, Jr., "Zirconium and Zirconium Alloys", American Soc. Metals(1953).

164. T.W. Haas, J.T. Grant and G.J. Dooley, Phys. Rev. B1, 1449(1970).

165. E. Fromm and O. Mayer, Surface Sci. 74, 259(1978).

166. K.A. Schneider, Solid State Phys. 16, 275(1964).

167. P.M. Gundry and F.C. Tompkins, Quart. Rev. 14, 257(1960).

168. R.W.G. Wyckoff, "Crystal Structures, Vol. 1", Interscience, N.Y.(1963).

169. E. Clementi and C. Roetti, "Atomic Data and Nuclear Data Table, Vol. 14", Academic Press(1970).

170. P.C. Wong, current studies, Univ. British Columbia.